eman ta zabal zazu

Universidad del País Vasco
Euskal Herriko Unibertsitatea

Crystal structure and phase transition studies in perovskite-type oxides using powder-diffraction techniques and symmetry-mode analysis.

$SrLnMRuO_6$ (*Ln*=La,Pr,Nd; *M*=Zn,Co,Mg,Ni,Fe)
and
$ALn_2CuTi_2O_9$ (*A*=Ca,Ba; *Ln*=La,Pr,Nd,Sm).

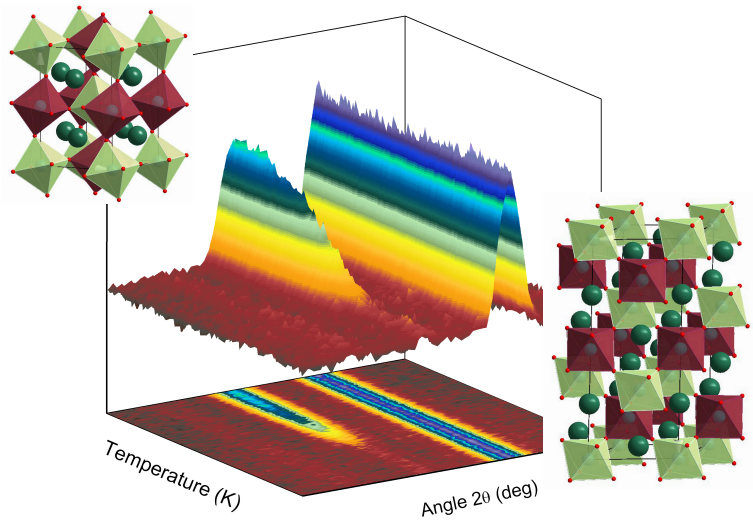

Edurne Iturbe Zabalo

A thesis submitted to apply for the degree of DOCTOR IN PHYSICS
"INTERNATIONAL DOCTOR" mention

Leioa, October 2012

Universidad del País Vasco
Euskal Herriko Unibertsitatea

NEUTRONS FOR SCIENCE®

ZTF-FCT
Zientzia eta Teknologia Fakultatea
Facultad de Ciencia y Tecnología

Crystal structure and phase transition studies in perovskite-type oxides using powder-diffraction techniques and symmetry-mode analysis.

$SrLnMRuO_6$ (*Ln*=La,Pr,Nd; *M*=Zn,Co,Mg,Ni,Fe)
and
$ALn_2CuTi_2O_9$ (*A*=Ca,Ba; *Ln*=La,Pr,Nd,Sm).

Edurne Iturbe Zabalo

Directed by Dr. Josu Mirena Igartua Aldamiz

Supervised at Institut Laue Langevin by Dr. Gabriel Julio Cuello

A thesis submitted to apply for the degree of Doctor in Physics
"International Doctor" mention

Leioa, October 2012

Aritz
eta
etxekoendako

This doctoral thesis has been partially performed within the Diffraction Group of the Institut Laue-Langevin's Science Division, under the scientific supervision of Dr. Gabriel Julio Cuello and the head of division Dr. Juan Rodríguez Carvajal. The PhD student has been the holder of a 3 years fellowship (ref. MBR-GL/09-056) sponsored by the Institut Laue-Langevin.

Acknowledgments

... eta zuk ez galdetu zergatik
nahi bada posible dela
ikusarazteagatik
Aitor Sarriegi
(Bertsolari Txapelketa Nagusia 2009)

It is an enriching exercise to reflect upon the many people who have made possible the culmination of this work, but I am sure will be impossible to mention everybody, so thanks to all (eskerrik asko, gracias, merci).

Lehenik eta behin eskerrak Josuri orain dela lau urte luze lan hau egiteko aukera emanagatik eta denbora guzti honetan erakutsitako laguntasun, konfiantza eta emaniko aholkuengatik. Argi dago momentu askotan ez dela erreza izan, aharik eta zailagoa 1000 Km-ra egonda; baina orain dakidan asko (ez dute dena esango, zerbait nire meritua ere izango da eta) zuri esker dakit, eskerrik asko.

Me gustaría agradecer a toda la gente que pertenece a los departamentos de Física de la Materia Condensada y de Física Aplicada II de la Universidad del País Vasco/Euskal Herriko Unibertsitatea que me ha ayudado durante estos años.

I would like to express my deep gratitude to all the Diffraction Group people from Institut Laue-Langevin (ILL) in Grenoble (France), and in particular to Gabriel J. Cuello, for their assistance during experiments, but especially to their kindness and availability every time I knocked their doors.

Me gustaría agradecer especialmente a Juan Rodríguez Carvajal, Oscar Fabelo, Laura Cañadillas, Alberto Rodríguez Velamazan, Irene Urcelay y Inés Puente por la ayuda prestada (científica y no científica) durante mi larga estancia en Grenoble.

Mil gracias a Abdo por la paciencia mostrada cuando empecé con todo esto y por

todas las cosas que me ha enseñado.

Zerbitzarian (*Bilbao Crystallographic Server*) lanean aritu diren guztiei, baina bereziki Daneli, urte hauetan guztietan nahiz eta gerra asko eman diedan beti laguntzeko prest egon direlako.

Como olvidarme de todas esas personas de los becádromos y posdoc de los departamentos de Física Aplicada II y Física de la Materia Condensada de la UPV/EHU, con las que he convivido al principio y finales de la tesis. A Nerea, cuya vida paralela (nacimiento, carrera, tesis, despacho y defensa) ha sido interesante compartir. La fecha de la boda te la elijo yo. A aquellos que me dieron la bienvenida: Txema, Miguel, Santi, David, Danel, Mariano, Josu, Ion, Josué, Pablo B., Urko, Ibon, Fermin, Luis, Unai U., Leire..., y los que me han dado la segunda bienvenida: Julen, Ainhoa, Brahim, Nora, Bea, Iñaki, Noelia, Emre, Gemma, Sofia, Gerardo...

También a todos aquellos con los que he disfrutado de jornadas de esquí, de montaña y alguna que otra cerveza en Grenoble.

Nola ahaztu Antzuolako kuadrilataz, azken aldian beraiekin pasatako uneek tesiaz gain bizia dagoela ikusten lagundu baitidate.

Eskerrak guraso, anai-arreba eta familiakoei. Badakit ez dela erreza izan une askotan ni alboan izatea, edo ez izatea, baina beti hor egon zarete animoak eman eta laguntzeko.

Eta amaitzeko ... zer esan Aritzi. Tesi hau ziurrenik ez litzateke amaitzear egongo zu alboan izan ez bazintut; bihotzez eskerrik asko poztasunean zein uholdeetan alboan egotearren!

This work would not be possible with out the financial support and multiple human, informatics, equipment, facilities... resources from Applied Physics II, Condensed Matter Physics, and Inorganic Chemistry departments from Universidad del País Vasco/Euskal Herriko Unibertsitatea (UPV/EHU), SGIker General Services from UPV/EHU, and Diffraction Group from Institut Laue-Langevin (ILL). I would like to acknowledge ILL for three years fellowship (MBR-GL/09-056), and Spanish and Basque Governments for financial support (projects MAT2008/05839 and IT-282-07, respectively).

Purpose and Scope of the thesis

Two previous PhD works, and the publications derived from them, in our group had dealt with the synthesis and characterization of families of double perovskites. In both cases the emphasis was sitting, mainly, on the structural characterization at different temperatures and on the analysis of the structural phase-transition sequences. Indeed, one of the main conclusions derived from the later, as a continuation of the conclusions of the former, was the (completed) common phase-transition-sequence vs tolerance-factor phase-diagram.

The starting purpose of the present PhD thesis work was to go a little bit further and try to focus on the physical properties of the new materials; usually showing double-perovskite structures but prone to show multiferroic, electric and magnetic, properties. With that aim in mind, we tried to synthesize some new bismuth containing materials: BiNa$BB'O_6$ (B=Co,Ni; B'=W,Sb), $Bi_2BB'O_6$ (B and B'=Co,Cr,Mn,Fe), and BiLa$BB'O_6$ (B and B'=Co,Cr,Mn,Fe).

The fundamental characteristic of ferroelectrics is the multistability of the polarization, that is coupled to the possibility of domains and the so-called "switching" or commutation of the polarization by means of an electrical field. Likewise, the ferroic materials are those in which the properties of multistability and commutation are associated with some tensor property of the crystal ("order parameter", or OP). The common characteristic of all ferroic materials is the existence of a structural phase transition between a "para"-phase of high symmetry in which the OP has a zero value by symmetry, and a "ferro"-phase where the OP is not zero, and has different possible orientations. In many cases, the structural transition may involve the multistability of several OPs in the low symmetry phase, and as a result, one speaks about "multiferroic" materials. In this case, the crossed couplings between these quantities can produce remarkable effects. In particular, in the last years the term "multiferroic" is being used in a somehow more restrictive way: it is referred to ferro-

electric materials that possess also some type of magnetic order, whose possible coupling to polarization results in electromagnetic effects of unusual characteristics.

The mechanisms that lead to magnetic order and ferroelectricity are very different and it is difficult to obtain materials with both properties simultaneously. In oxides of 3d transition metals the polar instability requires the presence of d^0 cations, while the presence of magnetism is due to half-filled d shells. In consequence, in a multiferroic oxide both type of cations must be combined, or one should consider systems with a ferroelectric instability of different origin: presence of lone pairs, steric type of effects, non-centrosymmetric magnetic orderings etc. In this context, the so called (ordered) double perovskites ($A_2BB'O_6$) are promising candidates. In these perovskites the B position of the simple perovskite structure is occupied with the same probability by two different species B and B', and in many cases the resulting structure is ordered. By combining a B magnetic cation and a B' cation of type d^0 both effects may be achieved. The ferroelectric instability may be favored by including A cations with stereochemical active lone pairs. Some experimentally confirmed examples of multiferroic double perovskites of this type are Pb_2CoWO_6, Pb_2FeTaO_6 y Pb_2FeNbO_6 [1]. The existence of ferrimagnetic ferroelectrics by combining two magnetic ions with different magnetic moments, and reducing the ferroelectric mechanism to the presence at the A position of a cation with a lone pair, like Bi or Pb, has been predicted recently [2]. Thus, it has been proposed Bi_2FeCrO_6 as a possible multiferroic [2]. The presence of two magnetic cations with different magnetic moments may be very favorable to produce ferrimagnetic orderings because even in the case of an essentially antiferromagnetic coupling the net magnetic moment is nonzero. On the other hand, the main problem to be solved is the usual weakness of the magnetoelectric coupling. We consider that the presence of two different magnetic cations may also favor this coupling. For that, the two species must be arranged in an ordered structure. In the case that the system has a ferroelectric instability, the corresponding polar mode may imply relative displacements of the magnetic cations of different type, and this will influence the magnetic degrees of freedom by means of changes in the effective exchange couplings between the atomic magnetic moments.

Double perovskites show a general trend: usually they stabilize in a distorted configuration regarding the ideal cubic structure. In most of the cases, the distortions are non-polar, and as a consequence, the resulting ferroic phases are ferroelastic but not ferroelectric. It has been shown, though (see above), that the inclusion of cations with "lone pairs", as Pb or Bi, in the A site favors the appearance of polar instabilities. In this context, and taking into account the background of the last years, we will explore some compositions that we consider optimal for leading to a multiferroic material.

This first period of the PhD Thesis work took nearly ten months: ten desperate never ending months of no outcomes, in the form of crystals. The initial project was left aside as impossible, at least in the conditions it was thought of at the beginning: even the collaborations established with some other groups (Dr. M.M. Gospodinov group in Sofia (Bulgaria), and Dr. K. Conder group in PSI-Villigen (Switzerland)) failed to give any result. Hence, we decided to change direction and we focused on some aspects not covered by the previous mentioned studies on some families of double perovskites. Nevertheless, I have to confess that this first period, not being, as it was not, at all encouraging, it gave me the opportunity to gain most valuable practical knowledge, background, record, maturity, know-how of the feet-to-earth experimental-education. In one of the appendices I have included a very complete list of the things (we now know) that should not be done. To obtain the first-target compounds, the list is the starting point from which to go further. The appendix is there to remain me that pressure is a very good parameter, a parameter to have in mind in the experimental life, synthesizing, for instance, and in the educational life: when pressure compresses time, if some other experimental conditions are present, maturity, good work, proper education, emerge.

The ruthenium containing compounds were gaining interest during the last years, due to their possible promising properties: $RuSr_2GdCu_2O_8$ where magnetism and superconductivity coexist [3], $SrRuO_3$ with high-temperature ferromagnetism [4], Sr_2FeRuO_6 where spin glass behavior is observed [5], and non-Fermi liquid behavior in $La_4Ru_6O_{19}$ [6]. Having been involved in the structural characterization of some Ru-containing compounds, it was thought of high interest to exploit the double experience in that field, double perovskites and Ru-based compounds, to accomplish the study of the $SrLnMRuO_6$ (Ln=La,Pr,Nd; M=Zn,Co,Mg,Ni,Fe) families. Indeed, some of the proposed materials had magnetic cations so we could complete the structural studies analyzing the magnetic phases, which, at the end, would contribute to enlarge my experimental preparation, as was thought at the beginning.

As the subject of the study, this thesis describes the crystal structure and temperature induced structural phase transitions in terms of symmetry-adapted modes of the high temperature prototype phase of some perovskite-related oxides in most cases containing both lanthanide and ruthenium ions, *i.e.*, $SrPrCoRuO_6$. In few materials magnetic structures have been studied. The lanthanide ion is relatively large, and tends to adopt high-coordination number, and sits in the A-site of the double perovskite $AA'BB'O_6$. By selecting large alkaline earth elements (Sr or Ba), and transition metals, generally lanthanide and alkaline earth ions share A/A'-site perovskite position, whereas ruthenium and transition metal oxides tend to adopt six-coordination number.

This thesis aims to investigate systematically the crystal structures of these compounds.

The memory is composed in four main parts:

- Part I: Introduction, Sample preparation, Structural Determination and Symmetry-mode analysis description chapters.
- Part II: SrNdMRuO_6, SrPrMRuO_6, SrLaMRuO_6, SrLnMRuO_6 (Ln=La,Pr,Nd; M=Co, Ni) Magnetic Structure Models, Sr$Ln$$FeRuO_6$ and $ALn_2CuTi_2O_9$ family chapters.
- Part III: Conclusions, Future work and Bibliography.
- Appendices: Symmetry-mode decomposition of published perovskite structures, Instrumentation, and Synthesis of bismuth-containing perovskites.

In the First part the Introduction, Structural determination, Sample synthesis, and Symmetry-mode analysis are described. This part brings together all the general features of the studied materials. The introduction chapter is a concise review of the principal characteristics of the simple and double perovskites: structural defects, order/disorder configuration, distorted structures and ordering properties.

There is a chapter dedicated to the synthesis of the samples. Nevertheless this chapter does not spread too much, since the purpose of the thesis was not the synthesis (though indispensable), but the characterization of the materials.

Structural determination chapter collects all the information depending on the structure characterization techniques, starting from a brief and general diffraction introduction and following with the techniques used along the execution of the thesis.

It is worth mentioning that although the most common notation for distorted perovskite classification is the proposed by Glazer, in this memory it will not be used, as a more modern notation based on group theory using symmetry-adapted modes is employed. There is a chapter dedicated to the general overview of the description and a step by step example is explained, which can be taken as a process model for the rest of the systems.

The second part of the memory is settled in the results and discussions of the studied materials. It is classified in two main blocks: SrLnMRuO_6 (Ln=La,Pr,Nd; M=Zn,Co,Mg,Ni, Fe) series and $ALn_2CuTi_2O_9$ (A=Ca,Ba; Ln=La,Pr,Nd,Sm) series. The first three chapters gather the structural discussion made for SrNdMRuO_6, SrPrMRuO_6, and SrLaMRuO_6

families. In the laster chapter a general overview of the results related to the three families is done. Chapter four assembles the possible magnetic models for Sr$Ln M$RuO_6 (Ln=La,Pr,Ni; M=Co,Ni). The fifth chapter is related to the crystal and magnetic structure of SrLnFeRuO_6 (Ln=La,Pr, Nd) materials.

The second block of the second part it is related to crystal structure of $ALn_2CuTi_2O_9$ (A=Ca,Ba; Ln=La,Pr,Nd,Sm) materials.

The laster part of the main memory is dedicated to the principal conclusions of four years work and the future perspectives concerning to this research topic. The selected bibliography related to this memory is the chapter that brings this part to an end.

The last part of the memory is dedicated to the appendices, gathering the Symmetry-mode decomposition of published perovskite structures, Instrumentation, and Synthesis of bismuth-containing materials.

Contents

Abbreviations

AFM	Antiferromagnetic
APB	Anti-phase boundaries
AS	Antisite
a.u.	Arbitrary unit
BCS	Bilbao Crystallographic Server
BVS	Bond-valence sum
ca.	*circa*, approximately
e.g.	*exempli gratia*, for example
FM	Ferromagnetic
g.s.	Ground state
HS	High spin
HT	High temperature
i.e.	*id est*, in other words
Irrep	Irreducible representation
JT	Jahn-Teller
LS	Low spin
LT	Low temperature
NPD	Neutron Powder Diffraction
PS	Phase transition
RT	Room temperature
SXRPD	Synchrotron Powder Diffraction
TIP	Temperature independent paramagnetism
XRPD	X-ray Powder Diffraction

Part I

General characteristics

Chapter 1

Introduction

Transition metal oxides occupy an area of material science which is arguably the most extensive to date. The wide variety of properties exhibited by these materials, from high-T_C superconductivity to magnetoresistance phenomena, or magnetic frustration, has provide a fruitful chance for investigation.

In particular, the perovskite structure can accommodate many transition metal ions. The nature of these materials is due to the remarkable stability of the perovskite framework. It should be no surprise then, that perovskites, and materials related to them, have provide entire series of technologically and theoretically important systems of study.

1.1 Perovskite background

The perovskite structure is one of the most extensively studied structure in solid-state chemistry and physics, material science and geology. German chemist and mineralogist Gustav Rose discovered the mineral perovskite ($CaTiO_3$) in the Ural Mountains in 1839 and the material was named after the Russian nobleman and mineralogist Lev Aleksevich von Perovski [7]. Since that time there have been many examples of perovskite materials, and almost every element in the periodic table may be found in a perovskite type structure with some exceptions like beryllium, boron, phosphorous and the noble gases. In fact, one of the most abundant materials in the Earth's lower mantle is a perovskite, $MgSiO_3$. V.M. Goldschmidt (1926) made and studied the first synthetic perovskite, including $BaTiO_3$ (a fundamental dielectric material). In his work [8] he pioneered many principles, like the re-

lationship between the radii of atoms and the structural features of the perovskite, known as *tolernace factor*, that remains applicable to the structure today.

1.2 The perovskite structure

The ideal simple perovskite has cubic symmetry (space group $Pm\bar{3}m$) as depicted in Figure 1.1. Its general formula is ABX_3, where A is typically a large, low oxidation state cation, B is a smaller cation that can adopt octahedral coordination (normally a transition metal), and X is an anion such as F^- or O^{2-}. It is composed of a three dimensional network of regular corner-shared MX_6 octahedra. Historically the octahedra site (M cation) is designated the B-site. The terms B-site and octahedral cation M are used interchangeably in this text. In the ideal case, the B-site cations are at the center of the octahedra with the A cations centrally located in the body center of the cube formed by eight corner-shared octahedra (twelve coordination).

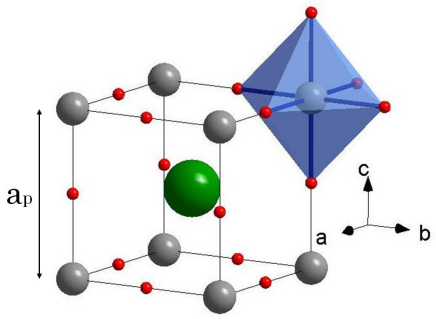

Figure 1.1: The schematic representation of the ABO_3 ideal perovskite structure, where the green, grey and red spheres represent, A, B and oxygen cations, respectively.

The perovskite structure has a high-degree of chemical versatility, allowing for numerous cation substitutions. Virtually nearly all the elements in the periodic table have been incorporated into the structure, with the exceptions of beryllium, boron, phosphorus and noble gases. The great part of the perovskite compounds are fluorides or oxides (type of materials in the present work), but the perovskite structure is also known for heavier halides ($LiGaCl_3$ [9] or $KMgF_3$ [10]), sulfides ($BaZrS_3$ [11]), hydrides ($CsCaH_3$ [12])... The number of perovskites is further extended by the aptitude of this structure to support defects, particularly anion and cation vacancies.

The wide range of composition leads to diverse physical properties in perovskite type materials. Perovskite compounds with catalytic, dielectric, electric, magnetic and opti-

cal properties are known and have been widely investigated (see Table 1.1). The technological applications of these type of materials vary from the dielectric properties of $Ba(Tb_{0.5}Nb_{0.5})O_3$ [13], used in capacitor industry, to superconductor/insulating properties in $YBa_2Cu_3O_{7-x}$ depending on oxygen quantity [14]. The technological relevance of these materials and many others, makes perovskite structure one of the most important structure in material science.

Table 1.1: Example of perovskite type material properties.

Application	Material	Ref.
Capacitors	$Ba(Tb_{1/2}Nb_{1/2})O_3$	[13]
Insulators	$YBa_2Cu_3O_{7-x}$ (0.7<x)	[14]
Superconductors	$YBa_2Cu_3O_{7-x}$ (0<x<0.7)	[14]
	$Sr_2HoRu_{1-x}Cu_xO_6$	[15]
Major Constituent of Earth	$MgSiO_3$	[16]
Metallic Conductor	$BaLa_4Cu_5O_{13.4}$	[17]
Piezoelectric	$Pb^{2+}(Zn_{1-x}Ti_x)O_3$	[18]
	$Pb(Zn_{1/3}Nb_{2/3})O_3$-$PbTiO_3$	[18]
Magnetoresistance	Sr_2FeMoO_6	[19]
Catalytic	$La_{1-x}Sr_xMnO_3$	[20]
	$La_{1-x}Sr_xCoO_3$	[21]
Ferromagnet	$La^{3+}Fe^{3+}O_3$-$La^{3+}Cr^{3+}O_3$	[22]
Ferroelectric	$Pb(Zn_{1/3}Nb_{2/3})O_{3-x}PbTiO_3$	[18]

1.3 The double perovskite structure

In addition to simple perovskites ABO_3, an expanded unit cell may occur when two or more types of cation are presented in A- and/or B-site of the perovskite Figure 1.2. The double perovskite general formula is $AA'BB'O_6$, where A- and A'-cation, and B- and B'-cations can be the same or different type.

In such a situation three simple patterns of ordering are envisioned for either A- or B-cations: rock salt, columnar or layered (Figure 1.3). The most symmetric and mostly observed type of ordering is the so called rock salt ordering; the lattice of A and A' (or B and B') cations is equivalent to the anion and cation positions in the rock salt structure. It is also called 0D ordering, since each BO_6 octahedron is isolated from all other BO_6 octahedra by B' cations. Columnar ordering allows the connectivity of the BO_6 octahedra in one

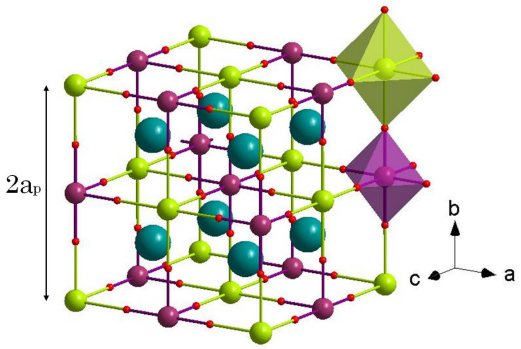

Figure 1.2: The schematic representation of the $AA'BB'O_6$ ideal double perovskite structure; where B-cation and BO_6 octahedra are represented in purple, B'-cation and $B'O_6$ octahedra in green, A / A'-cations in blue, and oxygens in red.

dimension, and it is known as 1D type ordering [23, 24]. Finally, the layered ordering corresponds to the 2D case, since the connectivity of BO_6 octahedra is allowed in two dimensions [25–27]. However, as mentioned before, the most common type of ordering is the rock salt ordering between B and B' cations, and from now on only this type of ordering will be taken into account.

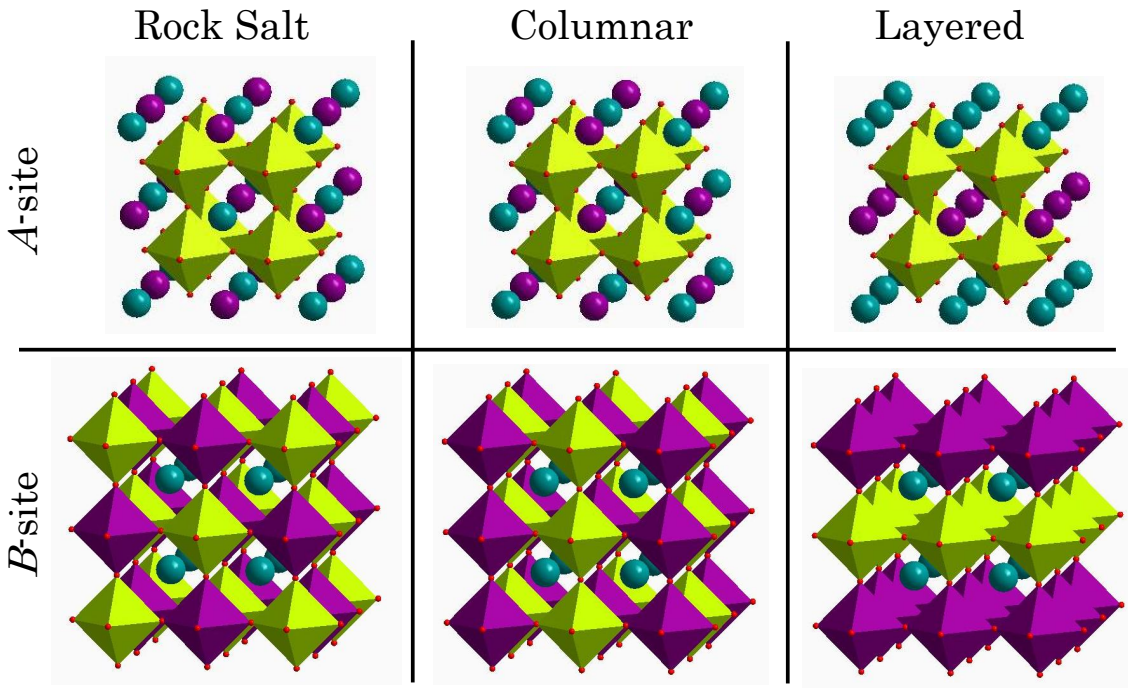

Figure 1.3: Cation ordering schemes in perovskites. From left to the right: 0D (rock salt), 1D (columnar ordering), and 2D (layered ordering) are shown for A-site ordering in $AA'B_2O_6$ perovskites (top) and for B-site ordering in $A_2BB'O_6$ perovskites (bottom).

An ideal double perovskite has a rock salt arrangements of B and B'-site cations on distinct crystallographic sites. For example, in the ideal cubic perovskite with space group $Fm\bar{3}m$ (cell parameter $2a_p$), one cation resides only on the 4*a* Wyckoff position (0,0,0); whereas the other fully occupies the 4*b* site (1/2,1/2,1/2). In reality, there are three different types of B-site cation ordering: complete rock-salt type order, partially rock-salt type order (*antisite* and *anti-phase boundaries*) and complete disorder. The different types of ordering are shown in Figure 1.4. Factors influencing the degree of cation order in double perovskites are charge difference between the B-cations, their differences in ionic radii, the polarization of certain cations and synthesis conditions.

1.3.1 Structural defects

Partially rock-salt type ordered double perovskite materials present cationic defects in their structures. As mentioned above, generally are two type of defects, *antisite* and *anti-phase boundaries*.

In ideal double perovskites B and B'-site cations are alternatively ordered in a three dimensional network; nevertheless, it is common to have some cationic defects were B-cation site is occupied by B'-cation and vice versa; this type of defects are called antisite (AS). In Figure 1.4(b)(red rectangle) it is schematically shown the presence of this type of defect in the structure. It has been demonstrated that by means of an appropriate synthesis protocol election can be controlled the quantity of antisite defects in the structure, observing samples with grater degree of ordering for higher annealing temperature [28]. Antisite defects can be quantify by eq.(1.1).

$$AS(\%) = \frac{\text{\# B-cations in B'-cation site}}{\text{\# total B- and B'-cations}} \times 100 = \frac{\text{\# B'-cations in B-cations site}}{\text{\# total B- and B'-cations}} \times 100 \quad (1.1)$$

where the quantity of B- and B'-cations can be easily obtained refining the Wyckoff position occupational factors during the Rietveld refinement.

Anti-phase boundary defects (APB) for double perovskites (Figure 1.4(b)(blue rectangle)) were suggested by Goodenough [29]. This type of defects, consist on the out-of-phase of crystal domain periodicity. Anti-phase boundaries can be detected by a transmission electron microscope [30].

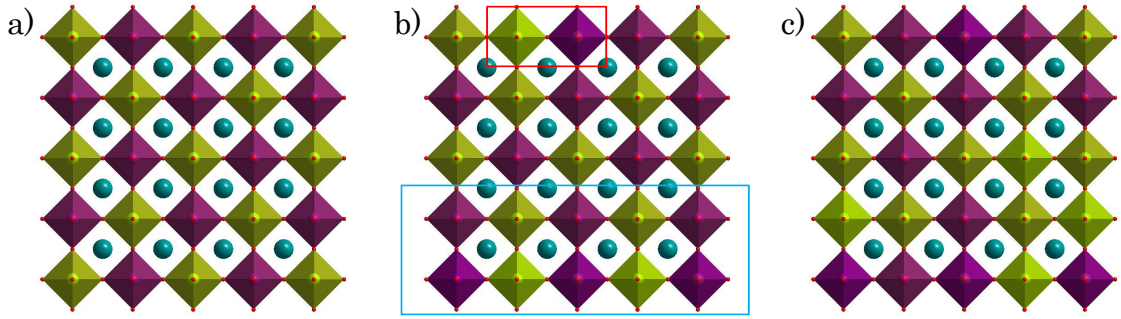

Figure 1.4: Types of ordering in perovskites with two different *B*-site cations. (a) Ideal rock-salt ordering; (b) partial rock-salt ordering with local disorder, called *antisite* (red rectangle) and *anti-phase boundary* defects (blue rectangle); (c) complete disorder. BO_6 octahedra: green; $B'O_6$ octahedra: purple; A/A'-site cations: blue spheres; oxygen: red spheres.

1.3.2 Cation ordering

The difference in charge between *B* and *B*′-cations is the most important factor influencing cation ordering [31]. If the difference in the oxidation state is two or less, all of the ordering arrangements listed above are possible, dominated by completely disordered and partially ordered arrangements. If the difference is greater than two, highly ordered compounds are generally observed, such as in $Sr_2Fe^{2+}W^{6+}O_6$ [32]. In some other cases, if the difference is equal to two, some of the compounds arrange a partially ordered structure (*e.g.* $Sr_2Fe^{3+}Sb^{5+}O_6$ [33, 34]) and others a disordered arrangement (*e.g.* $Sr_2Fe^{3+}Ru^{5+}O_6$ [5]).

The size difference of the *B*-site cations is the second most influential factor [31]. In general, larger differences in ionic radii ($\Delta_{rB/B'} = |r_B - r_{B'}|$) is correlated to higher degrees of cation ordering. In the Sr_2MTaO_6 family can be found examples of this. Sr_2MTaO_6 where M^{3+} = Sc,Cr,Fe [33, 35], have a *M*-cation charge difference of +2, but Sr2ScTaO$_6$ ($\Delta_{rSc/Ta}$=0.105 Å) is fully ordered, Sr_2CrTaO_6 ($\Delta_{rCr/Ta}$=0.025 Å) is partially ordered (0.8/0.2 proportion), and Sr_2FeTaO_6 ($\Delta_{rFe/Ta}$=0.005 Å) is completely disordered. Another example of size difference influence is observe in Sr_2ScSbO_6 ($\Delta_{rSc/Sb}$=0.145 Å) [36] and Sr_2MnSbO_6 ($\Delta_{rMn/Sb}$=0.045 Å) [37] compounds, the former completely ordered and the second one disordered.

The nature of the *B*-site cation can play a significant role in the observed degree of ordering. Ordered perovskites containing a highly charged *B*-cation, such as Sb^{5+}, are significantly more ordered than their analogue transition metal (*e.g.* Ta). Such an effect is observed when comparing Sr_2FeTaO_6 ($\Delta_{rFe/Ta}$=0.005 Å) to Sr_2FeSbO_6 ($\Delta_{rFe/Sb}$=0.045 Å).

Sr_2FeTaO_6 [38] material has not long-range ordering, whereas the Sr_2FeSbO_6 is 59% [33] or 89% ordered [34], depending on the synthesis. The reason for the difference in ordering is that the main group metals like Sb^{5+} do not form nearly linear Sb^{5+}-O-Sb^{5+} arrangements. Sb^{5+} has available only *s* and *p* orbitals which are not ideal to form such a linkages, formed by *d*-orbitals. Hence, the cation order minimizes adjacent Sb^{5+} interactions; nevertheless, for Ta^{5+} *d*-orbitals are available for bonding [39].

Finally, the method of preparation used and the final synthesis temperature can have a significant impact on the degree of ordering. Faik *et al*. [28] examined this factor in the cubic compound Sr_2AlSbO_6. The ordering in the compound increases as the final annealing temperature was increased; although non of the synthesized compound was completely ordered (highest synthesis temperature 1770 K). Another example was studied by Woodward in [38], examining Sr_2AlTaO_6 and Sr_2AlNbO_6 cubic compounds. As observed in the other example, the ordering generally increased as synthesis temperature increased. However, in this example for Sr_2AlNbO_6 material, the ordering reached a thermodynamic equilibrium at 1673 K and subsequent annealing at higher temperatures decreases the Al/Nb grade of ordering. In some compounds, both ordering and disordering arrangements have been observed, depending the synthesis method and temperature, such as in Sr_2MnSbO_6 [37, 40].

The effect of cation ordering in powder diffraction patterns

In the ordered cubic double perovskite (space group $Fm\bar{3}m$) with cell parameter $2a_p$ (where a_p is the primitive cubic cell parameter), the reflections can be separated into two groups based on their Miller indices.

- *hkl* all even: independent of cation ordering; subcell refections.
- *hkl* all odd: indicative of cation ordering; supercell reflections.

In a completely disordered double perovskite structure supercell reflections are absent due to random distribution of *B*- and *B*′-cations on the same crystallographic site. The subcell reflection are still present, although the space group symmetry is now the same as simple cubic perovskite ($Pm\bar{3}m$). Thus, the cell parameter is reduced to the half (a_p), and the indices corresponding to the subcell reflections are reduced by a factor two (Figure 1.5).

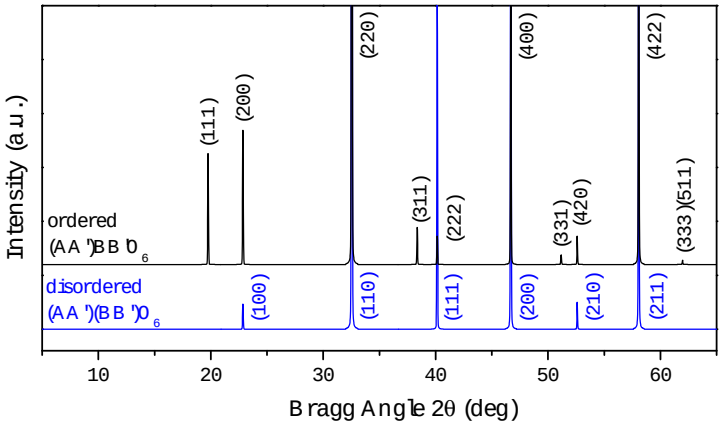

Figure 1.5: Simulated X-ray diffraction patterns for ordered $(AA')BB'O_6$ cubic structure (space group $Fm\bar{3}m$)(black) and disordered $(AA')(BB')O_6$ cubic structure (space group $Pm\bar{3}m$)(blue). (Simulation characteristics: $\lambda = 1.5406$ Å a_p=3.8873 Å, $2a_p$.)

1.4 Distorted perovskites

The ideal structure of a perovskite type material is cubic ($Pm\bar{3}m$ or $Fm\bar{3}m$). However, to the numerous combination of cations with different ionic radii, this ideal structure is seldom obtained; instead, structures with reduced symmetry are more common. The perovskite structure, even simple or double, is a corner-sharing octahedra framework and can be easily distorted from its cubic aristotype by change of chemical composition, temperature and/or pressure. Three distortion types have been identified [41–43]: tilting of the MO_6 octahedra relative to one another as practically rigid corner-sharing units, M-cations shifts within the octahedra, and/or distortion of MO_6 octahedral units. The most common distorted perovskites are characterized either by octahedra tilts or cation displacements.

The most of the distorted perovskites derive from the cubic aristotype phase, applying tilts to partially rigid octahedra. Tilts of the octahedra are defined along the simple cubic perovskite crystallographic axes; maintaining the octahedra regularity (order/disorder type distortions are not studied in this work) and corner connectivity. In such a way, the coordination of A cation changes (allows more flexibility, Figure 1.6), while B-cation neighboring is nearly kept unchanged. Marezio *et al*. [44] observed that the coordination-polyheron of the lanthanides in the A-site of the orthorhombic iron perovskites is achieved with lower coordination that $^{xii}Ln^{3+}$, i.e., a four-fold anti-prism ($^{viii}Ln^{3+}$) rather than a cubo-octahedron. The same search was done for double perovskite compounds, not only in materials with lanthanide cations in A/A'-site of the perovskite [44–46], but also in perovskites with alkaline earth metals [47]. This is due to the tilts of the octahedra to

compensate for the poor fit of the A/A'-site cations in the interstitial space; results in the degeneration of twelve A/A'-O bonds to eight/nine short A/A'-O bonds and four/three long bonds. Those two bond groups determine the first and second coordination-spheres for the A/A'-site cations. The degeneration of the coordination-spheres was suggested [44] to be due to the opposite trend, stretch and contract, of A/A'-O bond-lengths in the first and second coordination-spheres.

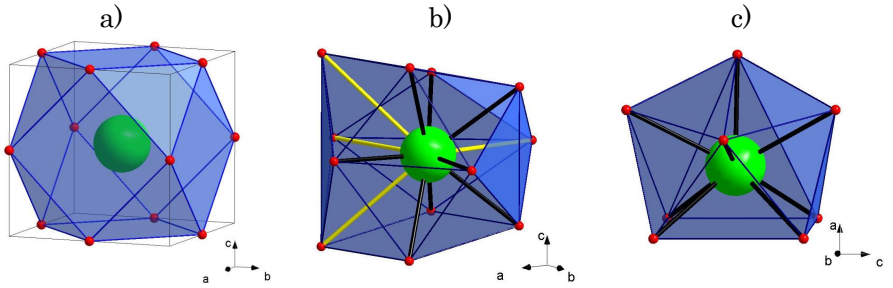

Figure 1.6: The coordination-polyhedron of A-site cation of the ABO_3 perovskite; (a) ideal 12-fold coordination (cubo-octahedron), (b) example of 12-fold coordination of a distorted perovskite (yellow bonds larger than the rest), and (c) more suitable 8-fold coordination for (b) example.

The crystallographic structure of a simple/double perovskite can be anticipated beforehand on the basis of the mismatch among the A-O and B-O distance. The tolerance factor (t) concept was first introduced by Goldschmidt [8] in 1926 and it is routinely used to analyze structure-property relations of ceramics with the perovskite crystal structure (ABO_3). The tolerance factor for perovskites is a geometrical parameter that provides a measure of how well the A-site cation fits the twelve-fold coordinated space within the corner-shared octahedral network formed by the B-site cation. Based on the ionic radii and assuming a sphere model where anions and cations are touching, t for perovskites can be expressed as eq.(1.2):

$$t = \frac{r_A + r_O}{\sqrt{2}(r_B + r_O)} \tag{1.2}$$

$$t_{obs} = \frac{d(A-O)}{\sqrt{2}d(B-O)} \tag{1.3}$$

where r_A, r_B and r_O are the ionic radii for A-, B-cation and O anion tabulated by Shannon [48], respectively; and d_{j-O} are the average atomic distances between the j atom (j=A, B) and the nearest oxygen neighbors that belong to the AO_{12}, BO_6 and $B'O_6$. Eq.1.3, which defines the observed tolerance factor (t_{obs}), is the experimental approach to the definition.

For more complex systems, like double perovskites with $AA'BB'O_6$ general formula, the tolerance factor can be written in the following way:

$$t = \frac{\frac{r_A + r_{A'}}{2} + r_O}{\sqrt{2}(\frac{r_B + r_{B'}}{2} + r_O)} \tag{1.4}$$

$$t_{obs} = \frac{\sqrt{2}d(A/A' - O)}{d(B - O) + d(B' - O)} \tag{1.5}$$

The measurements of t_{obs} entails an accurate determination of the oxygen positions. X-rays are weakly scattered by oxygens, so the most suitable technique for this propose is the neutron powder diffraction. Nevertheless, it might exist some discrepancy between the definition and the experimental value, because the former is based on calculated chemical bond-lengths of the atoms in different compounds and the latter on the experimental distances between nuclei. Except in rare cases, were there is an uncertainty in the valence estimation, one can readily observed that the following recipe holds true for the whole $AA'BB'O_6$ family: for t >1.06 a hexagonal structure is adopted, for 1.06> t > 1.00 the compounds becomes cubic within the $Fm\bar{3}m$ space group, for 1.00> t > 0.96 the most likely structure corresponds to the $I4/m$ tetragonal space group, and finally, if 0.96> t the structure is either monoclinic or orthorhombic [49]. Generally speaking, the trend of t_{obs} agrees with the theoretical one (t).

A number of systems of notations have been developed to describe these type of distortions. The most commonly used are those developed by Glazer [41] and Aleksandrov [50]. Glazer notation uses three letters with superscripts to indicate the rotations along the three cubic simple perovskite axis $[100]_p[010]_p[001]_p$: $a^\sharp b^\sharp c^\sharp$. The superscript ($\sharp$) may be + to indicate in-phase tilting or - to indicate out-of-phase tilting. When tilting is equal for two different axes, the same letter is used for both. For example, $a^-b^+a^-$ describes a distortion in which there are out-of-phase rotations of equal magnitude about the a and c-axes, and an in-phase distortion about the b-axis. In his work he found out 23 possible octahedra tilts related to 23 possible space groups. In Aleksandrov notation, the in-phase distortions are signified by a Greek letter ψ, and the out-of-phase distortions by a ϕ. Differences in magnitude are indicated by numerical subscript. The tilt system described in Glazer notation above would be shown as $\phi_1\psi_2\phi_1$ in Aleksandrov notation.

Woodward, in 1997, generalized Glazers' work [41] for ordered double perovskite structures ($(AA')BB'O_6$) [51]. The generalization process consist on the search of space groups for each 23 Glazer tilts, that allow B and B' cation ordering and maintain rigid

octahedra. 14 possible space groups were searched for 1:1 ordered double perovskites.

In the last years due to the work of Howard and Stokes [52] based on group theory, a great step forward in distorted perovskite classification have been done. In the mentioned work they based on the group theory to reduce the number of possible simple perovskite space groups from 23 to 15. For that purpose they recognized the irreducible representation (irreps) related to in-phase (+) and out-of-phase (-) tilts mentioned in Glazer notation: M_3^++R_4^+. A special emphasis on the symmetry-mode decomposition of the distortions based on the group theory will be done in Chapter 4.

Throughout this work non Glazers' neither Aleksandrovs' notation will be used; as all the analysis have been done using the symmetry-mode description.

The effect of distorted structures in powder diffraction patterns

It was mentioned above that ideal disordered perovskite structures belong to the cubic space group $Pm\bar{3}m$, whereas the ordered have $Fm\bar{3}m$ symmetry; and all the distorted structures (lower symmetry space groups) derived from the ideal structure either by octahedra tilts or cation displacements. In principle this reduction of symmetry can have three different effects on the diffraction patterns: splitting of the peaks, introduction of unobserved peaks and/or changes in the peaks intensities (Figure 1.7 and 1.8).

The peak splitting could be the most direct method to check if octahedral tilting has occurred, although there are many difficulties associated to the use of this effect independently. There is something that has to be taken into account when working with perovskite type structures, the high-degree of pseudo-symmetry. Often, the observed peaks indicate a higher degree of symmetry than it actually has. The most common examples of this effect are the ordered monoclinic perovskites and many errors in symmetry assignment have been done, particularly in older literature. Another obstacle could be the fact that in many structures the distortion is so small that it is very difficult to quantify or in some cases even detect; is the case of broadened peaks by size and/or strain effects.

In Figures 1.7 and 1.8 is shown the effect of the symmetry reduction of the disordered and ordered cubic structure, respectively, for the most observed crystal symmetries. When the symmetry reduction happens into a primitive space group (*e.g.* $P2_1/n$), new peaks are observed in the diffraction patterns related to primitive cell. This type reflection (hkl) condition are $h + k + l = 2n + 1$.

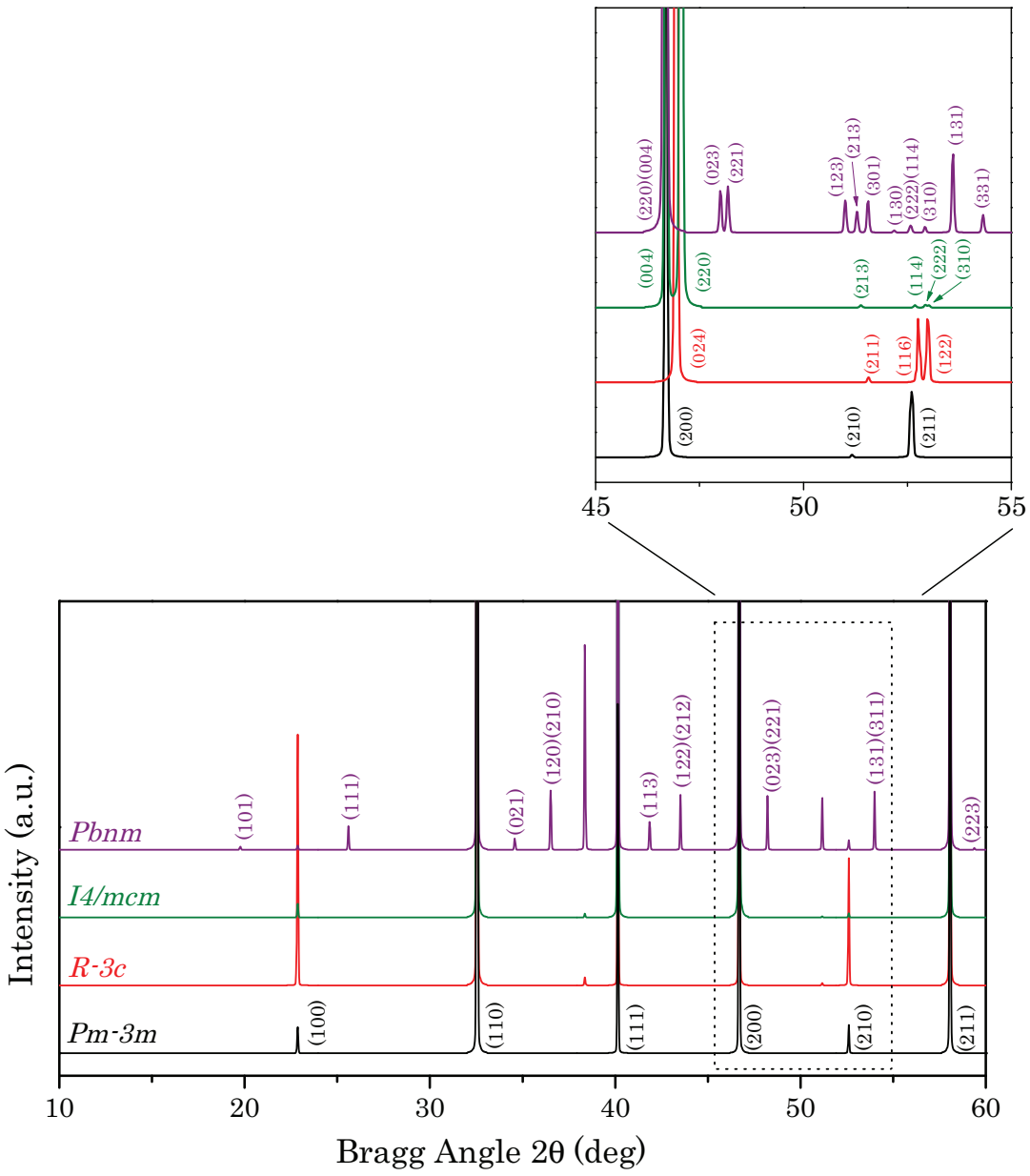

Figure 1.7: Simulated X-ray diffraction patterns for disordered $(AA')(BB')O_6$ cubic structure (black) and the most common distorted symmetries: $R\bar{3}c$ (red), $I4/mcm$ (green) and $Pbnm$ (purple). In the inset is shown the splitting of the peaks. (Simulation characteristics: $\lambda = 1.5406$ Å (XRPD), a_p=3.8873 Å, $Pm\bar{3}m$ (a=a_p), $R\bar{3}c$ (a≈ $\sqrt{2}a_p$, c≈2 $\sqrt{6}a_p$), $I4/mcm$ (a=b≈ $\sqrt{2}a_p$, c≈$2a_p$), and $Pbnm$ (a≈ b≈ $\sqrt{2}a_p$, c≈$2a_p$.)

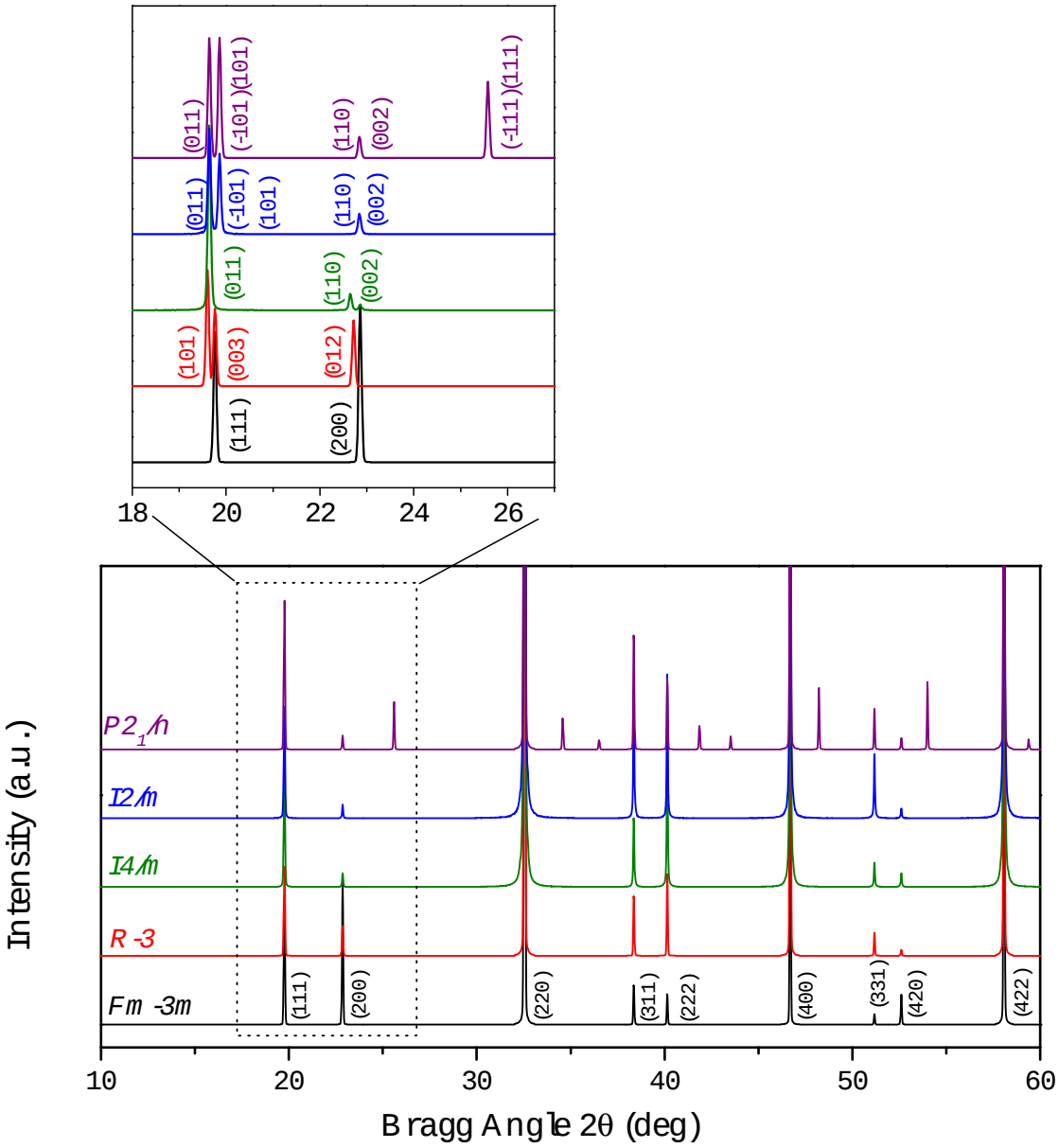

Figure 1.8: Simulated X-ray diffraction patterns for ordered $(AA')BB'O_6$ cubic structure (black) and the most common distorted symmetries: $R\bar{3}$ (red), $I4/m$ (green), $I2/m$ (blue) and $P2_1/n$ (purple). In the inset is shown the splitting of the peaks. (Simulation characteristics: $\lambda = 1.5406$ Å (XRPD), a_p=3.8873 Å, $Fm\bar{3}m$ (a=2a_p), $R\bar{3}$ (a≈ $\sqrt{2}a_p$, c≈2 $\sqrt{6}a_p$), $I4/m$ (a=b≈ $\sqrt{2}a_p$, c≈2a_p), $I2/m$ and $P2_1/n$ (a≈ b≈ $\sqrt{2}a_p$, c≈2a_p, $\beta \approx 90°$).)

1.5 Charge, Orbital, and Spin (magnetic) ordering

In a transition metal oxide materials, the presence of mixed-valent cations can give rise to charge ordering; due to cations with different charges ordered in the same crystallographic sites in the material. Spin (magnetic) ordering can exist from the arrangement of unpaired d and f electrons of transition metal and lanthanides, which result in various magnetic properties. Both, charge and spin ordering, are associated with orbital ordering, and fascinating properties can be observed occasioned by the interaction between charge, spin and orbital ordering.

1.5.1 Charge ordering

In late 1930s Eugene Wigner firstly predict charge ordering in solids [53]. The phenomena of charge ordering and the formation of modulated structures is of the most investigated research topics in mixed-valence transition metal oxides. When charge ordering occurs below the transition temperature T_{CO}, the electron jumping between cations is suppressed, therefor the electric resistivity of the material is increased. Magnetite (Fe_3O_4) is a classical charge ordering example which adopts an inverse spinel (AB_2O_4) structure $Fe^{3+}(Fe^{2+}Fe^{3+})O_4$. The material is a ferromagnet with moderate electrical conductivity. However, when a first order transition occurs cooling below 120 K [54], a significant increase of the resistivity is observed. It was proposed that the first order transition, so called Verwey transition, is attributed to the charge ordering of Fe^{2+} and Fe^{3+} at B-site [55].

The doped manganite perovskites have been widely studied due to the exhibited charge ordering character and subsequently different ground states and colossal magnetoresistence [56, 57]. For instance, the delocalized electrons of Mn cations in half doped $(La^{3+}_{0.5}Ca^{2+}_{0.5})Mn^{3.5+}O_3$ material become localized showing a charged ordered phase, $(La^{3+}_{0.5}Ca^{2+}_{0.5})(Mn^{3+}_{0.5}Mn^{4+}_{0.5})O_3$, below T_{CO} [58, 59]. Such charge ordered Mn^{3+} and Mn^{4+} layers can be represented by a *stripped* model [59, 60]. With different doping levels in $La_{1-x}Ca_xMnO_3$, the *stripped* model was observed with different periodicity.

In some undoped perovskite materials with unstable oxidation state cations, charge disproportionation can be observed showing ordering of the two more stable cations. Unlike the layered ordering shown above, a different type of ordering is noticed in the materials with charge disproportionation. A typical example is $Ba^{2+}Bi^{4+}O_3$, which becomes $Ba^{2+}(Bi^{3+}_{0.5}Bi^{5+}_{0.5})O_3$, or also written as $Ba^{2+}_2(Bi^{3+}Bi^{5+})O_6$ below the charge ordering transi-

tion temperature [61–63]. Charge disproportionation can also be observed in $CaFeO_3$ with Fe cation with different charges $Ca_2^{2+}(Fe^{3+}Fe^{5+})O_6$ [64], or in rare earth nickelates $LnNiO_3$ which can be represented as $Ln_2^{3+}(Ni^{2+}Ni^{4+})O_6$ [65–68].

1.5.2 Orbital ordering

In transition metal perovskites ABO_3 or double perovskites $AA'BB'O_6$, the transition metal forms a BO_6 octahedra configuration, in which its d orbitals split into t_{2g} (d_{xy}, d_{yz}, d_{xz}) and e_g ($d_{x^2-y^2}$, d_{z^2}) orbital groups. The e_g orbitals are higher in energy than t_{2g} orbitals, and point directly toward the ligands. This gives rise to two possible configurations of the d electron filling, the low-spin (LS) and high-spin (HS) states. In perovskite materials mainly the high-spin configuration is observed for $3d$ transition metals. Usually the elongation of the octahedra occurs when the t_{2g} and e_g orbitals are partially occupied, allowing two long and four short B-O bonds, which is known as Jahn-Teller (JT) effect [69]. The most typical examples of transition metals cations with Jahn-Teller effect are Mn^{3+} (d^4) and Cu^{2+} (d^9). JT distortion can also be observed in Ti^{3+} (d^1) and V^{3+} (d^2), nevertheless these distortions are more difficult to detect.

The arrangement of the distortion orientation in solid materials leads to so called cooperative Jahn-Teller distortions and long range orbital ordering, as shown in $LaMnO_3$ perovskite [58] Figure 1.9. The orbital ordering is also exhibited in charge ordered materials such as $La_{0.5}Ca_0.5MnO_3$ [59] or $Pr_{0.5}Ca_0.5MnO_3$ [70]. The ordering way of the orbitals may affect the spin ordering of a material, which is described by the Goodenough-Kanamori rules [71].

1.5.3 Magnetic (spin) ordering

Traditional magnetic materials are two- or three-dimensional arrays of inorganic atoms, composed of transition metal and/or lanthanide containing spin units; like perovskite materials. Apart from the diamagnetism which arises in all substances with the application of an external magnetic field, the magnetic behavior of a material results from the presence of unpaired electrons. Magnetic properties are mainly exhibited by materials containing transition metals and/or lanthanides Table 1.2, owing to their partially filled d and f orbitals, respectively.

On the atomic level there exist two fundamental type of magnetism: diamagnetism and paramagnetism. Diamagnetic behavior arises from the interaction of the applied mag-

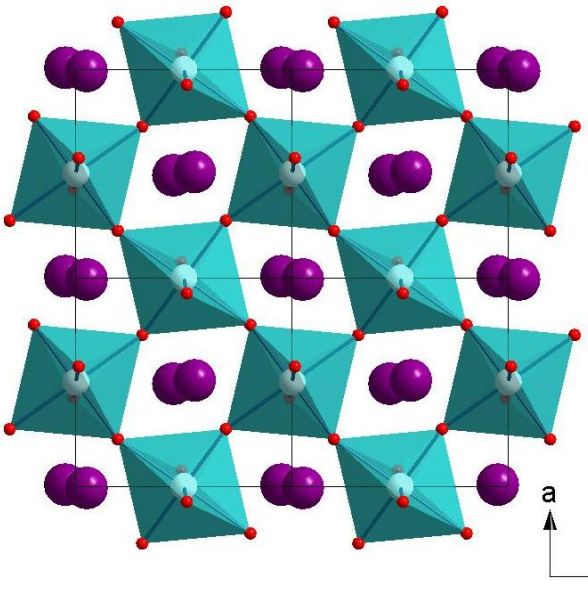

Figure 1.9: Cooperative Jahn-Teller distortion of $LaMnO_3$ [58] material.

Table 1.2: Selected ionic properties of the rare-earth elements [72].

Lanthanide ion	$4f^n$	g.s.	S	L	J	g	μ_{Ln}
La^{3+}, Ce^{4+}	$4f^0$	$^1S_0$	0	0	0	0	0
Ca^{3+}, Pr^{4+}	$4f^1$	$^2F_{5/2}$	1/2	3	5/2	6/7	2.54
Pr^{3+}	$4f^2$	$^3H_4$	1	5	4	4/5	3.58
Nd^{3+}	$4f^3$	$^4H_{9/2}$	3/2	6	9/2	8/11	3.62
Pm^{3+}	$4f^4$	$^5I_4$	2	6	4	3/5	2.68
Sm^{3+}	$4f^5$	$^6H_{5/2}$	5/2	5	5/2	2/7	0.845
Eu^{3+}, Sm^{2+}	$4f^6$	$^7F_0$	3	3	0	0	0
Gd^{3+}, Eu^{2+}, Tb^{4+}	$4f^7$	$^8S_{7/2}$	7/2	0	7/2	2	7.94
Tb^{3+}	$4f^8$	$^7F_6$	3	3	6	3/2	9.72
Dy^{3+}	$4f^9$	$^6H_{15/2}$	5/2	5	15/2	4/3	10.63
Ho^{3+}	$4f^10$	$^5I_8$	2	6	8	5/4	10.58
Er^{3+}	$4f^11$	$^4I_{15/2}$	3/2	6	15/2	6/5	9.59
Tm^{3+}	$4f^12$	$^3H_6$	1	5	6	7/6	7.55
Yb^{3+}	$4f^13$	$^2F_{7/2}$	1/2	3	7/2	8/7	4.54
Lu^{3+}, Yb^{2+}	$4f^14$	$^1S_0$	0	0	0	0	0

g.s.: ground state; g: Landé g factor; μ_{Ln}=$g\sqrt{J(J+1)}$: effective magnetic moment.

netic field with molecular or atomic orbitals containing paired electrons. With the exception of the hydrogen radical, all atomic or molecular materials exhibit some diamagnetic behavior. This magnetic conduct is temperature independent, and the strength of the interaction is almost proportional to the molecular weight of the material.

Paramagnetism is characterized by the attraction of a substance into an applied magnetic field. This behavior is originated as a result of an interaction between the applied magnetic field and the unpaired electrons in atomic or molecular orbitals. Typically, paramagnetic materials contain one or more unpaired electrons, and the power of paramagnetic interactions are temperature dependant. However, some substances show temperature independent paramagnetism (TIP), which occurs from a coupling between the magnetic ground state and non-thermally populated excited states. Usually TIP behavior is associated to electrically conducting materials.

Classically, the term magnetism refers to substances that at the atomic level exhibit temperature dependant paramagnetic behavior and will thus be used in this context. The non-zero spin angular moment associated with un unpaired electron gives rise to a magnetic moment. As a result of pairing, electrons within an orbital show opposing magnetic moments, resulting in no net magnetic moment. In general, bulk magnetic properties originate from long-range interactions between unpaired electrons.

Paramagnetism

In a paramagnetic material each individual electron spin is unaffected by its neighbors Figure 1.10(a). The spins of a paramagnetic material can easily be aligned by an applied magnetic field. However, the alignment is weak, and upon removal of the magnetic field the system relax back to a random distribution of magnetic moments. True paramagnetic materials are extremely rare, since most materials exhibit ferromagnetism, antiferromagnetism, or ferrimagnetism at very low temperature.

Ferromagnetism (FM)

Ferromagnetism is characterized by parallel alignment of adjacent magnetic spins that results in a large net magnetic moment Figure 1.10(b). Ferromagnetic alignment of adjacent magnetic spins is rare since it can only be achieved if there is zero quantum mechanical overlap between spin containing orbitals. In this case alignment of the spins, which correlates their motion and minimizes electron-electron repulsion, is the most stable state.

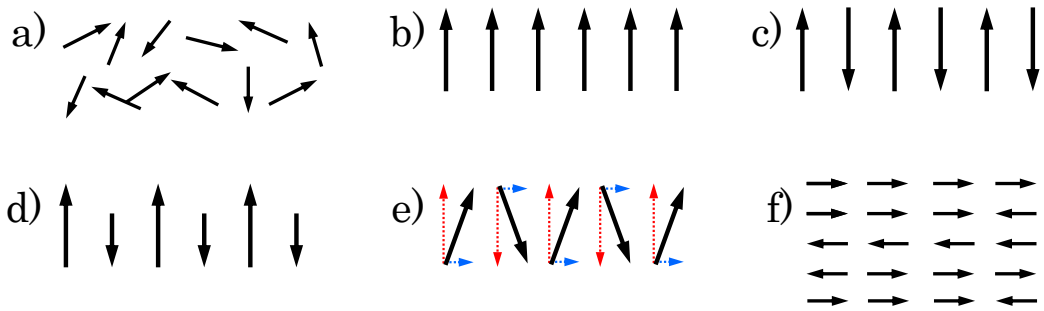

Figure 1.10: Schematic diagram s showing the spin arrangement of (a) paramagnet, (b) ferromagnet, (c) antiferromagnet, (d) ferrimagnet, (e) canted antiferromagnet (where the magnetic components in different directions are represented by dashed arrows), and (f) spin-glass.

Unlike paramagnets, ferromagnets exhibit a net magnetic moment in the absence of an applied field. This behavior can be found in $SrLaMnRuO_6$ [73] or Sr_2FeMoO_6 [33] double perovskites.

Antiferromagnetism (AFM)

In an antiferromagnet, magnetic spins are aligned antiparallel Figure 1.10(c), which results in a material with no net magnetic moment. At absolute zero, antiferromagnets show a diamagnetic response to an applied magnetic field. The alignment of spins antiferromagnetically is analogous to the process of bonding and is thus favorable. The spins can be aligned with several different arrangements as described by Wollan *et al*. [74]. Four common examples are shown in Figure 1.11. *A*-type antiferromagnetic ordering has the spins aligned ferromagnetically in *ab* plane, and each layer is antiferromagnetically to one other. This can be observed in $LaMnO_3$ perovskite [74], which is result of the Jahn-Teller distortion of Mn^{3+} cation. In *C*-type, the magnetic moments are aligned antiferromagnetically in the *ab* plane, and the *ab* layers stack ferromagnetically along the *c* axis, which can be found in $BiCoO_3$ perovskite [75] or Sr_2MnRuO_6 double perovskite [73]. *G*-type ordering is commonly adopted in perovskites, in which the spins of all nearest neighboring atoms are aligned antiferromagnetically by the superexchange interaction, as shown in $LaFeO_3$ [76], $LaCrO_3$ [77] or Sr_2CrRuO_6 [78]. Moreover, there are several more complex configuration like *E*-type AFM consisting of zigzag ferromagnetic chains, and observed in $HoMnO_3$ perovskite [79]. Antiferromagnetism is the most commonly observed bulk magnetic behavior, and long-range antiferromagnetism is even exhibited by materials that are locally ferromagnetically ordered.

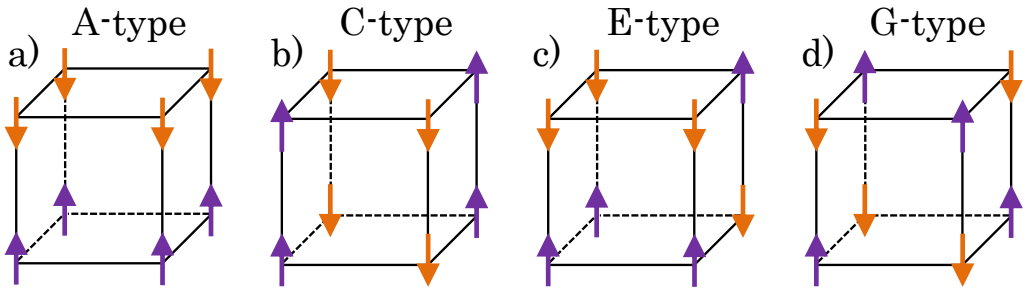

Figure 1.11: Schematic representation of the spin arrangements in (a) *A*-type, (b) *C*-type, (c) *E*-type, and (d) *G*-type antiferromagnetic ordering.

Ferrimagnetism

Ferrimagnetism is a special case of antiferromagnetism, where the material consists of a lattice of rigidly alternating spins of different magnitudes Figure 1.10(d). As in antiferromagnet, the adjacent magnetic spins are aligned antiparallel. However, since the adjacent spins are of different magnitudes, the resulting material exhibits a net magnetic moment in absence of an applied magnetic field. Ferromagnetism is responsible for the magnetism in magnetite, where Fe^{3+} ions (S=5/2) are observed to alternate with Fe^{2+} ions (S=2). In perovskites field Sr_2CrMoO_6 [80] or Sr_2CrOsO_6 [81] materials show ferrimagnetic behavior.

Spin-canted antiferromagnetism

Similar to simple ferrimagnetism, a residual magnetic moment exists in a canted antiferromagnet, which shows the almost antiparallel arrangement of the spins but with a canting angle Figure 1.10(e), like in $YbCrO_3$ [82]. The material is also called a weak ferromagnet owing to the net magnetic components.

Spin-glass

At low temperature, the magnetic moments of these materials are frozen in an arbitrary state, with no long range order. Spin glasses thus consist of an ensemble of disordered spins Figure 1.10(f), and represent a model system for the statistical mechanics of a system with quenched randomness. Because of the spin disorder, the spins are subject to interactions of different sign, positive: ferromagnetic or negative: antiferromagnetic, so that a particular spin will receive conflicting information on how to order from its neighbors,

and it might not be possible for the system to choose a certain spin configuration and minimize its energy. The phenomenon is referred to as frustration. It is typically the result of an antiferromagnetically ordered triangular lattice. As is illustrated in Figure 1.12, it is impossible to align a triangular arrangement of spins, such that all spins interact antiferromagnetically. Spin glass behavior is observed in ferromagnetic La_2CoMnO_6 double perovskite [83].

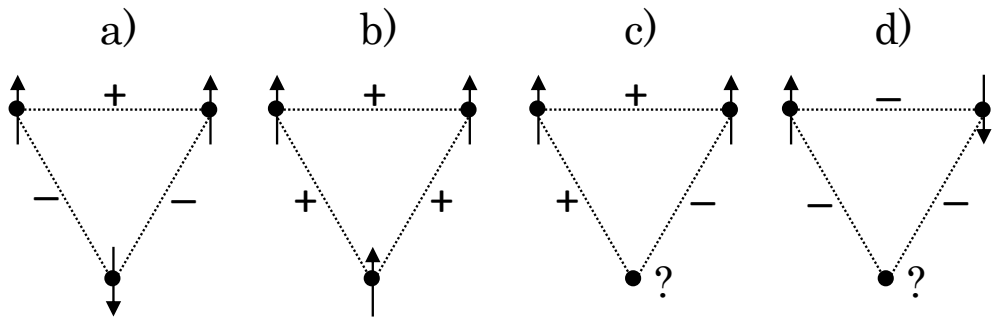

Figure 1.12: Examples of magnetic frustration on triangular lattice. (a) and (b) show no frustration, while, (c) and (d) show frustration associated to the disorder of the interaction (c) as well as to the geometry of the lattice (d).

Chapter 2

Sample preparation

2.1 Double perovskites

Transition metal perovskites are typically prepared by the so-called conventional solid state synthesis or commonly called *Conventional Ceramic Synthesis* method from the stoichiometric amounts of required elements in their oxide or carbonate forms. The high-purity starting materials are grounded using an agate pestle and mortar until a homogeneous mixture is obtained. Then the mixture is heated in an alumina crucible within a high temperature furnace, usually between 1270 K and 1570 K for the materials studied in this thesis. After a certain period of heating treatment, the products are quenched from high temperature in order to ensure homogeneity Figure 2.1. The progress of reaction is monitored with laboratory X-ray powder diffractometer (Stoe STADI-P, Figure B.9) after each heating process. Several intermediate re-grinds are applied in the synthesis to ensure the homogeneity of the required material and the completeness of the reaction. The repetition of heating process is halted when a single phase is confirmed by XRPD.

The studied compounds have been synthesized following the eq.(2.1) and eq.(2.2) stoichiometric equation, using $SrCO_3$ (99.995%), La_2O_3 (99,999%) or Pr_2O_3 (99.9%) or Nd_2O_3 (99.99%), RuO_2 (99.9%), MgO (99.998%) or CoO (99.99%) or NiO (99.99%) or ZnO (99.999%) or Fe_2O_3 (99.98%) agents as received from Sigma-Aldrich. In order to induce an oxidation state transformation in ruthenium ion: $Ru^{4+} \rightarrow Ru^{5+}$, all furnace treatments have been done under air atmosphere.

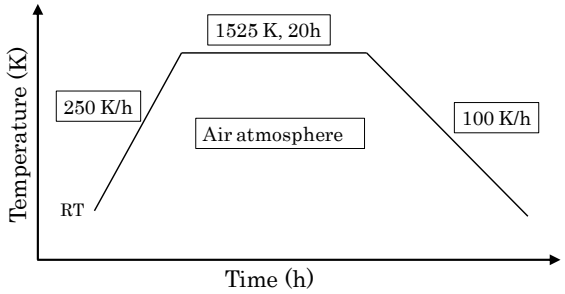

Figure 2.1: Schematic representation of the synthesis treatment for double perovskite compounds.

- Sr$Ln$$MRuO_6$ (Ln=Nd,Pr,La; M=Zn,Co,Mg,Ni)

$$2SrCO_3 + Ln_2O_3 + 2RuO_2 + 2MO \xrightarrow{\text{Air atmosphere}} 2SrLnMRuO_6 + 2CO_2 \uparrow \qquad (2.1)$$

- SrLnFeRuO$_6$ (Ln=Nd,Pr,La)

$$2SrCO_3 + Ln_2O_3 + 2RuO_2 + Fe_2O_3 \xrightarrow{\text{Air atmosphere}} 2SrLnFeRuO_6 + 2CO_2 \uparrow \qquad (2.2)$$

Table 2.1: Synthesis last treatment temperature (K) and duration (h) for double perovskite materials.

Sample	Temperature (K)	Duration (h)
$Sr^{2+}Nd^{3+}Zn^{2+}Ru^{5+}O_6^{2-}$	1525	20
$Sr^{2+}Nd^{3+}Co^{2+}Ru^{5+}O_6^{2-}$	1525	20
$Sr^{2+}Nd^{3+}Mg^{2+}Ru^{5+}O_6^{2-}$	1525	20
$Sr^{2+}Nd^{3+}Ni^{2+}Ru^{5+}O_6^{2-}$	1525	20
$Sr^{2+}Pr^{3+}Zn^{2+}Ru^{5+}O_6^{2-}$	1525	20
$Sr^{2+}Pr^{3+}Co^{2+}Ru^{5+}O_6^{2-}$	1525	20
$Sr^{2+}Pr^{3+}Mg^{2+}Ru^{5+}O_6^{2-}$	1525	20
$Sr^{2+}Pr^{3+}Ni^{2+}Ru^{5+}O_6^{2-}$	1525	20
$Sr^{2+}La^{3+}Zn^{2+}Ru^{5+}O_6^{2-}$	1525	17
$Sr^{2+}La^{3+}Mg^{2+}Ru^{5+}O_6^{2-}$	1525	17
$Sr^{2+}Nd^{3+}Fe^{3+}Ru^{4+}O_6^{2-}$	1525	20
$Sr^{2+}Pr^{3+}Fe^{3+}Ru^{4+}O_6^{2-}$	1525	20
$Sr^{2+}La^{3+}Fe^{3+}Ru^{4+}O_6^{2-}$	1525	17

2.2 Triple perovskites

Polycrystallines $ALn_2CuTi_2O_9$ (A=Ba,Ca and Ln=La,Pr,Nd,Sm) samples were prepared by Dr. A. Aatiq at Laboratoire de Chimie des Matériaux Solides in Casablanca (Marocco). The synthesis was done by classical high temperature solid-state chemistry from powder mixtures of $CaCO_3$ (99.995%) or $BaCO_3$ (99.98%), CuO (99.999%), TiO_2 (99.995%) and La_2O_3 (99.999%) or Pr_2O_3 (99.9%) or Nd_2O_3 (99.9%) or Sm_2O_3 (99.9%) as received from Sigma-Aldrich, being the stoichiometric ratio the following:

$$CaCO_3 + CuO + 2TiO_2 + Ln_2O_3 \xrightarrow{\text{Air atmosphere}} CaLn_2CuTi_2O_9 + CO_2 \uparrow \tag{2.3}$$

$$BaCO_3 + CuO + 2TiO_2 + Ln_2O_3 \xrightarrow{\text{Air atmosphere}} BaLn_2CuTi_2O_9 + CO_2 \uparrow \tag{2.4}$$

The mixtures were heated progressively with intermittent grinding at 1170 K (12 h), 1270 K (24 h), pressed into pellets and sintered at 1570 K for another 12 h in air atmosphere. The samples were cooled to room temperature for re-grinding several times.

Chapter 3

Structural determination

3.1 Diffraction method

Diffraction is a phenomenon that has been widely used to develop many useful and powerful techniques for the purpose of determination and characterization of crystalline material structures. A crystalline solid consist of a three-dimensional periodic array of atoms which can be considered as extended from its unit cell. When a wavelength of an incident-beam is comparable to the inter-atomic spacing in the crystal, the atoms can scatter and reflect the incident-radiation so a diffraction patterns can be generated. X-ray, neutron and electron beams have a range of different wavelength which are suitable to perform diffraction experiments for structure determination.

A crystalline material can be considered as consisting of layered parallel lattice planes which behave like semi-transparent mirrors. The constructive interference from incident-beam occurs when Bragg's Law is satisfied

$$n\lambda = 2d \sin\theta \tag{3.1}$$

when n is an integer determined by diffraction order, d inter-planar distance, λ is the incident-beam wavelength and θ is the incidence angle, as shown in Figure 3.1. From Bragg's Law, the symmetry and cell parameters of the unit cell of a material can be obtained from analyzing the Bragg peaks position (indexation process), while positions of the atoms within the cell are are related to the peak intensities.

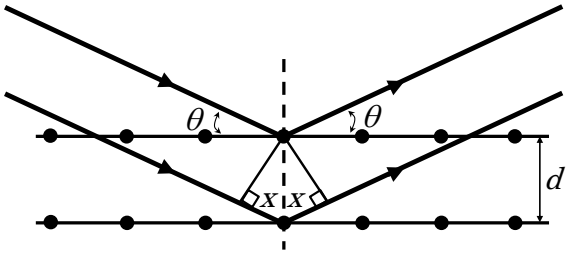

Figure 3.1: Diffraction of a beam from a set of lattice planes, separated by a distance d.

To relate the atomic planes to the unit cell parameters of a given crystalline material, the Miller indices are used. The Miller indices of a plane are commonly written (hkl), given by h=a/x, k=b/y and l=c/z where a, b and c are cell parameters of the unit cell and x, y and z are the fractionary coordinates where the planes intersect the crystallographic axes. Thus the distance between the family of (hkl) planes can be considered using the Bragg's Law λ=2d$_{hkl}$sin θ_{hkl}. From this consideration the position of the reflections can be predicted for a given periodic solid, and for an unknown solid the periodicity can be obtained from observed reflection positions.

The relative intensities of the observed reflections, I_{hkl}, are proportional to $|F_{hkl}|^2$, where F_{hkl} is the structure factor for the (hkl) reflections and is defined as

$$F_{hkl} = \sum_{j=1}^{N} f_j \exp[2\pi i(hx_j + ky_j + lz_j)] \exp[-B_j(sin^2\theta)/\lambda^2] \tag{3.2}$$

where F_{hkl} is the summation over all the atoms within the unit cell, f_j is the scattering factor or form factor for X-rays (scattering length b_j for neutrons) of atom j, x_j, y_j and z_j are the fractional coordinates of atom j in the unit cell. The thermal motion of the atoms is taking into account by the Debye-Waller factor, where B_j is the atomic temperature factor which is related to the mean square thermal displacement factor U_j by B=8π^2U.

In this way, the observed diffraction pattern can provide information about not only the symmetry and cell parameters of a particular crystalline material, but also the atomic contents and positions within its unit cell.

3.1.1 Powder diffraction

For many materials it is impossible or extremely difficult to produce sufficiently large single crystals for diffraction experiments. In contrast, many times crystalline powders are

relatively easy to synthesized. A crystalline powder sample consist of a large number of randomly orientated crystallites. For any given lattice plane there will be crystals in the material orientated with appropriate Bragg angle θ to occur the diffraction. These crystals will take up any possible angular positions with respect to the incident-beam and therefore the diffracted beams will be emitted as cones of radiation, as shown in Figure 3.2. Although the three-dimensional nature of single crystal diffraction is compressed into one-dimensional data, a powder diffraction pattern can still provide information to derive the cell parameters from diffraction peak positions and contents within the unit cell from peak intensities.

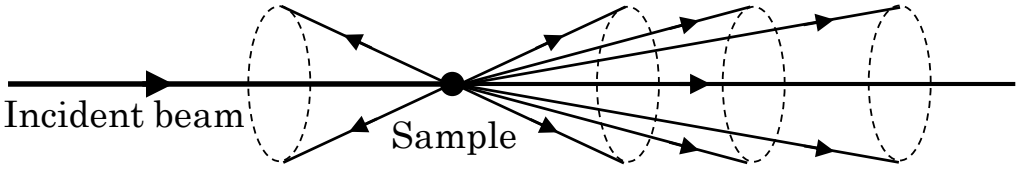

Figure 3.2: Cones of diffracted radiation from the incident-beam for a powder sample.

3.1.2 X-ray Powder Diffraction (XRPD)

In order to satisfy Bragg's Law eq.3.1, the incident-radiation with a comparable wavelength to the interatomic spacing in a given crystalline material is required. This corresponds to the X-ray region of the electromagnetic spectrum, thus X-rays are ideal and commonly used for conducting diffraction studies. X-ray beams can be described as electromagnetic waves which will interact with atom electron clouds. Hance, the scattering factor of an atom is related to its atomic number Z, *i.e.* the number of electrons in the atom. As a result it is difficult to distinguish neighboring atoms in the periodic table since they have similar scattering power. Light atoms are also hard to located, particularly in the presence of heavy atoms, as they only scattered weakly and are concealed by the heavy atoms scattering. The scattered intensity in XRPD is reduced rapidly with increasing scattering angle ($\sin\theta/\lambda$).

During the thesis work different powder diffractometers have been used: Stoe STADI-P, Philips X'Pert MPD and Bruker Advanced D8 (Vårio and Vantec). Characteristic of the instruments are reported in Appendix B.

3.1.3 Synchrotron X-ray Powder Diffraction (SXRPD)

Synchrotron radiation is the electromagnetic field radiated by relativistic accelerated charge particles, so that very intense and highly collimated radiation is generated in comparison to those from a conventional X-ray source. The emitted radiation has not only extremely high-brilliance and high-flux, but also a very broad spectrum which easily allows a desired wavelength to be selected for different experiment requirements. Moreover, the source is very stable and the beam can be polarized (both linear and circular). The peaks in the powder diffraction patterns become extremely sharp, so the overlap of the reflections with similar diffraction angles or interplanar d-spacing, is minimized. Instrumental information can be found in Appendix B

3.1.4 Neutron Powder Diffraction (NPD)

The neutron is a powerful tool to study the structure of crystalline materials as an alternative diffraction source to X-rays. A thermal neutron, which has an energy about 0.025 eV, can be useful in crystallography since its wavelength is comparable to interatomic distances.

Neutrons, unlike X-rays, interact with nuclei of atoms rather than electron cloud. Thus the fall-off of the scattering power in the case of X-ray diffraction is not seen. The neutron-nucleus interaction is of very short range compared to interatomic distances, so that scattering length are essentially independent of $\sin\theta/\lambda$. On the other hand, X-rays interact with the nucleus surrounding electron cloud which is comparable with the interatomic distances and thereby the X-ray form factors decrease quickly with increasing $\sin\theta/\lambda$; hence, neutrons provide information at larger scattering angles.

In addition, neutron scattering lengths b_j vary as an irregular function of atomic number Z as shown in Figure 3.3. Therefore not only can neighboring atoms in the periodic table be distinguished from each other, but also light atoms can be detected in presence of heavier atoms. The ability to scatter both light and heavy atoms in a material plays an important role, for example, in the completion of metal oxide structure determination.

Furthermore, the neutron has a spin quantum number 1/2 and the possession of a magnetic moment allows the neutron to interact with unpaired electron spins. This aspect make neutron diffraction a powerful tool to determine magnetic structure of materials. The magnetic scattering power of neutron diffraction, which can be expressed as a form factor f_m, is similar to the X-ray form factor. The scattered total intensity by unpolarized

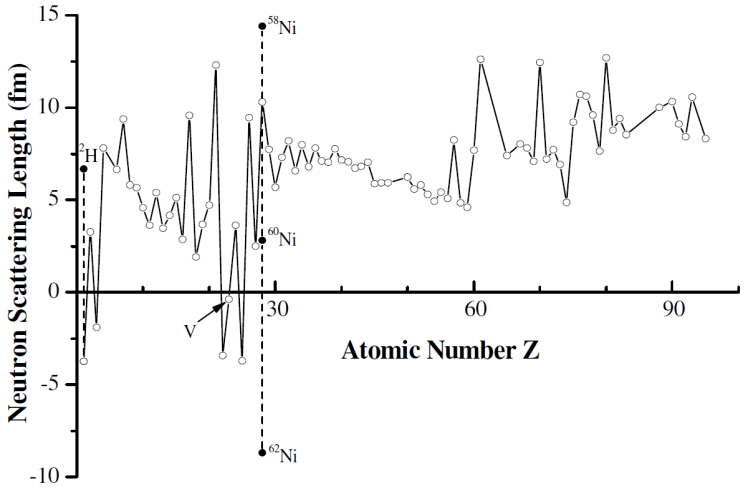

Figure 3.3: The irregular function of neutron scattering length against atomic number. The markers joined by dashed line indicate the difference of scattering length among isotopes.

neutrons which contain all directions of spins will be the sum of both nuclear and magnetic scattering, as shown below:

$$|F_{hkl}|^2 = |F_{hkl}^{nuc}|^2 + |F_{hkl}^{mag}|_{\perp}^2 \tag{3.3}$$

where $|F_{hkl}^{nuc}|$ and $|F_{hkl}^{mag}|$ are respectively the structure factors of nuclear and magnetic structures. The term $|F_{hkl}^{nuc}|$ is described in eq.3.2 and the magnetic structure factor $|F_{hkl}^{mag}|$ can be defined as:

$$F_{hkl}^{mag} = \sum_{j=1}^{N} q_j p_j \exp[2\pi i(hx_j + ky_j + lz_j)] \tag{3.4}$$

where q_j is the magnetic interaction vector which depends on magnetic moment and scattering vector of atom j, and p_j is the magnetic scattering length which is calculated from the magnitude of the magnetic moment and the magnetic form factor f_m.

When a material possesses magnetic moments which are oriented randomly as in a paramagnet, the incident neutron is scattered incoherently so that the background intensity increases. The magnetic Bragg peaks can be observed, on the other hand, if magnetic ordering appears in a material. For ferromagnetic structures, the magnetic ordering and the nuclear cell will have the same periodicity, hence the reflection of the nuclear and the magnetic structure will be superimposed. For commensurate antiferromagnetic structures, extra reflections from magnetic ordering will be observed in addition to the nuclear ones. This is due to the supercell of the magnetic structure, which has a greater periodic-

ity than that of the nuclear cell in one or more directions. For incommensurate magnetic structures, satellite peaks which surround the nuclear Bragg reflections are commonly observed. Therefore with information of nuclear and magnetic reflections, neutron diffraction is a powerful tool that enables both nuclear and magnetic structure of a material to be determined simultaneously.

The weak interactions of neutrons with atom nuclei provide a highly penetrating and non-destructive examination, which allows experimental configurations with complex sample environments such as cryostat, furnace, magnets and pressure cells. However, compared to X-rays a relatively large amount of sample is required for neutron diffraction due to the weak neutron-nucleus interaction and the low-intensity generated by neutron sources.

Instruments from three different facilities have been used to perform this work, SPODI in FRMII (Garching, Germany), HRPT in SINQ (Villigen, Switzerland), and D1B and D2B in ILL (Grenoble, France). Their characteristics are in Appendix B.

3.1.5 X-ray diffraction vs. Neutron diffraction

Although the basis theory of diffraction is similar for X-ray and neutrons, there are significant differences between both techniques. In the case of neutron scattering, and in absence of magnetic scattering, the fundamental scattering body is the nucleus not the electron. Since X-rays interact with the electrons, the interaction is dependent on the number of electrons, *i.e*. atomic number, and X-ray form factor increase rapidly with the atomic number of elements. The X-ray scattering intensity from lighter atoms is therefore relatively low and can be concealed by the heavier elements. In neutron scattering, on the other hand, the scattering length b_j varies somewhat irregularly with the atomic number; however, most of the atoms scatter neutron equally well in contrast to the rapid increase of the X-ray form factors with the atomic number. Neutron diffraction is therefore very useful to locate light elements in compounds containing heavy elements.

In the present work, XRPD was found to be not very sensitive to oxygen location in most of the studied materials. This is expected because of the low cross-section of oxygen for X-rays and the materials contain heavy scatters such as lanthanides. NPD was therefore used to determine the oxygen location in the studied materials. Due to differences in the scattering lengths, NPD can also differentiate adjacent elements in the periodic table and hence, almost undistinguishable in X-ray experiments. This is useful in characterizing mixed occupancy of crystallographic sites in materials such as mixed *A*-site and/or *B*-site

perovskites.

The magnetic interactions in materials containing magnetic ions (with unpaired electrons) can be studied by NPD. When the ions have their spins oriented in a random manner, as in a paramagnetic material, the magnetic scattering will be entirely incoherent and will contribute to the background of a powder pattern. Nevertheless, when the material exhibits a three-dimensional ordering of the magnetic moments, the magnetic scattering will contribute coherently to the scattered intensity. Thence, the NPD technique is useful to determine the magnetic structure as well as crystal structure. However, the electrons which determine the magnetic moment will be distributed over a space-volume having dimensions comparable to the neutron wavelength; the magnetic form factors will decrease with $\sin\theta/\lambda$ similar to X-rays scattering, although from factors are different since X-rays scatter from the whole electron cloud around the nucleus while neutrons scatter from valence electrons. NPD experiments at low temperature were used to characterized the magnetic structure of materials such as $SrLaFeRuO_6$ and $SrNdCoRuO_6$.

Neutrons are generally less absorbed by the materials than X-rays. The ability of neutron to penetrate more deeply in the materials is an advantage in studying materials with compositional gradient such as thin layers, where neutron diffraction will provide information representing the bulk structure whereas X-rays will give less information. However, neutron scattering from materials containing large neutron absorption cross section elements (*e.g.* Cd, Gd, Sm) is considerably reduced and a significant absorption correction may be necessary.

X-ray diffraction, with the advantage of being a laboratory-based technique and almost always more accessible than neutron techniques, is a strongly powerful technique which is frequently preferable to neutron diffraction. Nevertheless, it can be seen that NPD is superior/complementary in some situations when specific type of information is required.

XRPD was used in the present work to check the phase purity during the synthesis process and to determine the unit cell parameters and space group for room temperature data. High temperature XRPD data was used to follow the structure evolution and material cell parameters with temperature for some cases. Room- and high temperature NPD data, however, were used to study more reliably the crystal structures and temperature induced structural phase transitions; low temperature NPD data were used to determine the magnetic structure of magnetically ordered materials.

3.2 Rietveld Refinement

The Rietveld method [84] was developed in the late 1960s by Hugo Rietveld and is widely used to refine crystal and magnetic structures from obtained X-ray or neutron diffraction data. For most powder diffraction patterns, overlaps happen between Bragg reflections especially for lower symmetry materials due to the polycrystalline nature of a powder sample. Instead of analyzing the individual reflections or solving the reflection overlaps, the Rietveld method is performing a curve fitting procedure by considering the observed intensity $y_{i(\mathrm{obs})}$ of each equally spaced steps i over the entire pattern including the background intensity and the sum of the contribution of reflections close to the i powder pattern step:

$$y_{i(\mathrm{obs})} = i_{i(\mathrm{background})} + \sum_i y_{i(\mathrm{Bragg})} \tag{3.5}$$

The Rietveld method is a refinement technique to minimis the residual S_y between the observed intensity $y_{i(\mathrm{obs})}$ and the calculated intensity $y_{i(\mathrm{calc})}$ by the best least-square fits to all the steps:

$$S_y = \sum_i \frac{(y_{i(\mathrm{obs})} - y_{i(\mathrm{calc})})^2}{y_{i(\mathrm{obs})}} = \sum_i w_i (y_{i(\mathrm{obs})} - y_{i(\mathrm{calc})})^2 \tag{3.6}$$

where w_i is the statistical weight assigned to each point and $y_{i(\mathrm{calc})}$ is the intensity of each step which can be calculated by a mathematical expression that includes the factors related to both the structure and non-diffraction terms. Therefore a good initial structure model is required including information about space group, unit cell parameters, atomic positions an instrumental details. $y_{i(\mathrm{calc})}$ for each $2\theta_i$ can be calculated as:

$$y_{i(\mathrm{calc})} = S_\alpha \sum_{hkl} L_{hkl} |F_{hkl}|^2 h(2\theta_i - 2\theta_{hkl}) P_{hkl} A + y_{i(\mathrm{background})} \tag{3.7}$$

where hkl are the Miller indices for a certain reflection; S_α is the scale factor of the pure phase; L_{hkl} contains the Lorentz polarization and multiplicity factors; F_{hkl} is the structure factor which includes nuclear and magnetic structure factors if applicable; $h(2\theta_i - 2\theta_{hkl})$ is the peak shape function which describes the effects of the instrument and the sample on the reflection profiles; P_{hkl} is the preferred orientation function; A is the absorption factor and $y_{i(\mathrm{background})}$ is the background intensity at the step i of the diffraction pattern. During the refinement cycles, each of these terms and its parameters may be varied to improve the match between observed and calculated diffraction patterns, *i.e.* to minimize the S_y value.

The fitting results can be estimated by examining the plot of the difference between observed and calculated patterns. On the other hand, several numerical terms can be used to estimate the goodness of the least-square process. These residual values are defined as:

$$R_{\mathrm{p}}(\%) = 100 \times \frac{\sum_{i=1}^{n} |y_{i(\mathrm{obs})} - y_{i(\mathrm{calc})}|}{\sum_{i=1}^{n} y_{i(\mathrm{obs})}} \qquad \text{R-pattern} \tag{3.8}$$

$$R_{\mathrm{wp}}(\%) = 100 \times \sqrt{\frac{\sum_{i=1}^{n} w_i (y_{i(\mathrm{obs})} - y_{i(\mathrm{calc})})^2}{\sum_{i=1}^{n} w_i (y_{i(\mathrm{obs})})^2}} \qquad \text{R-weight pattern} \tag{3.9}$$

$$R_{\mathrm{exp}}(\%) = 100 \times \sqrt{\frac{N - P + C}{\sum_{i=1}^{n} w_i (y_{i(\mathrm{obs})})^2}} \qquad \text{R-expected pattern} \tag{3.10}$$

$$\chi^2 = \frac{R_{\mathrm{wp}}}{R_{\mathrm{exp}}} \qquad \text{Goodness of fit} \tag{3.11}$$

where N is the number of independent observations, P is the number of refined parameters and C is the number of constrains. A good fit with the refined structure model will accompany with a low residual value. The R_{wp} is commonly considered, since it contains S_y, the quantity to be minimized by the least-square refinements. The goodness of fit, χ^2, which is directly proportional to S_y, is also typically regarded and is ideally to be unity.

All refinements of nuclear and magnetic structure from X-ray and neutron powder diffraction patterns in this thesis were carried out with Rietveld method using the FullProf program [85].

3.3 Bond-valence calculations

Physical properties are directly dependent on the (valence) charge distribution in a crystal. Therefore, the trend of the valence state (oxidation state) within the present investigated system is of high importance. In the present a unique method (bond-valence sum, BVS) is employed in order to determine the charge distribution; in other words, the oxidation state of the ions involved.

The bond-valence sum method was historically derive from Pauling's rules for crystal chemistry and developed by I.D. Brown [86]. The calculation of the bond-lengths from the refined positions of the atoms allows the determination of the valence of the atoms by using the bond-valence sum method. This method serves to determine the valences of atoms in a chemical compound by the sum of the bond-valences for all bonds, in which the atoms participate. Thus for a mixed valent compound, the valence V_i of an atom i in the crystal structure is calculated as the sum of contributions of the bonds of atom i towards the atoms j in its first coordination-shell:

$$V_i = \sum_j v_{ij} = \sum_j exp[(R_{ij} - d_{ij})/b] \tag{3.12}$$

where v_{ij} is the bond-valence of the atom pair (i, j), b = 0.37 Å is a universal parameter and R_{ij} is an empirical parameter determined for almost any pair of atoms from fitting the atomic valences for many different compounds at room temperature.

Chapter 4

Symmetry-modes analysis

The last years, a new way to describe the distortion of the structures based on group theory has gain importance [87–89]. In this framework, perovskite type materials are prone to undertake structural phase transitions, and are the perfect materials to be studied using the symmetry-mode decomposition [52, 90–92]. New programs based on the distortion-mode decomposition have been developed in order to make easier *a priori* a very tedious procedure; AMPLIMODES [93, 94] and ISODISTORT [95]. This type of analysis gives the chance to refine the collective coordinates (distortion-mode amplitudes), substituting the individual atomic coordinates. A general overview of the description and an example using the programs is described below. For farther information the reader could have a look at [87–89] based on symmetry-mode decomposition, and at [52, 90–92] more particularly in perovskite distortions.

4.1 General description of distorted structures by symmetry-mode analysis

The crystal structure of many materials can be seen as the result of a distortion with respect to a structure of higher symmetry: parent structure (virtual or real). When the distortion is small (displacive type distortion), the distortion can be decomposed into two contributions, a homogeneous strain and an atomic displacement field given by each atomic displacement in the low symmetry phase with respect to its position at high symmetry phase. This separation makes the distinction between the elastic degrees of freedom and the internal atomic degrees of freedom. For full mathematical consistency, the symmetry-

modes analysis should be performed with out taking into account the cell deformation (strain component). The existing deformation can be added *a posteriori*, using the real cell instate of the idealized unstrained one, keeping the same relative coordinates.

Let $\mathbf{r}_0(\mu)$ be the atomic positions of the μ atoms (μ=1,...,s) within the asymmetric unit of the reference (parent) structure with space group G. The asymmetric unit of the distorted structure (space group H, subgroup of G) will generally have more atoms, due to the high symmetry structure Wyckoff orbital splitting; and the atomic positions within the H asymmetric unit, can be expressed as

$$\mathbf{r}(\mu, i) = \mathbf{r}_0(\mu, i) + \mathbf{u}(\mu, i) \tag{4.1}$$

where $\mathbf{r}_0(\mu, i)(\mu$=1,...,$n_\mu)$ denotes the atomic positions in the parent phase written in the low symmetry structure bases, with the i label enumerating the H space group Wyckoff orbitals arising from a unique orbital of G.

The magnitude of a displacive distortion can be measured by the amplitude of the displacement, and depends on the cell parameters values used in the scalar product (which generally corresponds to the parent phase cell), its variation will be minimum as long as the deformation of the cell is reasonable small. In general, any distortion can be expressed as the sum of the contributions of a set of symmetry-adapted modes. Each defined mode is compatible with an intermediate space group Z between G and H ($G \geq Z \geq H$), known as *isotropy* group and it is supergroup of H. This means that the symmetry-modes are restricted to the isotropy subgroup of the associated *irrep*.

The distortion modes of which the isotropy group is equal to H from the symmetry point of view can be considered as *primary* modes, whereas those other modes of which the isotropy group are subgroups of G and different from H can be considered as *secondary* ones. A primary distortion mode is enough to break totally the symmetry between the reference and the low symmetry phase; while, the secondary ones, will break the symmetry into intermediate symmetries.

To determine the amplitudes of the modes taking part in the symmetry-breaking, it is not necessary to know the *real* reference structure. The modes transforming according to the identity *irrep* are the unique amplitudes that depends on the specific atomic coordinates of the reference structure; those allowed in the reference structure, but who do not break the symmetry of the space group. Moreover, changes in the degrees of freedom of the atomic coordinates of the reference structure, means atomic displacements in those modes; leaving the rest of the modes, the ones involved in the symmetry-breaking

untouched.

The decomposition of the distorted structure could be performed by AMPLIMODES [93] available in the Bilbao Crystallographic Server (BCS) [96, 97] (http://www.cryst.ehu.es) or ISODISTORT [95] (http://stokes.byu.edu/isotropy.html). The analysis presented in this work have mainly been done with AMPLIMODES, and therefore only the procedure used in AMPLIMODES is explained.

There are two versions of the program: AMPLIMODES and AMPLIMODES for FullProf. The initial structural information needed for the symmetry-mode analysis is shown in Section A.1, and consists of: the high symmetry phase (prototype phase); the low symmetry phase (the cell parameters and the space group); and, finally, the transformation matrix between both cells. It is important to empathized the possibility to make the analysis in non-standard settings. AMPLIMODES, apart from the above mentioned information, needs the low symmetry phase atomic coordinates and in the output provides the amplitudes corresponding to each distortion mode; nevertheless, AMPLIMODES for FullProf does not requires that information, but in the output file prepared to introduce in a .pcr file (input file for FullProf) all the mode amplitudes are null.

In the first step we obtain, using the room temperature (RT) cell parameter values from the XRPD data, a complete basis of symmetry-adapted distortion modes. It is worth noting that for the symmetry-mode analysis AMPLIMODES (AMPLIMODES for Fullprof) performs, it is not necessary to know a real parent structure. Starting from the distorted phase (H space group) one can construct an ideal parent structure whose symmetry group (G, with $G > H$) is determined by the structural pseudo-symmetry of the low symmetry phase. The structural differences between that ideal parent structure and any other possible parent structure of this symmetry are due only to contributions of symmetry-modes compatible with G, i.e. the totally symmetric modes. The contributions of the much more important symmetry-breaking distortion-modes present in the distorted phase do not depend on any choice of the atomic coordinates of the parent structure. Hence, as for this subfamily of double perovskite ruthenates no parent phase is known experimentally, we have assumed there exists one (an example to obtain the parent phase by pseudosymmetry is explained below): expected to be found at high temperatures, should no decomposition of the material takes place.

The pseudosymmetry search of a distorted structure could be done by PSEUDO [98] available in the BCS. If the atomic displacements relating the two structures are smaller than 1 Å, it is probable that the structure undergoes a temperature induced phase transition of Landau type into a high symmetry configuration. The program is designed to

detect pseudosymmetry in any given structure, and derive a virtual parent high symmetry phase. The required initial information is the space group, cell parameters and atomic coordinates in the asymmetric unit and the structure has to be introduced using the conventional default setting of the space group. The information of all ready known equivalent structure can be used for this purpose. The tolerance factor which limits the maximal atomic displacements with respect to the high symmetry phase structure can be defined in each case.

4.2 Symmetry-Mode Analysis: an example

Let us consider as an example an ordered double perovskite monoclinic phase of space group $P2_1/n$ (ITA No.14, conventional default setting $P2_1/c$). The structure data are in a non conventional setting, thereby SETSTRU in the BCS need to be used to transform the structure into a conventional default setting; SETSTRU Input (left) and Output (right) are shown in Table 4.1.

Table 4.1: Transformation of the $P2_1/n$ monoclinic non-conventional structure to the conventional $P2_1/c$ setting by PSEUDO; the transformation matrix: **c**,**b**,-**a**-**c**;0, 0, 0.

14 (P 1 $2_1/n$ 1)						14 (P 1 $2_1/c$ 1)					
5.5428 5.5550 7.8333 90.00 90.044 90.00						7.8333 5.5550 9.5925 90.00 144.70 90.00					
6						6					
Ru	1	2a	0.00000	0.00000	0.00000	Ru	1	2a	0.00000	0.00000	0.00000
Co	1	2b	0.00000	0.00000	0.50000	Co	1	2b	0.50000	0.00000	0.00000
Sr	1	4e	-0.00730	0.46880	0.75160	Sr	1	4e	0.75890	0.46880	0.00730
O	1	4e	-0.28600	0.20300	-0.03690	O	1	4e	0.24910	0.20300	0.28600
O	2	4e	-0.78100	0.27700	0.03390	O	2	4e	0.81490	0.27700	0.78100
O	3	4e	0.07080	0.00910	0.75880	O	3	4e	0.68800	0.00910	-0.07080

By PSEUDO one can access the pseudosymmetry of a structure by checking the pseudosymmetry for the minimal supergroups of H, and if favorable for one of the results, repeat the process once more for its minimal supergroups, and so on, until the maximal supergroup is reached. That process has been followed by the example monoclinic default setting ($P2_1/c$) structure. The unique possible chain of minimal supergroups reaching the cubic ($Fm\bar{3}m$) structure is shown below. The reason to chose $Fm\bar{3}m$ space group for the parent phase is that the ideal ordered double perovskite is known to have that symmetry.

- $P2_1/c$ (No.14) – $Pnnm$ (No.58): index=2

$$(\mathbf{P},\mathbf{p})_1=\left(\begin{array}{ccc|c} 0 & 0 & -1 & 0 \\ 0 & 1 & 0 & 0 \\ 1 & 0 & -1 & 0 \end{array}\right)$$

- $Pnnm$ (No.58) – $Immm$ (No.71): index=2

$$(\mathbf{P},\mathbf{p})_2=\left(\begin{array}{ccc|c} 1 & 0 & 0 & 0 \\ 0 & 1 & 0 & 0 \\ 0 & 0 & 1 & 0 \end{array}\right)$$

- $Immm$ (No.71) – $I4/mmm$ (No.139): index=2

$$(\mathbf{P},\mathbf{p})_3=\left(\begin{array}{ccc|c} 1 & 0 & 0 & 0 \\ 0 & 1 & 0 & 0 \\ 0 & 0 & 1 & 0 \end{array}\right)$$

- $I4/mmm$ (No.139) – $Fm-3m$ (No.225): index=3

$$(\mathbf{P},\mathbf{p})_4=\left(\begin{array}{ccc|c} 1/2 & 1/2 & 0 & 0 \\ -1/2 & 1/2 & 0 & 0 \\ 0 & 0 & 1 & 0 \end{array}\right)$$

The transformation matrix $(\mathbf{P},\mathbf{p})$ for the pair $Fm\bar{3}m > P2_1/n$ can be obtained from the product of the matrices $(\mathbf{P},\mathbf{p})_i$ of the gradual procedure along the supergroups chain:

$$P2_1/n \xrightarrow{(\mathbf{P},\mathbf{p})_0} P2_1/c \xrightarrow{(\mathbf{P},\mathbf{p})_1} Pnnm \xrightarrow{(\mathbf{P},\mathbf{p})_2} Immm \xrightarrow{(\mathbf{P},\mathbf{p})_3} I4/mmm \xrightarrow{(\mathbf{P},\mathbf{p})_4} Fm\bar{3}m \tag{4.2}$$

$$(\mathbf{P},\mathbf{p}) = (\mathbf{P},\mathbf{p})_4(\mathbf{P},\mathbf{p})_3(\mathbf{P},\mathbf{p})_2(\mathbf{P},\mathbf{p})_1(\mathbf{P},\mathbf{p})_0 = \left(\begin{array}{ccc|c} 1/2 & 1/2 & 0 & 0 \\ -1/2 & 1/2 & 0 & 0 \\ 0 & 0 & 1 & 0 \end{array}\right) \tag{4.3}$$

For the mentioned example, ones the virtual parent phase and the transformation matrix between the cubic and monoclinic cell are known, the distortion decomposition is obtained by AMPLIMODES (see Table 4.2). It can be observed that a single irrep distortion component is not enough to explain the full symmetry-break, there is not a unique primary mode (no mode written in bold letters). That means that more than one distortion mode will be necessary to break totally the symmetry from the cubic prototype phase into the monoclinic distorted phase. In this kind of examples were there is not a unique primary mode, one can deduce the importance of each mode checking the amplitude values; directly introducing the low symmetry phase in AMPLIMODES or refining the mode amplitudes by a refinement program. The least case is the optimum choice as different refinement attempts could be done (giving zero values to different mode amplitudes) and

observed the best refinement result.

There are seven irreducible representations (irreps) of the $Fm\bar{3}m$ space group, that can take part in the symmetry-breaking from that space group to the RT $P2_1/n$ monoclinic space group: $GM_1^+(1)$ (totally symmetric), $GM_3^+(1)$, $GM_4^+(1)$, $GM_5^+(4)$, $X_2^+(1)$, $X_3^+(1)$ and $X_5^+(3)$. The numbers in parenthesis (Table4.2) indicate the number of modes transforming according to the corresponding irrep. Hence, there are 12 modes (one of them is the totally symmetric). In Table 4.2 there is part of the output from AMPLIMODES; the modes' labels indicate the atoms, with their corresponding Wyckoff position in the reference structure, involved in the modes. Therefore, from the twelve modes, 8 (+1) modes move only the oxygen atoms (24*e*) and the rest 3 modes, the Sr atoms (8*c*). As indicated in Table 4.2, the GM irreps have a (0,0,0) *k*-vector, they maintain the unit cell; and the X irreps have a (0,1,0) *k*-vector, they double the unit cell in the *b* direction. The isotropy groups stand for the possible intermediate groups, with a group-subgroup relation between the reference and the distorted symmetry phase (Figure 4.1). The atomic displacements involved in the modes imply the symmetry-breaking from the prototype symmetry to the isotropy group symmetry. A simulated diffraction pattern related to each isotropy group phase is shown in Figure 4.1; all the calculus are done in the monoclinic phase bases.

The geometrical representations of the distortion modes of the symmetry-breaking from the cubic prototype phase into the monoclinic $P2_1/n$ phase, taking as reference the monoclinic cell, are the following, see Figure A.2. In it, the Ru octahedra are in blue, and the Co, in gold. The A/A'-site cations are shown in green and the oxygens in red. As a reference, there are also plotted the simple perovskite cubic cell (red), the double perovskite parent phase cell (blue) and the monoclinic cell (black). The polarization vectors of the modes are shown by small black arrows. The effect of the mode can be appreciated by the two configurations shown: the cubic configuration, in which by definition the mode does not act, below the actual configuration corresponding to the isotropy group symmetry, resulting from the action of the mode. GM_3^+, expands the octahedra in the equatorial *ab* plane, while the apical (in the *c* axis) oxygens are moved along *c* axis to the center of the octahedra. GM_4^+, is essentially a rotation around the *b* axis; although it deforms a bit the octahedra (the displacement of the oxygens in the *ab* plane and the ones in *c* axis are not the same). GM_5^+ irrep is four dimensional, actuating on A/A'-site cations and oxygens. GM_5^+-A4 and GM_5^+-A5 modes, displace the A/A'-site cations in *a* and *c* axes, respectively. GM_5^+-A6, moves the equatorial oxygens in the *ab* plane, transforming in a rectangle the square formed by the oxygens; while GM_5^+-A7, is a kind of rotation along *b* axis, with the apical oxygens displaced in the opposite direction of the rotation. The mode transforming according to X_3^+ is a pure rotation of the octahedra around the *c* axis. X_2^+ mode actuates

Table 4.2: Summary of the symmetry mode decomposition, with respect to the ideal cubic perovskite $Fm\bar{3}m$, of the room temperature monoclinic phase ($P2_1/n$), as given by AMPLIMODES. The primary mode, if existing, is written in bold letters. For each irrep the number of basis modes associated to the indicated atoms is shown in parenthesis. Atom labels refer to the $Fm\bar{3}m$ structure. The column headed *Dimension* refers to number of basis modes necessary in general to describe the corresponding irrep distortion; whereas the one headed as *Direction* indicates, in the convention of ISOTROPY [99], the direction in the irrep space corresponding to the irrep distortion. Mode amplitudes are given in the last column and their standard deviations in parenthesis.

Atoms	WP	Modes
O1	24*e*	$GM^{1+}(1)$ $GM^{3+}(1)$ $GM^{4+}(1)$ $GM^{5+}(2)$ $X^{2+}(1)$ $X^{3+}(1)$ $X^{5+}(2)$
Sr1	8*c*	$GM^{5+}(2)$ $X^{5+}(1)$

K-vector	Irrep	Direction	Isotropy subgroup	Dimension	Amplitude (Å)
(0,0,0)	GM_1^+	(a)	$Fm\bar{3}m$ (ITA 225)	1	0.07(2)
(0,0,0)	GM_3^+	(a,0)	$I4/mmm$ (ITA 139)	1	0.06(2)
(0,0,0)	GM_4^+	(a,a,0)	$C2/m$ (ITA 12)	1	1.12(2)
(0,0,0)	GM_5^+	(-b,a,-a)	$C2/m$ (ITA 12)	4	0.16(1)
(0,1,0)	X_2^+	(0,a,0)	$P4_2/mnm$ (ITA 136)	1	0.04(1)
(0,1,0)	X_3^+	(0,a,0)	$P4/mnc$ (ITA 128)	1	0.79(1)
(0,1,0)	X_5^+	(a,a,0,0,a,-a)	$Pnnm$ (ITA 58)	3	0.366(4)
Global distortion: 1.4330 Å					

on the equatorial oxygens, deforming into a rhombus the square formed by the oxygens. Finally, there are three modes that transforms according to X_5^+ irrep. This mode actuates on the oxygens and on the A/A'-site cations (Sr/Nd). In the former case, it is a rotation around the *a* axis, although the amount of displacements in the *ac* plane and the ones in *b* are not the same. In the latter, displaces the Sr/Nd cations along the *b* axis.

In practice, when the virtual parent phase is obtained by pseudosymmetry search, that information together with the low symmetry phase cell parameters and space group (obtained by diffraction data indexation), and the transformation matrix are introduced in AMPLIMODES for FullProf. The program decomposes the distortion in terms of the basis of the symmetry-modes, but the amplitudes for each of the distortion modes are null. Next step in the analysis consists on refining the amplitudes of the basis modes obtained in the former step. In order to have the possibility to compare the different structure results, the same reference structure (one for ordered perovskites and another one for disordered) have been used for all the compounds. The parent phases are shown in Table 4.3.

Table 4.3: Reference structures (parent phase) for ordered ($Fm\bar{3}m$, No.225) and disordered ($Pm\bar{3}m$, No.221) perovskite structures. The same virtual reference structures have been used for all the compounds.

225
7.9209 7.9209 7.9209 90.00 90.00 90.00
6

Ru	1	4a	0.00000	0.00000	0.00000
Co	1	4b	0.50000	0.50000	0.50000
Sr	1	8c	0.25000	0.25000	0.25000
O	1	24e	0.24714	0.00000	0.00000

221
3.8438 3.8438 3.8438 90.00 90.00 90
6

Ru	1	1a	0.00000	0.00000	0.00000
Sr	1	1b	0.50000	0.50000	0.50000
O	1	3d	0.00000	0.00000	0.50000

Figure 4.1: Graph of maximal subgroups relating the $Fm\bar{3}m$ and the $P2_1/c$ space groups of room temperature Sr$Ln$$MRuO_6$ (Ln=La,Nd,Pr; M=Zn,Co,Mg,Ni) phases. For each space group, the irreducible representation of the distortion mode yielding this symmetry is indicated if existing. For the parent phase (red) and isotropy groups, the corresponding simulated patterns are plotted in the $P2_1/n$ non conventional monoclinic bases. The combination of distortion modes responsible for the $Fm\bar{3}m \rightarrow P2_1/n$ symmetry-breaking are plotted for $P2_1/n$ (orange).

Part II

Results

Ruthenium containing materials exhibit wide diversity of interesting characteristics. One of the most studied material is the $SrRuO_3$ perovskite [4, 100]. It is of interest since it has similarities to the parent perovskites (La,Ca)MnO_3 of the colossal magnetoresistance manganites. $SrRuO_3$ undergoes two structural phase transitions: $Pbnm \rightarrow I4/mcm \rightarrow Pm\bar{3}m$, at 825 K and 945 K, [100] respectively. Although pentavalent ruthenium is not found in nature, the average Ru-O bond-distance seen in the compound is 1.986 Å, slightly different from the sum of covalent radii for $^{vi}Ru^{4+}$ and $^{vi}O^{2-}$, 2.02 Å. This material displays interesting ferromagnetic properties; however, the literature shows that there is a controversy among scientist due to the nature of the ferromagnetism, the presence of significant Jahn-Teller distortion, and the spin state of the ruthenium. $BaRuO_3$ material it is also ferromagnetic below 60 K [101]; nevertheless, non-Fermi liquid behavior without magnetic transition is observed in $CaRuO_3$ [4, 102]. Moreover, anomalous low temperature electronic and structural behavior was discovered in $PbRuO_3$ [103]. The structure and metallic conductivity at room temperature are similar to those of $SrRuO_3$ and other ruthenate perovskites, but a sharp metal-insulator transition at which the resistivity increases by four orders of magnitude is detected. There some other compositions like Sr_2RuO_4, where the structure is a layered perovskite with an unconventional spin-triplet superconductivity below > 1 K [104, 105]; or $Ln_2Ru_2O_7$ pyrochlore system with spin-glass-like transition around 76 K and 145 K for $Y_2Ru_2O_7$ and $Nd_2Ru_2O_7$, respectively [106].

In order to understand the physical properties of any material, the arrangement and position of the ions in the frame must be elucidated. The B cation arrangement: random, rock-salt, or layered (see Chapter 1), generally determine the physical properties of perovskites ABO_3. Hereafter, the double perovskites with rock-salt type arrangement will be called ordered perovskites; and ones with random arrangement, disordered. There is ample evidence that partial substitution of one of the B-site cations can have a dramatic effect on the physical properties of the structure; altering the number of d-electrons of the metal-ion, and the energy of the d-levels relative to the oxygen $2p$ levels, can have significant effect on the electronic and magnetic properties of the transition oxides. A noteworthy material is $Sr_2Y(Ru_{1-x}Cu_xO_6$ [107]; the parent compound is an antiferromagnetic insulator with $T_N \sim 26$ K. By partial substitution of the Ru ion by Cu, cause a drastic increment on the conductivity and somewhen become superconducting. More fascinatingly is to observe the coexistence of superconductivity and magnetic ordering; moreover, the superconducting transition temperatures and the magnetic ordering temperature are of the same order.

The first studies perovskite-related materials with general formula $AA'BRuO_6$ (A and A' rare earth or alkaline-earth metal; B transition metal) were done in the eighties.

Fernandez *et al*. [108] synthesized and studied the magnetic properties of BaLaMRuO$_6$ (M=Mg,Fe,Co,Ni,Zn) compounds; and almost all the compounds crystallize in the cubic symmetry ($Fm\bar{3}m$), with the cell parameters a=a_p, and the ruthenium cation in pentavalent oxidation state. They show an ordered cation arrangement, except for BaLaFeRuO$_6$ with Fe^{3+} and Ru^{4+} disordered in perovskite B-site. All the compounds exhibit long-range antiferromagnetic order, with Néel temperatures in the range 20-40 K. At the end of the eighties Battle *et al*. [5] reported the spin-glass behavior of BaLaNiRuO$_6$, whereas BaLaZnRuO$_6$ shows A-type antiferromagnetism; and both compounds crystallize in monoclinic $I2/c$ symmetry at room temperature. Nevertheless, some years latter Hong *e*t *al*. [109] suggest the tetragonal $I4/m$ symmetry for Zn compound, the same that for SrLaCuRuO$_6$ [110]. Battle *et al*. [111] checked BaLaCoRuO$_6$ compound to be monoclinic $I2/m$ at room temperature.

To the best of our knowledge, up to the moment there are few compounds of the series SrLnMRuO$_6$ that have been synthesized and studied: SrLaMnRuO$_6$ [73, 112], SrLaCaRuO$_6$ [113], SrLaFeRuO$_6$ [114], SrLaCoRuO$_6$ [111, 115], SrLaNiRuO$_6$ [116] and SrLaCuRuO$_6$ [116]. Fe and Mn containing compounds have disordered ion arrangement, and were reported to crystallized in the orthorhombic $Pbnm$ symmetry; whereas the rest have the transition-metal and Ru^{5+} ordered, and distorted structure, space group $P2_1/n$. Structural phase transition were observed in SrLaMnRuO$_6$, SrLaNiRuO$_6$ and SrLaCuRuO$_6$. The former transforms from the orthorhombic $Pbnm$ space group to the trigonal $R\bar{3}c$ [112], and at low temperatures was reported to exhibit ferrimagnetic order at T_C=220 K [73]; and the other two show $P2_1/n \rightarrow R\bar{3}$ transition sequence [116]. Bos *et al*. [115] presented a study of the $Sr_{1-x}La_{1+x}CoRuO_6$ system, and they observed for x=0 an antiferromagnetic order around 85 K, which agree with the anomaly observed by Kim *et al*. [111] in the magnetic measurements. Nevertheless, depending on the size of the cations could happen a disorder among A- and B-site ions, as reported for SrLaCaRuO$_6$ [113]. Ca cation is too small to fit properly in the octahedra coordination, and its' natural position is the intersticial space formed by the octahedra. Thus, some Ca quantity takes La ion place in the structure, and viceversa; in that case the formula should be written as $Sr(La_{1-x}Ca_x)(Ca_{1-x}La_x)RuO_6$.

However, most of these studies are focused on the room- and low temperature studies, crystal structures and magnetic properties. It is worth mentioning the importance of the structural phase transition studies in order to understand the physical properties observed in the materials. The report on SrLaMRuO$_6$, SrPrMRuO$_6$ and SrNdMRuO$_6$ series shown in the following chapters is mainly focused on that aspect using the symmetry-mode analysis, although some magnetic structures are solved.

The different properties, symmetries, transition temperatures,... observed in different materials depending on the choice of the ions, make us think in several questions, and taking this premise as our starting-point we propose this thesis.

- Which is the evolution of the room temperature symmetry with the tolerance factor?
- What is the evolution of the symmetry-mode amplitudes with the tolerance factor in materials with the same symmetry?
- Which type of cationic arrangement is observed?
- Is there tetravalent or pentavalent ruthenium?
- What happens with the charge-state of the transition-metal?
- Is there any structural phase transition?
- Is it common for all the samples?
- Is it possible to construct a common phase-diagram?
- Is there any relation between the tolerance factor and phase transition temperature?

Chapter 5

$SrNdMRuO_6$ (M=Zn,Co,Mg,Ni) ordered double perovskites

5.1 Room temperature Structures

The tolerance-factor values t [8] for $SrNdMRuO_6$, using the ionic radii [48] are 0.949, 0.948, 0.954 and 0.961 for $SrNdZnRuO_6$, $SrNdCoRuO_6$, $SrNdMgRuO_6$ and $SrNdNiRuO_6$, respectively. These t values are smaller than those for $SrLaNiRuO_6$ ($t = 0.977$), $SrLaCuRuO_6$ ($t = 0.967$) [116] and $SrLaCoRuO_6$ ($t = 0.964$) [111], all of them monoclinically distorted. Thus, the tolerance-factor values suggest, in the one hand, that the room temperature (RT) structures of the title compounds should be, very probably, monoclinically distorted and, in the other hand, that the zinc compound will be the most distorted, and the nickel one, the less. Knowing that the symmetry of $SrLaNiRuO_6$, $SrLaCuRuO_6$ and $SrLaCoRuO_6$ is $P2_1/n$, the structure reported for $SrLaCoRuO_6$ at RT has been used as the starting model for our the refinements.

The laboratory X-ray powder-diffraction (XRPD) data analysis, using that monoclinic model, has shown that the a and b monoclinic cell parameters are very similar to each other and that the monoclinic angle (β) is very close to 90°: the monoclinic distortion is very small. This fact is very common in double perovskites. In this case, the a and b values suggest that the RT phase could have a higher symmetry. Common intermediate phases in double perovskites, below the cubic parent phase, have tetragonal and trigonal symmetries. All the tetragonal groups tried are primitive because the supercell reflections are present. The inset of the Figure 5.1 shows the presence of the primitive (monoclinic) Bragg

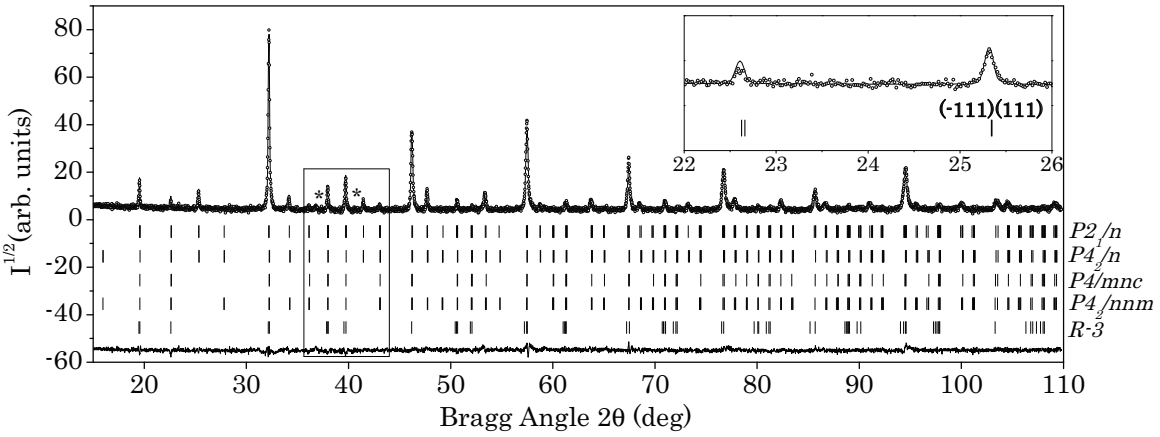

Figure 5.1: Experimental (symbols) and calculated (line) X-ray powder-diffraction profile for the Rietveld refinement of SrNdCoRuO$_6$ at room temperature, using a structural model with the space group $P2_1/n$. The bars in the lower part of the graphics represent the Bragg peaks positions that correspond to the SrNdCoRuO$_6$ phase: first row corresponds to the $P2_1/n$, second row to $P4_2/n$, third row to $P4/mnc$, fourth row to $P4_2/nnm$ and fifth row to $R\bar{3}$ space group. The black rectangle section is shown bigger in Figure 5.2. Inset shows in detail the appearance of the primitive Bragg peak reflections with $h+k+l = 2n+1$. * very small amount of unidentified impurity.

peaks (-111,111) at about 25.4°, that violate the I-centering condition on the *hkl* reflections with $h+k+l = 2n+1$. Figure 5.2 compares a section of the experimental (symbols) and calculated (line) XRPD profiles for the Rietveld refinements of SrNdCoRuO$_6$, at RT, using a structural model with the five different space groups: $P2_1/n$, $P4_2/n$ (ITA No.86), $P4/mnc$ (ITA No.128), $P4_2/nnm$ (ITA No.134) and $R\bar{3}$ (ITA No.148) [51]. The important point is that neither $P4/mnc$ and $P4_2/nnm$ tetragonal space groups nor the trigonal ($R\bar{3}$) should be assigned. Finally, it is not possible to distinguish between $P2_1/n$ and $P4_2/n$ space groups using the laboratory XRPD data.

To elucidate the RT space group ($P2_1/n$ or $P4_2/n$) a synchrotron radiation powder diffraction (SXRPD) experiment was performed. Figure 5.3 shows sections of the experimental (symbols), calculated (line) XRPD (panel (a) and (b)) and SXRPD (panel (c) and (d)) profiles for the Rietveld refinement of SrNdZnRuO$_6$ at RT, using a structural model with the $P2_1/n$ and $P4_2/n$ space groups. The splitting is evident in the SXRPD profiles and the monoclinic symmetry should be assigned to the RT structure of the title compounds.

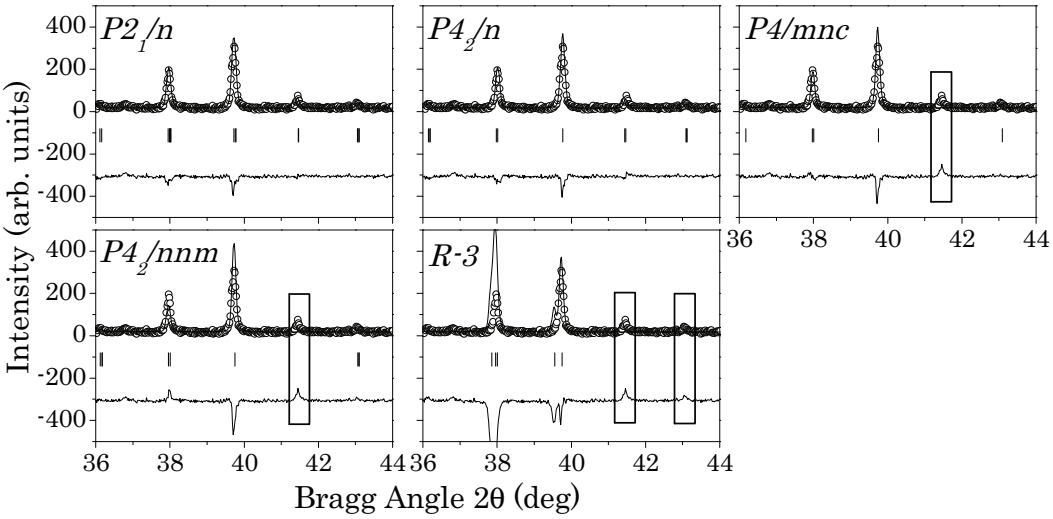

Figure 5.2: Results of the XRPD data refinements, in the 36-44° 2θ interval, in $SrNdCoRuO_6$, using five different models with $P2_1/n$, $P4_2/n$, $P4/mnc$, $P4_2/nnm$ and $R\bar{3}$ space groups. $P2_1/n$ and $P4_2/n$ models are able to take into account all the peaks of the pattern, whereas the other three models are not able (see the boxes).

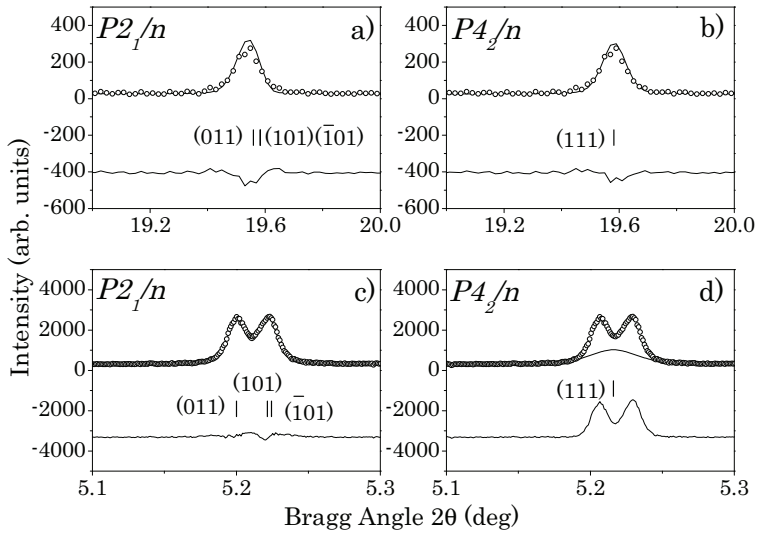

Figure 5.3: Results of the XRPD a) and b) and SXRPD c) and d) data refinements, in the 19-20° and 5.1-5.3° 2θ interval respectively, in $SrNdCoRuO_6$, using two different models with $P2_1/n$ and $P4_2/n$ space groups. The tetragonal space group has only one reflection in this 2θ interval, and is unable to take into account the splitting observed in SXRPD; on contrary, the monoclinic space group has three reflections and takes perfectly into account the splitting.

The neutron powder diffraction (NPD) patterns from the four compounds at RT are shown in Figure 5.4 and the Rietveld refinement results are given in Table 5.1. The isotropic temperature factors (Biso) for oxygen atoms were fixed to be equal in the refinements after several trials: all Biso independent, Biso for O1 and O2 fixed equal and O3 independent, and Biso for O1, O2 and O3 fixed equal. At different attempts, the most important distortion irrep amplitudes are the same as can be observed in panels (a), (b) and (c) of Figure 5.5. Panel (d) in Figure 5.5 show results of Biso factors for different attempts, causing a big distorting when Biso(O1)≠Biso(O2)≠Biso(O3). Although the Biso values are different, the average values (half-full black and blue labels) have the same value as obtained for Biso(O1)=Biso(O2)=Biso(O3) (red-star label). GM_1^+, X_2^+ and GM_3^+ irrep amplitudes are smaller than 0.1 Å and keep the same value for different refinements. The amplitude value for GM_5^+ is around 0.2 Å and the refinement values are the same except for Zn and Ni samples; nevertheless, the difference is small. Taking into account that the objective of the work is to follow the temperature induced phase transitions, and the distortion irrep amplitudes remain unchanged, the isotropic temperature factor values for oxygens were fixed to be equal in the refinements.

The refinements have shown that there is a total degree of ordering between the M and Ru atoms. The (nominal) oxidation states of the cations are M^{2+} and Ru^{5+}, which gives a charge difference of 3; rather high to be presented a disordered arrangement of the B-site cations [31]. Size differences between those cations also contribute to the ordering. The mean interatomic distances and some selected bond angles, extracted from the neutron-data refinements, are listed in Table 5.2 . For the Ru-O bonds, the average values of the bond distances are very close to the predicted values, although in two of the compounds ($SrNdZnRuO_6$ and $SrNdNiRuO_6$) the three Ru-O distances are different from each other. In all the compounds, the M cation is over-bonded with the bond lengths being shorter than the expected values obtained by calculating the distances in the bond-valence method [86].

At Figure 5.6 the relation between the cells of the RT structure and the reference structure is shown. All the crystallographic information given in Table 5.1 and Figure 5.6 is in the non-standard setting of the space group ITA No.14, $P2_1/c$, which the commonly used experimental setting, as it gives a unit cell best suited for comparisons. As mentioned above, the knowledge of the orientation of the cells (via the transformation matrix that relates the parent phase cell to the low symmetry phase) is necessary to perform the symmetry-mode analysis.

Table 5.1: Crystal structure data and refinement results for $SrNdMRuO_6$ (M=Zn,Co,Mg,Ni) from NPD at RT after the refinement of all modes. Sr/Nd (4e (x,y,z), $occ = 0.5/0.5$), M (2b (0,0,1/2), $B_{iso} = 0.5$ Å^2, $occ = 1$), Ru (2a (0,0,0), $B_{iso} = 0.5$ Å^2, $occ = 1$), O (4e (x,y,z), $occ = 1$). The B_{iso} value for M and Ru cations was fixed in 0.5 Å^2 in order to guarantee the convergence of the refinement.

		$SrNdZnRuO_6$	$SrNdCoRuO_6$	$SrNdMgRuO_6$	$SrNdNiRuO_6$
Space group		$P2_1/n$	$P2_1/n$	$P2_1/n$	$P2_1/n$
Sr/Nd	x	-0.0066(5)	-0.0073(6)	-0.0063(8)	-0.0053(9)
	y	0.4645(2)	0.4688(3)	0.4729(3)	0.4697(3)
	z	0.750(1)	0.7516(1)	0.750(1)	0.756(1)
	B_{iso}(Å^2)	0.27(2)	0.39(2)	0.31(2)	0.55(3)
O1	x	-0.2771(7)	-0.286(1)	-0.287(1)	-0.272(1)
	y	0.2168(7)	0.203(1)	0.205(1)	0.224(1)
	z	-0.0362(7)	-0.0369(8)	-0.0386(7)	-0.0286(7)
	B_{iso}(Å^2)	0.71(2)	0.71(2)	0.65(2)	0.61(2)
O2	x	-0.7982(7)	-0.781(1)	-0.776(1)	-0.790(1)
	y	0.2942(7)	0.277(1)	0.275(1)	0.293(1)
	z	0.0400(7)	0.0339(8)	0.0293(7)	0.0396(7)
	B_{iso}(Å^2)	0.71(2)	0.71(2)	0.65(2)	0.61(2)
O3	x	0.0753(4)	0.0708(6)	0.0721(6)	0.0778(7)
	y	0.0128(3)	0.0091(5)	0.0090(5)	0.0083(6)
	z	0.7580(8)	0.7588(9)	0.754(1)	0.759(1)
	B_{iso}(Å^2)	0.71(2)	0.71(2)	0.65(2)	0.61(2)
a (Å)		5.5570(1)	5.5428(2)	5.5434(2)	5.5301(2)
b (Å)		5.5932(1)	5.5550(2)	5.5537(2)	5.5388(2)
c (Å)		7.8647(2)	7.8333(3)	7.8361(3)	7.8166(3)
β (°)		90.013(8)	90.044(7)	90.052(6)	90.015(8)
V (Å^3)		244.45(1)	241.19(1)	241.24(1)	239.42(1)
R_p(%)		3.82	4.11	4.48	4.32
R_{wp}(%)		4.77	5.31	5.74	5.52
R_{exp}(%)		2.36	2.17	2.51	2.11
χ^2		4.08	5.98	5.23	6.84
R_{Bragg}(%)		6.33	7.31	8.32	6.79

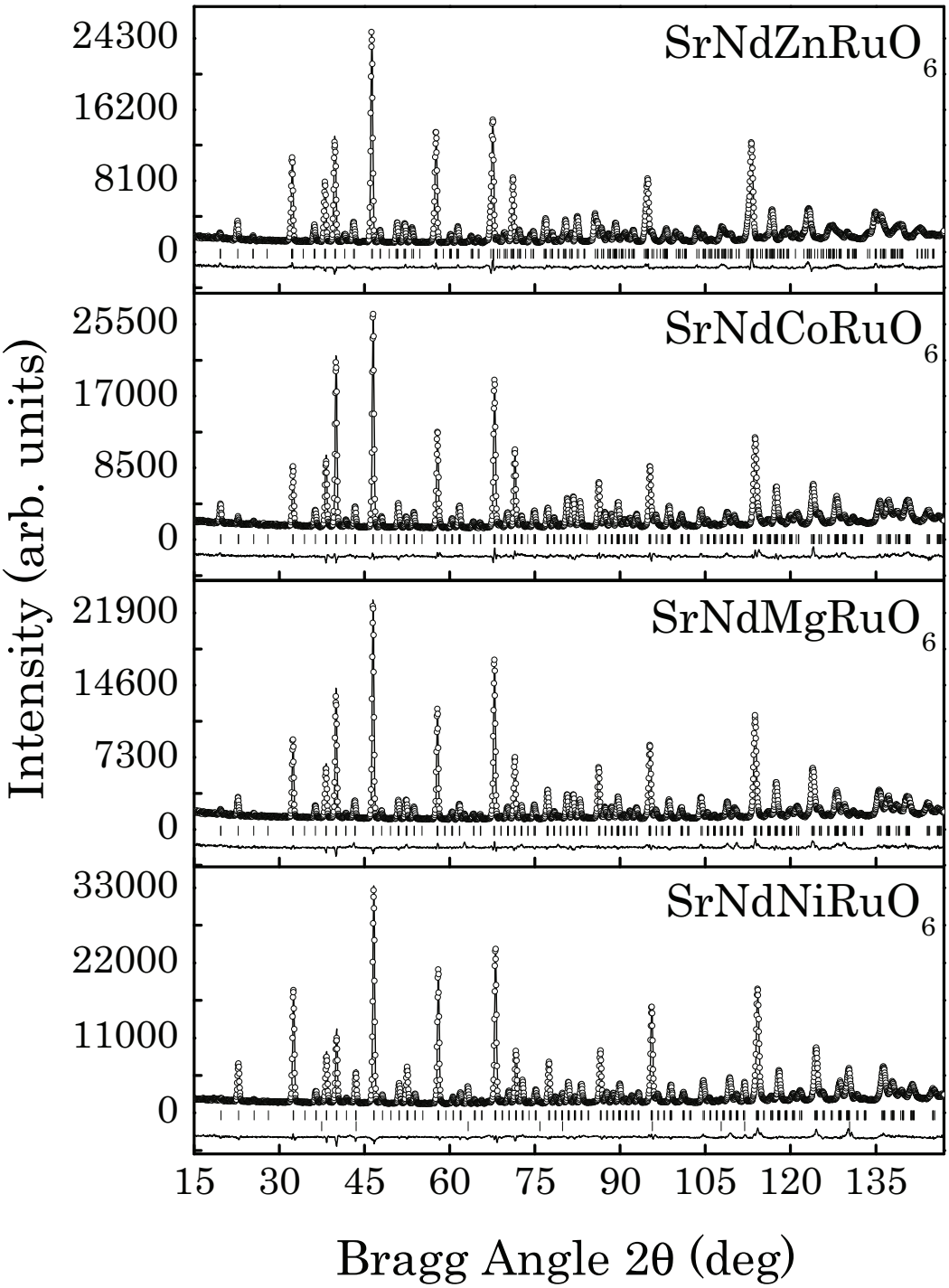

Figure 5.4: Experimental (symbols) and calculated (line) neutron powder-diffraction profiles for the Rietveld refinement of SrNdMRuO$_6$ (M=Zn,Co,Mg,Ni) at room temperature, using a structural model with the space group $P2_1/n$. The bars in the lower part of the graphics represent the Bragg peaks positions. In the case SrNdNiRuO$_6$, the lower set of bars correspond to the impurity NiO (4.84(7)%).

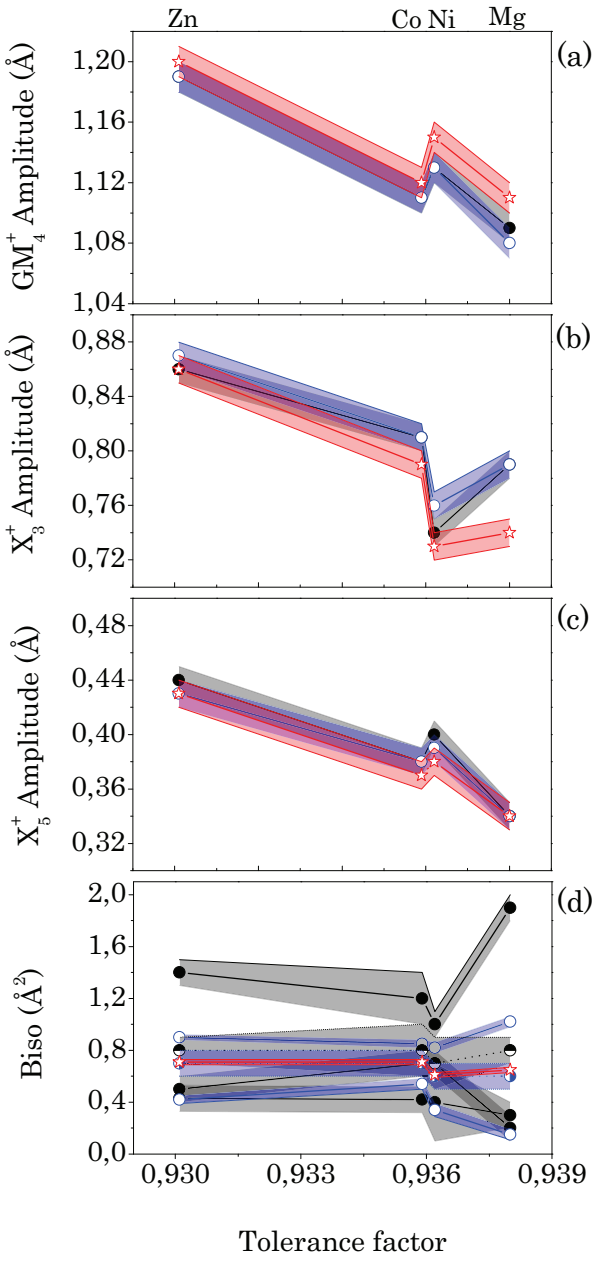

Figure 5.5: Variation of (a) GM_4^+ distortion irrep amplitude (Å); (b) X_3^+ distortion irrep amplitude (Å); (c) X_5^+ distortion irrep amplitude (Å), and (d) isotropic temperature factors (Å^2), as function of experimentally calculated tolerance factor for SrNd*M*RuO$_6$ (*M*=Zn,Co,Mg,Ni) at room temperature. Label color and symbol indicate three different refinements: black full circle, isotropic temperature factors for O1, O2 and O3 independent; blue empty circle, isotropic temperature factors of O1 and O2 refined with the same code and O3 independent; and red star, all isotropic temperature factors refined with the same code. In (d) half-full black and blue symbols, and dotted lines indicate the average value of the isotropic temperature factors for each refinement.

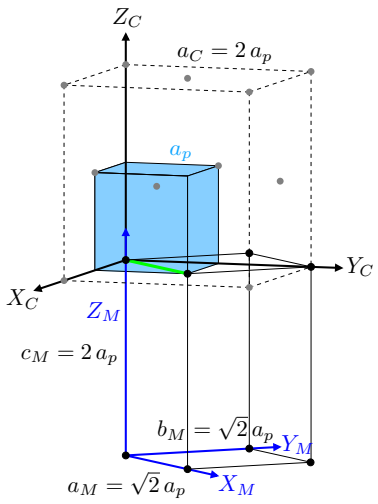

Figure 5.6: Relative orientation of the unit cell of the prototype cubic simple perovskite ($Pm\bar{3}m$)(blue), of the prototype cubic double perovskite ($Fm\bar{3}m$) (dashed line), and the distorted monoclinic $P2_1/n$ of the double perovskite (solid line).

The results of AMPLIMODES are show in Table 5.3 and 5.4. There are seven irreducible representations (irreps) of the $Fm\bar{3}m$ space group, that can take part in the symmetry breaking from that space group to the RT $P2_1/n$ monoclinic space group: $GM_1^+(1)$ (totally symmetric), $GM_3^+(1)$, $GM_4^+(1)$, $GM_5^+(4)$, $X_2^+(1)$, $X_3^+(1)$ and $X_5^+(3)$. The numbers in parenthesis (Table 5.3) indicate the number of modes transforming according to the corresponding irrep. (In Table 5.4 those numbers are the dimension (Dim. column) of the irrep.) Hence, there are 12 modes (one of them is the totally symmetric). In Table 5.3 we show part of the output from AMPLIMODES; the modes' labels indicate the atoms, with their corresponding Wyckoff position in the reference structure, involved in the modes. Therefore, from the twelve modes, 8 (+1) modes move only the oxygen atoms (24e) and the other 3 modes, the Sr/Nd atoms (8c) [36]. As indicated in Table 5.4, the GM irreps have a (0,0,0) k-vector, they maintain the unit cell; and the X irreps have a (0,1,0) k-vector, they double the unit cell in the b direction. The isotropy groups stand for the possible intermediate groups, with a group-subgroup relation between the reference and the distorted symmetry phase (see below). The atomic displacements involved in the modes imply the symmetry breaking from the prototype symmetry to the isotropy group symmetry. The final results of the refinement are indicated as the value of the amplitude associated to each mode transforming according to the irrep.

The geometrical representations of the distortion modes of the symmetry breaking from the cubic prototype phase into the monoclinic $P2_1/n$ phase, taking as reference the

monoclinic cell, are the following, see Figure 5.7. In it, we are plotting the Ru octahedra in blue, and the Co, in gold. The A/A'-site cations are shown in green and the oxygens in red. As a reference, we are also plotting the simple perovskite cubic cell (red), the double perovskite parent phase cell (blue) and the monoclinic cell (black). The polarization vectors of the modes are shown by small black arrows. The effect of the mode can be appreciated by the two configurations shown: the cubic configuration, in which by definition the mode does not act, below the actual configuration corresponding to the isotropy group symmetry, resulting from the action of the mode. GM_3^+, expands the octahedra in the equatorial *ab* plane, while the apical (in the *c* axis) oxygens are moved along *c* axis to the center of the octahedra. GM_4^+, is essentially a rotation around the *b* axis; although it deforms a bit the octahedra (the displacement of the oxygens in the *ab* plane and the ones in *c* axis are not the same). GM_5^+ irrep is four dimensional, actuating on A/A'-site cations and oxygens. GM_5^+-A4 and GM_5^+-A5 modes, displace the A/A'-site cations in *a* and *c* axes, respectively. GM_5^+-A6, moves the equatorial oxygens in the *ab* plane, transforming in a rectangle the square formed by the oxygens; while GM_5^+-A7, is a kind of rotation along *b* axis, with the apical oxygens displaced in the opposite direction of the rotation. The mode transforming according to X_3^+ is a pure rotation of the octahedra around the *c* axis. X_2^+ mode actuates on the equatorial oxygens, deforming into a rhombus the square formed by the oxygens. Finally, there are three modes that transforms according to X_5^+ irrep. This mode actuates on the oxygens and on the A/A'-site cations (Sr/Nd). In the former case, it is a rotation around the *a* axis, although the amount of displacements in the *ac* plane and the ones in *b* are not the same. In the latter, displaces the Sr/Nd cations along the *b* axis.

The theory predicts that there is not a single irrep that breaks the symmetry from the prototype structure to the monoclinically distorted RT structure; at least, the symmetry breaking needs two modes: thus, there is not a primary mode, necessarily there are two active modes that must couple and give rise to the observed RT symmetry. The theory also states that those modes that experimentally should break the symmetry down to the RT experimentally observed one should be the most intense ones; that is, the ones with the highest amplitudes. Indeed, this is the fact observed experimentally. Looking at the NPD refinement final-values for the amplitudes of the modes transforming according to the irreps (see Table 5.4), it is clear that there are three global mode-amplitudes (GM_4^+, X_3^+ and X_5^+ irreps) that are higher than the rest. The necessary ones to break the symmetry are GM_4^+ and X_3^+, as those are the ones that have the RT monoclinic space group as the maximum subgroup. The X_5^+ is half the value of those two and it is twice the next amplitude value of GM_5^+; and GM_1^+, GM_3^+ and X_2^+ have negligible values, two orders of magnitude lower than the highest amplitude value.

Table 5.2: Octahedra tilt angles (°), volume of the octahedra (Å^3), main bond distances (Å) and selected angles (°) for SrNdMRuO$_6$ (M=Zn,Co,Mg,Ni) at room temperature. The values were obtained refining all mode amplitudes.

M	Zn	Co	Mg	Ni
MO_6 octahedra				
Tilt angle $\psi_{[001]p}$	10.40(8)	6.6(1)	5.7(1)	9.4(1)
Tilt angle $\phi_{[110]p}$	11.8(2)	11.0(2)	11.4(2)	12.0(3)
V(MO_6)	11.43(1)	11.34(1)	11.00(1)	10.99(1)
M-O1($\times$2)	2.031(4)	2.052(6)	2.044(6)	1.996(6)
M-O2($\times$2)	2.042(4)	2.009(6)	1.989(6)	2.000(6)
M-O3($\times$2)	2.073(6)	2.065(7)	2.033(9)	2.073(9)
Average distance	2.049(2)	2.042(3)	2.022(3)	2.023(3)
Predicted distance	2.1105	2.0985	2.0995	2.0605
RuO_6 octahedra				
Tilt angle $\psi_{[001]p}$	7.00(9)	9.6(1)	9.4(1)	5.6(1)
Tilt angle $\phi_{[110]p}$	12.6(2)	11.8(2)	11.8(2)	12.9(3)
V(RuO_6)	10.37(1)	9.97(1)	10.24(1)	10.14(1)
Ru-O1($\times$2)	1.981(4)	1.967(6)	1.977(6)	1.960(6)
Ru-O2($\times$2)	2.016(4)	1.977(6)	1.981(6)	2.015(6)
Ru-O3($\times$2)	1.951(6)	1.931(7)	1.967(9)	1.930(9)
Average distance	1.982(2)	1.958(3)	1.975(3)	1.968(3)
Predicted distance	1.9675	1.9675	1.9675	1.9675
∠O1-M-O2	94.4(3)	88.4(2)	87.6(2)	94.7(2)
∠O1-M-O3	90.7(1)	90.5(2)	90.7(2)	87.7(2)
∠O2-M-O3	90.4(3)	90.1(2)	91.2(2)	90.1(2)
∠O1-Ru-O2	87.4(3)	93.9(2)	94.5(2)	87.3(2)
∠O1-Ru-O3	90.2(1)	90.3(2)	90.0(2)	92.7(2)
∠O2-Ru-O3	90.2(3)	89.2(2)	88.0(2)	90.2(2)
∠M-O1-Ru	158.7(2)	155.0(2)	154.7(2)	163.1(2)
∠M-O2-Ru	152.6(4)	159.7(2)	162.5(2)	154.2(2)
∠M-O3-Ru	155.6(2)	157.1(1)	156.8(1)	155.0(1)
Bond-Valence sum				
M	2.37(1)	2.34(2)	2.47(2)	2.22(2)
Ru	4.82(3)	5.13(4)	4.90(4)	5.01(4)

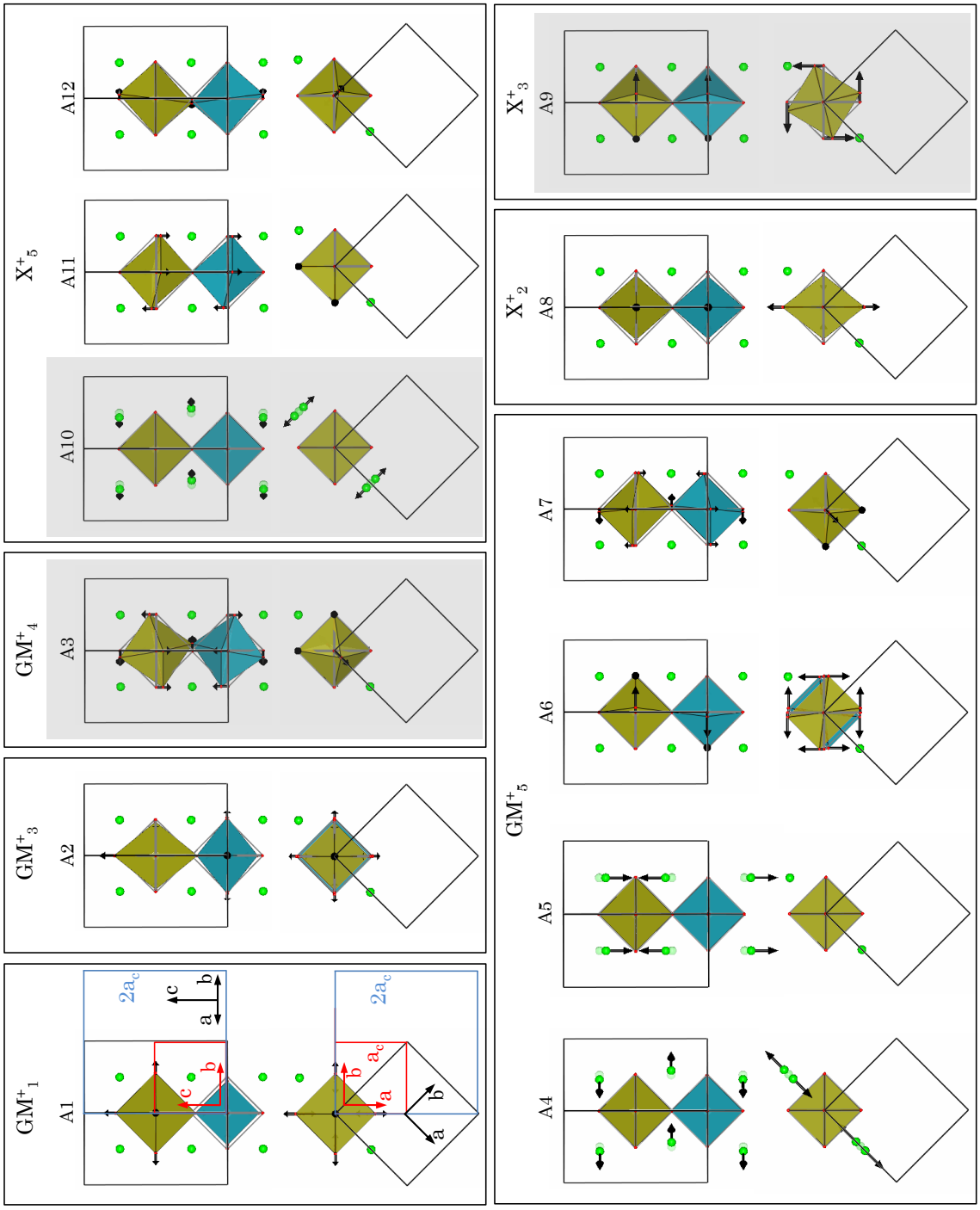

Figure 5.7: Geometrical representations of the distortion modes of the symmetry breaking from the cubic prototype phase into the monoclinic $P2_1/n$ phase: $GM_3^+(1)$, $GM_3^+(1)$, $GM_4^+(1)$, $GM_5^+(4)$, $X_2^+(1)$, $X_3^+(1)$ and $X_5^+(3)$. The numbers in parenthesis indicate the number of modes transforming according to the corresponding irrep. The principal modes are highlighted in grey.

Table 5.3: Resume of the irreps taking part in the symmetry breaking from the totally symmetric, cubic, space group ($Fm\bar{3}m$) to the room temperature $P2_1/n$ monoclinic and $P4_2/n$ tetragonal space group. The list is part of the output of AMPLIMODES for FullProf. The number in parenthesis indicate the number of modes transforming according to the irrep.

Atoms	WP	Modes
$Fm\bar{3}m \rightarrow P2_1/n$		
O1	24e	$GM^{1+}(1)$ $GM^{3+}(1)$ $GM^{4+}(1)$ $GM^{5+}(2)$ $X^{2+}(1)$ $X^{3+}(1)$ $X^{5+}(2)$
Sr1/Nd1	8c	$GM^{5+}(2)$ $X^{5+}(1)$
$Fm\bar{3}m \rightarrow P4_2/n$		
O1	24e	$GM^{1+}(1)$ $GM^{3+}(1)$ $GM^{4+}(1)$ $X^{2+}(1)$ $X^{3+}(1)$ $X^{4+}(2)$ $X^{5+}(2)$
Sr1/Nd1	8c	$X^{5+}(1)$

Indeed, all modes, except GM_4^+ and X_3^+, do appear as degrees of freedom due to the symmetry break. In symmetry jargon, and referring to displacive phase transitions, they represent allowed atomic displacements giving rise to configurations of higher symmetry than that of the low symmetry space group and compatible with the parent space group higher symmetry. The space groups of these (*intermediate*) configurations are the isotropy space groups. These compatible displacements are described by the amplitudes of the rest of the modes associated to the rest of the irreps: GM_3^+, GM_5^+ and X_2^+. Those amplitudes can have big (always smaller than the symmetry breaking ones) or small values. Indeed, some of them could have very small values, in which case, they could be set to zero: hence, they are formally excluded from the refinement process. And, this, in turn, means that the refinement is performed using less of the allowed degrees of freedom: the refinement requires less freed parameters. The efficiency of the refinement process is higher. This reduction in the number of refined parameters (degrees of freedom) is physically pertinent: it is the actual experimentally found structure that tells us that although symmetry permits some other displacements, there are some other physical reasons that discard those displacements from being present. Which, as mentioned, plays in favor of the refinement, simplifying it. Put into numbers, the actual freed parameters are 21, instead of the grand total 30 ones. This reduction in the freed parameters affects differently R reliability values, although the amplitude values of the necessary modes are unaffected, taking into account the errors (Table 5.4).

To illustrate this we have done, for each of the compound at RT, a set of three structural refinements (a), (b) and (c), as indicated in the Table 5.4. In the first refinement all the amplitudes were freed, in the second one the amplitudes of the modes transforming according to GM_1^+, GM_3^+ and X_2^+ were set to zero: as mentioned their values are two orders of magnitude lower than the highest. Finally, in the third refinement, the amplitude of GM_5^+ was also nullified, which is one order of magnitude lower that the highest. The

effect of the three refinements on the reliability factors is clear: a reduction of six degrees of freedom (50% of the total) increases the R factors less than a 10% (mean value).

Looking at the classification of the modes in irreps (Table 5.3) and to the atoms they affect to, we infer that the coupled modes only involve oxygen atoms (Figure 5.7). And the physical interpretation of the oxygens' displacements, in those modes, is the rotation, tilt, of the octahedra Figure 5.8. For sure, this is the known result for these kind of materials: the symmetry-breaking phase transitions are originated by the tilting of the octahedra, accompanied by some small displacement of the A-site cations. It is worth noting here that it is clear that in all the members of the materials the same two coupled modes are expected, as this is a result of the symmetry-mode analysis: the differences among the members of the family are in the values of the refined amplitudes, which indicate the grade of (monoclinic) distortion of the materials.

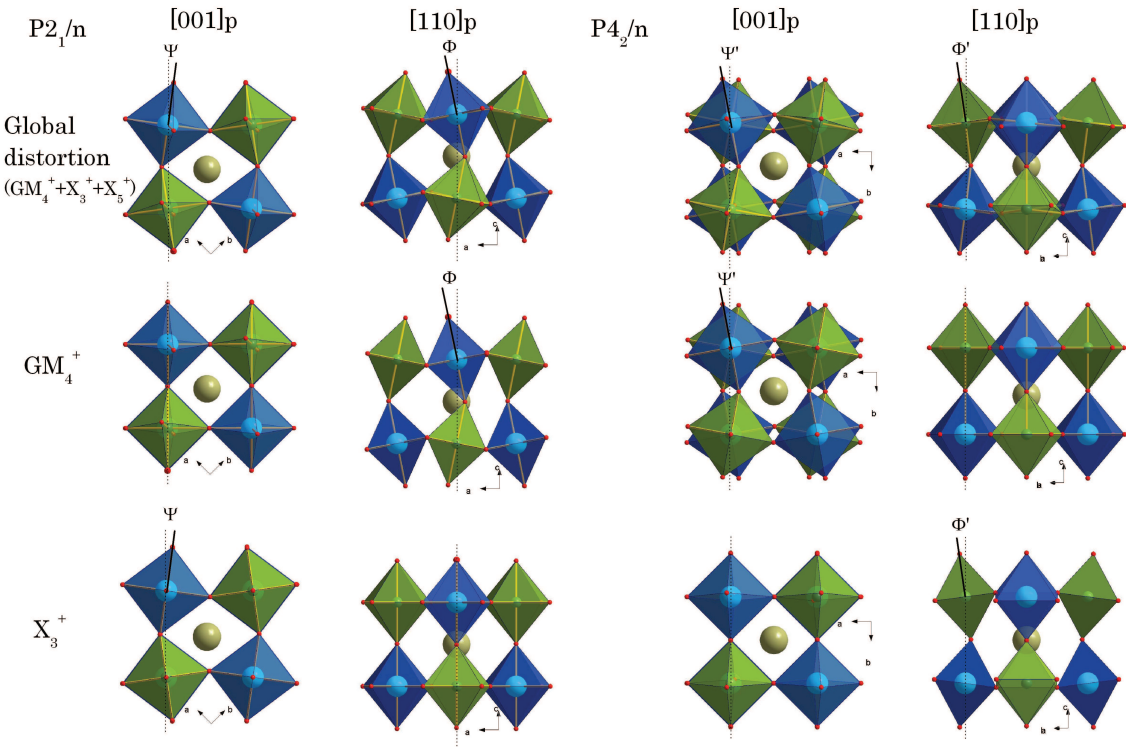

Figure 5.8: Projection along the cubic (simple) perovskite $[001]_p$ and $[110]_p$ directions, of a section of the unit cell of the double perovskite with $AA'BB'O_6$ general formula in the $P2_1/n$ and $P4_2/n$ space groups. There is a direct relation between the octahedra tilt and symmetry-adapted mode.

Table 5.4: Values after the refinement of the amplitudes (in Å) of the irreps taking part in the symmetry breaking from $Fm\bar{3}m$ space group to the room-temperature $P2_1/n$ monoclinic space group, refining (a) all modes, (b) 4 and (c) 3 highest amplitudes modes for SrNdMRuO$_6$ (M=Zn,Co,Mg,Ni) compounds.

Irrep	Isotropy subgroup	Dim	Amplitude											
			Zn			Co			Mg			Ni		
			(a)	(b)	(c)	(a)	(b)	(c)	(a)	(b)	(c)	(a)	(b)	(c)
GM_1^+	$Fm\bar{3}m$	1	0.04(1)	0.00	0.00	0.07(8)	0.00	0.00	0.00(2)	0.00	0.00	0.02(2)	0.00	0.00
GM_3^+	$I4/mmm$	1	0.07(1)	0.00	0.00	0.06(2)	0.00	0.00	0.03(2)	0.00	0.00	0.11(2)	0.00	0.00
GM_4^+	$C2/m$	1	1.200(3)	1.202(3)	1.205(4)	1.122(4)	1.119(3)	1.119(4)	1.109(4)	1.102(4)	1.108(4)	1.152(5)	1.129(4)	1.127(4)
GM_5^+	$C2/m$	4	0.194(9)	0.18(1)	0.00	0.163(1)	0.13(2)	0.00	0.19(1)	0.17(1)	0.00	0.23(2)	0.10(2)	0.00
X_2^+	$P4_2/mnm$	1	0.012(4)	0.00	0.00	0.036(7)	0.00	0.00	0.041(8)	0.00	0.00	0.036(8)	0.00	0.00
X_3^+	$P4/mnc$	1	0.855(4)	0.857(4)	0.851(5)	0.790(5)	0.798(5)	0.797(5)	0.737(5)	0.743(5)	0.737(5)	0.733(6)	0.760(5)	0.764(5)
X_5^+	$Pnnm$	3	0.425(3)	0.424(2)	0.403(3)	0.365(5)	0.367(3)	0.352(3)	0.336(6)	0.323(3)	0.304(3)	0.376(6)	0.365(3)	0.345(3)
R_p(%)			3.82	4.06	5.02	4.11	4.23	4.58	4.48	4.66	5.05	4.32	4.45	4.79
R_{wp}(%)			4.77	5.04	6.51	5.31	5.33	5.85	5.74	5.91	6.46	5.52	5.64	6.05
R_{exp}(%)			2.36	2.36	2.36	2.17	2.17	2.17	2.51	2.51	2.51	2.11	2.11	2.11
χ^2			4.08	4.56	7.59	5.98	6.01	7.25	5.23	5.55	6.60	6.84	7.11	8.18
R_{Bragg}(%)			6.33	7.02	9.49	7.31	7.80	8.97	8.32	9.03	10.4	6.79	6.96	7.92

K-vector: GM_1^+ (0,0,0), GM_3^+ (0,0,0), GM_4^+ (0,0,0), GM_5^+ (0,0,0), X_2^+ (0,1,0), X_3^+ (0,1,0), X_5^+ (0,1,0)

Direction: GM_1^+ (a), GM_3^+ (a,0), GM_4^+ (a,a,0), GM_5^+ (-b,a,-a), X_2^+ (0,a,0), X_3^+ (0,a,0), X_5^+ (a,a,0,0,a,-a)

We want to quantify the effect of the size of the cations placed in the *B* position on the RT structure, via the symmetry-mode amplitudes. Focusing on the compounds reported in this work, there is a clear connection between the *B*-cation size and the distortion of the structure: the bigger the tolerance factor (the smaller the average experimental atomic radius of the *B*-cations), the smaller are the values of the amplitudes. This means that the smaller the size of the *B*-position cation the less distorted monoclinic structure stabilizes at RT. But, this is the trend observed in three of the four compounds: there is one exception, $SrNdNiRuO_6$. It has higher mode amplitudes than $SrNdMgRuO_6$. This suggests that although the main contribution to the stabilization of the RT distortion is steric, i.e. related to the size, some other factors could also be responsible for the grade of distortion.

5.2 High temperature induced phase transitions

Figure 5.9 presents the thermal evolution, from XRPD, of the scattering intensity for two 2θ intervals, corresponding to 2θ=24°-26° (111;-111) monoclinic primitive reflections and to 2θ=92°-96° (see below, (642) cubic $Fm\bar{3}m$ reflection).

In all the compounds of the family, it can be observed that the monoclinic distortion reduces as temperature increases. Indeed, at 740, 660, 560 and 440 K, for SrNdMRuO$_6$

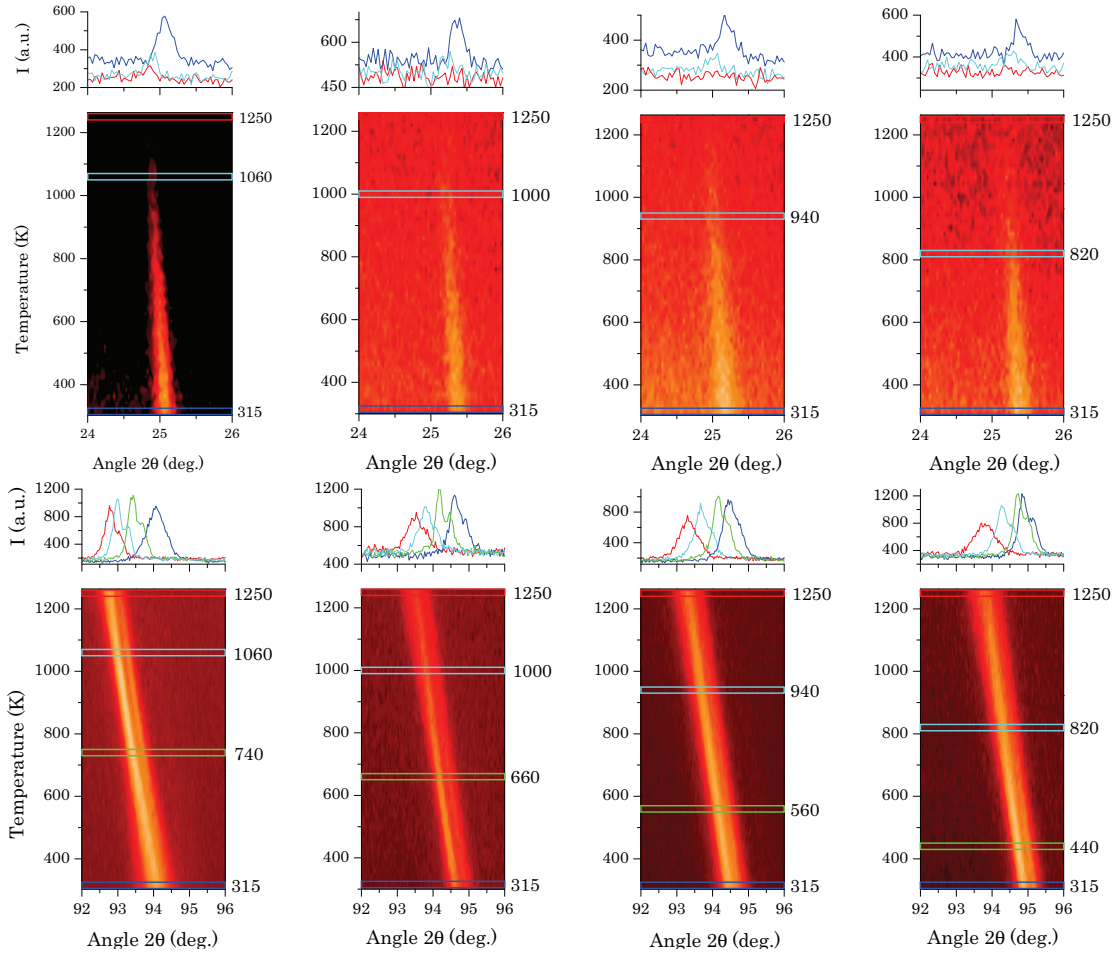

Figure 5.9: Thermal evolution of the (111)(-111) primitive and (642) cubic reflections, (top) and (bottom) respectively, of (left) SrNdZnRuO$_6$, (middle-left) SrNdCoRuO$_6$, (middle-right) SrNdMgRuO$_6$ and (right) SrNdNiRuO$_6$ obtained from XRPD experiment. The scattered intensity is represented with yellow-red scale, light-yellow being high-intensity and dark-red lowest intensity. At the green temperature the primitive Bragg peaks are maintained, whereas the monoclinic splitting transforms into a tetragonal one. At the light-blue temperature the tetragonal splitting disappears evolving the tetragonal reflections into a single cubic one , at the same temperature disappear the primitive reflections.

(M=Zn,Co,Mg,Ni), respectively, a sudden increase of the distortion is observed. We have interpreted this anomaly as a structural phase transition, with a first order character, as the splitting change is abrupt. This fact is clearly seen in the Figure 5.10 for $SrNdZnRuO_6$. Nevertheless, as it is shown in Figure 5.9 (2θ=24°-26°), the hkl reflections with $h+k+l = 2n+1$, the primitive ones, do not disappear at the mentioned temperatures. Our interpretation is that the system suffers a discontinuous phase transition to a primitive cell. At higher temperatures, the XRPD data, (Figure 5.9 and Figure 5.10), suggest a second phase transition, approximately at 1060, 1000, 940 and 820 K, for $SrNdMRuO_6$ (M=Zn,Co,Mg,Ni) respectively: evidenced by the complete losing of the splitting accompanied by the disappearance of the primitive reflections. We interpret this as a second phase transition. In this case the primitive reflections disappear (go to the background) in a continuous way; and, at the same time the splitting disappears also continuously. Thus, the second phase transition is of the second order.

$P4_2/n$ space group was tested as the possible symmetry of the intermediate phase Table 5.5. It is a group with a primitive cell, as needed; and, the tetragonal cell is suggested by the close values of the a and b cell parameters at RT. Tests have been performed with different monoclinic, tetragonal and trigonal models (Figure 5.11). Although this space group is not very common for the double perovskites, it is the less symmetric tetragonal primi-

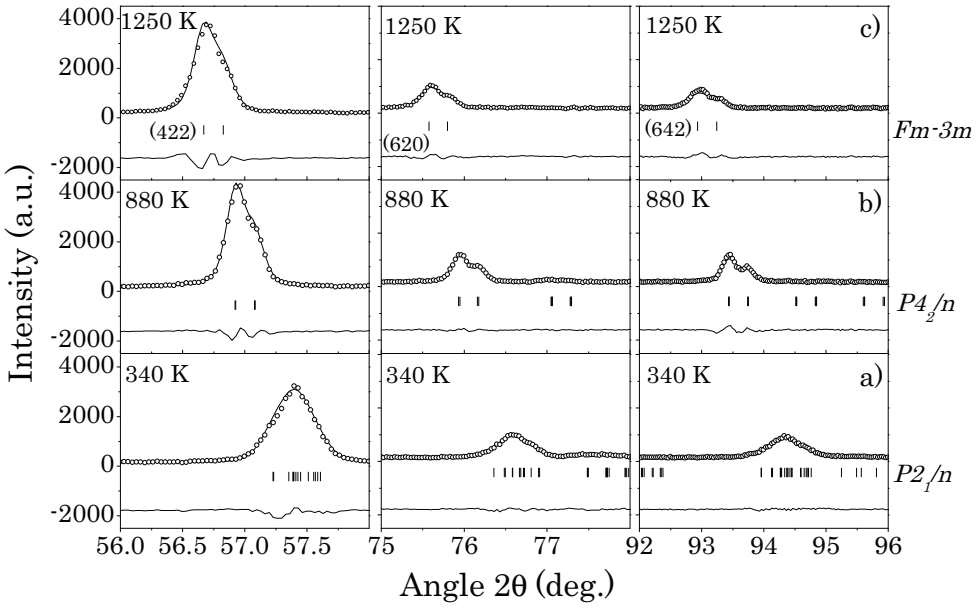

Figure 5.10: The thermal evolution of the (422), (620) and (642) cubic reflections as determined from XRPD measurements for $SrNdZnRuO_6$ are shown in left, middle and right panels, respectively. Each panel represent a 2θ section of the whole pattern at a fixed temperature: a) 340 K, b) 880 K and c) 1250 K.

Table 5.5: Crystal structure data and refinement results for $SrNdCoRuO_6$ from NPD at 653 K using $P4_2/n$ model. Cell parameters: a=7.8688(4) Å; c=7.8728(8) Å; V=487.47(6) Å^3. Reliability factors (NPD): R_p=8.75%, R_{wp}=11.6%, R_{exp}=4.80%, R_{Bragg}=15.8%. The B_{iso} value for Co and Ru cations was fixed in 0.5 Å^2 in order to guarantee the convergence of the refinement.

Atom	Site	x	y	z	B_{iso}(Å^2)	Occupancy
Sr/Nd	2a	0.25	0.25	0.25	1.28(6)	0.5/0.5
Sr/Nd	4e	0.75	0.25	0.775(1)	1.28(6)	0.5/0.5
Sr/Nd	2b	0.75	0.75	0.25	1.28(6)	0.5/0.5
Co	4d	0.5	0.5	0.5	0.5	1
Ru	4c	0	0	0	0.5	1
O1	8g	0.031(2)	0.013(2)	0.227(1)	1.57(6)	1
O2	8g	0.240(2)	-0.049(1)	-0.023(1)	1.57(6)	1
O3	8g	0.040(1)	0.264(2)	-0.033(1)	1.57(6)	1

tive space group possible for ordered double perovskites. We have checked the possible symmetry miss-assignment, analyzing the possible presence of pseudo-symmetry, utilizing the PSEUDO program [98]. The results show that none of the minimal supergroups of$P4_2/n$ given by PSEUDO ($P4_2/m$ (ITA No.84), $P4_2/nnm$ and $P4_2/ncm$ (ITA No.138)) can be assigned to the experimental observed structure. Finally, the refinements suggest that the high temperature phase is the parent cubic phase: $Fm\bar{3}m$ space group.

Figure 5.12 presents the variation with the temperature of the cell parameters, as ob-

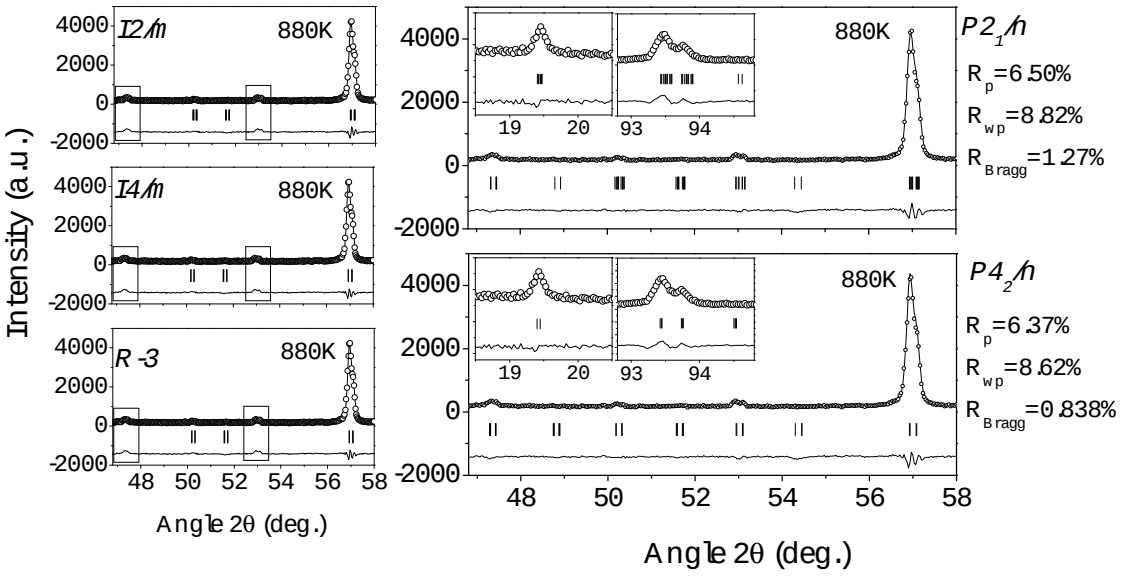

Figure 5.11: Results of the XRPD data refinements at 880 K in $SrNdZnRuO_6$, using five different models with $P2_1/n$, $P4_2/n$, $I2/m$, $I4/m$ and $R\bar{3}$ space groups. The failure of $I2/m$, $I4/m$ and $R\bar{3}$ symmetries is clear, since small peaks are observed in the pattern which are not indexed by the models. The tetragonal $P4_2/n$ symmetry is suggested for the intermediate phase.

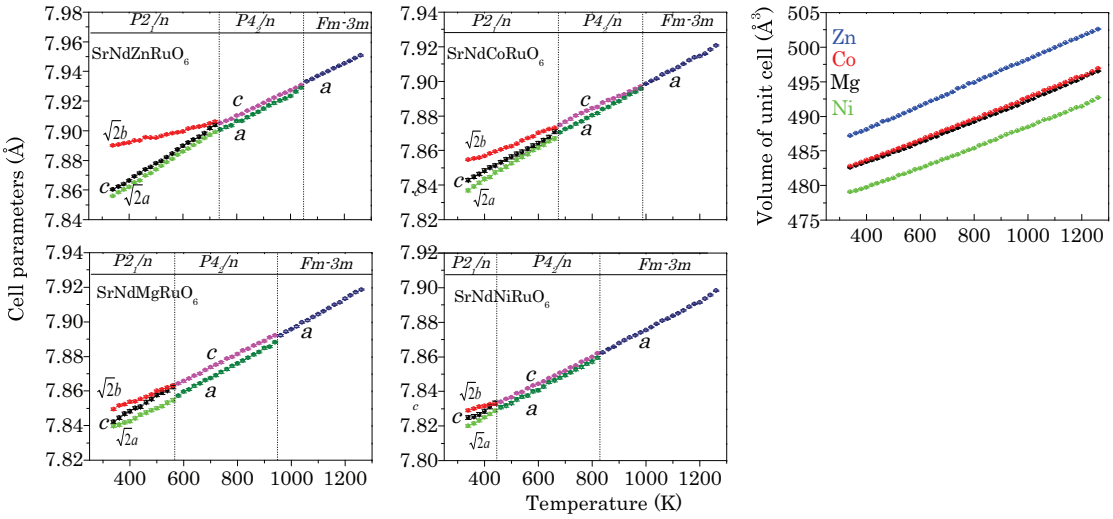

Figure 5.12: Temperature evolution of the cell parameters and cell-volume of SrNdMRuO$_6$ (M=Zn,Co,Mg,Ni). The monoclinic a and b cell parameters have been scaled to be comparable with the tetragonal and cubic cell parameters. The transition temperatures (T$_1$: $P2_1/n$ $P4_2/n$; T$_2$: $P4_2/n$ $Fm\bar{3}m$) for SrNdMRuO$_6$ (M=Zn,Co,Mg,Ni) are the following: T$_1$=740, 660, 560, 440 K, and T$_2$=1060, 1000, 940, 820 K, respectively.

tained by XRPD, of SrNdZnRuO$_6$, SrNdCoRuO$_6$, SrNdMgRuO$_6$ and SrNdNiRuO$_6$. The monoclinic parameters have been scaled to compare with the edge of the tetragonal and centered cubic final structure. As far as we know, it is the first time that this phase transition sequence, $P2_1/n \rightarrow P4_2/n \rightarrow Fm\bar{3}m$, is observed in ruthenate materials with the double perovskite structure.

As mentioned at room temperature section, the oxygen isotropic temperature factors are taken with the same value. Figure 5.14 shows the three different refinement results, presenting equal conclusions as at room temperature. Moreover, in this case the big oscillations of Biso values suggest to keep the oxygen isotropic temperature factors the same to follow with major accuracy the phase transition, as it is related to octahedra tilts.

There is no group-subgroup relation between the monoclinic and tetragonal space group (see Figure 5.13). This implies, in the one hand, that experimentally it should be observed a first order (discontinuous) phase transition, as we have observed. And, in the other hand, that the intermediate tetragonal phase will not be the reference structure for the monoclinic RT phase. Both phases can be referred to the same parent cubic phase. In the case of the monoclinic phase, the parent cubic phase was virtual, as mentioned, as no cubic phase was known. In our temperature XRPD analysis, due to the response from the heater in the diffraction profiles and the overlap of the reflections of the heater and the

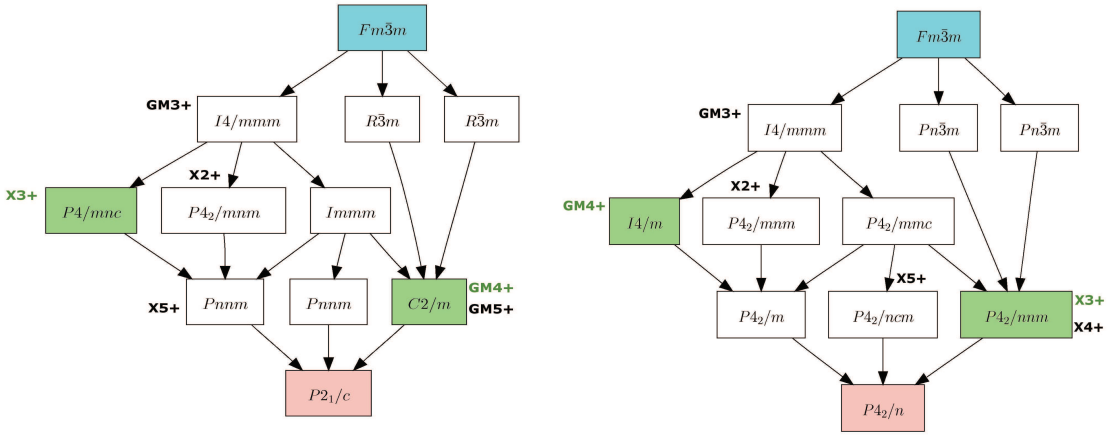

Figure 5.13: Graph of maximal subgroups relating the space groups of the parent (highlighted in blue) and distorted $P2_1/n$ and $P4_2/n$ phase (highlighted in red) of SrNdMRuO$_6$ compounds. For each subgroup any irrep yielding this symmetry is indicated and the two primary active irreps evidenced by the Rietveld refinement are highlighted in green. In the scheme we are using the standard settings of the space groups as the BCS does for generating these graphs. $P2_1/c$ is the standard setting of $P2_1/n$.

sample, we were not able to determine with accuracy *the* cubic structure. Hence, in the symmetry-mode analysis of the high temperature intermediate tetragonal phase we are using the same *virtual* reference structure for the tetragonal phase.

In the symmetry breaking from the cubic ($Fm\bar{3}m$) to tetragonal ($P4_2/n$) phase, there are seven irreps that can take part (see Table 5.3 and Figure 5.15) and AMPLIMODES suggests that there is no primary mode.

The geometrical description, in the tetragonal cell, of the distortion modes of the symmetry breaking from the prototype phase into the tetragonal intermediate phase is the following. GM$_3^+$, expands the octahedra in the equatorial ab plane, while the apical oxygens are moved along c axis to the center of the octahedra. The mode transforming according to GM$_4^+$ is a pure rotation along c axis; rotates the alternating octahedra along c in the opposite direction: out-of-phase tilting. X$_2^+$ actuates on the equatorial oxygens, deforming into a rhombus the square formed by the oxygens. X$_3^+$, it is a rotation of the octahedra around the bisection of the $-a$ and b axis. There two modes that transforms according to X$_4^+$ irrep, acting on the oxygens. X$_4^+$-A6, displaces the equatorial oxygens along c axis and the apical ones in the ab place, deforming the octahedra; while X$_4^+$-A7 is a deformation of the equatorial plane of the octahedra, from a square into a rectangle. Finally, the X$_5^+$ irrep is three dimensional, acting on A/A'-site cations and oxygens. X$_5^+$-A8, represents a displacement of the A/A'-site cations along c axis. The X$_5^+$-A9 mode displaces the apical oxygens in the ab plane; and X$_5^+$-A10, tilts the equatorial plane, displacing two of the oxygens positively

and the other two with the same amount negatively along *c*.

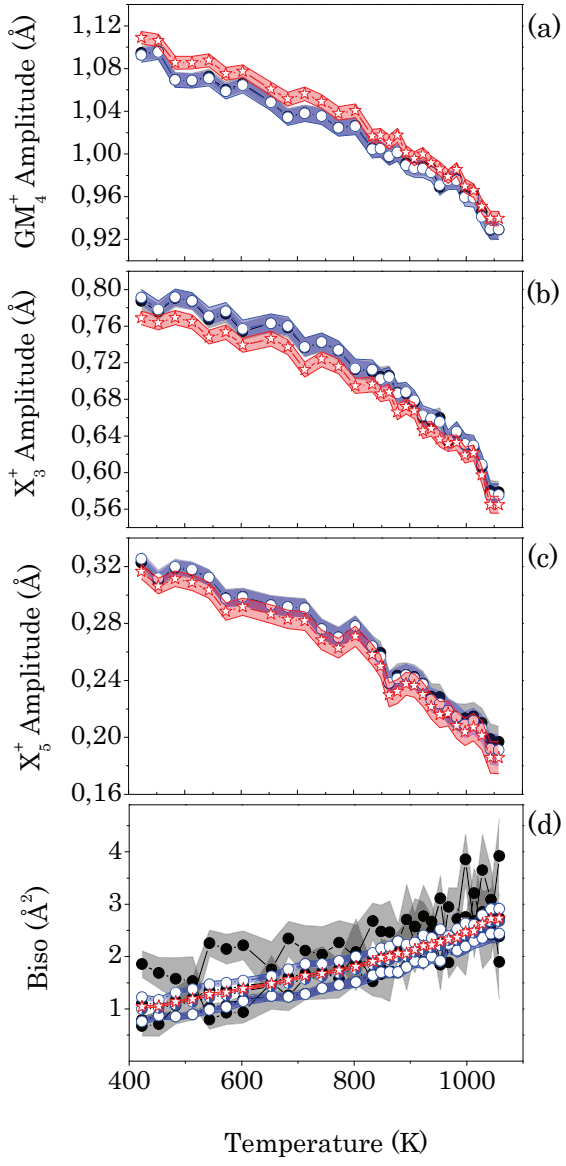

Figure 5.14: Variation of (a) GM_4^+ distortion irrep amplitude (Å); (b) X_3^+ distortion irrep amplitude (Å); (c) X_5^+ distortion irrep amplitude (Å), and (d) isotropic temperature factors (Å^2) as function of the temperature (K) for $SrNdCoRuO_6$. Label color and symbol indicate three different refinements: black full circle, isotropic temperature factors for O1, O2 and O3 independent; blue empty circle, isotropic temperature factors of O1 and O2 refined with the same code and O3 independent; and red star, all isotropic temperature factors refined with the same code. In (d) half-full black and blue symbols, and dotted lines indicate the average value of the isotropic temperature factors for each refinement.

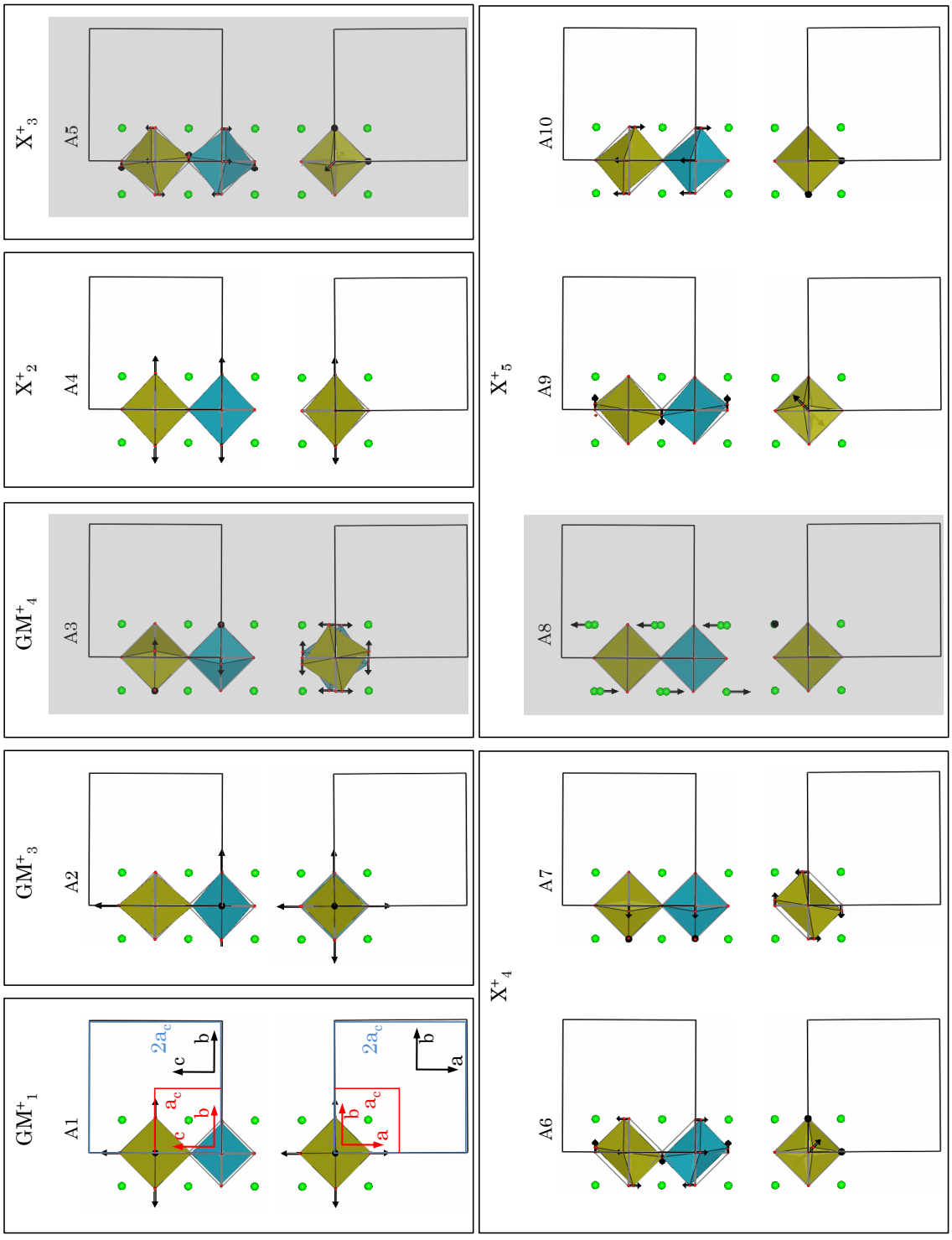

Figure 5.15: Geometrical representations of the distortion modes of the symmetry breaking from the cubic prototype phase into the tetragonal $P4_2/n$ phase: $GM_3^+(1)$, $GM_3^+(1)$, $GM_4^+(1)$, $X_2^+(1)$, $X_3^+(1)$, $X_4^+(2)$ and $X_5^+(3)$. The numbers in parenthesis indicate the number of modes transforming according to the corresponding irrep. The principal modes are highlighted in grey.

Although the label of the irreps taking part in the symmetry breaking from the prototype cubic phase to the low symmetry monoclinic and tetragonal phase are the same, the direction of actuation of each irrep is not the same ($Fm\bar{3}m \rightarrow P2_1/n$, GM_4^+ (a,a,0) and X_3^+ (0,a,0); $Fm\bar{3}m \rightarrow P4_2/n$, GM_4^+ (0,0,a) and X_3^+ (-a,0,-a)) (see Figure 5.8); which means that they are not the same mode, although, they are the same order parameter. The non-appreciable change of the amplitude value through the discontinuous $P2_1/n$-to-$P4_2/n$ phase transition is not surprising: in fact, as mentioned, it is the same order parameter, with different symmetry, oriented in a different way, what we are following. It is by coincidence that the labels for the irreps are the same. Although we do not expect a linear behavior of the evolution with temperature of the order parameter, the amplitude of the mode, it seems that it is linear, at least in the temperature interval we have experimentally accessed. It is worth noting that despite the fact that the irreps lowering successively the symmetry from the cubic to the tetragonal ($P4_2/n$), and from the cubic to the monoclinic ($P2_1/n$) involve mainly oxygen atoms, the cubic-to-tetragonal phase transition is continuous, whereas the tetragonal-to-monoclinic is discontinuous. In other words, essentially both phase transitions are originated by the tilting of the octahedra, accompanied by Sr/Nd displacements. The different character of the phase transition, though, arises from the fact that the involved tilts are differently orientated in the parent cubic phase. In fact, there is no miss-orientation between the tetragonal and the cubic cells; hence, a continuous reduction of the tilts of the tetragonal phase gives rise to the cubic symmetry. But, quite the contrary, the monoclinic and the cubic (so are the monoclinic and the tetragonal) cells are differently oriented.

Although the final refinement values of the modes' amplitudes involved in the symmetry-breaking to the tetragonal symmetry do not suggest that some amplitudes should be set to zero, we have set to zero all of them but three: GM_4^+, X_3^+ and X_5^+ irreps) improve considerably the R values. We reduced from 27 to 20 the refinable parameters.

To study the thermal evolution of the symmetry-adapted mode amplitudes in the case of the new structural phase transition sequence proposed for this family, the $SrNdCoRuO_6$ compound was measured by means of NPD.

Figure 5.16 and Table 5.6 exhibit the temperature evolution of the amplitude of GM_4^+, X_3^+ and X_5^+ modes, the rest are negligible, in the monoclinic and in the tetragonal phases. As mentioned, the physical interpretation of the modes taking part in the symmetry breaking is the tilting of the octahedra. In Figure 5.16 we have also shown the octahedral tilt angles (tilt systems: $a^+b^-b^-$ ($P2_1/n$) and $a^+a^+c^-$ ($P4_2/n$)). The matching of the mode amplitudes and tilt angles is perfect (Figure 5.8). GM_4^+ and X_3^+ modes (rotation and inclination

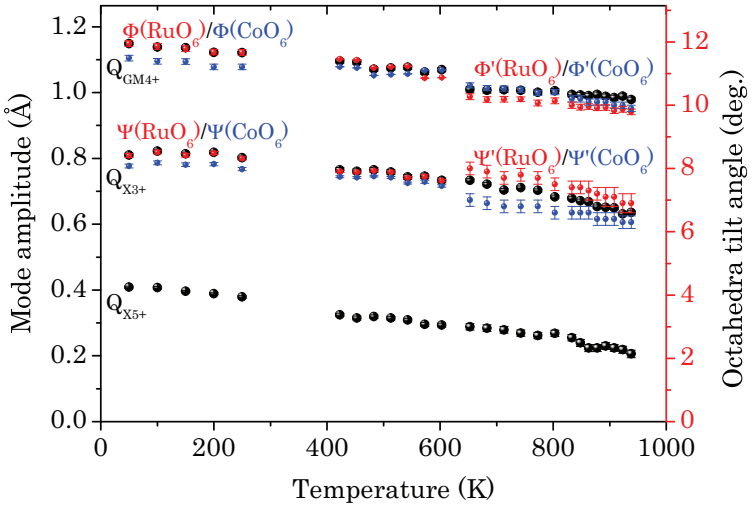

Figure 5.16: Temperature dependence of the amplitudes of three modes (black symbol) conforming the $P2_1/n$ and $P4_2/n$ structure of SrNdCoRuO$_6$, and Ψ(Ψ′) and Φ(Φ′) CoO$_6$ (blue symbol) and RuO$_6$ (red symbol) octahedra tilt angles, as obtained from the NPD data refinement (GM_4^+, X_3^+ and X_5^+ the freed modes in the refinement). The amplitudes of the irreps in the high symmetry phase have been scaled, since AMPLIMODES uses mode normalization within the corresponding primitive unit cell.

of the octahedra around the monoclinic axis) are the two order parameters associated to the phase transition. The diminishing of the mode amplitudes with temperature, involves the reducing of the rotation of the octahedra and displacement of the cations, getting more symmetric.

Table 5.6: Amplitude of the modes (in Å) of phase $P2_1/n$ and $P4_2/n$ for $SrNdCoRuO_6$. In column labeled (*a*) calculated from all refined amplitudes and in (*b*), with some amplitudes set to zero. RT and HT data set are not measured in the same experimental conditions.

Irrep	Mode	300 K (*a*)	300 K (*b*)	453 K (*a*)	453 K (*b*)	603 K (*a*)	603 K (*b*)
$P2_1/n$							
GM_1^+	A1	-0.070(8)	0.000	-0.04(2)	0.000	-0.00(1)	0.000
GM_3^+	A2	0.06(2)	0.000	0.01(3)	0.000	0.15(4)	0.000
GM_4^+	A3	-1.122(4)	-1.119(4)	-1.112(7)	-1.106(6)	-1.087(8)	-1.078(6)
GM_5^+	A4	0.082(7)	0.000	0.07(2)	0.000	0.03(2)	0.000
	A5	0.03(1)	0.000	0.09(3)	0.000	0.06(2)	0.000
	A6	0.14(2)	0.000	0.16(2)	0.000	0.29(2)	0.000
	A7	0.001(8)	0.000	0.09(1)	0.000	0.15(2)	0.000
X_2^+	A8	0.038(7)	0.000	0.07(2)	0.000	0.02(2)	0.000
X_3^+	A9	-0.790(5)	-0.797(5)	-0.746(7)	-0.764(8)	-0.725(9)	-0.739(8)
X_5^+	A10	-0.349(3)	-0.351(3)	-0.309(7)	-0.306(6)	-0.296(9)	-0.292(6)
	A11	0.03(2)	0.000	0.15(2)	0.000	0.04(3)	0.000
	A12	0.102(6)	0.000	0.10(1)	0.000	0.06(1)	0.000
Reliability factors							
R_p(%)		4.11	4.58	6.99	7.27	6.92	6.97
R_{wp}(%)		5.31	5.86	8.91	9.32	8.84	8.91
R_{exp}(%)		2.17	2.18	4.77	4.78	4.78	4.79
χ^2		5.98	7.24	3.49	3.80	3.42	3.46
R_{Bragg}(%)		7.31	8.96	7.60	8.52	8.20	8.72

Irrep	Mode	653 K (*a*)	653 K (*b*)	803 K (*b*)	953 K(*b*)
$P4_2/n$					
GM_1^+	A1	-0.15(3)	0.000	0.000	0.000
GM_3^+	A2	0.45(3)	0.40(2)	0.34(2)	0.24(3)
GM_4^+	A3	-1.40(2)	-1.46(1)	-1.43(1)	-1.37(1)
X_2^+	A4	0.38(4)	0.000	0.000	0.000
X_3^+	A5	-1.12(1)	-1.04(1)	-0.98(1)	-0.90(1)
X_4^+	A6	0.13(3)	0.000	0.000	0.000
	A7	0.15(4)	0.000	0.000	0.000
X_5^+	A8	-0.38(2)	-0.38(1)	-0.37(1)	-0.31(2)
	A9	0.28(4)	0.000	0.000	0.000
	A10	0.16(3)	0.000	0.000	0.000
Reliability factors					
R_p(%)		8.75	8.36	7.51	6.98
R_{wp}(%)		11.6	11.0	9.93	8.97
R_{exp}(%)		4.80	4.81	4.79	4.79
χ^2		5.79	5.23	4.30	3.51
R_{Bragg}(%)		15.8	13.5	13.4	14.1

5.3 Conclusions

The structure of the double perovskite oxides SrNdMRuO$_6$ (M=Zn,Co,Mg,Ni) have been studied by means of XRPD, NPD and SXRPD techniques. At room temperature their symmetry was found to be monoclinic with the space group $P2_1/n$. The symmetry mode decomposition of the compounds, with respect to the $Fm\bar{3}m$ parent phase, have demonstrated that at room temperature the structure is dominated by two primary active distortion modes (GM_4^+ and X_3^+) corresponding to the two independent octahedral tilts in $P2_1/n$; however, a small but necessary distortion mode (X_5^+ actuating on A-site cations) is present. The effect of the B-site cations size (via the tolerance factor) on the RT structure has been quantified by the symmetry-mode amplitudes: the bigger the tolerance factor, the smaller are the mode amplitude values. The three distortion modes' amplitudes are temperature dependent and temperature dependence is essentially identical to the octahedral tilt-angle temperature evolution calculated from the refined structures. None of the modes is lost in the first order phase transition to $P4_2/n$ phase. The transition temperatures from the monoclinic to the tetragonal phase are, estimated by XRPD data, 740 (Zn), 660 (Co), 560 (Mg) and 440 K (Ni). The symmetry mode decomposition for the intermediate tetragonal phase shows that three distortion modes, GM_4^+, X_3^+, X_5^+, are necessary to describe the structure. By XRPD data a second phase transition is identified to the cubic parent phase at 1060 (Zn), 1000 (Co), 940 (Mg) and 820 K (Ni). Due to experimental limitation no NPD data was collected at such high temperature and was not possible to observe the distortion mode evolution up to the parent phase.

Chapter 6

$SrPrMRuO_6$ (M=Zn,Co,Mg,Ni) ordered double perovskites

6.1 Room temperature structures

At ambient temperature and pressure, iso-structural perovskites $SrPrMRuO_6$ (M=Zn,Co,Mg,Ni) were formed. In this series, the ionic radius for M^{2+}, in six-fold coordination, decreases from 0.74 Å ($^{vi}Zn^{2+}$) to 0.69 Å ($^{vi}Ni^{2+}$) [48]. Hence, Goldschmidt tolerance-factors [8] for these praseodymium compounds in combination with $^{ix}Sr^{2+}$ (1.31 Å), $^{ix}Pr^{3+}$ (1.179 Å) and $^{vi}Ru^{5+}$ (0.565 Å) range from 0.908 to 0.920. Those values are smaller than the tolerance-factor for $SrLaNiRuO_6$ (t=0.929) [116], monoclinically ($P2_1/n$, ITA No.14 non conventional setting) distorted at room temperature. Hence, that space group was used as the starting model for the X-ray powder diffraction (XRPD) room temperature (RT) pattern analysis.

In Figure 6.1(1) laboratory X-ray diffraction refinements are shown for $SrPrMgRuO_6$ using the monoclinic space group $P2_1/n$. In the dashed box it is emphasized the peak formed by the (-101),(011),(101) monoclinic reflections, which, when present, indicate that the cation distribution over the B-sites of the double perovskite is ordered [31]. Although tolerance-factor values suggest that the structure is monoclinically distorted, as mentioned, several trials have been done with other space groups, to ensure the RT symmetry assignment. The body centered monoclinic space group is adopted at RT by other known double perovskites such as Sr_2CrSbO_6 [117], Ba_2LnNbO_6 [118] or Sr_2NiTeO_6 [119], and $P4_2/n$ symmetry is observed as intermediate phase in the more distorted $SrNdMRuO_6$ perovskites [120]. Despite the fact that the A-site cation atomic displacement reflections

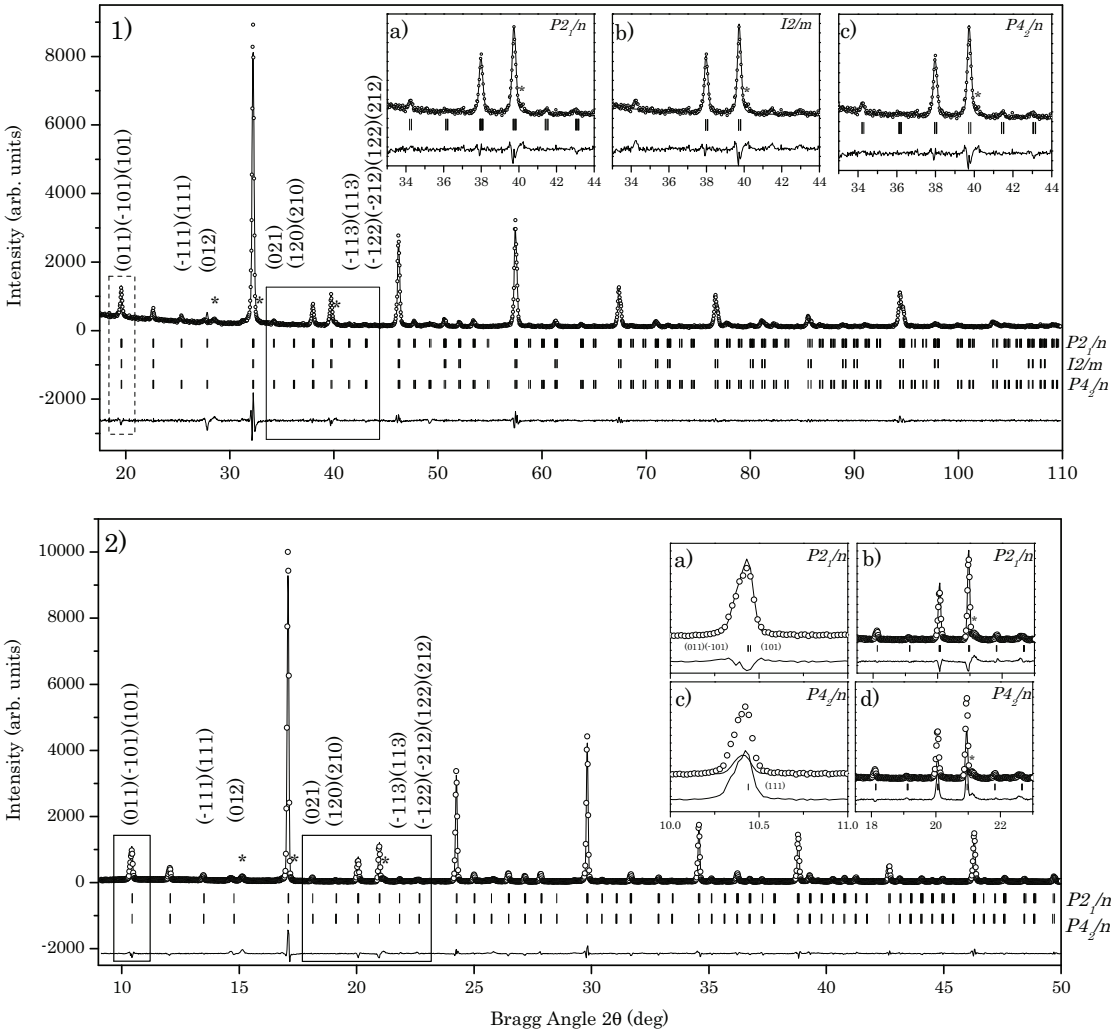

Figure 6.1: (1)Observed (symbols), calculated (line) and difference (bottom line) XRPD (λ=1.5406 Å) profile for SrPrMgRuO$_6$ at room temperature. The bars in the lower part of the graphic represent the Bragg-reflections' positions for three different models: first row, $P2_1/n$; second row, $I2/m$ and third row, $P4_2/n$. The rectangular section is enlarged in the inset, showing in detail the presence of supercell reflections. The arrows in panel b) indicate the absence of those reflections in the $I2/m$ space group model. (2) Observed (symbols), calculated (line) and difference (bottom line) SXRPD (λ=0.8256 Å) profile for SrPrMgRuO$_6$ at room temperature using a structural model with the $P2_1/n$ space group. The bars indicate the Bragg-reflections' positions for $P2_1/n$ and $P4_2/n$ models. The inset shows the monoclinic splitting, the tetragonal symmetry does not take into account the observed splitting, ((a) and (c) panels). * indicates very small quantity of an unidentified impurity.

[90] are usually small, they are observed in the patterns of our samples. Thus, the monoclinic body centered space group model should be rejected as possible space group at RT.

$P2_1/n$ monoclinic space group and the tetragonal primitive $P4_2/n$ space group can not be distinguished by laboratory X-ray diffraction experiments, unless the monoclinic splitting is large. RT space group for the iso-structural compounds was clarified by a synchrotron radiation powder diffraction experiment (SXRPD). Figure 6.1(2) shows SXRPD pattern refinement with the monoclinic $P2_1/n$ space group; and in the lower part of the figure the Bragg reflection positions for $P2_1/n$ and $P4_2/n$ are indicated. The observed monoclinic splitting, as shown in the inset of Figure 6.1(2) (panels (a) and (c)) rule out the tetragonal symmetry. NiO (≈3.75% weight fraction) was included as an additional phase in the Rietveld refinements of the $SrPrNiRuO_6$ sample.

Refinement results for the NPD data in the $P2_1/n$ space group are given in Table 6.1 and Figure 6.2. As in [120] isotropic temperature factors for the oxygens were fixed to be equal in the refinements, to compare to the crystallographic information in [120]. Despite that constraint, the crystal information remains unchanged for equal or independent oxygen isotropic temperature factors.

It is known, and was first reported in [44], and after it has been observed, for instance, in [45, 46], that the coordination polyhedron of the lanthanides in the A-site of distorted perovskites is achieved with lower coordination than $^{\mathrm{xii}}Ln^{3+}$, i.e., a four-fold anti-prism ($^{\mathrm{viii}}Ln^{3+}$) rather than a cubo-octahedron, the expected coordination in the parent cubic phase. Of course, that coordination decrement is due to the tilts of the octahedra, to compensate for the poor fit, mis-match, of the lanthanide cations in the interstitial space amongst the octahedra; and results in the separation of the 12-fold degenerate Sr/Ln-O bonds into eight/nine short Sr/Ln-O bonds and four/three long bonds. Those two bond groups determine the first and second coordination-spheres for the A-site cations. The distortion of the polyhedron is also accompanied by the displacement of the A-site cations off-center of the polyhedron. The separation into two degenerate sets of bonds, two coordination-spheres, was suggested [44] to be due to the opposite trend, stretch or contract, of the Ln-O bond-lengths in the first and second coordination-spheres.

As expected for these strongly distorted structures, the A-site coordination polyhedron is a completely distorted cubo-octahedron; observing the Sr/Pr-O bond-lengths, Table 6.2, four of the largest bonds belong to the second coordination-sphere. In Figure 6.3 we show two projections (along $\vec{a}+\vec{b}$ and $\vec{c}$ axes) of the ideal, (a) and (c), and distorted, (b) and (d), Sr/PrO_{12} cubo-octahedral configuration (highlighted in blue) for $SrPrZnRuO_6$, in the $P2_1/n$ space group at room temperature. The yellowish sphere, the light and dark blue spheres, and the red sphere stand for the A/A'-site cation, the B and B'-site cation and the oxygen cation, respectively. The B-O and B'-O bonds are indicated in orange. The white

Table 6.1: Crystal structure data and refinement results for SrPrMRuO$_6$ (M=Zn,Co,Mg,Ni) from NPD at RT, refining all mode amplitudes. Sr/Pr (4e (x,y,z), $occ = 0.5/0.5$), M (2b (0,0,1/2), $occ = 1$), Ru (2a (0,0,0), $occ = 1$), O (4e (x,y,z), $occ = 1$).

		SrPrZnRuO$_6$	SrPrCoRuO$_6$	SrPrMgRuO$_6$	SrPrNiRuO$_6$
Space group		$P2_1/n$	$P2_1/n$	$P2_1/n$	$P2_1/n$
Sr/Pr	x	-0.0053(9)	-0.0067(9)	-0.008(1)	-0.003(1)
	y	0.4672(3)	0.4693(4)	0.4760(5)	0.4728(5)
	z	0.754(2)	0.752(1)	0.748(2)	0.754(2)
	B_{iso}(Å^2)	0.84(2)	0.53(4)	0.63(3)	0.63(4)
M	B_{iso}(Å^2)	0.37(2)	0.12(2)	0.04(2)	0.15(1)
Ru	B_{iso}(Å^2)	0.37(2)	0.12(2)	0.04(2)	0.15(1)
O1	x	-0.278(1)	-0.278(1)	-0.273(1)	-0.285(1)
	y	0.215(1)	0.214(1)	0.220(1)	0.212(1)
	z	-0.0377(8)	-0.0291(8)	-0.033(1)	-0.0374(8)
	B_{iso}(Å^2)	0.92(1)	0.72(2)	0.70(2)	0.69(2)
O2	x	-0.796(1)	-0.790(1)	-0.794(1)	-0.784(2)
	y	0.291(1)	0.285(1)	0.285(1)	0.279(1)
	z	0.0377(8)	0.0381(8)	0.033(1)	0.0334(8)
	B_{iso}(Å^2)	0.92(1)	0.72(2)	0.70(2)	0.69(2)
O3	x	0.0704(6)	0.0709(6)	0.0642(7)	0.0649(7)
	y	0.0150(5)	0.0109(6)	0.0083(7)	0.0125(6)
	z	0.757(1)	0.755(1)	0.751(1)	0.7541(8)
	B_{iso}(Å^2)	0.92(1)	0.72(2)	0.70(2)	0.69(2)
a (Å)		5.56808(8)	5.5550(1)	5.5590(1)	5.54586(8)
b (Å)		5.59283(7)	5.5608(1)	5.5559(1)	5.54072(7)
c (Å)		7.8739(1)	7.8475(1)	7.8502(1)	7.82905(9)
β (°)		90.025(4)	90.051(4)	89.954(4)	90.081(1)
V (Å^3)		245.205(6)	242.412(8)	242.454(9)	240.571(5)
R_p(%)		3.43	2.26	3.07	3.72
R_{wp}(%)		4.58	2.96	4.66	4.98
R_{exp}(%)		3.00	3.84	3.89	3.94
χ^2		2.34	0.60	1.43	1.60
R_{Bragg}(%)		4.51	3.89	3.60	3.07

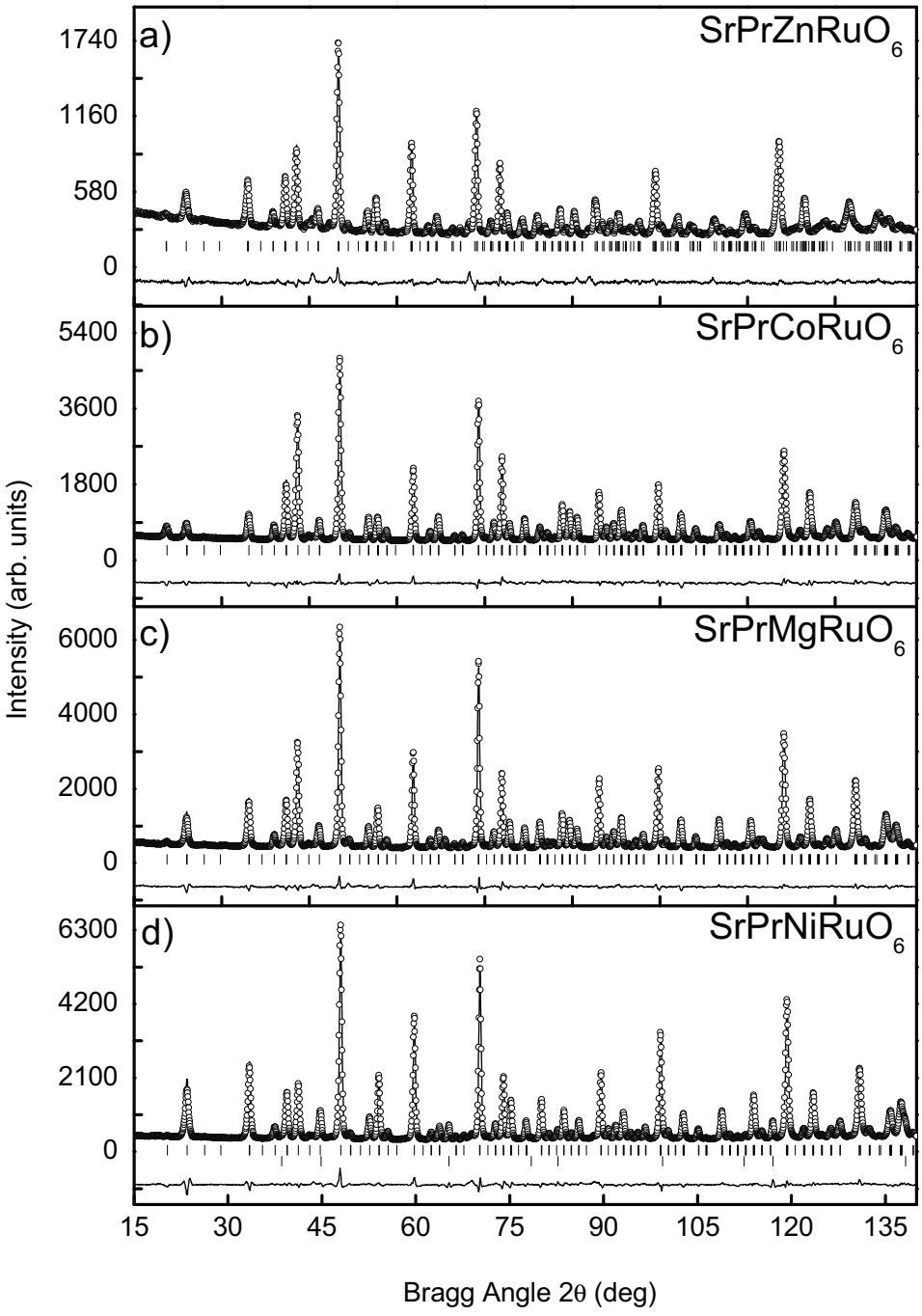

Figure 6.2: Experimental (symbols) and calculated (line) neutron powder-diffraction profiles (D2B λ=1.594 Å) for the Rietveld refinement of SrPrMRuO$_6$ (M=Zn,Co,Mg,Ni) at room temperature, using a structural model with the space group $P2_1/n$. The bars in the lower part of the graphics correspond to the Bragg-reflections' positions. In the case SrPrNiRuO$_6$, the lower set of bars correspond to the impurity NiO (3.75(6)%).

lines represent A/A'-O bonds in the undistorted polyhedron; in the distorted configuration, the eight shortest A/A'-O bonds are in white and the four largest bonds in red. Just as a guide for the eye, in (b) and (d) we have surrounded in grey the two B- or B'-site cations getting inside the second coordination-sphere, in the distorted configuration. For comparative purposes with the previous published data, all the crystallographic information in Table 6.3 and Figure 6.4 have been obtained on the assumption of an 8-fold coordination (first coordination-sphere) for the A/A'-site cations.

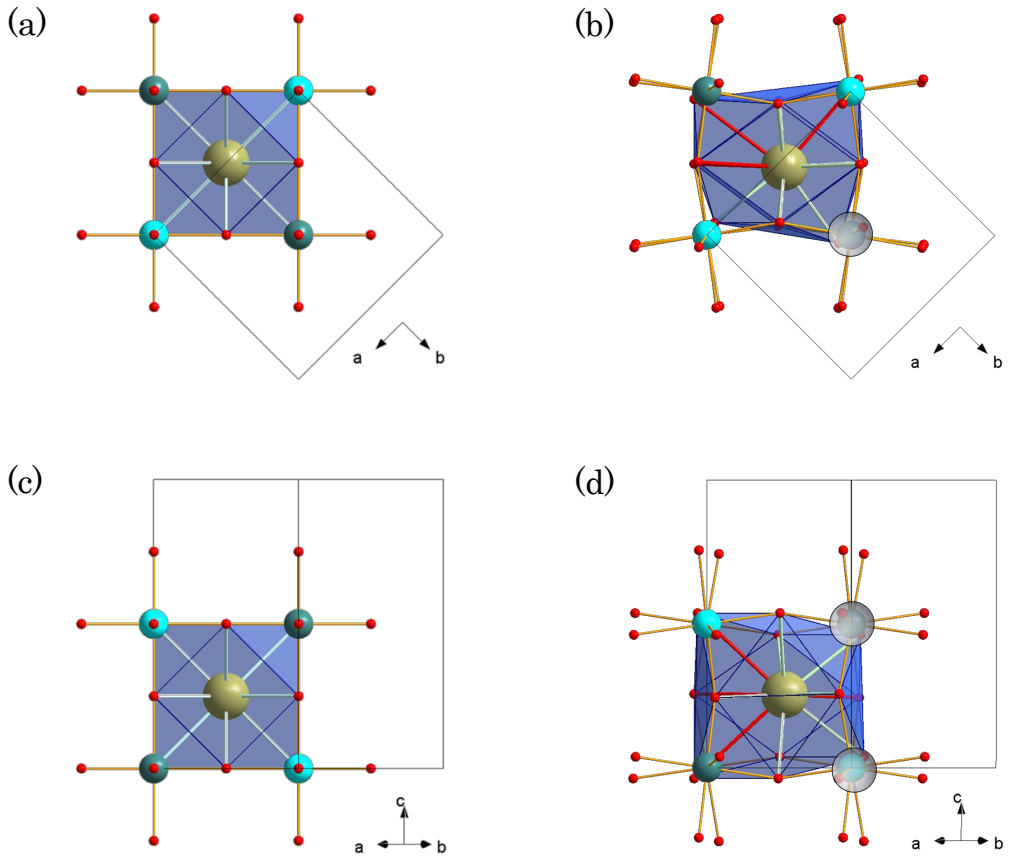

Figure 6.3: Graphical representation of (a) and (c) ideal, and (b) and (d) distorted Sr/PrO$_{12}$ cuboctahedral configuration (highlighted in blue) for SrPrZnRuO$_6$ in the $P2_1/n$ space group at room temperature. Projections along the cubic (simple) perovskite axes, (a) and (b) along $[001]_p$, and (c) and (d) along $[010]_p$. Yellowish sphere, light and dark blue spheres, and red sphere are A/A'-site cation, B and B'-site cation, and oxygen cation, respectively. B-O and B'-O bonds are indicated in orange. In (a) white lines represent A/A'-O bonds, and in (b) eight shortest A/A'-O bonds are in white and four largest bonds in red. Grey circles highlight the B and B'-site cations inside the second coordination-sphere.

Table 6.2: Octahedra volume (Å^3), selected bond-lengths (Å) and angles (°) for SrPr*M*RuO_6 (*M*=Zn,Co,Mg,Ni) at room temperature, refining all mode amplitudes.

M	Zn	Co	Mg	Ni
Sr/PrO_{12} polyhedra				
Sr/Pr-O1	2.50(1)	2.52(1)	2.49(1)	2.45(1)
Sr/Pr-O1	2.65(1)	2.69(1)	2.67(1)	2.69(1)
Sr/Pr-O1	2.81(1)	2.74(1)	2.79(1)	2.76(1)
Sr/Pr-O1	3.26(1)	3.21(1)	3.20(1)	3.25(1)
Sr/Pr-O2	2.40(1)	2.42(1)	2.43(1)	2.47(1)
Sr/Pr-O2	2.71(1)	2.70(1)	2.74(1)	2.71(1)
Sr/Pr-O2	2.76(1)	2.74(1)	2.74(1)	2.73(1)
Sr/Pr-O2	3.37(1)	3.32(1)	3.26(1)	3.23(1)
Sr/Pr-O3	2.44(1)	2.43(1)	2.48(1)	2.44(1)
Sr/Pr-O3	2.56(1)	2.59(1)	2.63(1)	2.58(1)
Sr/Pr-O3	3.09(1)	3.04(1)	2.98(1)	3.01(1)
Sr/Pr-O3	3.16(1)	3.14(1)	3.10(1)	3.12(1)
MO_6 octahedra				
V(MO_6)	11.41(2)	11.16(2)	10.97(2)	10.94(1)
M-O1(×2)	2.038(6)	2.027(8)	2.019(7)	2.015(7)
M-O2(×2)	2.045(6)	2.028(8)	2.041(7)	2.013(7)
M-O3(×2)	2.059(9)	2.039(8)	2.00(1)	2.022(6)
< *M*-O>	2.047(3)	2.031(3)	2.020(3)	2.017(3)
Predicted distance	2.1105	2.0985	2.0995	2.0605
RuO_6 octahedra				
V(RuO_6)	10.38(1)	10.23(2)	10.27(1)	10.24(2)
Ru-O1(×2)	1.984(6)	1.961(8)	1.965(7)	1.990(7)
Ru-O2(×2)	2.004(6)	1.992(8)	1.971(7)	1.972(7)
Ru-O3(×2)	1.959(9)	1.965(8)	1.99(1)	1.960(6)
<Ru-O>	1.983(3)	1.972(3)	1.975(3)	1.974(3)
Predicted distance	1.9675	1.9675	1.9675	1.9675
∠O1-*M*-O2	93.6(2)	92.3(2)	93.9(2)	89.9(2)
∠O1-*M*-O3	90.2(2)	91.7(2)	90.3(2)	89.4(2)
∠O2-*M*-O3	90.7(2)	90.5(2)	89.7(2)	90.6(2)
< ∠O-*M*-O>	91.5(2)	91.5(2)	91.3(2)	90.0(2)
∠O1-Ru-O2	88.4(2)	89.7(2)	87.9(2)	92.3(2)
∠O1-Ru-O3	89.1(2)	91.5(2)	89.7(2)	88.9(2)
∠O2-Ru-O3	89.8(2)	90.3(2)	90.4(2)	89.4(2)
< ∠O-Ru-O>	89.1(2)	90.5(2)	89.3(2)	90.2(2)
∠*M*-O1-Ru	157.7(2)	160.5(2)	161.1(3)	156.3(2)
∠*M*-O2-Ru	154.1(2)	155.8(2)	156.7(3)	159.3(2)
∠*M*-O3-Ru	157.0(1)	157.0(1)	159.2(1)	158.8(2)
< ∠*M*-O-Ru>	156.3(2)	157.8(2)	159.0(2)	158.1(2)

Table 6.3: Crystal chemistry of Sr$Ln M$RuO$_6$ (Ln=La,Pr,Nd; M=Zn,Co,Cu,Mg,Ni) perovskites [115, 116, 120] at room temperature.

	t^a	$t_0{}^b$	$AO_8{}^c$	$<A\text{-O}>_{8\text{short}}{}^d$	$<A\text{-O}>_{4\text{long}}{}^e$	$AO_{12}{}^f$	$\Psi_{[001]M}{}^g$	$\Psi_{[001]\text{Ru}}{}^h$	$\Phi_{[110]M}{}^i$	$\Phi_{[110]\text{Ru}}{}^j$	GM_4^{+k}	X_3^{+l}	X_5^{+m}
Crystal chemistry of SrPrMRuO$_6$ (M=Zn,Co,Ni,Mg)													
Zn	0.8933	0.913(1)	27.71(1)	2.60(1)	3.22(1)	51.95(1)	7.5(2)	9.6(2)	11.3(3)	12.0(3)	1.155(4)	0.843(5)	0.404(4)
Co	0.8955	0.920(1)	27.54(1)	2.60(1)	3.18(1)	51.32(1)	7.1(2)	8.6(2)	11.3(2)	11.7(2)	1.094(4)	0.777(5)	0.378(7)
Ni	0.9043	0.823(1)	27.44(1)	2.60(1)	3.15(1)	51.92(1)	7.2(2)	8.3(1)	10.4(2)	10.8(2)	1.075(4)	0.761(5)	0.338(6)
Mg	0.8977	0.928(1)	27.79(1)	2.62(1)	3.14(1)	51.32(1)	9.2(1)	5.9(1)	10.4(3)	10.4(3)	1.026(4)	0.737(6)	0.285(6)
Crystal chemistry of SrNdMRuO$_6$ (M=Zn,Co,Ni,Mg) [120]													
Zn	0.8801	0.911(1)	27.56(1)	2.60(1)	3.23(1)	51.77(1)	10.40(8)	7.00(9)	11.8(2)	12.6(2)	1.200(3)	0.855(4)	0.425(3)
Co	0.8823	0.919(1)	27.37(1)	2.60(1)	3.18(1)	51.04(1)	6.6(1)	9.6(1)	11.0(2)	11.8(2)	1.122(4)	0.790(5)	0.365(5)
Ni	0.8909	0.923(1)	27.33(1)	2.60(1)	3.15(1)	51.62(1)	9.4(1)	5.6(1)	12.0(3)	12.9(3)	1.152(5)	0.733(6)	0.376(6)
Mg	0.8844	0.922(1)	27.43(1)	2.61(1)	3.15(1)	51.02(1)	5.7(1)	9.4(1)	11.4(2)	11.8(2)	1.109(4)	0.737(5)	0.335(6)
Crystal chemistry of SrLaMRuO$_6$ (M=Co,Cu,Ni) [115][116]													
Co	0.9018	0.933(1)	28.20(1)	2.64(1)	3.12(1)	51.69(1)	7.7(1)	4.8(1)	10.5(2)	10.9(2)	1.01(1)	0.62(1)	0.274(7)
Cu	0.9014	0.93(1)	28.10(1)	2.64(1)	3.12(1)	51.67(1)	7.0(4)	5.8(5)	10.9(6)	11.5(7)	1.04(6)	0.63(5)	0.26(4)
Ni	0.9103	0.93(1)	28.98(1)	2.64(1)	3.10(1)	51.18(1)	4.8(2)	7.6(2)	10.0(4)	10.4(5)	1.00(4)	0.60(3)	0.27(2)

[a] [viii] t Goldschmidt tolerance factor, calculated from tabulated Shannon radii [48].

[b] [viii] t_0 observed tolerance factor, calculated from observed interatomic distances.

[c,f] AO_8 and AO_{12} volumes of polyhedra (Å^3) with A-site cation in eight- and twelve-fold coordination.

[d,e] $<A\text{-O}>_{8\text{short}}$ and $<A\text{-O}>_{4\text{long}}$ mean bond-lengths (Å) for the first and second coordination-spheres.

[g,h,i,j] $\Psi_{[001]}$ and $\Phi_{[110]}$ octahedra tilt-angles (°) along [001] and [110] cubic simple perovskite directions.

[k,l,m] GM_4^+, X_3^+ and X_5^+ distortion irrep amplitudes (Å).

All of the ruthenate perovskites listed in Table 6.3 (except the Mg-containing compounds), show a common trend: the volume of the first coordination-sphere increases with the *expansion* of the lanthanide Figure 6.4(a), it is just a steric effect: the bigger size of the cation. However, among the series within the same lanthanide, the volume remains almost unchanged: the *B*-site cation chemical pressure is not enough to cause important changes in the distances. Mg-containing compounds (in red in the figure) are the exception, probably due to different type of orbitals in comparison to those of the transition metals. The trend of the second coordination-sphere, Figure 6.4(b), is to increase the volume with the contraction of the *Ln*: due to the smaller size of the lanthanide, the octahedra tilt, to compensate for the lesser fit of the A/A'-site cation. In this case, the *B*-site chemical pressure results in small but observable volume differences. Again, the Mg compound follows, but on its own. We have included the Cu compound results for completeness, although we only have data for one compound with Cu.

Figure 6.5 shows the maximum *A*-O (open circles) and minimum *A*-*B* distances (black filled circles). When the minimum *A*-*B* distance is smaller than the maximum *A*-O distance, the *B*-site cation gets inside the second coordination-sphere of the A/A'-site cations. Merizio *et al.* [44] suggested that this fact promotes the lengthening of the second coordination-sphere radius, due to a screening effect. In the lanthanum series, the *B*-site cation remain out of the second coordination-sphere, Figure 6.5(a): the minimum *A*-*B* distance is always bigger than the maximum *A*-O. In the second series, the praseodymium containing materials, the two lines cross: increasing the the *B*-site cation, increasing the *B*-site chemical pressure, gets that cation in the second coordination-sphere, Figure 6.5(b): $SrPrZnRuO_6$ and $SrPrCoRuO_6$ are in, whereas $SrPrMgRuO_6$ and $SrPrNiRuO_6$ remain out. Finally, for the last series, neodymium, the *B*-site cation is always in the second coordination-sphere, Figure 6.5(c).

The distance between the *A*-site and *B*-site cations is approximately constant amongst the $SrLa\mathit{M}RuO_6$, $SrPr\mathit{M}RuO_6$ and $SrNd\mathit{M}RuO_6$ compounds; although the distances for $Sr\mathit{Ln}ZnRuO_6$, $Sr\mathit{Ln}CoRuO_6$, $Sr\mathit{Ln}MgRuO_6$ or $Sr\mathit{Ln}NiRuO_6$ materials change with the size of the lanthanide, due to steric effects. The trend of the maximum *A*-O distance along *B*-cation, is to increase with the expansion of the *B* radii Figure 6.5. It is purely steric, as the larger size of the *B*-cation causes bigger tilts of the octahedra, separating more the oxygens from A/A'-cations. Results for Mg containing compounds are in red Figure 6.5(b) and (c) since we think these materials behave in a particular way attributed to the cation type.

Following the theoretical predictions and the discussion in [120], the symmetry-mode decomposition and the subsequent Rietveld refinement of the mode amplitudes (see Table

6.4) indicate that there is not a unique active mode that breaks the symmetry from the prototype cubic space group ($Fm\bar{3}m$) to the monoclinic $P2_1/n$ space group. This means that the $P2_1/n$-symmetry phase cannot be generated by a single mechanism: GM_4^+ and X_3^+ irreps transforming symmetry-adapted modes (and eventually, X_5^+) are necessary. The distortion-mode amplitudes in the title compounds are smaller than the ones we reported for the neodymium series, these are less distorted structures: praseodymium is bigger than neodymium and this size increase reduces the octahedral tilts. It is worth noting that in this case we have used the same *virtual* structure used in [120] to perform the symmetry-mode decomposition analysis.

In addition to provide various bond-lengths, the obtained atomic coordinates were used to calculate the magnitude of the tilts about the [001] (Ψ) and [110] (Φ) axes of the simple perovskite parent cubic. There are two different octahedra, MO_6 and RuO$_6$, and, therefore, two different tilt-angles for each tilt-type: however, both tilt-angles are not independent. In Table 6.3 tilt-angles for the two octahedra are shown. We have to note also that there is the possibility of calculating more than one value for a tilt-angle of a particular octahedron. For the monoclinic structure in $P2_1/n$ the tilt-angle can be calculated from either the position of the apical oxygen O3 or the equatorial oxygens O1 or O2. The Φ angle is obtained from the O3 apical oxygen, and $\Psi(M)$ from O1 and Ψ(Ru) from O2; from our data $\Psi(M)$O1 and Ψ(Ru)O1, and $\Psi(M)$O2 and Ψ(Ru)O2 are very similar. By examining the magnitude of the tilt in Table 6.3, it can be seen that the tilt around [110] axis is larger than that around the [001] axis. It is worth mentioning that when the main structural distortion

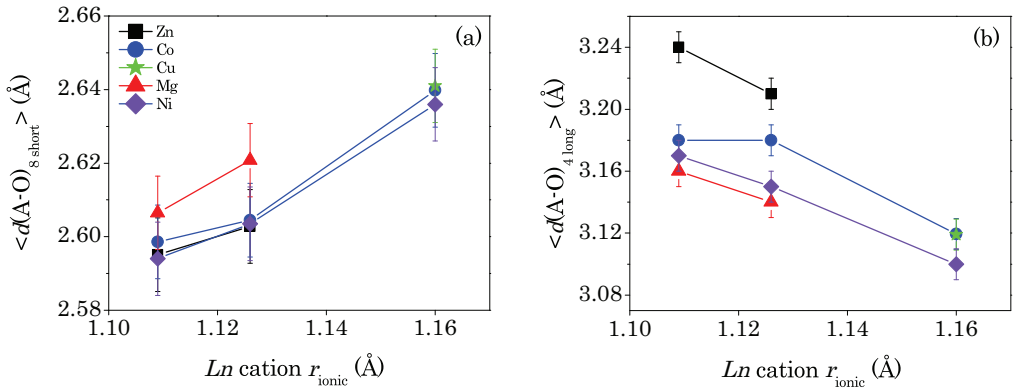

Figure 6.4: Features of the A-site cation coordination polyhedra (AO_8) for $P2_1/n$ SrLnRuO$_6$ perovskites [115, 116, 120]. Evolution of (a) the first coordination-sphere's mean A-O bond-lengths, and (b) second coordination-sphere's mean A-O bond-lengths as a function of the lanthanide ionic radii (Å). Black filled rectangle stands for zinc; blue filled circle, cobalt; green star, copper; red triangle, magnesium; and, finally, purple rhombus, nickel.

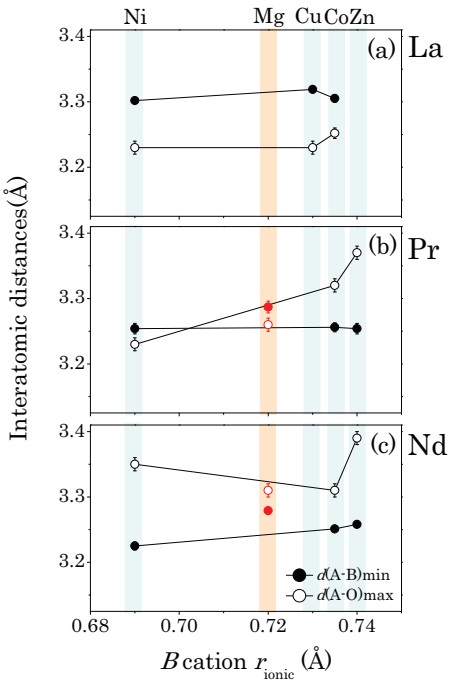

Figure 6.5: *A*-*B* interatomic minimum distances and *A*-O maximum distances (indicating the limit of the second coordination-sphere) for (a) lanthanum [115, 116], (b) praseodymium, and (c) neodymium compounds [120], as a function of the *B*-site cation radii (Å); showing which materials have *B*-site cations inside the second coordination-sphere. Mg compounds are shown in red, to indicate the particular behavior attributed to cation type.

is associate to GM_4^+ and X_3^+ distortion irreps, the tilt-angles are linearly related to them. In other words, the two primary modes are interpreted as the tilt-angles of the octahedra, as usual. These results are summarized in Figure 6.6.

As observed for $SrNdMRuO_6$ compounds [120] the bigger the *B*-site cation size, the bigger is the distortion of the structure. This is a behavior followed by three of the compounds: $SrPrMgRuO_6$, as mentioned, is an exception, Table 6.4. It has smaller mode-amplitudes than $SrPrNiRuO_6$. The same behavior was observed in the case of $SrNdMgRuO_6$ and $SrNdNiRuO_6$ [120]. This fact makes us think that although having a bigger experimental atomic radius the different nature of the Mg cation (does not belong to 3d transition metals) plays an important role in the stabilization of the RT distorted structure.

Table 6.4: Irrep amplitude (in Å) value after the refinement for SrPrMRuO$_6$ (M=Zn,Co,Mg,Ni) compounds at room temperature for cubic ($Fm\bar{3}m$) to monoclinic ($P2_1/n$) phase transition; from which GM_4^+ and X_3^+ irreps are the ones breaking the symmetry.

Irrep	Isotropy subgroup	Dim	K-vector	Direction	Amplitude			
					Zn	Co	Mg	Ni
GM_1^+	$Fm\bar{3}m$ (225)	1	(0,0,0)	(a)	0.04(1)	0.026(7)	0.00(2)	0.00(1)
GM_3^+	$I4/mmm$ (139)	1	(0,0,0)	(a,0)	0.04(2)	0.02(2)	0.04(3)	0.03(1)
GM_4^+	$C2/m$ (12)	1	(0,0,0)	(a,a,0)	1.155(4)	1.094(4)	1.026(4)	1.075(4)
GM_5^+	$C2/m$ (12)	4	(0,0,0)	(-b,a,-a)	0.16(2)	0.11(2)	0.18(2)	0.10(2)
X_2^+	$P4_2/mnm$ (136)	1	(0,1,0)	(0,a,0)	0.006(6)	0.021(9)	0.012(9)	0.011(8)
X_3^+	$P4/mnc$ (128)	1	(0,1,0)	(0,a,0)	0.843(5)	0.777(5)	0.737(6)	0.761(5)
X_5^+	$Pnnm$ (58)	3	(0,1,0)	(a,a,0,0,a,-a)	0.404(4)	0.378(7)	0.285(6)	0.338(6)
R_p(%)					3.43	2.26	3.07	3.72
R_{wp}(%)					4.58	2.96	4.66	4.98
R_{exp}(%)					3.00	3.84	3.89	3.94
χ^2					2.34	0.60	1.43	1.60
R_{Bragg}(%)					4.51	3.89	3.60	3.07

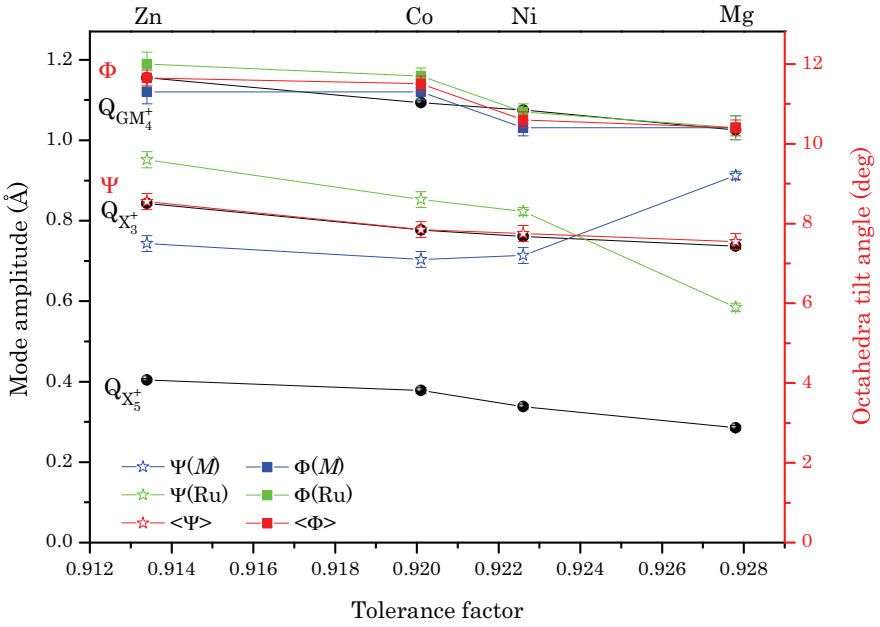

Figure 6.6: Amplitudes of GM_4^+, X_3^+ and X_5^+ irreps (black balls) conforming the RT phase of SrPrMRuO$_6$ (M=Zn,Co,Mg,Ni) compounds, and Ψ (star) and Φ (square) tilt-angles, as function of the observed tolerance factor. MO_6, RuO$_6$ and average tilt-angles are indicated in blue, green and red color, respectively.

6.2 High temperature induced phase transitions

Figure 6.7 shows the temperature dependence of the laboratory X-ray diffraction profile projections around the (111;-111) monoclinic primitive reflections (2θ=24°-26°) and (642) cubic reflection (2θ=92°-96°). The reflections shift to lower 2θ positions due to thermal expansion. At low temperatures the monoclinic primitive reflection is clearly seen and disappears at higher temperatures, indicating a phase transition to a non-primitive space group. All compounds undergo a temperature induced structural phase transition taking place at $\approx$ 1225, 1050, 950 and 1025 K, SrPrMRuO$_6$ (M=Zn,Co,Mg,Ni) respectively. The XRPD experiment was not enough good to determine the new phases' symmetry.

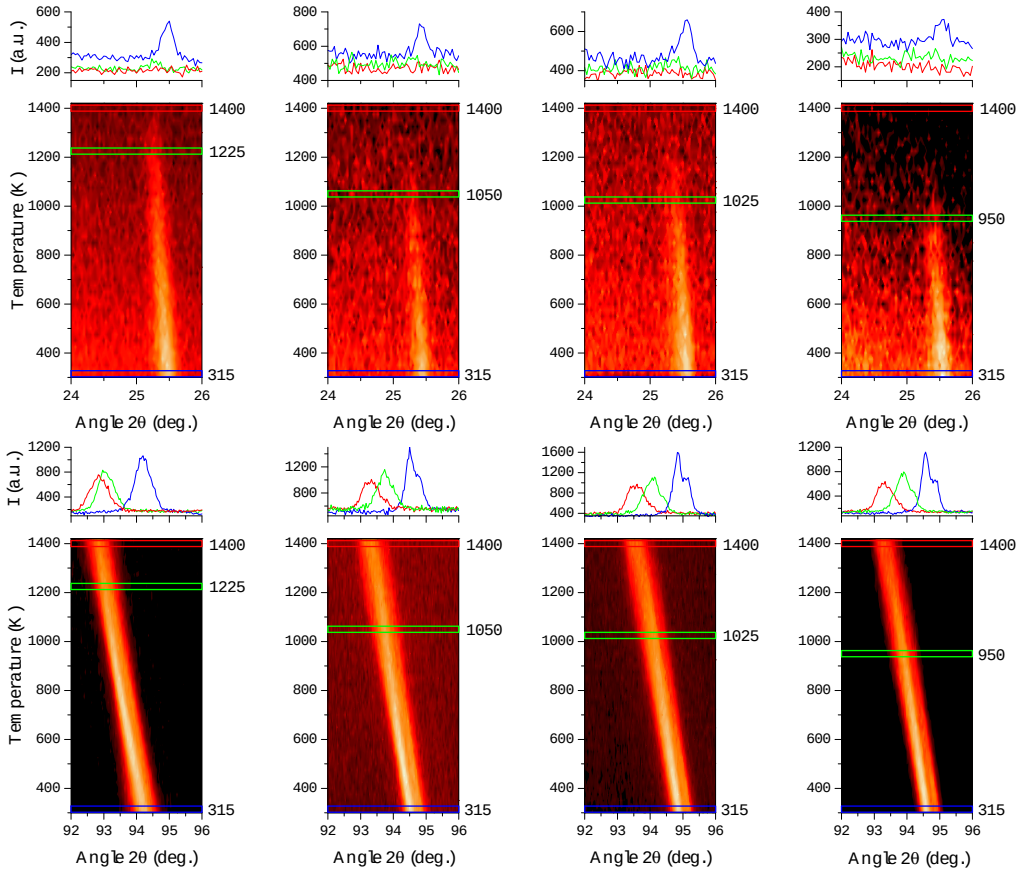

Figure 6.7: Thermal evolution of the (111)(-111) primitive monoclinic and (642) cubic reflections, (top) and (bottom) respectively, of (left) SrPrZnRuO$_6$, (middle-left) SrPrCoRuO$_6$, (middle-right) SrPrNiRuO$_6$ and (right) SrPrMgRuO$_6$, obtained from XRPD (Cu K$\alpha_{1,2}$) experiment. The scattered intensity is represented with yellow-red scale, light-yellow being high-intensity and dark-red lowest intensity. At the temperature indicated by a green line the primitive Bragg reflections disappear, and, at the same time, the monoclinic splitting transforms into a trigonal one.

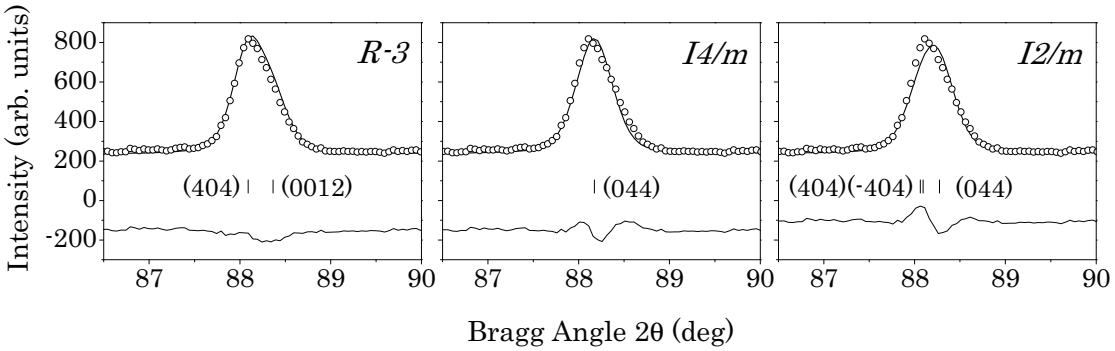

Figure 6.8: Results of the NPD (D2B λ=1.594 Å) data refinement, for SrPrMgRuO$_6$ at 1123 K, using three different models with the $R\bar{3}$, $I4/m$ and $I2/m$ space group. The bars indicate the Bragg reflections. We are showing only the 87.5-90° 2θ interval.

The thermal evolution of the structure of SrPrZnRuO$_6$, SrPrMgRuO$_6$ and SrPrNiRuO$_6$ was explored by means of neutron powder diffraction (NPD) measurements at different temperatures. From the structural point of view, different symmetries have been reported for double perovskite compounds ($I2/m$, $I4/m$, $R\bar{3}$, ...) [34, 36, 51, 117, 121–123]. We tested the space groups expected for ordered double perovskites, and the best results were obtained for the space group $R\bar{3}$ (see Figure 6.8). It is not the first time that this intermediate phase is observed in ruthenium-containing double perovskites [116]. The structural details obtained from the refinement of the crystal structure of SrPrMRuO$_6$ (M=Mg,Ni) at 1123 K and 1200 K, respectively, are collected in Table 6.5. By means of the NPD experiment up to 1100 K, we were not able to observe any structural phase transition in SrPrZnRuO$_6$. Quite the contrary, we observed an irreversible phase-transformation at about 1360 K in NPD patterns for Zn, although it was not observed by XRPD patterns up to 1400 K. This make us think that there was a temperature shift between the conventional X-ray and neutron diffractometer. In Figure 6.9 cell parameters of SrPrMRuO$_6$ (M=Zn,Mg,Ni), obtained upon heating are plotted, as deduced from the NPD data refinement.

Temperature studies of the bond-lengths have shown that, while the mean bond-length of the first coordination-sphere $<A\text{-O}>_{8\text{short}}$ increases, the mean of the second one $<A\text{-O}>_{4\text{long}}$, decreases. In Figure 6.10(a) and (c) a progressive merging of both parameters is seen. This is a natural trend in perovskites, as the tendency of the structure at higher temperatures is to lose the distortion; until the twelve A/A'-O bond-lengths are equal in the cubic symmetry. As expected, bond-length analysis shows that B-site cation leaves the second coordination-sphere of the A/A' cations for Zn compound at $\approx$ 800 K (Figure 6.10(d)), allowing a hop in the distances not observed in the rest of the compounds.

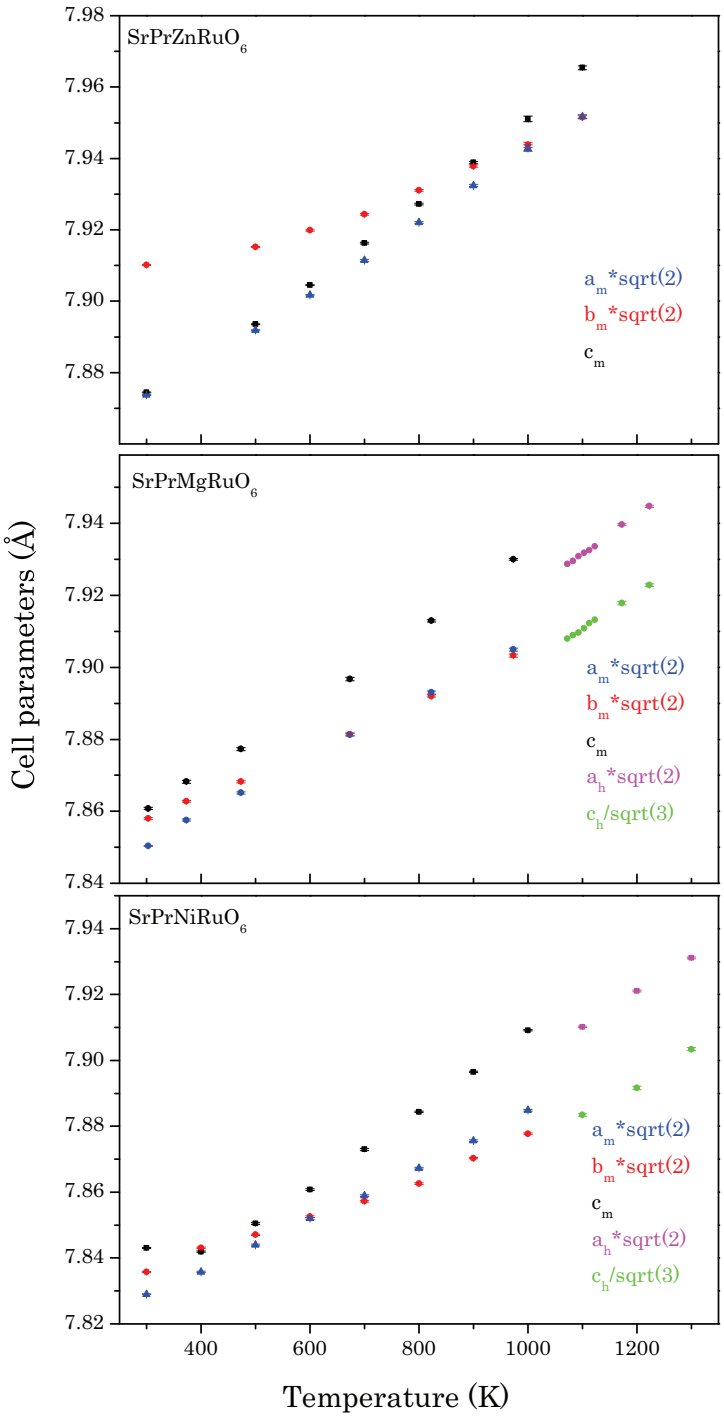

Figure 6.9: Temperature evolution of the cell parameters of SrPrMRuO$_6$ (M=Zn,Mg,Ni) as obtained from the NPD data (HRPT λ=1.494 Å(Zn, Ni), D2B λ=1.594 Å(Mg)): cell parameters for the monoclinic and trigonal phases. For comparison the parameters have been scaled as indicated by the legends.

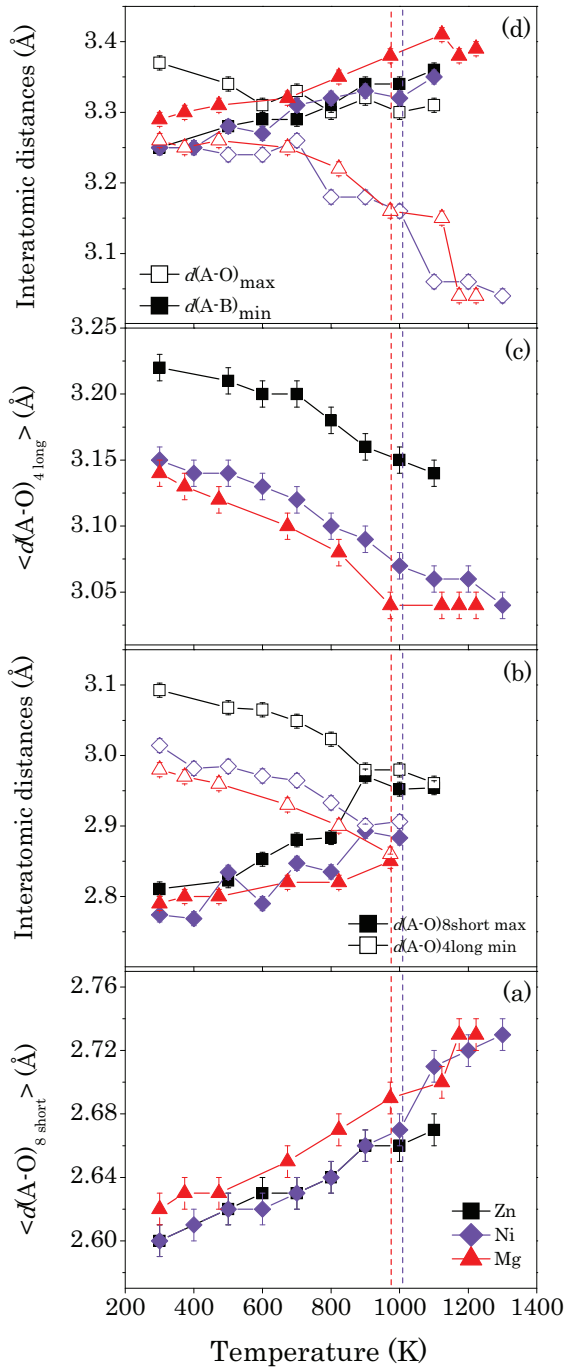

Figure 6.10: Features of the A-site cation coordination polyhedra (AO_8) for Sr$Ln$$MRuO_6$ (M=Zn,Mg,Ni) perovskites. Evolution of (a) the first coordination-sphere's mean A-O bond-lengths, (b) longest first coordination-sphere (AO_8) bond-length and shortest second coordination-sphere bond-length, (c) second coordination-sphere's mean A-O bond-lengths, and (d) longest A-O and shortest A-B bond-lengths, as a function of temperature. Black-rectangle, red-triangle, and purple-rhombus stand for zinc, magnesium and nickel compounds, respectively. In (b) bond-lengths for the trigonal phase for Ni- and Mg-compounds are not indicated. Structural phase transition temperatures are indicate by dotted red and purple lines for magnesium and nickel compounds, respectively.

Table 6.5: Details of the $SrPrMgRuO_6$ and $SrPrNiRuO_6$ intermediate-phase structures obtained from NPD data refinement, refining all mode amplitudes.

Atom	Site	x	y	z	B_{iso}(Å^2)	Occupancy
$SrPrMgRuO_6$, T=1173 K, $R\bar{3}$, a=5.6149(1) Å, c=13.7096(5) Å, γ=120°						
Ru	3a	0	0	0	0.97(3)	1
Mg	3b	0	0	0.5	0.97(3)	1
Sr/Pr	6c	0	0	0.247(1)	2.40(4)	0.5/0.5
O1	18f	0.665(2)	0.8735(9)	0.0781(5)	3.20(3)	1
R_p=4.41%, R_{wp}=6.40%, R_{exp}=5.68%, χ^2=1.27, R_{Bragg}=12.2%						
$SrPrNiRuO_6$, T=1200 K, $R\bar{3}$, a=5.5981(1) Å, c=13.6659(5) Å, γ=120°						
Ru	3a	0	0	0	1.52(2)	1
Ni	3b	0	0	0.5	1.52(2)	1
Sr/Pr	6c	0	0	0.256(2)	2.95(5)	0.5/0.5
O1	18f	0.673(2)	0.882(1)	0.0852(9)	3.95(5)	1
R_p=4.22%, R_{wp}=5.55%, R_{exp}=3.30%, χ^2=2.83, R_{Bragg}=12.4%						

The distance separating the first and second coordination-sphere (difference among the eighth and ninth A-O longest bond-lengths) decreases with temperature, until they become equal Figure 6.10(b). This suggests a change in the coordination polyhedron of cations occupying the A/A'-site of the double perovskite; the coordination of the $SrPrMRuO_6$ (M=Zn,Mg,Ni) compounds above 900 K could be nine or higher. This reflects the convergence of the cell parameters, if pertinent, leading to the formation of the twelve-fold coordinated (cubo-octahedra coordination) A/A'-cations at high temperatures.

According to the theory, the two order parameters (GM_4^+ and X_3^+ irreps, in this case) actuating in the monoclinic phase are expected to thermalize and become zero at higher temperatures. From that point of view, one can expect two intermediate phases before reaching the parent phase: as GM_4^+ mode is larger than X_3^+, the second one would arrive sooner to zero, and GM_4^+ would be the only active mode in the new phase. The symmetry of the new intermediate phase would then be $C2/m$ (commonly used setting $I2/m$). This general rule could be violated by a first order phase transition, what we experimentally observed: before reaching the $C2/m$ phase, a transition between $P2_1/n$ phase and trigonal structure with space group $R\bar{3}$ occurs. Although a phase transition occurs between $P2_1/n$ and $R\bar{3}$ space group structures, $R\bar{3}$ space group model could not be the parent phase for $P2_1/n$ structure, because there is not group-subgroup relation between the space groups Figure 6.11. The same *virtual* reference structure is used for the monoclinic and the trigonal symmetry-mode analysis decomposition.

In the symmetry-breaking from the cubic ($Fm\bar{3}m$) to the trigonal ($R\bar{3}$) phase, there are three irreps (GM_1^+, GM_4^+, and GM_5^+) that can take part, Table 6.6 and 6.7. From those three

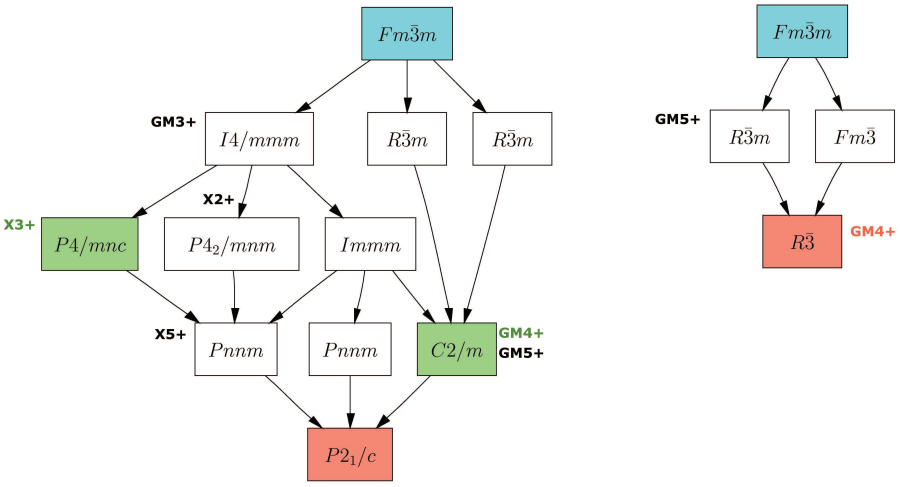

Figure 6.11: Schematic of the group-subgroup chains, going from the prototype cubic symmetry ($Fm\bar{3}m$) to the room temperature space group ($P2_1/n$) and to the intermediate-phase space group ($R\bar{3}$). The labels for the possible irreducible representations (irreps) capable of yielding those symmetry are indicated. In the symmetry-breaking from the cubic to the monoclinic space group, the irreps marked in green mean the two necessary irreps for the symmetry to be broken, two active modes. From the cubic to the trigonal space group, the irrep marked in red means the primary mode in that case.

irreps, AMPLIMODES suggests that there is a unique irrep taking part in the symmetry-breaking, one primary (active) mode, GM_4^+, being the rest secondary contributions. In Table 6.6 we show part of the output of AMPLIMODES, the mode label indicate the atom and the corresponding Wyckoff position, involved in the modes. The geometrical description, in the trigonal cell, of those distortion modes is the following. There is a unique mode that transforms according to GM_4^+ irrep, involves the movements of all the oxygen atoms in the octahedra, displacing the atoms in the *ab* plane in the hexagonal lattice (see Figure 6.12). There are two modes that transforms according to GM_5^+ irrep, acting on the A/A'-site cations and oxygens. GM_5^+-A3, represents a displacement of the A/A'-site cations along *c* axis; while GM_5^+-A4 is a deformation of the octahedra along the three axis. The atomic displacement involved in the modes imply the symmetry-breaking from the prototype symmetry to the isotropy subgroup; in the symmetry-breaking that concerns us $R\bar{3}$ is the isotropy subgroup of the GM_4^+ distortion. If eventually there would be another phase transition to the parent cubic phase ($Fm\bar{3}m$), it would be of the second order (continuous).

Distortion mode-amplitudes have been obtained and octahedra tilt-angles have been also derived from NPD data refinement Figure 6.12. Despite the two types of octahedra present, as mentioned, and two tilt-angles for each type, in Figure 6.12 only the mean value

Table 6.6: Resume of the *irreps* taking part in the symmetry-breaking from the totally symmetric, cubic, space group ($Fm\bar{3}m$) to the intermediate phase $R\bar{3}$ trigonal space group. The list is part of the output of the AMPLIMODES for FullProf. The number in parenthesis indicate the number of modes transforming according to the irrep and the primary mode is written in bold letters.

Atoms	WP	Modes
$Fm\bar{3}m \rightarrow R\bar{3}$		
O1	24e	$GM_1^+(1)$ $\mathbf{GM_4^+(1)}$ $GM_5^+(1)$
Sr1/Pr1	8c	$GM_5^+(1)$

are plotted. Notable is the nearly continuous behavior of the magnitude of the mean tilt-angle (Φ), and the very small jump in the GM_4^+ irrep's distortion-amplitude through the phase transition. The the tilt-axis switches discontinuously from $[110]_p$ to $[111]_p$, directions of the simple perovskite parent cubic. Nevertheless the amplitude changes seemly continuously: in fact, the primary order in both phase transitions is the same.

In Table 6.7 are collected the results of three structural refinements. The goal if this triple refinement set is to illustrate experimentally that there is a unique active mode in the cubic ($Fm\bar{3}$m) to trigonal ($R\bar{3}$) symmetry-breaking. Columns (a), (b), and (c) in Table 6.7 indicate, structural refinement releasing all mode-amplitudes, structural refinement setting the GM_1^+ irrep mode-amplitude to zero, and structural refinement freeing only GM_4^+ irrep, respectively. The effect of the three refinements can be observed in the reliability factors: the reduction of three degrees of freedom (75% of the total mode-amplitudes) gives comparable R factors; corroborating the theoretical prediction of unique active mode in the symmetry-breaking.

The transition temperatures observed from the monoclinic to the trigonal phase could be related with the stabilization of the distorted structure at room temperature. The analysis shows that the more distorted is the structure at RT, the higher is the transition temperature; except for $SrPrNiRuO_6$ member; as observed in the mode amplitudes.

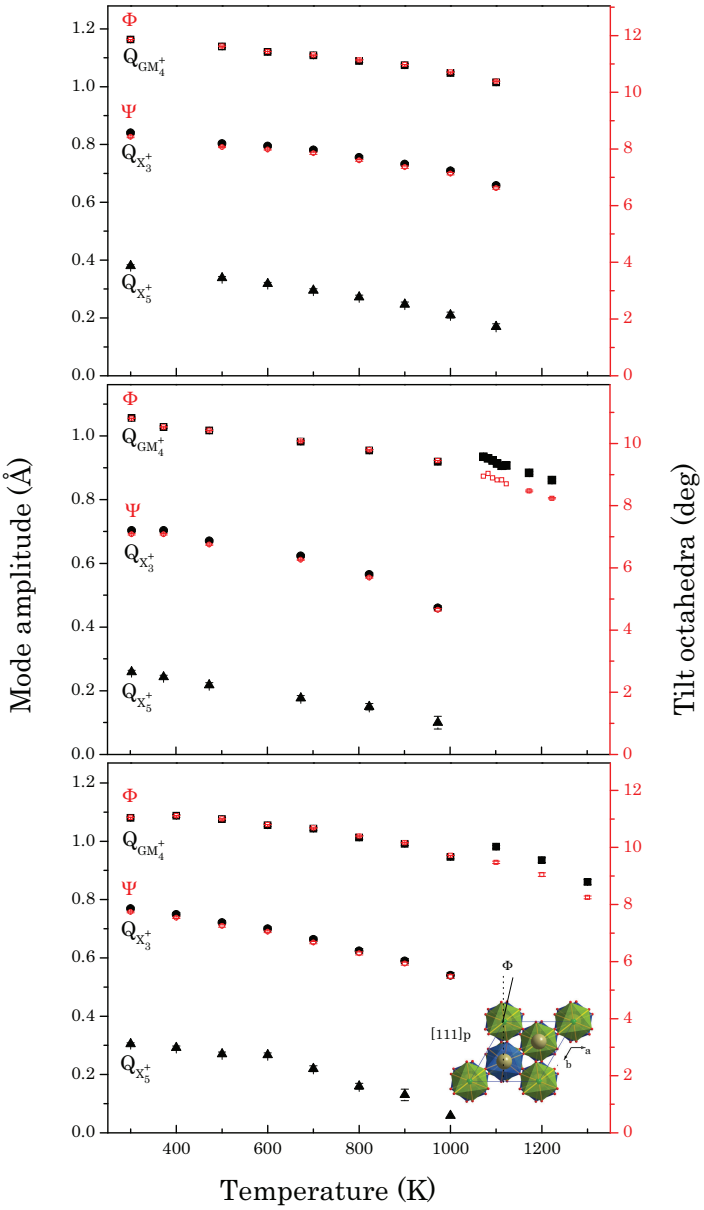

Figure 6.12: Temperature dependence of the amplitudes of the modes conforming the $P2_1/n$ and $R\bar{3}$ structure of SrPrMRuO$_6$ (M=Zn(top), Mg(middle), Ni(bottom)), and Ψ and Φ tilt-angles, as obtained from the NPD data refinement. The amplitudes of the irreps in the high symmetry phase have been scaled (multiplied by 3/2) to see the evolution, since AMPLIMODES uses mode normalization within the corresponding primitive unit cell.

Table 6.7: Mode amplitude (in Å) value after the refinement for $SrPrMRuO_6$ (Mg,Ni) compounds at 1173 K and 1200 K, respectively, for cubic ($Fm\bar{3}m$) to trigonal ($R\bar{3}$) phase transition; refining (a) all modes, (b) 3 and (c) 1 highest amplitude modes.

Irrep	Mode	Isotropy subgroup	Amplitude					
			Mg			Ni		
			(a)	(b)	(c)	(a)	(b)	(c)
GM_1^+	A1	$Fm\bar{3}m$	-0.03(2)	0.00	0.00	0.03(2)	0.00	0.00
GM_4^+	A2	$R\bar{3}$	-0.566(7)	-0.567(6)	-0.584(4)	-0.628(8)	-0.608(8)	-0.613(5)
GM_5^+	A3	$R\bar{3}m$	-0.06(2)	-0.06(2)	0.00	0.11(4)	0.03(2)	0.00
	A4		-0.16(2)	-0.14(2)	0.00	0.09(3)	0.16(2)	0.00
R_p(%)			4.41	4.27	4.30	4.22	4.29	4.26
R_{wp}(%)			6.40	6.32	6.35	5.55	5.68	5.65
R_{exp}(%)			5.68	5.67	5.68	3.30	3.30	3.30
χ^2			1.27	1.23	1.25	2.83	2.96	2.92
R_{Bragg}(%)			12.2	11.5	11.6	12.4	12.0	11.5

K-vector: GM_1^+ (0,0,0), GM_4^+ (0,0,0), GM_5^+ (0,0,0)
Direction: GM_1^+ (a), GM_4^+ (a,a,a), GM_5^+ (a,a,a)

6.3 Conclusions

Symmetry-mode decomposition of the room temperature monoclinic ($P2_1/n$) phase of SrPrZnRuO$_6$, SrPrCoRuO$_6$, SrPrMgRuO$_6$ and SrPrNiRuO$_6$ shows that these phases can be described mainly due to the presence of two different distortion modes, with respect to the $Fm\bar{3}m$ parent phase, although the small contribution of X_5^+ is also necessary. The refinements of the structures based on symmetry-adapted modes allows the reduction of the number of structural refined degrees of freedom. All those modes with amplitudes close to zero, could be set up as zero, their contribution to the distorted structure is negligible. Those two modes (GM_4^+ and X_3^+) that describe mainly the instability of the monoclinically distorted structure are (linearly related to) the tilt systems of the octahedra, Φ and Ψ.

The temperature evolution of the structures of SrPrMgRuO$_6$ and SrPrNiRuO$_6$ shows a phase transition to a trigonal phase ($R\bar{3}$), at 950 and 1025 K, respectively. The theory predicts a unique active mode in the intermediate trigonal phase, GM_4^+; which was experimentally corroborated.

The study has shown a connection between the B-site cation size, the mode amplitudes (structural distortion) and transition temperatures; the bigger the B-site cation size, the less symmetric is the structure at RT (except for SrPrMgRuO$_6$), and therefore higher transition temperatures for less symmetric structures. In SrPrMRuO$_6$ (M=Zn,Co,Mg,Ni), the observed effects are thought not to be purely steric.

Chapter 7

SrLaMRuO$_6$ (M=Zn,Mg) ordered double perovskites

7.1 Room temperature structures: SrLaZnRuO$_6$ and SrLaMgRuO$_6$

The crystal structure of ordered double perovskite can show different symmetries at room temperature (RT), depending on many factors, such as the size of the A- and B-site cations. For many double perovskite oxides the sizes of the cations A and A' are too small to stabilize the cavity formed by the twelve oxygen atoms resulting in tilting of the octahedra and shifts of the cations, hence lowering the symmetry of the structure, from that of the ideal cubic double perovskite. The effect of the cation size on the structure can be quantified by using the so called Goldschmidt *tolerancefactor* [8]: $t = \frac{\bar{r}_{A,A'}+r_O}{\sqrt{2}(\bar{r}_{B,B'}+r_O)}$. The cubic symmetry is expected when t is close to one, while at t <1 distorted structures are favored.

The tolerance factors for SrLaZnRuO$_6$,SrLaMgRuO$_6$, and other previously reported Sr$Ln$$MRuO_6$ materials, calculated using ionic radii from [48], are listed in Table 7.1 (a). The strontium and rare-earth radii were chosen in IX coordination. As can been seen, the values for SrLaZn(Mg)RuO$_6$ are smaller than those for SrLaNiRuO$_6$ [116]. Given that the structure of SrLaNiRuO$_6$ (the material with the highest t value in the table) at room temperature has a space group $P2_1/n$, we have used this space group as a starting model in the Rietveld refinements.

Analyses of the NPD data from SrLaZnRuO$_6$ using the monoclinic $P2_1/n$ (complete ordering of the Zn and Ru atoms over the B and B' sites) and orthorhombic $Pbnm$ (random

Table 7.1: A summary of the symmetries and phase transitions reported for compounds with the general formula $Sr^{2+}Ln^{3+}M^{2+}Ru^{5+}O_6^{2-}$. t stands for tolerance factors calculated from (a) the ionic radii in [48] and (b) Rietveld refinement interatomic distances (the strontium and rare-earth radius in nine coordination is chosen since it is the highest coordination number available for all tabulated rare-earths); symmetry of the structure at room temperature; transition temperature; intermediate-phase symmetry and high temperature phase symmetry; literature reference. PW stands for present work.

Compound	(a) t	(b) t	RT symmetry	T_{trans}	High symmetry	Ref.
$SrLaNiRuO_6$	0.9266	0.9460	$P2_1/n$	670 K	$R\bar{3}$	[116]
$SrLaMgRuO_6$	0.9198	0.9534	$P2_1/n$	673 K	$R\bar{3}$	Chap.7
$SrLaCuRuO_6$	0.9176	0.9458	$P2_1/n$	730 K	$R\bar{3}$	[116]
$SrLaCoRuO_6$	(LS)0.9357	0.9439	$P2_1/n$			[111]
	(HS)0.9143					
		0.9457	$P2_1/n$			[115]
$SrLaZnRuO_6$	0.9154	0.9422	$P2_1/n$	923 K	$R\bar{3}$	Chap.7
$SrNdNiRuO_6$	0.9174	0.9358	$P2_1/n$	500 K, 900 K	$P4_2/n$, $Fm\bar{3}m$	Chap.5
$SrNdMgRuO_6$	0.9108	0.9380	$P2_1/n$	580 K, 920 K	$P4_2/n$, $Fm\bar{3}m$	Chap.5
$SrNdCoRuO_6$	(LS)0.9265	0.9359	$P2_1/n$	660 K, 980 K	$P4_2/n$, $Fm\bar{3}m$	Chap.5
	(HS)0.9053					
$SrNdZnRuO_6$	0.9064	0.9301	$P2_1/n$	780 K, 1120 K	$P4_2/n$, $Fm\bar{3}m$	Chap.5
$SrPrNiRuO_6$	0.9202	0.9389	$P2_1/n$	1100 K	$R\bar{3}$	Chap.6
$SrPrMgRuO_6$	0.9135	0.9420	$P2_1/n$	900 K	$R\bar{3}$	Chap.6
$SrPrCoRuO_6$	(LS)0.9293	0.9373	$P2_1/n$	1000 K		Chap.6
	(HS)0.9080					
$SrPrZnRuO_6$	0.9091	0.9324	$P2_1/n$	1300 K		Chap.6

occupation of the B and B'-sites by Zn and Ru) space groups give fits with reliability parameters that are only slightly better for the monoclinic model. Careful examination of the calculated profile in the orthorhombic model, however shows a peak at low-angles (see Figure 7.1, inset $P2_1/n$ and $Pbnm$) that is not well fitted. This peak is indicative of the B and B'-site cation ordering [31]. To clarify the ordering state of the B-site cations X-ray powder diffraction data were collected (see Figure 7.1). X-ray diffraction is sensitive to the ordering between Zn^{2+} and Ru^{5+} because of the large difference in the number of electrons of these two cations, 28 and 39, respectively. In the XRPD data the peak related to the B and B'-site cation ordering is clearly seen. This result suggests that at RT $SrLaZnRuO_6$ crystallizes in the monoclinic $P2_1/n$ space group.

For the NPD measurements of $SrLaMgRuO_6$ at RT only a small amount of material was available and this resulted in much lower diffraction intensities (Figure 7.1). Due to the reduced signal to noise ratio weak reflections were not observed in the pattern and it could be refined with the monoclinic ($P2_1/n$), tetragonal ($I4/m$) or trigonal ($R\bar{3}$) symmetries with the following reliability factors: R_p=2.44%, R_{wp}=3.18%, R_{exp}=6.29% and R_{Bragg}=7.26%; R_p=3.36%, R_{wp}=4.70%, R_{exp}=6.31% and R_{Bragg}=8.79%; R_p=2.74%, R_{wp}=3.69%, R_{exp}=6.30% and R_{Bragg}=7.33%, respectively. Nevertheless, Figure 7.1 shows the presence of a very

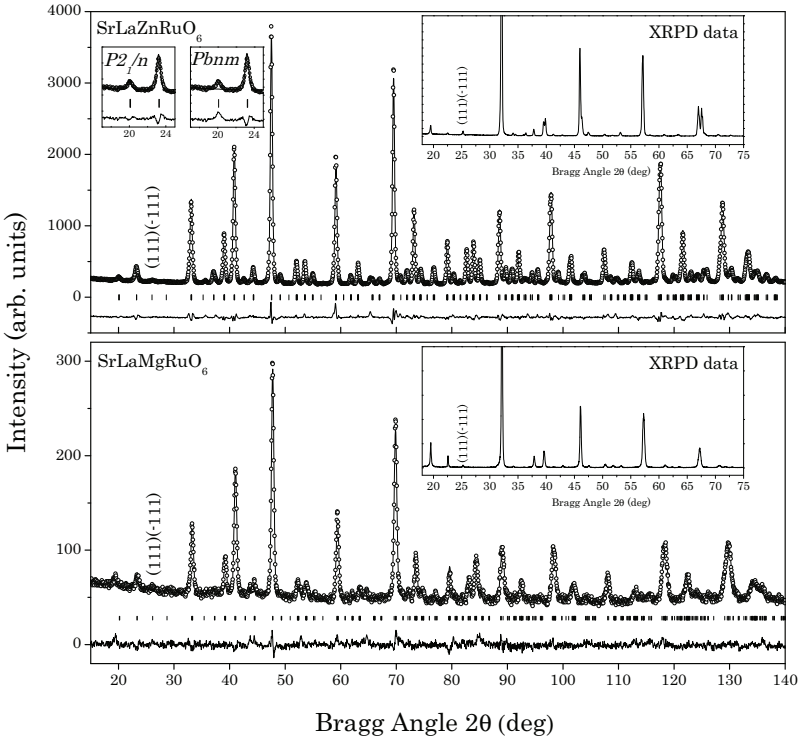

Figure 7.1: Experimental (circles) and calculated (line) neutron diffraction profiles for the Rietveld refinements of $SrLaZnRuO_6$ and $SrLaMgRuO_6$ at room temperature using structural models with $P2_1/n$ space group. Markers below correspond to Bragg reflections. Insets show NPD R-point reflection refinement using monoclinic and orthorhombic models; and XRPD data.

weak Bragg peaks (111/-111 assuming monoclinic unit cell) at about 26.1°. The presence of this peak is not allowed for structures with I-centering. Hence, we propose the monoclinic $P2_1/n$ space group for the structure of $SrLaMgRuO_6$ at RT.

The difference in charge between B and B'-cations is the most important factor influencing cation ordering [31]. If the difference in the oxidation state is two or less, all of the ordering arrangements (complete rock-salt ordering, partial rock-salt ordering and complete disorder) are possible, dominated by completely disordered and partially ordered arrangements. If the difference is greater than two, highly ordered compounds are generally observed, such as in [124]. Hence, double perovskites of the ruthenium family have shown different ordering arrangements when M^{2+} and Ru^{5+}, such as in $SrLaZnRuO_6$, $SrLaMgRuO_6$, $SrNdMRuO_6$ [120] and $SrPrMRuO_6$ [125] with a complete ordering; and a partially ordered arrangement in $SrLaCoRu_6$ [111, 115], $SrLaCuRuO_6$ and $SrLaNiRuO_6$ [116]. The degree of ordering can also be affected by other effects such as the preparation conditions; ionization potentials, etc. [5, 28, 34].

Table 7.2: Crystal structure data and refinement results for $SrLaZnRuO_6$ and $SrLaMgRuO_6$ at RT obatined from NPD using a $P2_1/n$ structural model.

Reliability factors	Lattice parameters	Atom	Site	x	y	z	B_{iso} (Å^2)	Occ
$SrLaZnRuO_6$, T=300 K								
R_p = 3.32%	a= 5.6036(2) Å	Ru	2a	0	0	0	0.29(2)	1
R_{wp}= 4.55%	b= 5.5874(2) Å	Zn	2b	0	0	0.5	0.29(2)	1
R_{exp}= 5.45%	c= 7.9016(2) Å	Sr/La	4e	-0.0034(6)	0.4746(3)	0.752(1)	0.69(3)	0.5/0.5
R_{Bragg}= 3.48%	β= 90.051(6)°	O1	4e	-0.268(1)	0.220(1)	-0.0294(7)	0.78(2)	1
	V= 247.39(1) Å^3	O2	4e	-0.792(1)	0.280(1)	0.0371(7)	0.78(2)	1
		O3	4e	0.0666(5)	0.0063(5)	0.753(1)	0.78(2)	1
$SrLaMgRuO_6$, T=300 K								
R_p = 3.77%	a= 5.583(1) Å	Ru	2a	0	0	0	0.5(1)	1
R_{wp}= 4.85%	b= 5.555(1) Å	Mg	2b	0	0	0.5	0.5(1)	1
R_{exp}= 13.01%	c= 7.871(3) Å	Sr/La	4e	-0.001(5)	0.487(4)	0.757(7)	1.0(2)	0.5/0.5
R_{Bragg}= 9.80%	β= 90.04(7)°	O1	4e	-0.285(7)	0.216(7)	-0.027(5)	1.2(1)	1
	V= 244.1(1) Å^3	O2	4e	-0.758(7)	0.252(7)	0.021(5)	1.2(1)	1
		O3	4e	0.068(5)	0.003(6)	0.746(7)	1.2(1)	1

Table 7.2 shows the cell parameters, volume and atomic coordinates of SrLaMRuO$_6$ (M=Zn,Mg) at room temperature obtained after the structural refinement with the NPD data. The mean interatomic distances and some selected bond angles for are listed in Table 7.3.

The symmetry-mode decomposition of the symmetry breaking from the cubic prototype phase $Fm\bar{3}m$ to the monoclinic $P2_1/n$ space group have been previously analyzed in other double perovskite compounds [36, 120, 125]. Both space groups are related by the transformation matrix (**1/2a-1/2b, 1/2a+1/2b, c**; 0,0,0) (in the following, we use the $P12_1/n1$, origin choice 2, non-standard setting of the $P2_1/c$ No. 14 monoclinic space group). The theoretical predictions and the Rietveld refinement of the mode amplitudes suggest that there is more than one active modes responsible for the $Fm\bar{3}m \rightarrow P2_1/n$ symmetry break. This means that $P2_1/n$ phase cannot be generated by a single mechanism, or a single unstable mode of the cubic configuration. At least two modes must be present. These two active modes responsible for the stabilization of the $P2_1/n$ phase in double perovskites are known to be transforming according to the GM_4^+ and X_3^+ irreps [36, 120].

A summary of the mode decomposition of the monoclinic distortion in the structures of $SrLaZnRuO_6$ and $SrLaMgRuO_6$ at RT obtained by the NPD data refinement is shown in Table 7.4. As can be seen, there are three global amplitudes (GM_4^+, X_3^+ and X_5^+ irreps) that are higher than the rest. GM_4^+ and X_3^+ are the modes necessary to break the symmetry from the cubic to the monoclinic phase. X_5^+ has an amplitude that is about half of the value of X_3^+, and two times higher than GM_5^+. The rest of the modes have negligible amplitudes. In

Table 7.3: Octahedra volume (Å^3), main bond lengths (Å), selected angles (°) and bond-valence sum [86] for Sr*La*$M$$RuO_6$ (M=Zn,Mg) at room temperature.

	$SrLaZnRuO_6$	$SrLaMgRuO_6$
MO_6 octahedra		
V(MO_6)	11.467(2)	10.42(6)
M-O1(×2)	2.048(6)	1.99(4)
M-O2(×2)	2.069(6)	2.00(4)
M-O3(×2)	2.034(9)	1.97(6)
Average distance	2.050(9)	1.99(6)
Predicted distance	2.1105	2.0995
RuO_6 octahedra		
V(RuO_6)	10.195(3)	10.51(5)
Ru-O1(×2)	1.954(6)	2.00(4)
Ru-O2(×2)	1.972(6)	1.95(4)
Ru-O3(×2)	1.985(9)	2.04(6)
Average distance	1.971(9)	2.00(6)
Predicted distance	1.9675	1.9675
∠O1-M-O2	93.8(2)	84.1(5)
∠O1-M-O3	91.0(2)	91.0(5)
∠O2-M-O3	90.3(2)	87.1(5)
∠O1-Ru-O2	88.3(2)	97.4(5)
∠O1-Ru-O3	91.0(2)	92.3(5)
∠O2-Ru-O3	91.2(2)	87.0(5)
∠M-O1-Ru	162.8(2)	160.1(6)
∠M-O2-Ru	156.6(2)	170.1(7)
∠M-O3-Ru	158.5(1)	158.1(4)
Bond-Valence sum		
M	2.36(2)	2.7(1)
Ru	4.96(4)	4.6(2)

other structural studies of double perovskites [36, 120, 125], the negligible contribution of some modes to the atomic positions in the distorted configuration was observed and used to reduce the number of degrees of freedom released during the refinement. Three sets of refinements have been performed, as in previous studies (results in Table 7.4). In the first attempt, Table 7.4(a), all mode amplitudes were refined. In the second, (b), GM_1^+, GM_3^+ and X_2^+, were set to zero. Finally, in (c) only GM_4^+, X_3^+ and X_5^+ were refined. The effect of the three refinements on the reliability factors is clear and agrees with the behavior observed in [120, 125]: a reduction of six refined parameters (50% of the total) increases the R factors less than c.a. 10% (e.g. 4.55 to 5.07%, or 4.85 to 4.93% for $SrLaZnRuO_6$ and $SrLaMgRuO_6$, respectively), and the amplitudes of the active modes do not suffer any significant variations.

In all SrLnMRuO$_6$ materials with $P2_1/n$ symmetry at RT, the same two coupled modes are expected to be responsible for the reduction of symmetry. The differences among the family members are in the amplitudes of the modes. In order to compare the different structures, the same *virtual* reference structure as in [120, 125] has been used because no cubic phase was experimentally observed for these compounds.

The effect of the size of the Zn and Mg cations on the RT structures can be quantified by comparing the amplitudes of the modes. As can be observed for SrLaZnRuO$_6$ and SrLaMgRuO$_6$ in Table 7.4, larger atomic radii of the B-site cations (smaller tolerance factor) correspond to increased amplitudes of the distortion modes. This is a trend observed also in other SrLnMRuO$_6$ compounds reported in [115, 116, 120, 125], except for SrLaCoRuO$_6$ [111]. The correlation between the B-site cation and the distortion of the structure is represented in Figure 7.2. The reason for SrLaCoRuO$_6$* not following the trend, could be the accuracy of the oxygen positions, obtained from XRPD data or variations in the stoichiometry of the material.

The effect of the increased size of the A/A'-site cation is to stabilize less distorted structures as can be also observed in Figure 7.2. Comparing different SrLnMRuO$_6$ compounds with the same M cation, it can be seen that the Nd containing compounds have the most distorted structures, whereas the La containing materials are less distorted. This observation is in agreement with the sizes of the lanthanide cations (in IX coordination): $r_{\mathrm{La}} > r_{\mathrm{Pr}} > r_{\mathrm{Nd}}$ [48]. Figure 7.2 also shows the variation of the the tilt angles of the octahedra with the tolerance factor. For small amplitudes of the distortion modes there is a linear dependence between the mode amplitudes and the tilt angles.

Table 7.4: Refined values of the irrep amplitudes (in Å) taking part in the symmetry breaking from $Fm\bar{3}m$ space group to $P2_1/n$ monoclinic (RT) and intermediate phase $R\bar{3}$ space group (923 K for $SrLaZnRuO_6$ and 673 K for $SrLaMgRuO_6$). $Fm\bar{3}m \rightarrow P2_1/n$: (a) all modes , (b) 4 and (c) 3 highest irrep amplitudes. $Fm\bar{3}m \rightarrow R\bar{3}$: a) all modes, (b) GM_1^+ fixed to zero and (c) only GM_4^+.

Irrep	Isotropy subgroup	Dim	Amplitude					
			$SrLaZnRuO_6$			$SrLaMgRuO_6$		
			(a)	(b)	(c)	(a)	(b)	(c)
$Fm\bar{3}m \rightarrow P2_1/n$								
GM_1^+	$Fm\bar{3}m$ (225)	1	0.06(1)	0.00	0.00	0.1(1)	0.00	0.00
GM_3^+	$I4/mmm$ (139)	1	0.04(2)	0.00	0.00	0.1(1)	0.00	0.00
GM_4^+	$C2/m$ (12)	1	1.055(3)	1.053(3)	1.058(3)	0.91(4)	0.93(2)	0.94(2)
GM_5^+	$C2/m$ (12)	4	0.15(2)	0.17(1)	0.00	0.4(1)	0.2(1)	0.00
X_2^+	$P4_2/mnm$ (136)	1	0.000(7)	0.00	0.00	0.04(7)	0.00	0.00
X_3^+	$P4/mnc$ (128)	1	0.670(5)	0.670(4)	0.663(4)	0.44(4)	0.45(4)	0.43(4)
X_5^+	$Pnnm$ (58)	3	0.306(6)	0.298(3)	0.290(3)	0.17(6)	0.18(4)	0.17(4)
R_p(%)			3.32	3.47	3.78	3.77	3.70	3.85
R_{wp}(%)			4.55	4.69	5.07	4.85	4.78	4.93
R_{exp}(%)			5.45	5.46	5.46	13.01	13.01	13.01
R_{Bragg}(%)			3.48	3.82	4.53	9.80	9.70	9.97
K-vector: GM_1^+ (0,0,0), GM_3^+ (0,0,0), GM_4^+ (0,0,0), GM_5^+ (0,0,0), X_2^+ (0,1,0), X_3^+ (0,1,0), X_5^+ (0,1,0)								
Direction: GM_1^+ (a), GM_3^+ (a,0), GM_4^+ (a,a,0), GM_5^+ (-b,a,-a), X_2^+ (0,a,0), X_3^+ (0,a,0), X_5^+ (a,a,0,0,a,-a)								
$Fm\bar{3}m \rightarrow R\bar{3}$,								
GM_1^+	$Fm\bar{3}m$ (225)	1	0.03(2)	0.00	0.00	0.00(5)	0.00	0.00
GM_4^+	$R\bar{3}$ (148)	1	0.646(4)	0.647(4)	0.652(3)	0.63(1)	0.627(9)	0.605(7)
GM_5^+	$R\bar{3}m$ (166)	2	0.14(2)	0.10(2)	0.00	0.09(5)	0.07(8)	0.00
R_p(%)			3.48	3.47	3.47	2.77	2.74	2.64
R_{wp}(%)			4.78	4.79	4.82	3.69	3.66	3.54
R_{exp}(%)			5.84	5.84	5.84	7.00	7.00	7.00
R_{Bragg}(%)			7.83	7.82	7.91	8.81	8.37	7.40
K-vector: GM_1^+ (0,0,0), GM_4^+ (0,0,0), GM_5^+ (0,0,0)								
Direction: GM_1^+ (a), GM_4^+ (a,a,a), GM_5^+ (a,a,a)								

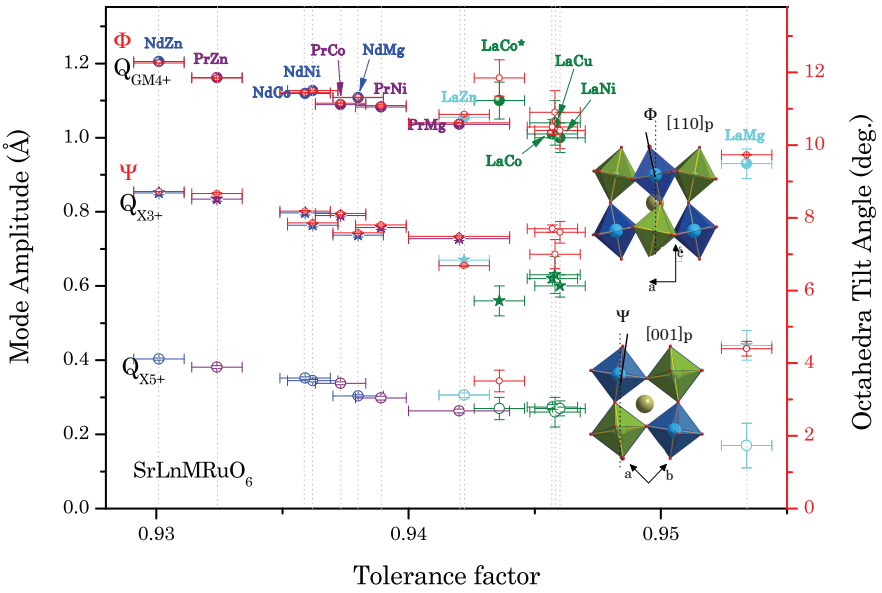

Figure 7.2: Amplitudes of GM_4^+ (filled circles), X_3^+ (stars) and X_5^+ irreps (empty circles) in the RT structures of the $SrLaMRuO_6$ (M=Zn^a,Mg^a) (PW) (light-blue), $SrLaMRuO_6$ (M=Cu^b[116],Ni^b[116],Co^{*a}[111],Co^c[115]), $SrNdMRuO_6$ (M=Zn^a,Co^a,Mg^a,Ni^a) (dark-blue) [120] and $SrPrMRuO_6$ (M=Zn^a,Co^a,Mg^a,Ni^a) (purple) [125] compounds, and Ψ and Φ tilt-angles (red symbols), as obtained from the NPD^a, synchrotron radiation^b or XRPD^c data refinement, in function of calculated tolerance factors (Sr/Ln-O distance in nine coordination is chosen since it is the highest coordination number available for all tabulated rare-earths). Lines in the figure are guide to the eyes. PW stands for present work.

7.2 High temperature structures: $SrLaZnRuO_6$ and $SrLaMgRuO_6$

The thermal evolution of the structures of $SrLaZnRuO_6$ and $SrLaMgRuO_6$ was studied by means of NPD. The diffracted intensity projections (rainbow scale) in three 2θ intervals (54-55.5°, 87-90°, and 95-99°) are shown in Figure 7.3 for $SrLaZnRuO_6$. As it can be concluded from Figure 7.3, $SrLaZnRuO_6$ undergoes a temperature-induced discontinuous structural phase transition taking place between 800 to 900 K.

In order to determine the space group of the high temperature phase symmetry analysis has been used. The discontinuous character of the phase transition suggests that the

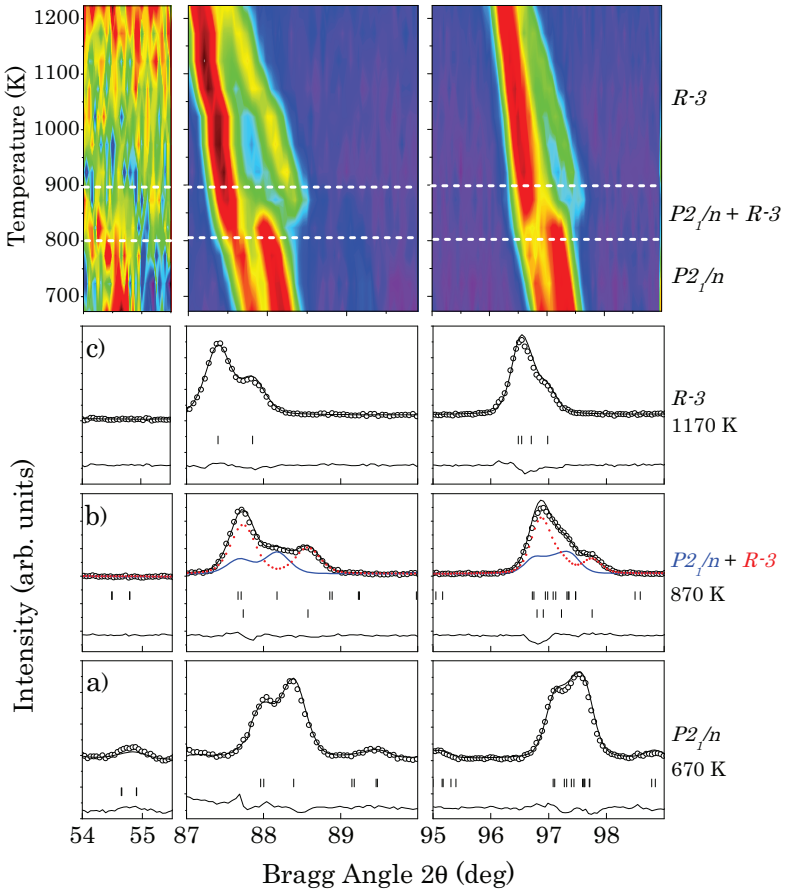

Figure 7.3: Temperature evolution of 54-55.5° (primitive peak, (-311;311;-131;131)), 87.8-90° (cubic (444) reflection) and 95-99° (cubic (642) reflection) 2θ ranges for $SrLaZnRuO_6$. The calculated and the difference of the diffraction profiles are obtained after NPD data Rietveld refinement of the structure at each temperature. The structural models used in the refinements have the following symmetries: (a) $P2_1/n$ for 670 K, (b) coexistence of $P2_1/n$ and $R\bar{3}$ phases for 870 K, and $R\bar{3}$ for (c) 1170 K. Markers indicate Bragg reflections. In (b) blue continued line corresponds to $P2_1/n$ phase and red dotted line to $R\bar{3}$ phase.

maximal subgroups relating the space group of the parent phase ($Fm\bar{3}m$) and the RT distorted phase ($P2_1/n$) could be rejected.

Several possible models were tested for the structure of the high temperature phase. Refinements with four of these models, with the $I2/m$, $I4/m$, $R\bar{3}$, and $Fm\bar{3}m$ space groups, respectively, are shown in Figure 7.4 and Figure 7.5. The tetragonal space group has only one reflection (044) in the 86-90° 2θ interval, and is unable to take into account the observed peak splitting. On the other hand, the trigonal space group has two reflections (404) and (0012) in this interval, and fits well the experimental pattern. Due to the high degree of pseudo-symmetry of the perovskite materials often it is not easy to distinguish between the monoclinic ($I2/m$) and the trigonal ($R\bar{3}$) symmetries. In $I2/m$ the (110) and (002) reflections may be resolved when the $\sqrt{2}a/c$ ratio is different from one. In $R\bar{3}$ however, (012) does not overlap with any other reflection [31] and therefore, the observation of a second peak around the (110) reflection is an evidence that the structure has the monoclinic symmetry. The structural model with with the $I2/m$ symmetry did not produce satisfactory results for the high temperature phases of SrLaZnRuO$_6$ and SrLaMgRuO$_6$ (see Figure 7.5) and thereby the trigonal symmetry is proposed for the high temperature phase.

At the highest temperature measured, 1220 K, the compound remains in the trigonal symmetry. Only one structural phase transition is observed experimentally for SrLaZnRuO$_6$ in the measured temperature range. The attempt to refine the diffraction pattern collected

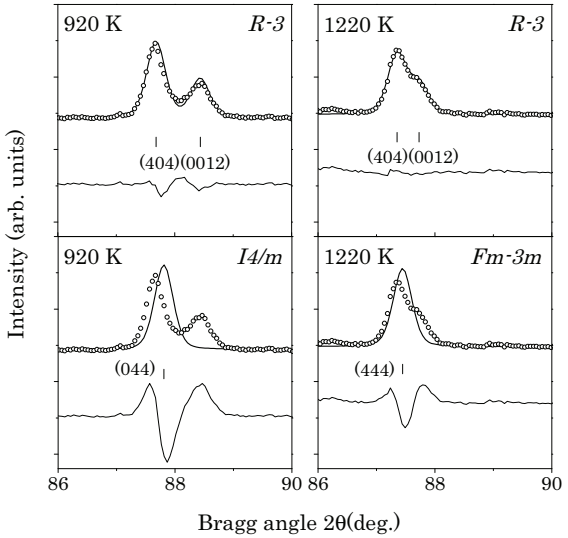

Figure 7.4: Refinements results for SrLaZnRuO$_6$, in the 86-90° 2θ interval at 920 and 1220 K temperatures, using different models with $R\bar{3}$ and $I4/m$ space groups, and $R\bar{3}$ and $Fm\bar{3}m$, respectively. The bars in lower part indicate the Bragg reflections with Miller indices.

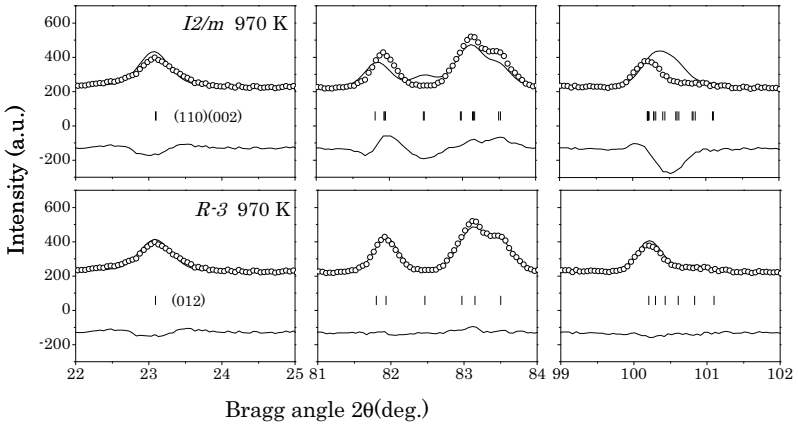

Figure 7.5: Refinements results for $SrLaZnRuO_6$, in the 22-25° (cubic (200) reflection), 81-84° (cubic (533) and (622) reflections) and 99-102° (cubic (577;731) reflections) 2θ interval at 970 K, using different models with $R\bar{3}$ and $I2/m$ space groups.

at 870 K for $SrLaZnRuO_6$ using the structural models with either $P2_1/n$ or $R\bar{3}$ space groups separately, cannot reproduce the observed splitting, Figure 7.3(b). This is solved by considering a mixture of two phases with the two different symmetries coexisting in the temperature interval between 800 and 900K. The refinement of the data collected at 870K (Figure 7.6) shows that at this temperature the relative ratio is 35% of $P2_1/n$ and 65% of $R\bar{3}$.

The data analysis for $SrLaMgRuO_6$ between RT and ∼800 K, suggests that the same structural phase transition $P2_1/n \rightarrow R\bar{3}$ occurs between 520 and 620 K. The structural details for the trigonal phases of both compounds are presented in Table 7.5 and the temperature evolution of the cell parameters and the amplitudes of the distortion modes are shown in Figure 7.7 and Figure 7.8, respectively. The temperature dependence of the rhombohedral angle α in the trigonal phase of $SrLaZnRuO_6$ is shown in Figure 7.9. The rhombohedral angle linearly decreases with the temperature. The dependence can be expressed with the formula α=a-bT, where a=60.86(1)° and b=5.6(1)$\times 10^{-4}$. Extrapolation from this dependence to higher temperature shows that at ∼1535 K the rhombohedral angle α should become equal to 60°. This suggests the possible existence of a second order phase transition from $R\bar{3}$ to $Fm\bar{3}m$ (prototype phase). For such transition it is expected that α varies linearly with temperature [126] and the transition to the cubic phase should occur when α=60°.

There are three irreps that can take part in the symmetry breaking from the cubic ($Fm\bar{3}m$) to the trigonal $R\bar{3}$ phase: $GM_1^+(1)$, $GM_4^+(1)$ and $GM_5^+(2)$, the number in parenthesis indicate the number of modes transforming according to the corresponding irrep. The symmetry mode decomposition performed by AMPLIMODES suggests that there is a single primary mode responsible for the symmetry breaking: the one transforming according

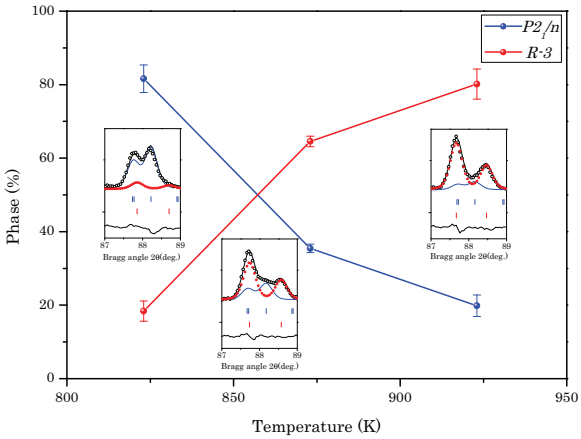

Figure 7.6: Temperature evolution of the concentration of the $P2_1/n$ (blue) and $R\bar{3}$ (red) phases in the co-existence range for SrLaZnRuO$_6$. Inset show NPD data Rietveld refinement in combination of two symmetries: blue continued line corresponds to $P2_1/n$ phase and red dotted line to $R\bar{3}$ phase.

to GM_4^+. Several refinements (results shown in Table 4) have been done: (a) all mode amplitudes refined, (b) GM_1^+ fixed to zero and (c) only GM_4^+ refined. The three refinements show that the reduction of the total number of refined mode amplitudes from 4 to 1 gives an increment of the R factors of less than 2%; moreover, the amplitude of the theoretically predicted active mode GM_4^+ does not vary at all.

In the first order phase transition $P2_1/n \rightarrow R\bar{3}$ the order parameter GM_4^+ changes its direction from (a,a,0) to (a,a,a), see Table 7.4. Despite this change in direction the amplitude of GM_4^+ shows only a small discontinuity at the phase transition temperature in

Table 7.5: Crystal structure data and refinement results for SrLaZnRuO$_6$ and SrLaMgRuO$_6$ from NPD using $R\bar{3}$ space group, at 1173 K and 773 K, respectively.

Reliability factors	Lattice parameters	Atom	Site	x	y	z	B_{iso} (Å^2)	Occ
SrLaZnRuO$_6$, T=1173 K								
R_p = 3.712%	a= 5.6540(1) Å	Ru	3a	0	0	0	1.32(3)	1
R_{wp}= 5.35%	c= 13.7860(4) Å	Zn	3b	0	0	0.5	1.32(3)	1
R_{exp}= 5.78%	γ= 120°	Sr/La	6c	0	0	0.2523(9)	2.69(4)	0.5/0.5
R_{Bragg}= 9.60%	V= 381.67(2) Å^3	O1	18f	0.661(2)	0.8724(9)	0.0778(6)	3.68(3)	1
Rhombohedral axis: a_r=5.6368(1) Å, α_r=60.20(1)°								
SrLaMgRuO$_6$, T=773 K								
R_p = 2.82%	a= 5.6055(3) Å	Ru	3a	0	0	0	0.44(5)	1
R_{wp}= 3.77%	c= 13.667(1) Å	Mg	3b	0	0	0.5	0.44(5)	1
R_{exp}= 6.40%	γ= 120°	Sr/La	6c	0	0	0.251(2)	2.3(1)	0.5/0.5
R_{Bragg}= 11.62%	V= 371.89(4) Å^3	O1	18f	0.655(4)	0.872(2)	0.080(1)	2.08(7)	1
Rhombohedral axis: a_r=5.588(1) Å, α_r=60.20(3)°								

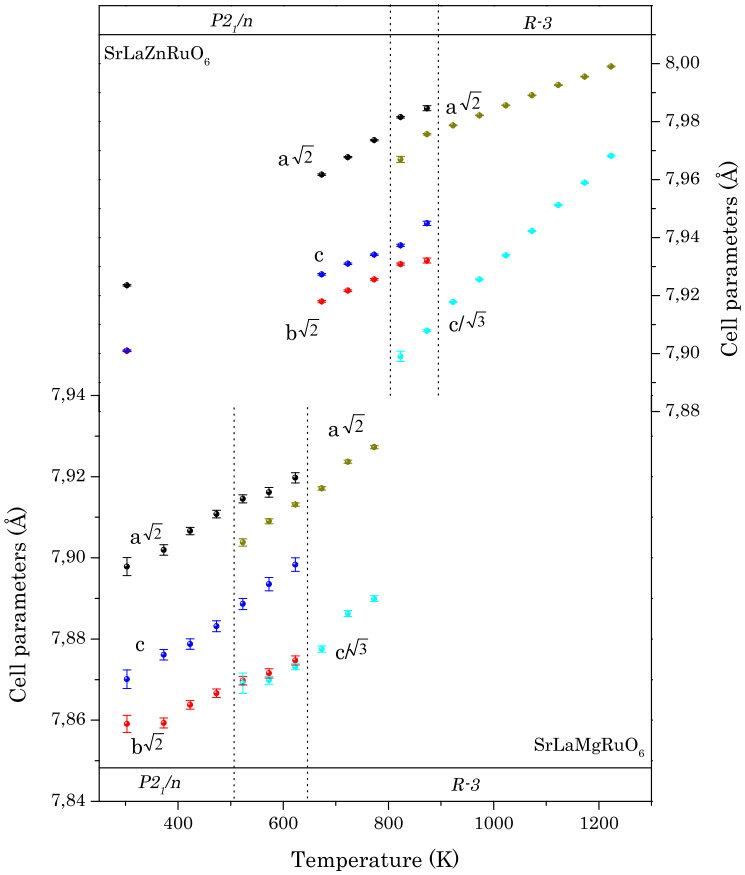

Figure 7.7: Variation of the cell parameters for $SrLaZnRuO_6$ and $SrLaMgRuO_6$ with the temperature. Dashed lines indicate the coexistence temperature range between $P2_1/n$ and $R\bar{3}$ phases.

$SrLaMgRuO_6$ and varies almost continuously in $SrLaZnRuO_6$ (see Figure 7.8). It should be mentioned that the discontinuous character of the phase transition is originated by the change of the rotation direction of the octahedra and that there is no physical restriction on the variation of the rotation angle, which can be continuous. Such continuous variation is observed for the title compounds.

The phase diagram (phase transition temperatures *vs*. tolerance factors) of several $SrLnMRuO_6$ compounds is presented in Figure 7.10. From this figure it can be concluded that there are two phase transition sequences possible depending on the size of the lanthanide cations. The Nd^{3+} cation has the smallest ionic radii among the three lanthanides (Nd,Pr,La) and the compounds of the type $SrNdMRuO_6$ undergo a $P2_1/n \rightarrow P4_2/n \rightarrow Fm\bar{3}m$ phase transition sequence [120]. The rest of the compounds, with lanthanum (present work and [116]) and praseodymium cations [125], show a trigonal intermediate phase and higher transition temperatures compared to the $SrNdMRuO_6$ compounds.

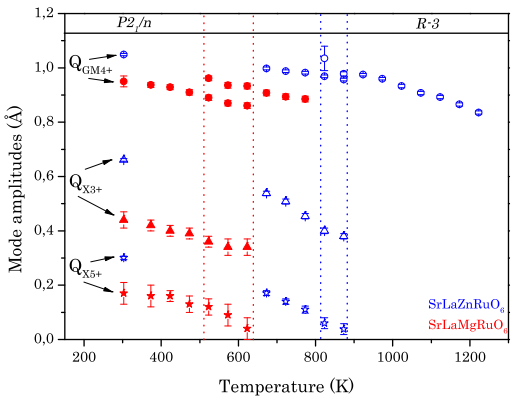

Figure 7.8: Temperature evolution of the GM_4^+, X_3^+ and X_5^+ mode amplitudes, as obtained from refinement of the NPD data for $SrLaZnRuO_6$ (blue, opened symbols) and $SrLaMgRuO_6$ (red, closed symbols). Dashed lines indicate the temperature range of coexistence between the $P2_1/n$ and $R\bar{3}$ phases.

Figure 7.10 also shows a common trend among the compounds included there. The materials with more distorted structures at RT (larger amplitudes of the distortion modes) show higher transition temperatures.

In [116] the authors observed a range of co-existence of two phases (monoclinic and trigonal) in the case of $SrLaCuRuO_6$ and $SrLaNiRuO_6$. The same effect have been observed for the compounds in the present work and also for other double perovskites. For example, Narayanan *et al*. in [127] reported for $SrLaCoIrO_6$ two different monoclinic phases $P2_1/n$ and $I2/m$ co-existing over a broad temperature range (∼300 K). Sayed *et al*. [128] and Faik *et al*. [122] reported the coexistence of $P2_1/n$ and $R\bar{3}$ phases for La_2NiMnO_6 and Sr_2LnSbO_6 (Ln=La,Sm), respectively.

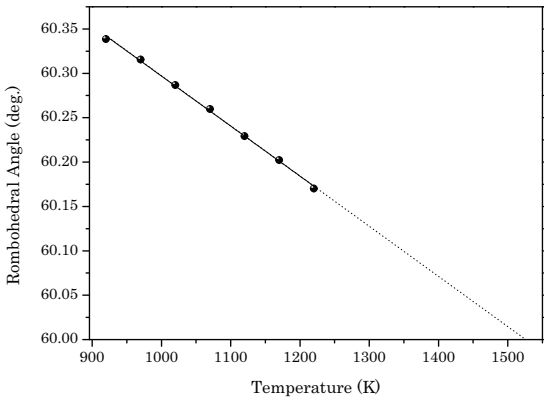

Figure 7.9: Temperature dependence of the rhombohedral angle α for $SrLaZnRuO_6$. The solid line is a linear fit to the experimental points data (follows α=60.86(1)-5.6(1)E^{-4}T equation) and the dashed line an extrapolation to α=60°, T_C≈1535 K.

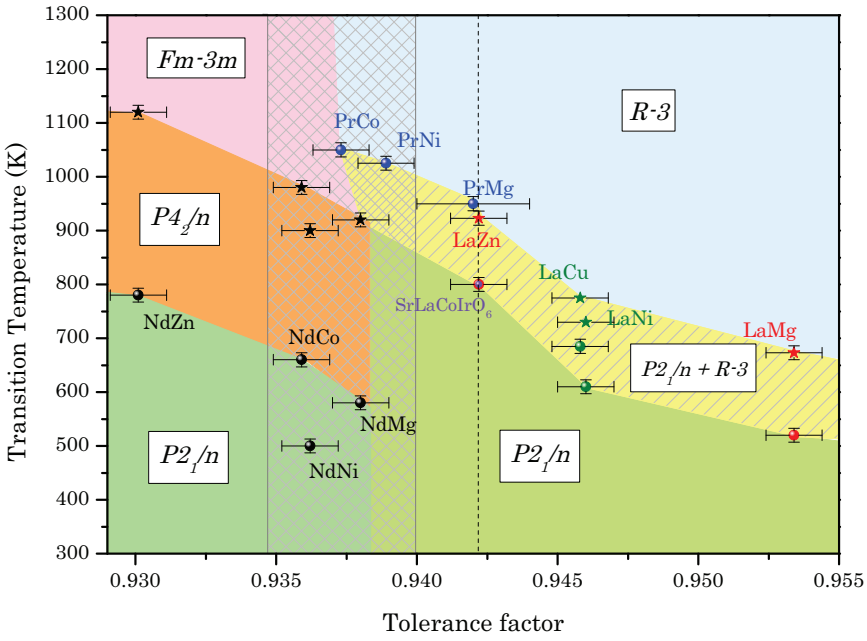

Figure 7.10: Experimentally calculated tolerance factor and temperature dependence phase diagram of $SrLaMRuO_6$ (M=Zn[PW],Cu[116],Mg[PW],Ni[116]), $SrNdMRuO_6$ (M=Zn,Co,Mg,Ni) [120] and $SrPrMRuO_6$ (M=Co,Mg,Ni) [125]. PW stands for present work. Two green tonality are used in $P2_1/n$ phase to distinguish the different transition sequences. Two-phase region separating $P2_1/n$ from $R\bar{3}$ is shown in striped-yellow area. Grilled area highlights two phase transition overlapped area. Vertical dotted line is indicative of the same theoretical tolerance factor for $SrLaZnRuO_6$ and $SrLaCoIrO_6$ [127].

7.3 Conclusions

A combination of X-ray and high-resolution neutron powder diffraction techniques has been used to investigate the structures and phase transitions in SrLaZnRuO$_6$ and SrLaMgRuO$_6$. The structures of the room temperature phases for both compounds have been proposed as monoclinic, with the space group $P2_1/n$. Symmetry-mode decomposition of the room temperature structures shows that the structures are dominated by GM_4^+ and X_3^+ distortion modes and to a lesser extent by X_5^+. Tolerance-factors *vs*. room temperature distortion mode amplitudes calculations for present work compounds and other compounds of the Sr$Ln$$MRuO_6$ family [111, 115, 116, 120, 125] have been done. We have observed that the bigger B-site cation, the bigger the distortion mode amplitude; and smaller the A-site cation, bigger the distortion mode amplitude.

Phase transition analysis was done by use of NPD. $P2_1/n \rightarrow R\bar{3}$ sequence was observed in both compounds, with a co-existence range of 150 K, beginning at about 800 K for SrLaZnRuO$_6$ and 500 K for SrLaMgRuO$_6$. Such transition sequence has been reported also for other ruthenium compounds [116, 125].

For Sr$Ln$$MRuO_6$ (Ln=La,Nd,Pr; M=Zn,Co,Cu,Mg,Ni) [116, 120, 125] different phase transition behaviors have been observed in the phase diagram depending on A-site cation size: Nd, $P2_1/n \rightarrow P4_2/n \rightarrow Fm\bar{3}m$; La, $P2_1/n \rightarrow P2_1/n + R\bar{3} \rightarrow R\bar{3}$; Pr, $P2_1/n \rightarrow R\bar{3}$. Among the compounds undergoing each of the phase transitions higher transition temperatures have been observed for the compound with larger distortion mode amplitudes (more distorted structures).

Chapter 8

Sr$Ln$$MRuO_6$ (Ln=La,Pr,Nd; M=Co,Ni) Magnetic Structure Models

In addition to the nuclear reflections, a series of magnetic diffraction peaks are observed for $SrLaCoRuO_6$, $SrPrCoRuO_6$, $SrPrNiRuO_6$, $SrNdCoRuO_6$ and $SrNdNiRuO_6$ materials in the neutron diffraction patterns. The data were collected in D1B (ILL, Grenoble) with λ=2.52 Å [1] from 4 K to 135 K. Comparing 135 K and room temperature diffraction patterns, the magnetic diffraction peaks are nonexistent at both temperatures; only thermal expansion is observed, which indicates that neither structural nor magnetic phase transition takes place over the interval. As can be perceive at Figure 8.1 the magnetic peak intensities decrease to zero at very similar temperatures for all samples in 70-90 K temperature range. These peak are indexed by a magnetic propagation vector (1/2,0,1/2) for all materials.

The compounds are ordered double perovskites with Sr and Ln (La, Nd or Pr) in A and A'-site of the perovskite (Wyckoff position 4e); while Co or Ni are placed in B-site (Wyckoff position 2b) and Ru cations in B'-site (Wyckoff position 2a). It is worth mentioning that among the studied lanthanides, neodymium and praseodymium cations are magnetic at very low temperatures, nevertheless not the lanthanum Table 1.2. Although the magnetic nature of the neodymium atom the experimentally studied temperature range is above the ordering temperature; thus, the neodymium atom will be considered as non-magnetic atom.

[1] D1B instrument is operated with a wavelength of 2.52 Å produced by a high mosaicity pyrolytic graphite monochromator; even when in order to avoid the high order contaminations a set of filters are installed between monochromator and sample, a non-negligible amount of $\lambda/2$ contamination is observed in some cases (ca. 0.3%).

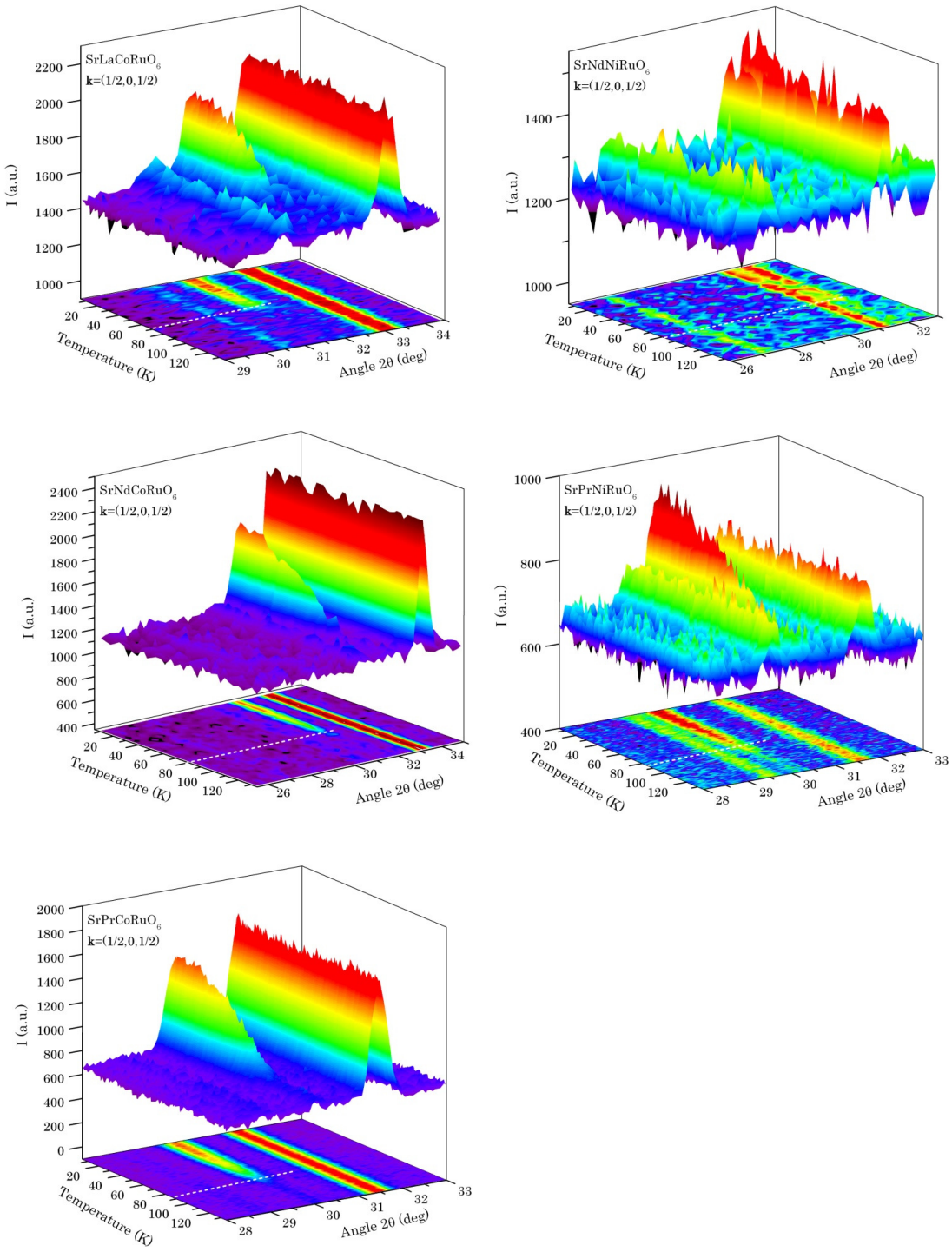

Figure 8.1: Thermal variation of the NPD patterns acquired with λ=2.52 Å in the temperature range 10< T <135 K of a) SrLaCoRuO$_6$ (T=≈70 K), b) SrNdCoRuO$_6$ (T=≈80 K), c) SrPrCoRuO$_6$ (T=≈85 K), d) SrNdNiRuO$_6$ (T=≈80 K) and e) SrPrNiRuO$_6$ (T=≈85 K).

The possible magnetic structures compatible with the space group symmetry were determined by the representation analysis described by Bertaut [129]. For that purpose BASIREPS (included in the FullProf Suite [85]) and Sarah [130] were used. The magnetic representation Γ_M for each magnetic site can be decomposed as direct sum of irreps by applying the great orthogonality theorem.

$$\Gamma_{M,2a} = 3\Gamma_1 \oplus 3\Gamma_3 \tag{8.1}$$

$$\Gamma_{M,2b} = 3\Gamma_2 \oplus 3\Gamma_4 \tag{8.2}$$

$$\Gamma_{M,4e} = 3\Gamma_1 \oplus 3\Gamma_2 \oplus 3\Gamma_3 \oplus 3\Gamma_4 \tag{8.3}$$

The decomposition of the magnetic representations for *Ln*, Co(Ni) and Ru sites, and their associated basis vectors are given in Table 8.1. The lanthanum and neodymium containing compounds have two magnetic sites (2*a* and 2*b*); nevertheless SrPr*M*RuO$_6$ compounds have three magnetic sites (2*a*, 2*b* and 4*e*), which makes such a complex magnetic structure. Cobalt/niquel atoms (site 2*b*) related by (1/2,1/2,1/2) translation vector can have their spins arranged in two possible ways, corresponding to the irreducible representation (irrep) $\Gamma_{M,2b}$=Γ_2 or Γ_4. Ru atoms in site 2*a* related by the same translation vector can have their moments arranged according to Γ_1 or Γ_3; and for the praseodymium ion in site 4*e*, the possible irreducible representations are: Γ_1, Γ_2 , Γ_3 or Γ_4.

For SrLaCoRuO$_6$ compound, the magnetic representations for 2*a* and 2*b* sites have the same basis vectors and therefore describes essentially the same magnetic structure. The symmetry allowed models were refined using the FullProf program to obtain the final

Table 8.1: Basis vectors of Γ_1, Γ_2, Γ_3, and Γ_4 irreducible representations for the sites Co or Ni(2*b*)=(0,0,1/2), Ru(2*a*)=(0,0,0) and Pr(4*e*)=($\simeq$0,$\simeq$1/2,$\simeq$3/4).

Basis vectors		(1)	(2)	(3)	(4)	(5)
Γ_1	Ru (2*a*)	{(100),(010),(001)}	{(-100),(010),(00-1)}			
	Pr (4*e*)	{(100),(010),(001)}		{(100),(0-10),(001)}	{(100),(010),(001)}	{(100),(0-10),(001)}
Γ_2	*M* (2*b*)	{(100),(010),(001)}	{(-100),(010),(00-1)}			
	Pr (4*e*)	{(100),(010),(001)}		{(100),(0-10),(001)}	{(-100),(0-10),(00-1)}	{(-100),(010),(00-1)}
Γ_3	Ru (2*a*)	{(100),(010),(001)}	{(100),(0-10),(001)}			
	Pr (4*e*)	{(100),(010),(001)}		{(-100),(010),(00-1)}	{(100),(010),(001)}	{(-100),(010),(00-1)}
Γ_4	*M* (2*b*)	{(100),(010),(001)}	{(100),(0-10),(001)}			
	Pr (4*e*)	{(100),(010),(001)}		{(-100),(010),(00-1)}	{(-100),(0-10),(00-1)}	{(100),(0-10),(001)}

(1):x, y, z; (2):$-x+\frac{1}{2}, y+\frac{1}{2}, -z+\frac{1}{2}$; (3):$-x+\frac{1}{2}, y-\frac{1}{2}, -z+\frac{3}{2}$; (4):$-x+1, -y+1, -z+1$; (5):$x+\frac{1}{2}, -y+\frac{3}{2}, z-\frac{1}{2}$

Table 8.2: Magnetic representations, magnetic moments at 4 K, for Co and Ru atoms, and w_{RP} values (multipattern refinement) for four magnetic structure models for SrLaCoRuO$_6$. Graphical representation in Figure 8.2.

	$\Gamma_1 \oplus \Gamma_2$		$\Gamma_3 \oplus \Gamma_2$		$\Gamma_1 \oplus \Gamma_4$		$\Gamma_3 \oplus \Gamma_4$	
Cation	Ru	Co	Ru	Co	Ru	Co	Ru	Co
μ_x (μ_B)	0.1(1)	1.4(1)	-0.0(1)	1.4(1)	-0.0(1)	1.3(1)	1.1(1)	1.1(1)
μ_y (μ_B)	0	0	0	0	0	0	0	0
μ_z (μ_B)	-0.8(1)	-1.3(1)	-0.8(1)	-1.3(1)	-0.9(1)	1.3(1)	-0.2(1)	1.4(1)
μ_T (μ_B)	0.8(1)	0.8(1)	0.8(1)	1.9(1)	0.9(1)	1.9(1)	1.1(1)	1.8(1)
w_{RP} (%) (pattern 1)	25.2		25.7		25.7		25.4	
w_{RP} (%) (pattern 2)	16.6		17.3		17.3		17.1	

pattern 1: D1B old detector, 2θ=19-98°; pattern 2: D1B new detector, 2θ=0.8-128°

solutions for the magnetic structure: $3\Gamma_1 \oplus 3\Gamma_2$, $3\Gamma_1 \oplus 3\Gamma_4$, $3\Gamma_3 \oplus 3\Gamma_2$ or $3\Gamma_3 \oplus 3\Gamma_4$. Non of the previously mentioned symmetry allowed models (6 degrees of freedom) converge during the refinement process, and big oscillations were observed along refinement steps. In $3\Gamma_1 \oplus 3\Gamma_2$ model, for example, μ_y for site 2*a* is near zero and μ_x and μ_z have comparable magnitudes. Moreover, Bos *et al*. in [115] discussed the magnetic structure of SrLaCoRuO$_6$ material. They observed that the moments lie in the (010) plane, and Co moment were founded to be perpendicular to the Ru moments in all refined models. In the final attempt μ_y was set to zero for all models to guarantee the convergence and obtain more precise values for μ_x and μ_z. The final results are gathered in Table 8.2. For any model, the magnitude of Co and Ru moments are very highly correlated, so that refinements with Co and Ru models, or the refinements with spin only at Co or Ru, gave equivalent fits. Actually, there are too many degrees of freedom for the poor magnetic signal in comparison with the dominant nuclear contributions, and there is no chance to elucidate among the models given by the group theory Figure 8.2.

The Rietveld refinement of the diffraction data with magnetic models for SrPrMRuO$_6$ (M=Co,Ni) at very low temperatures is even more tricky than for Sr$Ln M$RuO$_6$ (Ln=La,Nd; M=Co,Ni) structures, since there are nine degrees of freedom. As could be observed in Figure 8.3, the signal of the magnetic structure after interaction with neutrons is similar for all Co compounds, and decreases for Ni containing materials. In fact, it would not be rare to think that if it was difficult (restrains are necessary) to obtained the correct magnetic structure model for SrLaCoRuO$_6$, it would be even more difficult in these cases.

The decomposition of the magnetic representations for SrPrMRuO$_6$ (M=Co,Ni) allows sixteen possible magnetic models (combination of the possible magnetic represen-

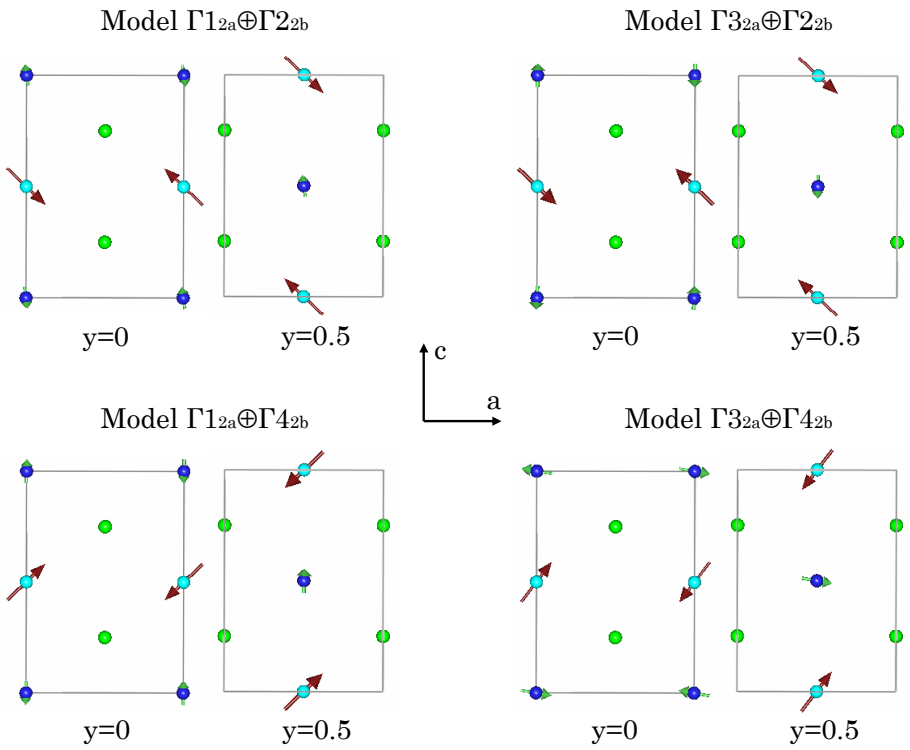

Figure 8.2: Spin directions in a fitted magnetic models for $SrLaCoRuO_6$. The moments lie in the (010) plane. Co/Ru atoms are shown as light/dark blue balls; green balls represent Sr/La atoms. Oxygen atoms have been omitted for clarity. The atoms are shown in the nuclear cell; magnetic propagation vector (1/2,0,1/2).

tations for each magnetic site, eq.8.1, eq.8.2, eq.8.3). Although all models were tried as possible to describe the studied magnetic structure, none of them gave suitable solution. Too many restrains were necessary to reach, with some models, the convergence point. The result obtained with one of those models is shown in Figure 8.4.

We attempted to determine the magnetic structures by using representation analysis, and the data refinement by different magnetic models, but all attempts failed due to low magnetic intensities in comparison with the dominant nuclear contributions. Many restrains were necessary to obtain suitable models.

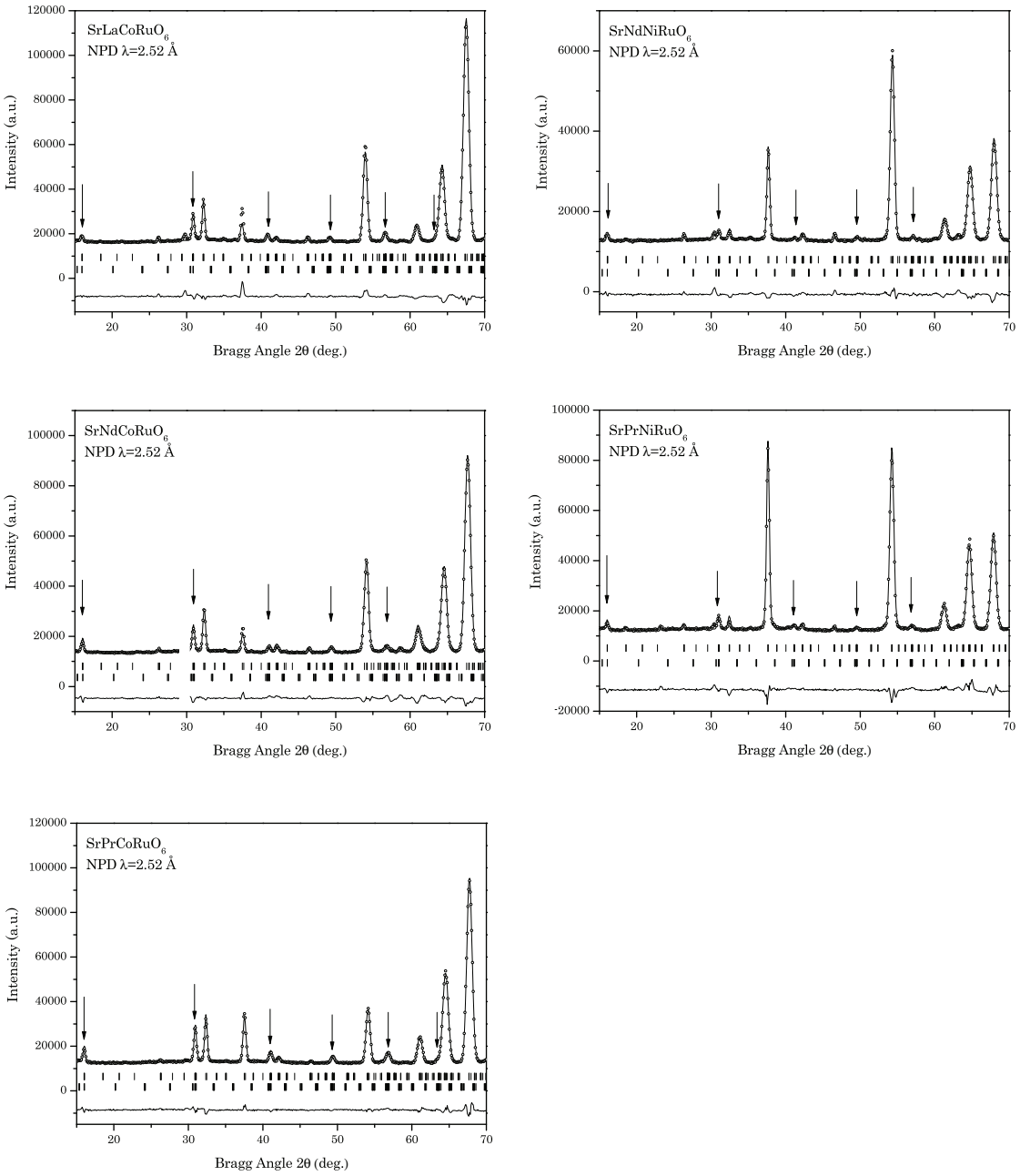

Figure 8.3: Observed (circles), calculated (full line), and difference NPD (D1B, λ=2.52 Å) Rietveld profiles for SrLaCoRuO$_6$, SrNdCoRuO$_6$, SrPrCoRuO$_6$, SrNdNiRuO$_6$ and SrPrNiRuO$_6$ at 4 K. Reflection markers correspond to the positions of Bragg reflections of crystal structure (up) and magnetic structure (bottom). The magnetic reflections are marked with the arrow.

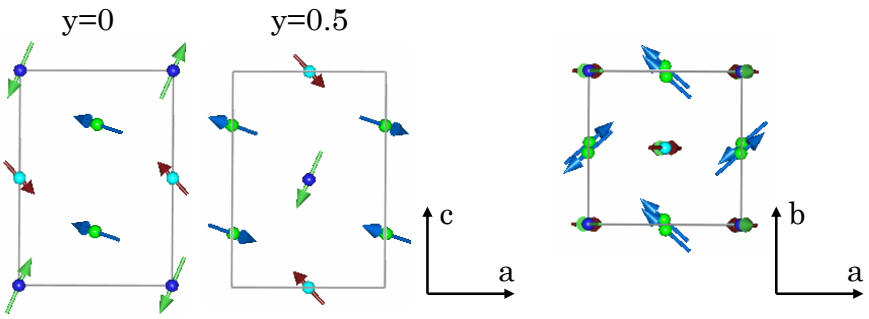

Figure 8.4: Possible magnetic model of the final refined ($3\Gamma1_{2a} \oplus 3\Gamma2_{2b} \oplus 3\Gamma1_{4e}$) magnetic structure for $SrPrCoRuO_6$ at 4 K. $\mu_{y(Co,Ru)}$=0 was set in order to guarantee the convergence of the model ($\mu_{TOT,Pr}$=1.201 μ_B, $\mu_{TOT,Co}$=0.326 μ_B, $\mu_{TOT,Ru}$=2.810 μ_B). Sr/*Ln* green circles, blue vectors; Co, light blue circles, brown vectors; and Ru dark blue circles, green vectors. The atoms are shown in the nuclear cell; magnetic propagation vector (1/2,0,1/2).

Chapter 9

SrLnFeRuO$_6$ (Ln=La,Nd,Pr) disordered double perovskites

9.1 Room temperature Structures

Room temperature (RT) powder-diffraction data for SrLaFeRuO$_6$, SrPrFeRuO$_6$ and SrNdFeRuO$_6$, obtained by X-ray powder diffraction (XRPD), are shown in Figure 9.1. In the insets of Figure 9.1 the positions of the B/B' ordering superstructure reflections are marked around 2θ=19.5° with arrows, making clear the absence of such reflections. This fact indicates that these compounds do not present an ordered arrangement of the B-site cations, and, therefore, only space groups allowing disorder were considered [51]. In fact, the orthorhombic *Pbnm* space group has been proposed for the RT structure of SrLaFeRuO$_6$ compound [114]; hence, we used this space group as the starting model for our refinements. After the XRPD data refinement, *Pbnm* (ITA No. 62 non-standard setting of *Pnma*) space group should be assigned to SrLaFeRuO$_6$, SrPrFeRuO$_6$ and SrNdFeRuO$_6$ compounds.

The structures of the title compounds were refined from neutron powder diffraction (NPD) data in the *Pbnm* space group Figure 9.2, with the unit cell parameters chosen as $a \sim b \sim \sqrt{2}a_p$, $c \sim 2a_p$ (a_p is the cubic archetype simple perovskite cell parameter) and with the following atomic positions: Sr/Ln 4c (x,y,1/4), Fe/Ru 4a (0,1/2,0), O1 4c (x,y,1/4) and O2 8d (x,y,z).

The intensity of some of the reflections was not possible to fit properly by the orthorhombic structural model; and a magnetic model was necessary to be included at RT

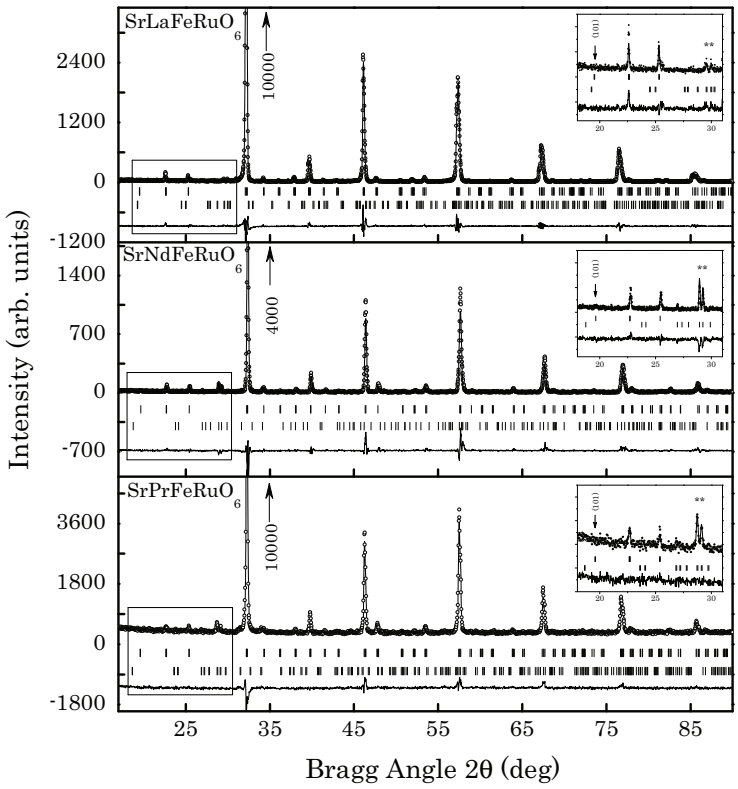

Figure 9.1: Experimental (symbols) and calculated (line) X-ray powder-diffraction profiles for the Rietveld refinement of SrLnFeRuO$_6$ (Ln=La,Nd,Pr) at room temperature, using a disordered orthorhombic (*Pbnm*) structural model. The upper (lower) markers indicate the position of the structural SrLnFeRuO$_6$ (impurity: La_3RuO_7, Nd_3RuO_7 and Pr_3RuO_7) Bragg reflections. The inset shows the absence of the superstructure reflection, indicated with an arrow. * indicates the impurity.

(see section 9.3). The detailed information of the refinements is given in Table 9.1.

Table 9.2 lists selected interatomic distances and bond angles. The average <Fe/Ru-O> bond-lengths in the octahedra are 1.991(2), 1.994(2) and 1.993(2), for SrLaFeRuO$_6$, SrPrFeRuO$_6$ and SrNdFeRuO$_6$, respectively. These values are close to 2.03 Å the distance calculated from the effective ionic radii [48] for Fe/Ru-O. The Sr^{2+}/Ln^{3+} cations are located in the cavities formed by the corner-sharing Fe/RuO$_6$ octahedra. The average <Sr/Ln-O> distances, shown in Table 9.2, are typical for Sr^{2+}/Ln^{3+} disordered cations in a nine-fold coordination. The Bond-valence Sum method [86] allowed us to have an estimation of the oxidation states of the Fe and Ru cations. The calculated valences, shown in Table 9.2, suggest that Fe is trivalent and Ru is present in a tetravalent oxidation state. Regarding the Sr/Ln-O distances, there is no notable difference among the three compounds; with a slightly larger distance for Sr/La-O, caused by the bigger size of La cation. Being bigger induces a smaller tilt in the octahedra, which in turn, increases the distance. The

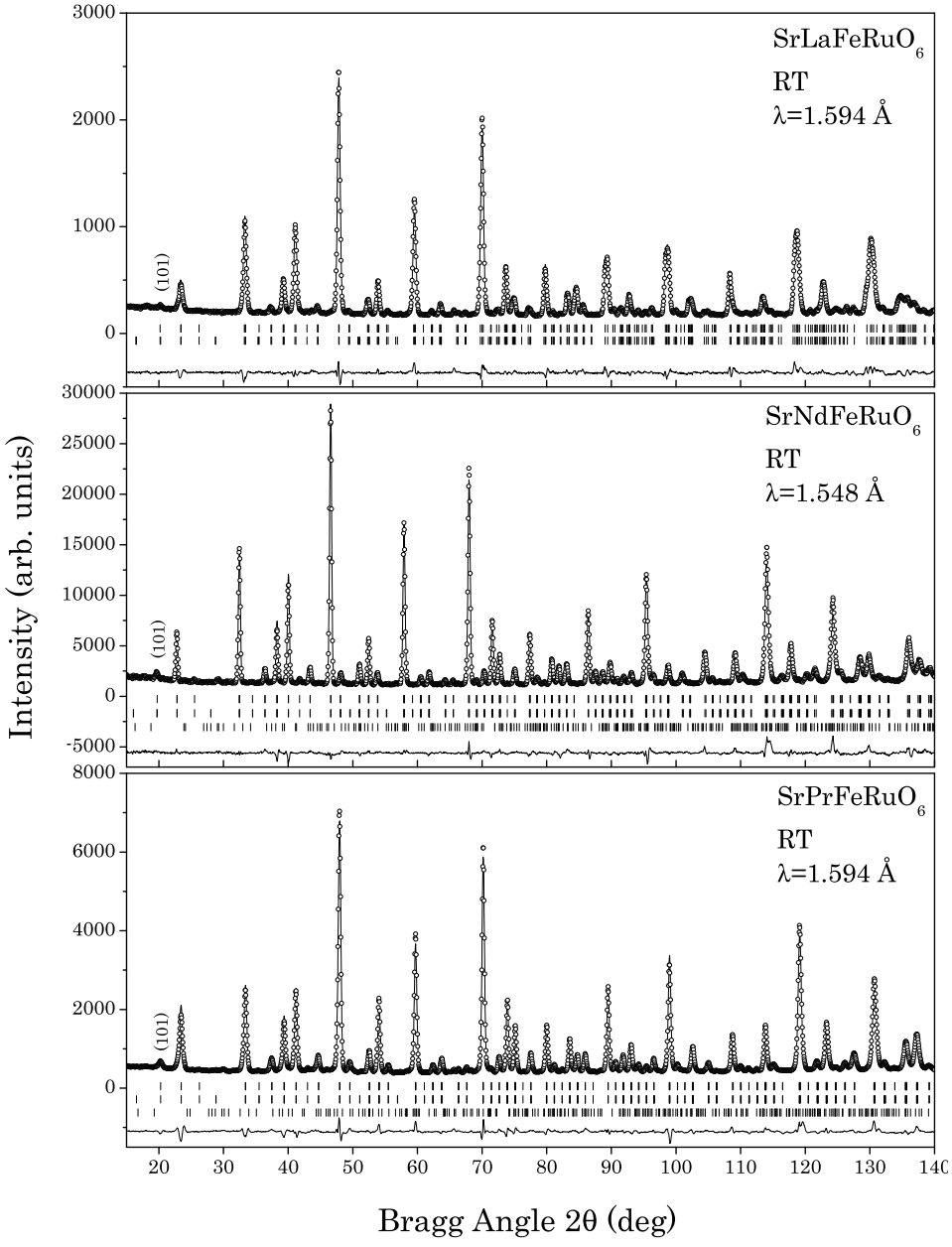

Figure 9.2: Experimental (symbols) and calculated (line) neutron powder-diffraction profiles for the Rietveld refinement of Sr*Ln*FeRuO$_6$ (*Ln*=La,Nd,Pr) at room temperature, using a disordered orthorhombic (*Pbnm*) structural model. The upper (middle) markers indicate the position of the structural (magnetic) Bragg reflections and the lower markers the impurity (Nd_3RuO_7 and Pr_3RuO_7) Bragg reflections. La_3RuO_7 impurity was excluded in order to guarantee the convergence of the refinement.

Table 9.1: Structural details of SrLaFeRuO6, SrPrFeRuO$_6$ and SrNdFeRuO$_6$ obtained at room temperature from NPD data using *Pbnm* structural model, refining all mode amplitudes. The B_{iso} value for Fe/Ru cations was fixed in 0.5 Å in order to guarantee the convergence of the refinement.

		SrLaFeRuO$_6$	SrPrFeRuO$_6$	SrNdFeRuO$_6$
Instrument		D2b (ILL)	D2b (ILL)	Spodi (FRMII)
Sr/Ln	4c (x,y,1/4)			
	x	0.0000(9)	0.001(1)	0.0023(7)
	y	-0.0166(6)	-0.0245(5)	-0.0294(3)
	B_{iso}(Å^2)	0.66(3)	0.56(3)	0.24(2)
Fe/Ru	4a (0,1/2,0)			
	B_{iso}(Å^2)	0.5	0.5	0.5
O1	4c (x,y,1/4)			
	x	-0.0661(7)	-0.0790(5)	-0.0837(5)
	y	0.507(1)	0.5096(7)	0.5089(6)
	B_{iso}(Å^2)	0.89(2)	0.81(2)	0.67(2)
O2	8d (x,y,z)			
	x	0.7277(5)	0.7223(5)	0.7229(4)
	y	0.2719(5)	0.2784(5)	0.2790(4)
	z	0.5289(3)	0.5291(3)	0.5298(3)
	B_{iso}(Å^2)	0.89(2)	0.81(2)	0.67(2)
a (Å)		5.5752(2)	5.5477(2)	5.5357(2)
b (Å)		5.5463(2)	5.5463(2)	5.5432(2)
c (Å)		7.8557(3)	7.8390(2)	7.8257(3)
V (Å^3)		242.91(2)	241.20(2)	240.13(1)
R_p(%)		3.76	3.84	4.70
R_{wp}(%)		4.78	4.88	6.31
R_{exp}(%)		6.10	3.81	2.29
R_{Bragg}(%)		5.53	4.70	7.49

higher variation for the Fe/Ru-O bond-length values reported in [114] for SrLaFeRuO$_6$, could be due to the experimental method used in [114], (XRPD): the scattering power of oxygen atoms compared to the rest of the cations of the structure is low for X-rays and, hence, the lower is the reliability of the oxygen positions compared to the ones from NPD.

The mode decomposition (Table 9.3) suggests that there are five irreducible representations (irreps) of the $Pm\bar{3}m$ space group that take part in the symmetry breaking from that space group to the RT *Pbnm* orthorhombic space group: $R_4^+(1)$, $R_5^+(2)$, $X_5^+(2)$, $M_2^+(1)$ and $M_3^+(1)$. The numbers in parenthesis indicate the number of modes transforming according to each irrep. There are 7 modes in total. For each mode we indicate the atom it involves with its corresponding Wyckoff position in the reference structure. From the seven modes, 5 involve the oxygen atoms (3d) and the other 2 modes, Sr/Ln atoms (1b).

Table 9.2: Bond lengths (Å), octahedra tilt angles (°) selected angles (°) and bond-valence sum for Sr*Ln*FeRuO$_6$ (*Ln*=La,Pr,Nd) at room temperature obtained from NPD data using *Pbnm* structural model and refining all mode amplitudes. Sr/*Ln*-O distance in nine coordination is chosen since it is the highest coordination number available for all tabulated rare-earths.

	SrLaFeRuO6	SrPrFeRuO6	SrNdFeRuO6
Sr/*Ln*-O1(×1)	2.668(7)	2.621(5)	2.603(4)
Sr/*Ln*-O1(×1)	2.927(7)	2.995(5)	3.022(4)
Sr/*Ln*-O1(×1)	2.423(6)	2.347(7)	2.327(5)
Sr/*Ln*-O1(×1)	3.159(6)	3.213(7)	3.225(5)
Sr/*Ln*-O2(×2)	3.109(4)	3.161(4)	3.180(3)
Sr/*Ln*-O2(×2)	2.544(4)	2.525(4)	2.527(3)
Sr/*Ln*-O2(×2)	2.791(4)	2.741(4)	2.734(3)
Sr/*Ln*-O2(×2)	2.707(4)	2.710(5)	2.683(3)
$<$Sr/*Ln*-O2(×2)$>_{coord.9}$	2.68(1)	2.66(1)	2.65(1)
Tilt angle $\psi_{[001]P}$	5.05(7)	6.37(6)	6.39(5)
Tilt angle $\phi_{[110]P}$	10.70(1)	12.71(1)	13.48(1)
Fe/Ru-O1$_{ax}$(×2)	1.999(1)	2.009(1)	2.011(1)
Fe/Ru-O2$_{eq}$(×2)	1.984(3)	1.989(3)	1.992(2)
Fe/Ru-O2$'_{eq}$(×2)	1.989(3)	1.984(3)	1.977(2)
Average distance	1.99(1)	1.99(1)	1.99(1)
∠O1$_{ax}$-Fe/Ru-O2$_{eq}$	89.1(1)	87.7(1)	87.2(1)
∠O1$_{ax}$-Fe/Ru-O2$'_{eq}$	91.2(1)	92.5(1)	92.7(1)
∠O2$_{eq}$-Fe/Ru-O2$'_{eq}$	91.0(1)	90.8(1)	90.8(1)
∠Fe/Ru-O1$_{ax}$-Ru/Fe	158.6(2)	154.6(2)	153.2(2)
∠Fe/Ru-O2$_{eq}$-Ru/Fe	163.5(2)	161.6(2)	161.4(2)
Bond-Valence sum			
Fe	3.21(1)	3.18(1)	3.19(1)
Ru	3.93(1)	3.90(1)	3.90(1)

Theoretical considerations show [52, 92, 131] that there is no single irrep that breaks the symmetry from $Pm\bar{3}m$ to *Pbnm*. At least two modes are needed: R_4^+ and M_3^+. These necessary symmetry-breaking modes should be the most intense ones. The other modes appear as additional degrees of freedom allowed by symmetry. These secondary modes reduce the symmetry into intermediate symmetries (see Figure 9.3), never to the space group of the low symmetry phase.

Table 9.3: Summary of the *irreps* involved in the symmetry breaking from the totally symmetric, cubic, space group ($Pm\bar{3}m$) to the room temperature $Pbnm$ orthorhombic space group and $R\bar{3}c$ trigonal space group.The list is part of the output of the AMPLIMODES for FullProf. The number in parenthesis indicate the number of modes transforming according to the irrep.

Atoms	WP	Modes
$Pm\bar{3}m \rightarrow Pbnm$		
O1	3d	$R^{4+}(1)$ $R^{5+}(1)$ $X^{5+}(1)$ $M^{2+}(1)$ $M^{3+}(1)$
Sr1/Ln1	1b	$R^{5+}(1)$ $X^{5+}(1)$
$Pm\bar{3}m \rightarrow R\bar{3}c$		
O1	3d	$\mathbf{R^{4+}(1)}$

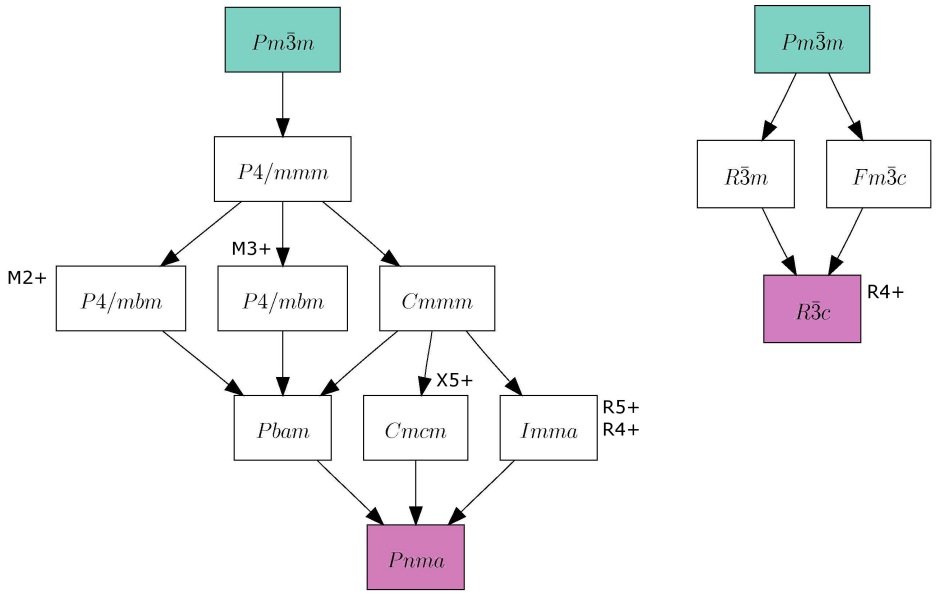

Figure 9.3: Graph of maximal subgroups relating the space group of the archetype (high lighted in blue) and distorted $Pbnm$ and $R\bar{3}$ phase (high lighted in pink) of SrLnFeRuO$_6$. For each subgroup any irrep yielding this symmetry is indicated.

Table 9.4: NPD data refinement results for the amplitudes (in Å) of irreps taking part in the symmetry breaking from $Pm\bar{3}m$ space group to the room temperature *Pbnm* orthorhombic space group, refining (a) all the modes and (b) 3 and (c) 2 highest amplitudes modes for Sr*Ln*FeRuO6 (*Ln*=La,Pr,Nd) compounds.

Irrep	Isotropy subgroup	Dim	Amplitude								
			LaFe			PrFe			NdFe		
			(a)	(b)	(c)	(a)	(b)	(c)	(a)	(b)	(c)
R_4^+	*Imma* (74)	1	0.980(4)	0.974(4)	0.971(4)	1.085(4)	1.047(3)	1.045(4)	1.133(4)	1.086(4)	1.089(6)
R_5^+	*Imma* (74)	2	0.07(1)	0.00	0.00	0.165(7)	0.00	0.00	0.193(7)	0.00	0.00
X_5^+	*Cmcm* (63)	2	0.201(8)	0.195(8)	0.00	0.294(6)	0.266(6)	0.00	0.344(4)	0.327(4)	0.00
M_2^+	*P*4/*mbm* (127)	1	0.01(1)	0.00	0.00	0.01(1)	0.00	0.00	0.021(9)	0.00	0.00
M_3^+	*P*4/*mbm* (127)	1	0.494(7)	0.500(7)	0.522(7)	0.627(4)	0.674(4)	0.695(5)	0.627(5)	0.686(5)	0.736(7)
R_p(%)			3.76	3.79	4.08	3.84	3.95	4.52	4.70	5.17	6.72
R_{wp}(%)			4.78	4.84	5.27	4.88	5.10	5.98	6.31	6.75	9.45
R_{exp}(%)			6.10	6.11	6.11	3.81	3.81	3.81	2.29	2.30	2.30
R_{Bragg}(%)			5.53	5.75	6.54	4.70	5.82	6.90	7.49	9.00	12.0

K-vector: R_4^+ (1/2,1/2,1/2), R_5^+ (1/2,1/2,1/2), X_5^+ (0,1/2,0), M_2^+ (1/2,1/2,0), M_3^+ (1/2,1/2,0)
Direction: R_4^+ (0,a,a), R_5^+ (0,a,-a), X_5^+ (0,0,0,-a,0,0), M_2^+ (a,0,0), M_3^+ (a,0,0)

Looking at the amplitudes of the modes transforming according to the irreps in Table 9.4, it is clear that there are two global amplitudes (R_4^+ and M_3^+) that are higher than the rest. The X_5^+ is less than half the value of M_3^+; and R_5^+ and M_2^+ have negligible values. Despite the fact that, some of the amplitudes of these modes could be excluded from the refinement process, it has to be taken into account that the experimental data should be respected. And all the structural information in Table 9.1 and Table 9.5 has been obtained refining all the amplitudes. However, for some studies, like phase transition studies, the refinement can be simplified by using only some of the allowed degrees of freedom. To illustrate the effect of the reduction of degrees of freedom, three refinement attempts have been done, Table 9.4; (a) freed all mode amplitudes, (b) set up to zero the amplitudes of the modes transforming according to R_5^+ and M_2^+, and finally, (c) freed only R_4^+ and M_3^+ modes. The effect of the three approaches on the reliability factors of the refinements is clear: the more symmetric the structure at RT the smaller is the effect when R_5^+ and M_2^+ are set to zero (Table 9.4 (a) and (b)). This is clearly observed for SrLaFeRuO$_6$: all modes with amplitudes close to zero, could be nullified, with an increment in the R factors less than a 3%. For the other two compounds, which are less symmetric at RT, the effect of the reduction of refined mode amplitudes on the reliability factors is larger (increment of the R factors around 20%). Nevertheless, although the reduction of degrees of freedom increases the inaccuracy of atomic positions, the refinements done in this way could be enough to study the structural phase transitions. The third refinement attempt (c), suggests that although X_5^+ mode is not one of the active modes, it is necessary to describe the structure, and should be kept in the refinement.

The geometrical representation of the distortion modes, taking as reference the orthorhombic cell, are shown in Figure 9.4. R_4^+ mode, is essentially a rotation around the b axis; although it deforms slightly the octahedra: the displacement of the oxygen atoms in ab plane and the ones along c are not the same. R_5^+ is a bi-dimensional mode, acting on the oxygen atoms and on the A/A'-site cations. The main part of R_5^+-A2 distortion mode is a rotation along b axis, with the apical oxygen atoms displaced in the opposite direction to the rotation. R_5^+-A3 displaces the A/A'-site cations along the a axis. The mode transforming according to X_5^+ is bi-dimensional, acting on the oxygen atoms and on the A/A'-site cations. X_5^+-A4, displaces the apical oxygen atoms along the b axis; and X_5^+-A5, the A/A'-site cations along b. M_2^+ mode acts on the equatorial oxygen atoms, deforming into a rhombus the square formed by them. Finally, M_3^+ is a pure rotation of the octahedra around the c axis.

The physical interpretation of the modes taking part in the symmetry breaking is the tilting of the octahedra. If the values of the mode amplitudes are small and are defined

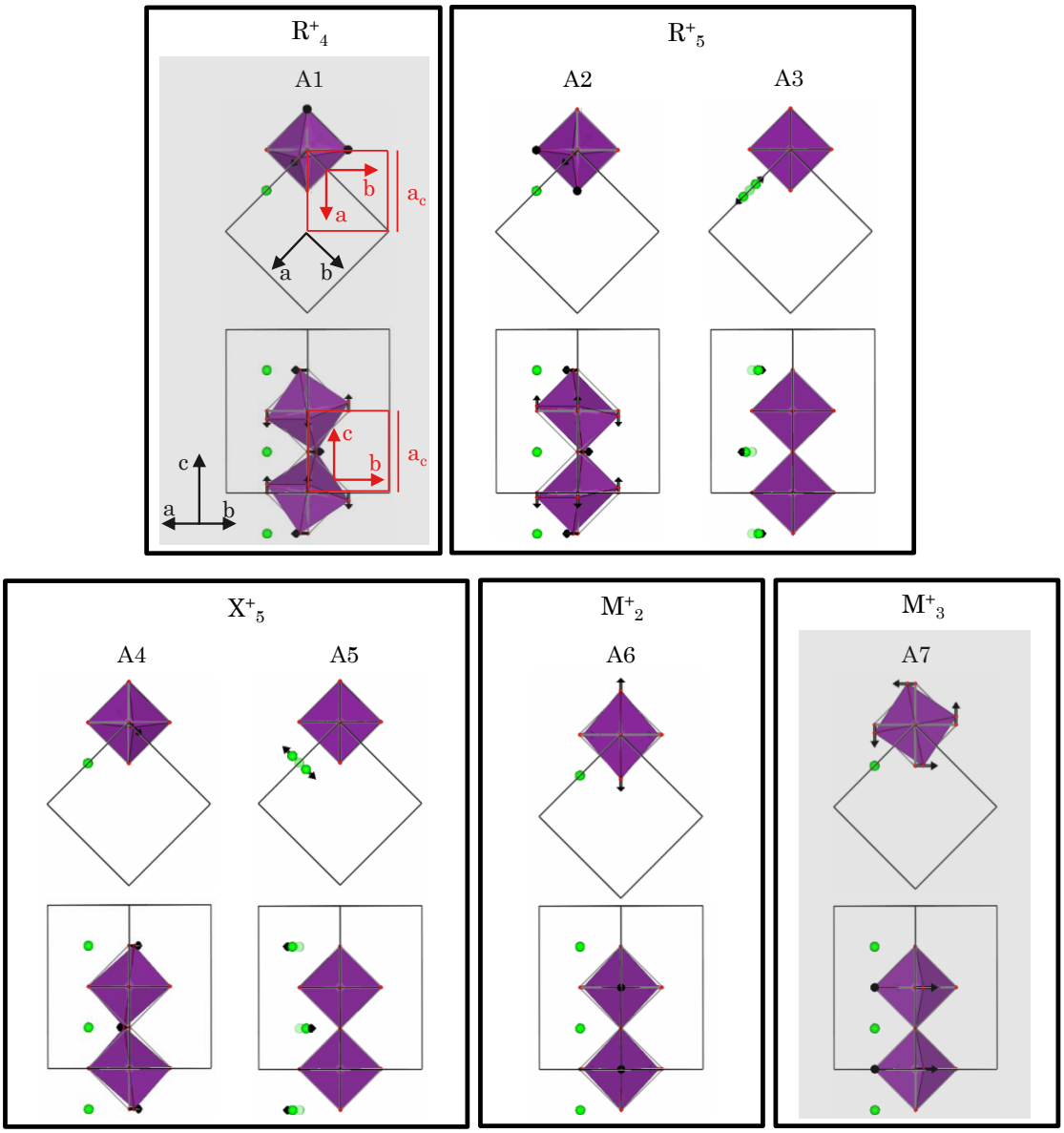

Figure 9.4: Schematic representation of the five irrep distortions allowed in the *Pbnm* configuration, corresponding to M_2^+, M_3^+, R_4^+, R_5^+ and X_5^+. Fe/Ru disordered octahedra in purple, the A/A'-site Sr/Ln cations in green and, oxygen atoms, in red. As a reference, we are also plotting the simple perovskite cubic cell (red) and the double perovskite orthorhombic cell (black). The polarization vectors are shown by small black arrows.

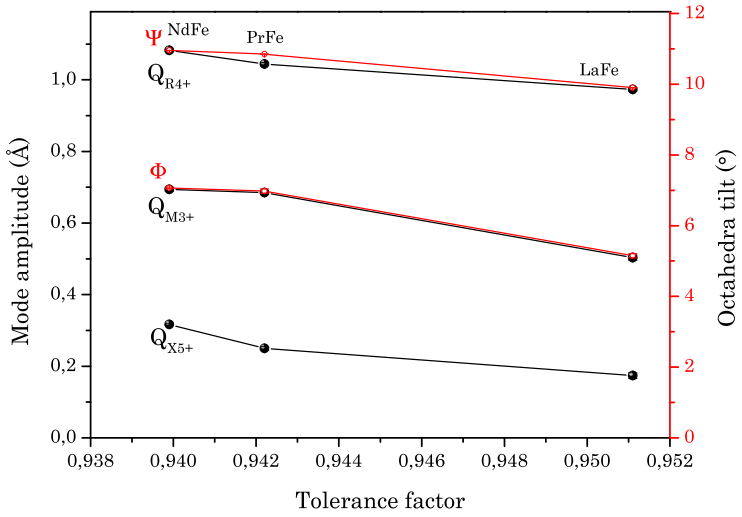

Figure 9.5: Amplitudes of R_4^+, M_3^+ and X_5^+ irreps conforming the RT phase of the SrLaFeRuO$_6$, SrPrFeRuO$_6$ and SrNdFeRuO$_6$ compounds, and Ψ and Φ tilt angles, as obtained from the NPD data refinement (3 mode refined), in function of the tolerance factors. The tolerance factors are calculated with Sr/*Ln*-O distance in nine coordination. Ψ and Φ represent rotation of octahedra about the pseudo-cubic $[110]_p$ and $[001]_p$ axes, respectively.

in one-dimensional space, these are linearly related to the tilts of the octahedra: $a^+b^-b^-$ tilt system (*Pbnm*) [41, 42]. The variation of the obtained mode amplitudes (and octahedral tilt angles) versus the tolerance factors is plotted in Figure 9.5. It shows a clear trend: the less distorted the structure, the smaller are the amplitudes of the modes. Among the SrLaFeRuO$_6$, SrPrFeRuO$_6$ and SrNdFeRuO$_6$ compounds, the former is less distorted. This observation is in perfect agreement with the fact that La cation is bigger than Pr and Nd, needing a bigger cubo-octahedral space and preventing the tilt of the octahedra. Hence, the smaller the value of the mode amplitudes, the smaller the tilting of the octahedra and the more symmetric the structure at RT. SrLaFeRuO$_6$, with smallest symmetry-mode amplitude values, is the more symmetric of the three reported here.

9.2 High temperature structural phase transitions: $SrPrFeRuO_6$

The thermal evolution of $SrPrFeRuO_6$ was studied by means of laboratory X-ray powder diffraction measurements at different temperatures. As mentioned in the Introduction, several different symmetries have been reported for disordered double perovskites at RT, however only a few temperature dependent structural studies have been done. To search for structural phase transitions in our sample, we analyzed the intervals 24-26° and 93-96° corresponding to the (111) primitive peak and (321) cubic reflections, shown in Figure 9.6. In the first 2θ range it is clearly observed a diminishing of the intensity when heating and, about 1075 K, the reflections of the type hkl, with $h+k+l$=2n+1 disappear, indicating a structural phase transition from a primitive to a non-primitive space group. One of the usual intermediate space groups is the trigonal $R\bar{3}c$ [112]. XRPD and NPD data at 1200 K confirm $R\bar{3}c$ to be the space group of the intermediate phase. The structural information for $SrPrFeRuO_6$ at 1200 K is presented in Table 9.5 and the evolution of the cell parameters evolution with the temperature is shown in Figure 9.7. It is not the first time that $Pbnm \rightarrow R\bar{3}c$ structural phase transition it is observed in double perovskites [112].

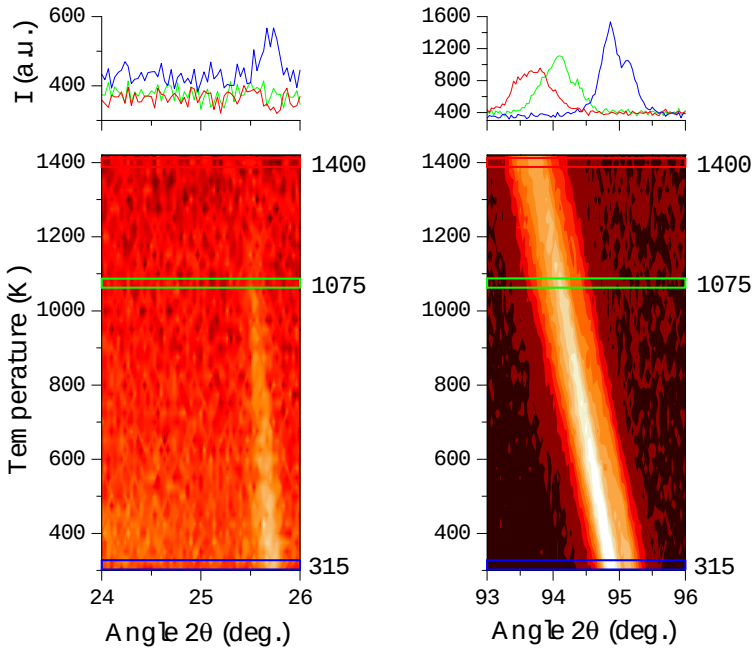

Figure 9.6: Thermal evolution of the (111) primitive peak and (321) cubic reflections of $SrPrFeRuO_6$ obtained from XRPD experiment. The scattered intensity is represented with yellow-red scale, light-yellow being high intensity and dark-red lowest intensity. At 1075 K the intensity of the peaks related to the primitive cell disappear, transforming into a trigonal cell.

Table 9.5: Crystal structure data and refinement results for SrPrFeRuO$_6$ from NPD (HRPT, PSI) at 1200 K using $R\bar{3}c$ model.

Reliability factors	Lattice parameters	Atom	Site	x	y	z	B_{iso} (Å^2)	Occ
R_p = 4.14%	a= 5.5977(2) Å	Sr/Pr	6a	0.0000	0.0000	0.2500	2.52(4)	0.5/0.5
R_{wp}= 5.53%	c= 13.720(1) Å	Fe/Ru	6c	0.0000	0.0000	0.0000	1.02(2)	0.5/0.5
R_{exp}= 3.34%	$\gamma = 120°$	O1	18e	0.5424(3)	0.0000	0.2500	3.42(3)	1
R_{Bragg}= 10.1%	V= 372.31(3) Å^3							

Irrep	K-vector	Dir.	Iso. subgroup	Dim	Ampl. (Å)
R_4^+	(1/2,1/2,1/2)	(a,a,a)	$R\bar{3}c$	1	0.571(5)

In the symmetry breaking from cubic archetype ($Pm\bar{3}m$) to trigonal ($R\bar{3}c$) phase, there is a single irrep that takes part (Table 9.3): R_4^+. That mode displaces the oxygen atoms of the asymmetric unit along the a axis.

There is no group/subgroup relation between the orthorhombic $Pbnm$ and trigonal $R\bar{3}c$ space groups (Figure 9.3). This means that the structural phase transition experimentally observed between the RT structure and the intermediate phase will be a first order (discontinuos). Both phases can be referred to the same cubic archetype phase. As it is very common in many distorted double perovskite compounds ([116][125]) and, in particular, in this sample, due to experimental limitations, no cubic phase is known. Thus, a virtual archetype cubic phase is used as the reference structure (Table 9.6).

Despite the fact that the irreps lowering successively the symmetry from the cubic to the trigonal ($R\bar{3}c$) and from the cubic to the orthorhombic ($Pbnm$) involve, mainly, oxygen displacements, the cubic-to-trigonal phase transition is continuous (second order); while, as mentioned, the trigonal-to-orthorhombic is discontinuous (first order).

Although the structural phase transitions in these kind of materials are essentially originated by the tilting of the octahedra, some of them are continuous while other are discontinuous. In fact, a continuous reduction of the octahedral tilts in the trigonal phase gives rise to not tilted octahedra and, hence, to a continuous phase transition between the trigonal and the cubic. The discontinuous character of the orthorhobic-to-trigonal phase transition is related to the change of the direction of the R_4^+ (same) irrep, in the three-dimensional representation space, as can be seen in Tables 9.4 and 9.5. The direction of the R_4^+ for the $Pbnm$ phase is (0,a,-a) while it changes to (a,a,a) for the trigonal phase.

To study the thermal evolution of the amplitudes of the symmetry-adapted modes we have measured SrPrFeRuO$_6$ by means of NPD. From Table 9.4 can be concluded that even excluding some mode-amplitudes from the refinements, the obtained biased results

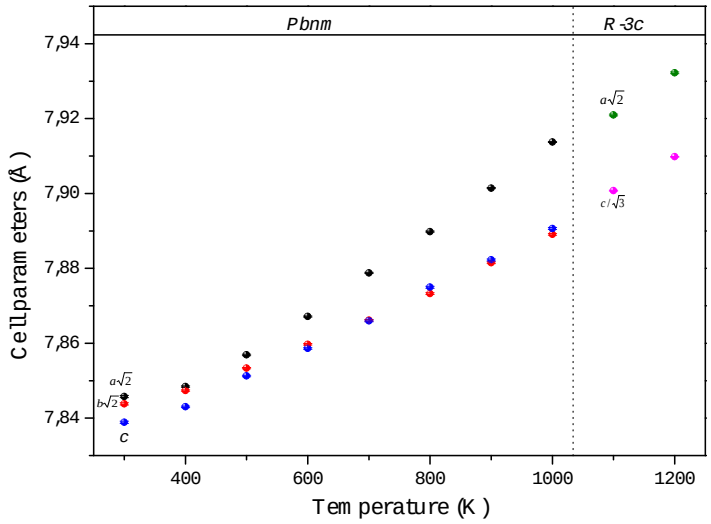

Figure 9.7: Temperature evolution of the cell parameters of $SrPrFeRuO_6$ as obtained from the NPD measurements: cell parameters of the orthorhombic and trigonal phase. The parameters have been scaled to the setting of the double perovskite cubic structure, a_c=2a$_p$, in order to compare.

"are not far away" from the real ones, and the exclusion of some modes could be done in a first approximation. In Figure 9.8 we show the temperature evolution of the amplitudes of R_4^+, M_3^+ and X_5^+ modes (the rest are negligible) in the orthorhombic phase and the single

Table 9.6: Input information for AMPLIMODES for FullProf: high symmetry phase information (virtual prototype structure), low symmetry structure information (cell parameters obtained by XRPD data refinement) and transformation matrix. *Pm*$\bar{3}$*m* (ITA No. 221, standard setting), *Pbnm* (ITA No. 62, non-standard setting) and *R*$\bar{3}$*c* (ITA No. 167, standard setting).

High symmetry structure
221
3.8438 3.8438 3.8438 90.00 90.00 90.00
4

Fe	1	1a	0.00000	0.00000	0.00000
Sr	1	1b	0.50000	0.50000	0.50000
O	1	3d	0.00000	0.00000	0.50000

Low symmetry structure
062
5.5350 5.5434 7.8246 90.00 90.00 90.00

Transformation matrix

$$\left(\begin{array}{ccc|c} 1 & 1 & 0 & 1/2 \\ -1 & 1 & 0 & 1/2 \\ 0 & 0 & 2 & 0 \end{array}\right)$$

Low symmetry structure
167
5.5973 5.5973 13.7181 90.00 90.00 120.00

Transformation matrix

$$\left(\begin{array}{ccc|c} 0 & 1 & 2 & 0 \\ -1 & 0 & 2 & 0 \\ 1 & -1 & 2 & 0 \end{array}\right)$$

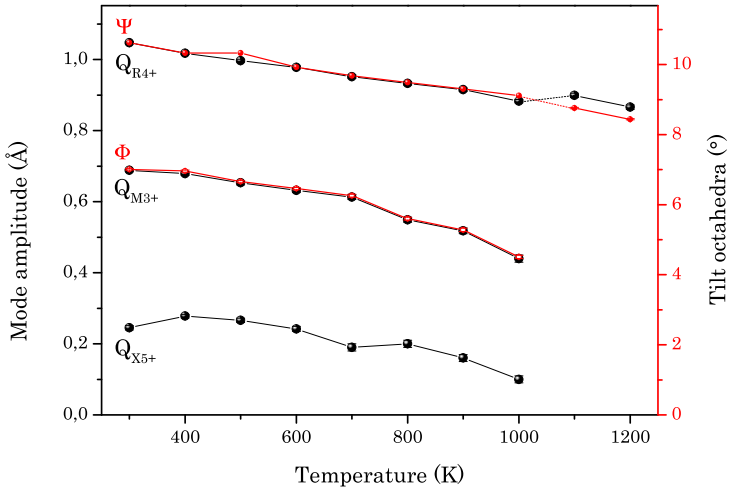

Figure 9.8: Temperature dependence of the amplitudes of the irreps conforming the *Pbnm* and *R*$\bar{3}$*c* structure of SrPrFeRuO$_6$, and Ψ and Φ tilt angles, as obtained from the NPD data refinement. The amplitudes of the irreps in the high symmetry phase have been scaled (multiplied by 3/2) to see the evolution, since the program AMPLIMODES uses mode normalization within the corresponding primitive unit cell.

active mode R_4^+ in the trigonal phase. Although the highest amplitude in the orthorhombic phase and the amplitude in the trigonal, R_4^+, have the same label, the irrep taking part in the symmetry breaking from the cubic to the orthorhombic and from the cubic to the trigonal are not the same: the acting direction of each irrep is different. Together with the mode amplitudes, we show the octahedral tilts in Figure 9.8. The correlation between the mode amplitudes and tilt angles are very good.

9.3 Magnetic structures

Based on the observation of the NPD patterns at RT, neutron diffraction experiments were undertaken at low temperature, to determine the magnetic structures. The compounds were analyzed from a set of NPD patterns collected at D1B instrument in ILL (Grenoble) with λ=2.52 Å. The La and Pr containing compounds were measured at 2 K; whereas $SrNdFeRuO_6$ was measured at 10 K, due to experimental limitations.

The neutron powder diffraction patterns of $SrLaFeRuO_6$, $SrPrFeRuO_6$ and $SrNdFeRuO_6$ show an increase in the intensity in some low angle reflections, which the nuclear model is not able to refine correctly and are not visible in XRPD patterns (see Figure 9.9). These peaks have been related to the magnetic ordering and from Figure 9.10 the magnetic ordering temperatures are *ca*. 450 K, *ca*. 475 K, and *ca*. 430 K for Sr*Ln*$FeRuO_6$ (*Ln*=La,Pr,Nd), respectively.

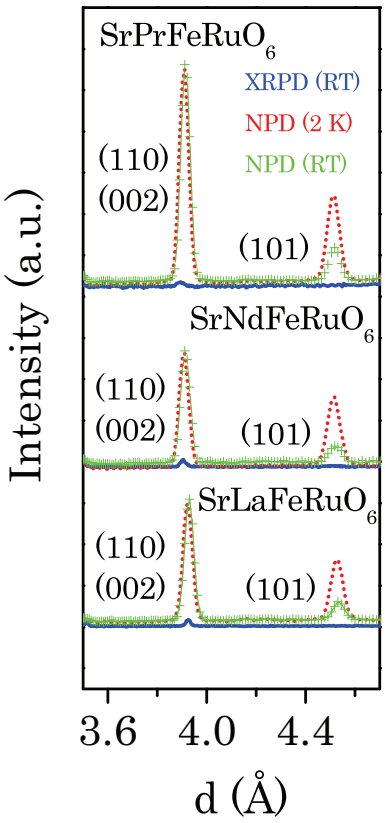

Figure 9.9: XRPD data at RT (blue line), NPD data at 2 K (red dotted line) and RT (green crossed line) in d space (in Å). All patterns are re-normalized with respect to the peak height of the main (112/200) index peak at $2\theta \sim 32.6^\circ$ ($d \sim 2.7$ Å).

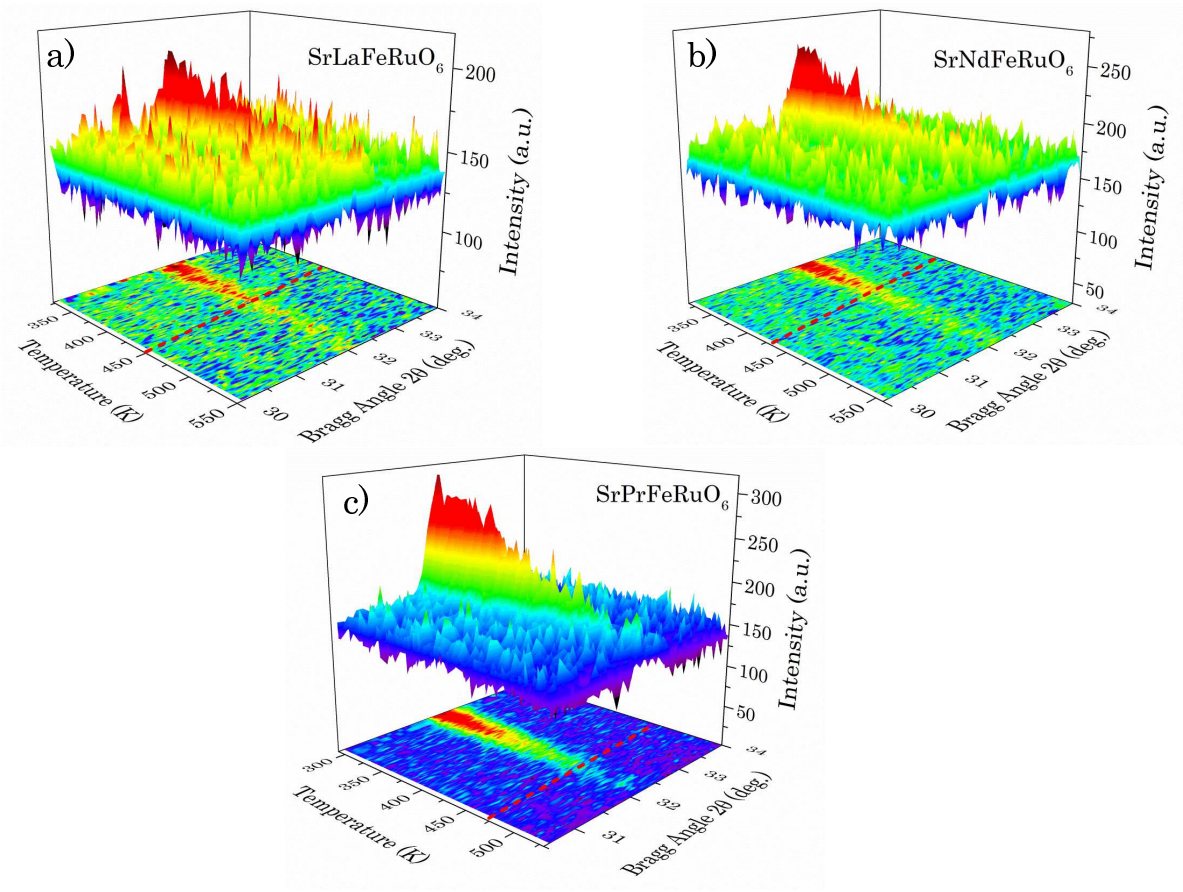

Figure 9.10: Thermal evolution of the (101) reflection of (a) SrLaFeRuO$_6$, (b) SrNdFeRuO$_6$ and (c) SrPrFeRuO$_6$ collected with λ=2.52 Å between RT and 573 K, in D1B neutron powder diffractometer.

None of the compound undergoes a structural phase transition between RT and the lowest temperature measured. However, the change in the intensity of some nuclear reflections is observed, in particular at low angles, and no new reflections appear decreasing the temperature; this fact suggests **k**=(0,0,0) to be the propagation vector for the three compounds. As the magnetic scattering factor for Ru^{4+} is not available, the magnetic structures were refined using the scattering factor of Ru^{1+}, an approximation used by [109].

To determine the possible magnetic structures compatible with the symmetry of the crystal structure of SrLaFeRuO$_6$, SrPrFeRuO$_6$ and SrNdFeRuO$_6$ the representation analysis described by Bertaut [129] have been performed. For that purpose BASIREPS (included in FullProf Suite [85]) and Sarah [130] programs were used. The magnetic representation Γ_M for each magnetic site can be decomposed as direct sum of irreps, by applying the Great Orthogonality Theorem.

Table 9.7: Basis vectors of 4 possible irreducible representations for the sites Fe and Ru(4*a*)=(0,$\frac{1}{2}$,0) and Pr(4*c*)=(0.001(1),-0.0255(4),$\frac{1}{4}$).

Basis vectors		x,y,z	$-x,-y,z+\frac{1}{2}$	$x+\frac{1}{2},-y+\frac{1}{2},-z$	$-x+\frac{1}{2},y+\frac{1}{2},-z+\frac{1}{2}$
Γ_1	Fe/Ru (4*a*)	{(100),(010),(001)}	{(-100),(0-10),(001)}	{(100),(0-10),(00-1)}	{(-100),(010),(00-1)}
	Pr (4*c*)	{(001)}	{(001)}	{(00-1)	{(00-1)}
Γ_3	Fe/Ru (4*a*)	{(100),(010),(001)}	{(-100),(0-10),(001)}	{(-100),(010),(001)}	{(100),(0-10),(001)}
	Pr (4*c*)	{(001)}	{(001)}	{(001)}	{(001)}
Γ_5	Fe/Ru (4*a*)	{(100),(010),(001)}	{(100),(010),(00-1)}	{(100),(0-10),(00-1)}	{(100),(0-10),(001)}
	Pr (4*c*)	{(100),(010)}	{(100),(010)}	{(100),(0-10)}	{(100),(0-10)}
Γ_7	Fe/Ru (4*a*)	{(100),(010),(001)}	{(100),(010),(00-1)}	{(-100),(010),(001)}	{(-100),(010),(00-1)}
	Pr (4*c*)	{(100),(010)}	{(100),(010)}	{(-100),(010)}	{(-100),(010)}

$$\Gamma_{4a} = 3\Gamma_1 \oplus 3\Gamma_3 \oplus 3\Gamma_5 \oplus 3\Gamma_7 \tag{9.1}$$

$$\Gamma_{4c} = 1\Gamma_1 \oplus 2\Gamma_2 \oplus 1\Gamma_3 \oplus 2\Gamma_4 \oplus 2\Gamma_5 \oplus 1\Gamma_6 \oplus 2\Gamma_7 \oplus 1\Gamma_8 \tag{9.2}$$

There is a single magnetic site for $SrLaFeRuO_6$ and $SrNdFeRuO_6$, 4*a*; the Γ_1, Γ_3, Γ_5 or Γ_7 irrep could be the one that describes the magnetic moment. In the case for $SrPrFeRuO_6$, if we consider that both sites are ordered at the same moment, the magnetic structure can only be described by Γ_1, Γ_3, Γ_5 or Γ_7. This is because Γ_2, Γ_4, Γ_6 or Γ_8 are not contained in irrep Γ_{4a}. The possible four basis vectors are shown in Table 9.7. From the symmetry point of view, any of Γ_1, Γ_3, Γ_5 or Γ_7 could be the irrep that describes the magnetic structure. To clarify the possible magnetic model Rietveld refinement of the neutron diffraction patterns should be done.

The magnetic ordering for $SrLaFeRuO_6$ and $SrNdFeRuO_6$ is due to Fe^{3+} and Ru^{4+} cations, which share 4*a* Wyckoff position. The magnetic refinement of the pattern at low temperature was carried out with all possible models, although the best refinement of the magnetic structure is described by irrep Γ_5 for $SrLaFeRuO_6$ and Γ_3 for $SrNdFeRuO_6$. The magnetic moment of the four sublattices of site 4*a* for irrep Γ_5 are $\mathbf{m}_{4a}(1)$=(u,v,w), $\mathbf{m}_{4a}(2)$=(u,v,-w), $\mathbf{m}_{4a}(3)$=(u,-v,-w) and $\mathbf{m}_{4a}(4)$=(u,-v,w); and for irrep Γ_3: $\mathbf{m}_{4a}(1)$=(u,v,w), $\mathbf{m}_{4a}(2)$=(-u,-v,w), $\mathbf{m}_{4a}(3)$=(-u,v,w) and $\mathbf{m}_{4a}(4)$=(u,-v,w). The magnetic structures have three degrees of freedom (u,v,w).

The $\mathbf{m}_T(4a)$, determined by NPD data refinement (see Figure 9.11), is 1.88(3) μ_B for $SrLaFeRuO_6$ and 2.01(3) μ_B $SrNdFeRuO_6$, the components along the crystallographic axes are listed in Table 9.8. This value is far below that expected for Fe and Ru shared site, 4.5 μ_B, S=5/2 and S=2, respectively. In Figure 9.12(a) and (b) we illustrate the magnetic structure

Table 9.8: Magnetic moment components (in μ_B) determined for each Pr and Fe/Ru site and Rietveld reliability factors for SrLnFeRuO$_6$ (Ln=La,Nd,Pr).

		SrLaFeRuO$_6$ (2 K)	SrPrFeRuO$_6$ (2 K)	SrNdFeRuO$_6$ (10 K)
Γ_{mag}		$3\Gamma_5$	$3\Gamma_3 \oplus 1\Gamma_3$	$3\Gamma_3$
Pr(4c)	m_z	———	0.63(9)	———
	m_{TOT}	———	0.63(9)	———
Fe/Ru(4a)	m_x	0.74(7)	1.89(1)	1.81(1)
	m_y	0.43(4)	0.28(4)	0.12(8)
	m_z	1.67(1)	-0.16(9)	1.07(5)
	m_{TOT}	1.88(3)	1.92(3)	2.01(3)
R_p(%)		1.49	1.64	1.37
R_{wp}(%)		2.16	2.31	1.90
R_{exp}(%)		0.84	0.82	0.89
R_{Bragg}(%)		3.25	6.58	4.57
R_{mag}(%)		4.64	6.96	4.53

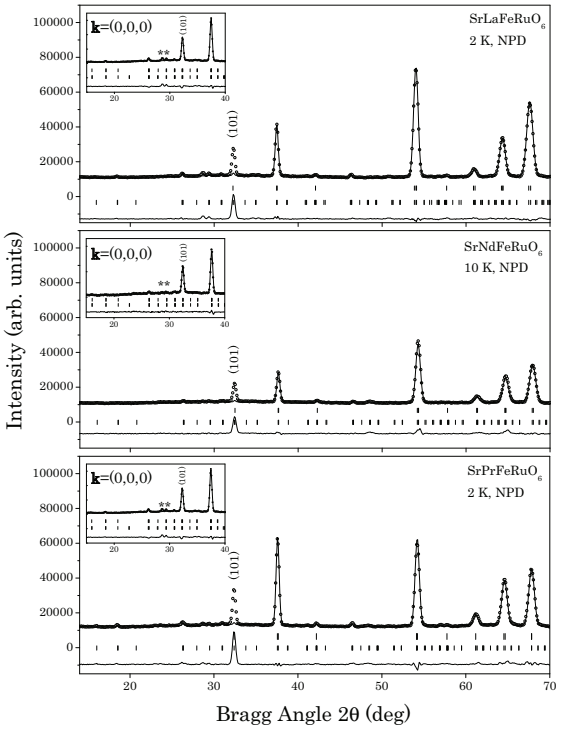

Figure 9.11: Low angle region of the neutron powder diffraction patterns collected at low temperature, including the observed intensity (open circles), calculated fit to the data (continuous line) and the difference curve. Tick marks correspond to Bragg peak location, (up) λ=2.52 Å and (bottom) $\lambda/2$=1.26 Å. The inset show the data refinement using the crystal and magnetic model. The upper (lower) marks correspond to crystal (magnetic) structure using λ=2.52 Å and $\lambda/2$=1.26 Å. * La_3RuO_7, Nd_3RuO_7 and Pr_3RuO_7 impurity.

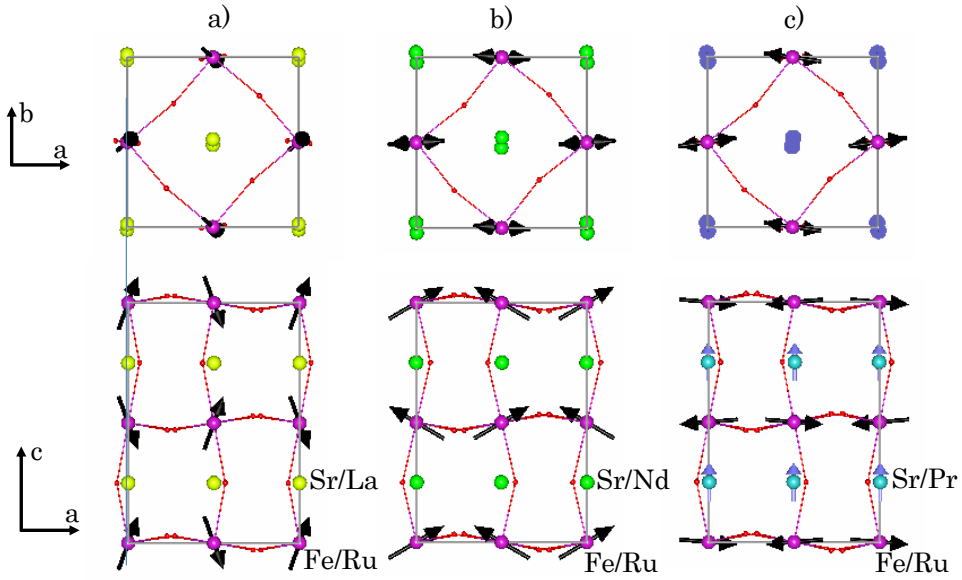

Figure 9.12: Magnetic structure models, a) $SrLaFeRuO_6$, $3\Gamma_5$ solution; b) $SrNdFeRuO_6$, $3\Gamma_3$ solution; and c) $SrPrFeRuO_6$, $3\Gamma_3 \oplus 1\Gamma_3$ solution: Sr/La, yellow balls; Sr/Nd, green balls; Sr/Pr, blue balls, blue arrows; Fe/Ru, purple balls, black arrows; and O, red balls.

for $SrLaFeRuO_6$ and $SrNdFeRuO_6$, respectively. The models describe a spin canted-AFM structure along *a* axis for La compound and along *c* for Nd compound. In Table 9.9 is gathered the structural information at selected temperatures and in Figure 9.13 the temperature evolution of the magnetic moment in the 4*a* site.

$SrPrFeRuO_6$ shows a more complex magnetic structure, due to the presence of two magnetic sites generated by Pr ion and Fe/Ru cations. Based on the representation analysis, the only possible irreducible representations are: Γ_1, Γ_3, Γ_5 or Γ_7 (see Table 9.7, explanation in the previous paragraph). The symmetry analysis is not able to discard more models, nor to give information about the phase existing between both magnetic sites. To elucidate the correct magnetic model, irrep Γ_3, NPD data refinement is necessary. The reliability factor for the fitting is R_{mag}=6.96%. The magnetic moment of site 4*a* is obtained from the basis vectors as $\mathbf{m}_{4a}(1)$=(u,v,w), $\mathbf{m}_{4a}(2)$=(-u,-v,w), $\mathbf{m}_{4a}(3)$=(-u,v,w) and $\mathbf{m}_{4a}(4)$=(u,-v,w), and the ones of site 4*c* $\mathbf{m}_{4c}(1)$=(0,0,p), $\mathbf{m}_{4c}(2)$=(0,0,p), $\mathbf{m}_{4c}(3)$=(0,0,p) and $\mathbf{m}_{4c}(4)$=(0,0,p) for irrep Γ_3. The magnetic model is described by four degrees of freedom (u,v,w,p).

The model for $SrPrFeRuO_6$ is shown in Figure 9.12(c). The magnetic structure is described by two sites: the spins of Pr cation in 4*c* site is strictly FM ordered along *c* axis; whereas the magnetic moments on Fe/Ru ions in 4*a* site are AFM ordered with a very small canting along *c* axis, probably induced by the 4*c* site magnetic moments. For the Pr containing compound, the global magnetic moment is strictly ferrimagnetic. However, the

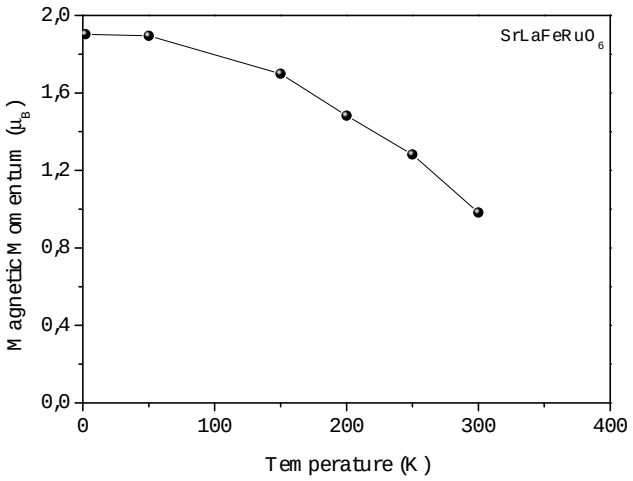

Figure 9.13: Temperature dependance of SrLaFeRuO$_6$ 4a site Fe/Ru magnetic momentum for $3\Gamma_5$ solution.

small value of z component for site 4a is uncertain. Due to the refinement limitations as a result of few magnetic peaks and their low intensities there is not enough information to be sure of the sign of the value. Nevertheless, it is reported with a negative sign since it is the refinement result. $\mathbf{m}_{4a}$ for Pr compound is 1.92(3) μ_B, and $\mathbf{m}_{4c}$ for Pr 0.63 μ_B (Table 9.8 shows the list of the components along the crystallographic axes).

The room temperature structural information reported for SrLaFeRuO$_6$ compound by Shaheen et al. in [114] is somewhat different from the one shown in Table 9.1. Shaheen et al. conclude from their Mössbauer spectroscopy experiment that their compound does not have any long range magnetic ordering at room temperature. Nevertheless, during the experiments done to complete this work it became clear that the compound reported here is magnetic at room temperature, and the characterization of the magnetic moment at room temperature have been done (see Table 9.9). The small differences in cell parameters and small atomic position variations between the compound presented here and in [114] could be the reason to observe long range magnetic ordering at room temperature in our sample; these small variations could have influence in the spin arrangements, rising a completely different magnetic lattice.

Table 9.9: Structural details of $SrLaFeRuO_6$ obtained at different temperatures from NPD (D1B, ILL) data using *Pbnm* structural model with R_4^+, M_3^+ and X_5^+ modes refined.

Temp.(K)		2	50	150	200	250
Sr/La	(x,y,1/4)					
	x	0.00(0)	0.00(0)	0.00(0)	0.00(0)	0.00(0)
	y	-0.0204(6)	-0.0215(5)	-0.0192(6)	-0.0191(6)	-0.0186(6)
	B_{iso}(Å^2)	0.31(5)	0.26(5)	0.49(4)	0.57(4)	0.69(5)
Fe/Ru	(0,1/2,0)					
	B_{iso}(Å^2)	0.22(4)	0.19(4)	0.28(4)	0.28(4)	0.32(4)
	$m(Fe/Ru)$ (μ_B)	1.90(1)	1.89(1)	1.70(1)	1.49(1)	1.31(1)
O1	(x,y,1/4)					
	x	-0.0695(3)	-0.0697(3)	-0.0680(3)	-0.0669(3)	-0.0660(3)
	y	0.50698	0.50698	0.50698	0.50698	0.50698
	B_{iso}(Å^2)	0.45(3)	0.42(3)	0.57(3)	0.67(3)	0.81(3)
O2	x	0.7235(3)	0.7236(3)	0.7243(3)	0.7244(3)	0.7251(3)
	y	0.2760(3)	0.2760(3)	0.2752(3)	0.2751(3)	0.2744(3)
	z	0.5306(1)	0.5307(1)	0.5299(1)	0.5293(1)	0.5288(1)
	B_{iso}(Å^2)	0.45(3)	0.42(3)	0.57(3)	0.67(3)	0.81(3)
a (Å)		5.5703(3)	5.5706(3)	5.5730(2)	5.5748(3)	5.5774(3)
b (Å)		5.5490(3)	5.5495(3)	5.5503(2)	5.5516(3)	5.5533(3)
c (Å)		7.8480(3)	7.8471(3)	7.8511(3)	7.8538(3)	7.8563(3)
V (Å^3)		242.58(2)	242.59(2)	242.85(2)	243.07(2)	243.33(2)
R_p(%)		1.44	1.44	1.45	1.43	1.45
R_{wp}(%)		2.13	2.17	2.09	2.08	2.11
R_{exp}(%)		0.84	0.84	0.84	0.84	0.83
R_{Bragg}(%)		3.12	3.06	3.28	3.38	3.82
R_{mag}(%)		4.78	3.86	6.05	6.72	7.42

9.4 Conclusions

The crystal and magnetic structure of SrLnFeRuO$_6$ (Ln=La,Pr,Nd) double perovskites have been studied by means of X-ray and neutron powder diffraction techniques. Diffraction experiments show that SrLnFeRuO$_6$ materials have completely disordered arrangements of Fe^{3+} and Ru^{4+}, due to small charge and size differences between Fe and Ru cations. All compounds crystalize in the orthorhombic space group *Pbnm*. Analysis of distortion modes shows that the symmetry breaking from the archetype cubic phase to the orthorhombic phase is driven by R_4^+ and M_3^+, in agreement with earlier works [131][132]. R_4^+ and M_3^+ distortion mode amplitudes for La, Pr and Nd materials are 0.980(4) Å and 0.494(7) Å, 1.085(4) Å and 0.627(4) Å, and 1.133(4) Å and 0.627(5) Å, respectively.

Temperature induced structural phase transition was studied for SrPrFeRuO$_6$. NPD pattern refinement suggest $Pbnm \rightarrow R\bar{3}c$ transition at about 1075 K.

The spin structure for the three phases is described by (0,0,0) propagation vector. SrLaFeRuO$_6$ and SrNdFeRuO$_6$ order antiferromagnetically with spin canting along *a*- and *c* axis, respectively. SrPrFeRuO$_6$ is more complex as a result of two magnetic sites generated by Pr and Fe/Ru cations. The global magnetic moment is strictly ferrimagnetic.

Chapter 10

$(ALn_2)(CuTi_2)O_9$ (A=Ca,Ba; Ln=La,Pr,Nd,Sm) triple perovskites

10.1 Results

Room temperature X-ray diffraction patterns collected for $CaLn_2CuTi_2O_9$ and $BaLn_2CuTi_2O_9$ are shown in Figure 10.1 and Figure 10.2. The inspection of the patterns for the former materials show that many diffraction lines clearly split, indicating that the unit cells are distorted with respect to the aristotype cubic phase, $Pm\bar{3}m$ (ITA No.221). The most common and plausible space groups for distorted perovskites are *Pbnm* (ITA No.62, non-conventional setting), *Cmcm* (ITA No.63) and *Imma* (ITA No.74). *Imma* should be excluded due to the presence of $h+k+l=2n+1$ type hkl reflections, characteristic of a primitive cell. *Cmcm* and *Pbnm* structures are very closely related in perovskite type oxides. In the absence of a clear splitting of the (022,202) type reflections in *Pbnm*, it is extremely difficult to distinguish between these two possibilities in X-ray powder diffraction studies. However, the splitting is clearly observed, Figure 10.1, rejecting the *Cmcm* space group.

The other set of compounds, $BaLn_2CuTi_2O_9$, are more symmetric than $CaLn_2CuTi_2O_9$ materials: Ba cation is larger than Ca, preventing the tilting of the octahedra due to the misfit of the cations in the interstitial space amongst the octahedra. Although the splitting of the peaks is not clearly visible for $BaLn_2CuTi_2O_9$ compounds Figure 10.2, the broadening of them suggest that the cubic space group is not the proper one at RT: the pattern analysis indicates that the tetragonal space group $I4/mcm$ (ITA No.140) should be the RT space group.

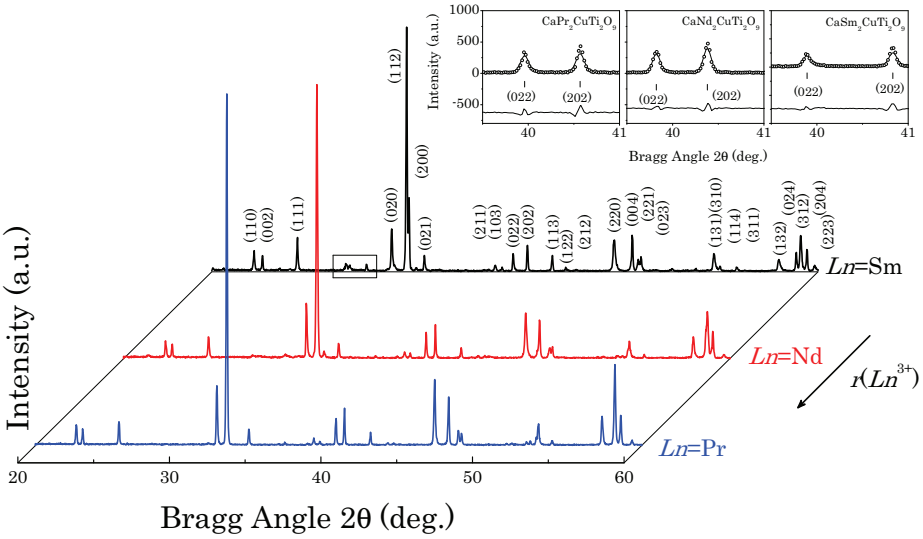

Figure 10.1: X-ray powder diffraction patterns (λ=1.5406 Å) for Ca$Ln_2$$CuTi_2O_9$ (Ln=Pr,Nd,Sm) at room temperature. The groups of peaks are indexed in the orthorhombic system ($Pbnm$). Inset shows the (022)-(202) peak splitting. The black rectangle in the Ln=Sm case indicates an unidentified impurity.

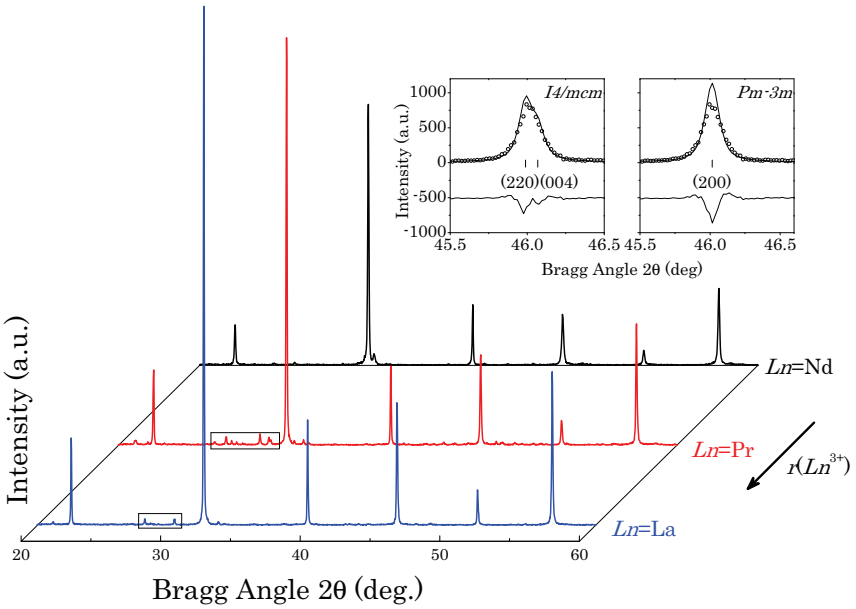

Figure 10.2: X-ray powder diffraction patterns (λ=1.5406 Å) for Ba$Ln_2$$CuTi_2O_9$ (Ln=La,Pr,Nd) at room temperature. The groups of peaks are indexed in the tetragonal system ($I4/mcm$). Inset shows Rietveld refinement results using $I4/mcm$ and $Pm\bar{3}m$ models for $BaNd_2CuTi_2O_9$). The black rectangles indicate, as in previous figure, the presence of an impurity.

It is noted in Figure 10.1 and 10.2 that the peak positions shift to lower 2θ with the increase of the *A*-site cation radius, which means the cell-volume increases due to the substitution of a larger lanthanide, as could be expected.

The atomic coordinates given by Aatiq *et al.* [133] were used as input for the symmetry mode model for AMPLIMODES for FullProf program [93]. The same virtual archetype phase was used for all the compounds (no real $Pm\bar{3}m$ phase is known). This virtual phase was obtained using PSEUDO [98].

There is some symmetry breaking that does not have a single active irrep Figure 10.3, *i.e*. the symmetry reduction cannot be explained by a unique irrep, as the symmetry of the distorted phase is not an isotropy subgroup of the archetype phase; this is quite common in distorted perovskite structures [36, 120, 131, 134]. In Figure 10.3 it is shown the graph of the intermediate subgroups (minimal subgroups in each step) relating the archetype phase and the distorted RT phase *Pnma* (ITA No.62; the structural models are described in the *Pbnm* non-standard setting), for $CaLn_2CuTi_2O_9$ materials. For each of the subgroups, the corresponding active irrep yielding that symmetry has been identified. The *Pnma* symmetry, resulting from the presence of two of the possible distortions of the archetype-phase space group, is the intersection of the two corresponding isotropy subgroups; and is given by their first common maximal subgroup. The two actives modes breaking the symmetry from the archetype phase to the orthorhombic symmetry *Pnma*, in these type of materials, are R_4^+ and M_3^+. From the Figure 10.3 one can identify alternative, possible, sets of primary order parameters that could had driven the symmetry breaking to the same distorted low symmetry structure. For this case, eight are the possible combinations (M_2^++X_5^+, M_2^++R_4^+, M_2^++R_5^+, M_3^++X_5^+, M_3^++R_4^+, M_3^++R_5^+, X_5^++R_4^+, and X_5^++R_5^+), since the addition of R_4^+ to R_5^+ do not decrease further the symmetry; and the combination of M_2^+ and M_3^+ do not decrease it down to *Pnma*. The true active modes are those that take into account the actual low symmetry structure: the ones which reduce the symmetry down to the experimentally observed phase. Symmetry considerations cannot distinguish between the possible irrep combinations and further methods, *e.g*. Rietveld refinement, are necessary.

Rietveld refinement of the diffraction patterns (NPD refined pattern for $CaNd_2CuTi_2O_9$ shown in Figure 10.4) should elucidate the active irreps, by showing the largest amplitude-values for the actual active modes. Looking at the refinement values for the amplitudes of the irreps in Table 10.1, it is clear that there are two global amplitudes (R_4^+ and M_3^+) larger in value than the rest. These two irreps are related to the tilts of the octahedra: R_4^+ mode, is essentially a rotation around the *b* axis; although it deforms a bit the octahedra (the displacement of the oxygens in *ab* plane and the ones along *c* are not the same);

Table 10.1: Refined distortion mode amplitudes (Å) at room temperature obtained by AMPLIMODES for FullProf [93] and FullProf [85]. The primary mode, if any, is written in bold letters. The column headed as *Dim* referees to the number of basis modes necessary in general to describe the corresponding irrep distortion; and the *direction* in the irrep space corresponding to the irrep distortion in the convention of ISOTROPY [99] is indicated in the bottom of the columns.

Irrep	Isotropy subgroup	Dim	Mode	Amplitude				
				$CaPr_2CuTi_2O_9$		$CaNd_2CuTi_2O_9$		$CaSm_2CuTi_2O_9$
				XRPD	NPD	XRPD	NPD	XRPD
$Pm\bar{3}m \rightarrow Pbnm$								
R_4^+	*Imma* (74)	1	A1	1.22(3)	1.20(1)	1.25(4)	1.26(1)	1.40(4)
R_5^+	*Imma* (74)	2	A2	0.04(3)	0.03(1)	0.06(4)	0.04(1)	-0.04(4)
			A3	-0.08(1)	-0.06(1)	-0.09(1)	-0.03(1)	-0.12(1)
X_5^+	*Cmcm* (63)	2	A4	0.21(2)	0.24(1)	0.22(3)	0.21(1)	0.36(3)
			A5	0.50(1)	0.52(1)	0.51(1)	0.44(1)	0.61(1)
M_2^+	*P*4/*mbm* (127)	1	A6	0.09(3)	0.01(1)	0.08(4)	0.01(1)	0.07(4)
M_3^+	*P*4/*mbm* (127)	1	A7	0.94(3)	1.03(1)	0.95(4)	0.96(1)	1.09(4)
K-vector: R_4^+ (1/2,1/2,1/2), R_5^+ (1/2,1/2,1/2), X_5^+ (0,1/2,0), M_2^+ (1/2,1/2,0), M_3^+ (1/2,1/2,0)								
Direction: R_4^+ (0,a,-a), R_5^+ (0,a,a), X_5^+ (0,0,a,0,0,0), M_2^+ (a,0,0), M_3^+ (a,0,0)								
				$BaLa_2CuTi_2O_9$		$BaPr_2CuTi_2O_9$		$BaNd_2CuTi_2O_9$
				XRPD		XRPD		XRPD
$Pm\bar{3}m \rightarrow I4/mcm$								
$\mathbf{R_4^+}$	*I*4/*mcm* (140)	1	A1	-0.27(6)		-0.37(8)		-0.35(9)
K-vector: R_4^+ (1/2,1/2,1/2); Direction: R_4^+ (a,0,0)								

and M_3^+ is a pure rotation of the octahedra around the *c* axis. The X_5^+ irrep (*A*-site cation displacement and rotation of the octahedra Figure 10.3) is allowed by symmetry and it is also necessary to describe the final distortion. For $CaPr_2CuTi_2O_9$ and $CaNd_2CuTi_2O_9$, mode-amplitude results from XRPD and NPD pattern analysis are gathered in Table 10.1. Despite the low quality of the NPD data, the results obtained using two complementary techniques are in a very good agreement. Observing the mode-amplitude values in Table 10.1 for Ca$Ln_2CuTi_2O_9$ (*Ln*=Pr,Nd,Sm) suggest the materials have very distorted structures.

Symmetry mode decomposition of the tetragonal phase (*I*4/*mcm* space group) for Ba$Ln_2CuTi_2O_9$ (*Ln*=Pr,Nd,Sm) materials, shows a unique irrep in the symmetry breaking from the cubic archetype phase ($Pm\bar{3}m$): R_4^+. This irrep lowers the symmetry rotating the adjacent octahedra in opposite directions along *c*-axis Figure 10.3.

The crystallographic information of the materials after the refinements and reliability factors for the orthorhombic and tetragonal model refinements are shown in Table 10.2.

Table 10.2: Lattice parameters, Wyckoff sites, atomic fractional coordinates, occupancies, and isotropic temperature factors of the room temperature structures for $ALn_2CuTi_2O_9$ (A=Ca,Ba;Ln=La,Pr,Nd,Sm) obtained from XRPD patter refinements.* fixed in 0.5 Å to guarantee the convergence of the refinement.

Atom	Site	x	y	z	Occupancy	B_{iso} (Å^2)
$CaPr_2CuTi_2O_9$						
Pbnm; a=5.4821(1) Å, b=5.5942(1) Å, c=7.6869(1) Å, R_p=16.4%, R_{wp}=23.6%, χ^2=1.74, R_{Bragg}=8.34%						
Ca/Pr	4*c*	-0.0069(5)	-0.0452(3)	0.75	0.35/0.65	0.34(5)
Cu/Ti	4*b*	0.5	0	0	0.35/0.65	0.5*
O1	4*c*	0.423(3)	0.019(2)	0.75	1	0.7(2)
O2	8*d*	0.203(2)	0.789(2)	0.459(1)	1	0.7(2)
$CaNd_2CuTi_2O_9$						
Pbnm; a=5.4557(1) Å, b=5.5769(1) Å, c=7.6594(2) Å, R_p=18.0%, R_{wp}=26.0%, χ^2=2.12, R_{Bragg}=9.77%						
Ca/Nd	4*c*	-0.0079(6)	-0.0467(4)	0.75	0.35/0.65	0.70(6)
Cu/Ti	4*b*	0.5	0	0	0.35/0.65	0.5*
O1	4*c*	0.423(3)	0.020(3)	0.75	1	1.5(3)
O2	8*d*	0.202(2)	0.790(2)	0.458(2)	1	1.5(3)
$CaSm_2CuTi_2O_9$						
Pbnm; a=5.4221(2) Å, b=5.6097(2) Å, c=7.6129(3) Å, R_p=20.5%, R_{wp}=27.8%, χ^2=2.43, R_{Bragg}=12.1%						
Ca/Sm	4*c*	-0.0109(6)	-0.0558(4)	0.75	0.35/0.65	0.84(7)
Cu/Ti	4*b*	0.5	0	0	0.35/0.65	0.5*
O1	4*c*	0.406(4)	0.033(3)	0.75	1	1.5(3)
O2	8*d*	0.197(3)	0.797(3)	0.456(2)	1	1.5(3)
$BaLa_2CuTi_2O_9$						
*I*4/*mcm*; a=5.6032(2) Å, c=7.9192(6) Å, R_p=14.2%, R_{wp}=22.6%, χ^2=1.99, R_{Bragg}=3.65%						
Ba/La	4*b*	0	0.5	0.25	0.35/0.65	2.32(7)
Cu/Ti	4*c*	0	0	0	0.35/0.65	1.8(1)
O1	4*a*	0	0	0.25	1	5.4(4)
O2	8*h*	0.268(4)	0.232(4)	0	1	5.4(4)
$BaPr_2CuTi_2O_9$						
*I*4/*mcm*; a=5.5837(2) Å, c=7.8882(5) Å, R_p=17.0%, R_{wp}=27.0%, χ^2=2.80, R_{Bragg}=3.84%						
Ba/Pr	4*b*	0	0.5	0.25	0.35/0.65	2.64(9)
Cu/Ti	4*c*	0	0	0	0.35/0.65	2.0(2)
O1	4*a*	0	0	0.25	1	6.6(6)
O2	8*h*	0.275(5)	0.225(5)	0	1	6.6(6)
$BaNd_2CuTi_2O_9$						
*I*4/*mcm*; a=5.5773(2) Å, c=7.8743(5) Å, R_p=17.5%, R_{wp}=25.9%, χ^2=2.08, R_{Bragg}=6.62%						
Ba/Nd	4*b*	0	0.5	0.25	0.35/0.65	1.5(1)
Cu/Ti	4*c*	0	0	0	0.35/0.65	0.5*
O1	4*a*	0	0	0.25	1	5.8(6)
O2	8*h*	0.273(6)	0.227(6)	0	1	5.8(6)

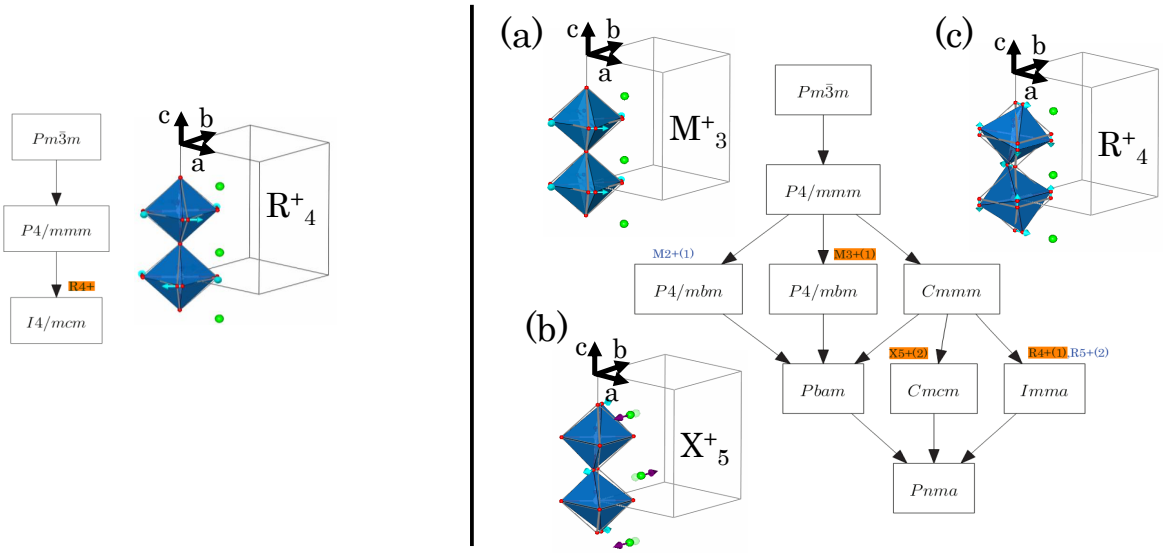

Figure 10.3: Graph of maximal subgroups connecting the space group $Pm\bar{3}m$ and its subgroups (left) $I4/mcm$ (ITA No.140) and (right) $Pbnm$ (ITA No. 62) via the (**a**-**b**,**a**+**b**,2**c**;0,0,0) and (**a**+**b**,**a**-**b**,-2**c**;1/2,1/2,0) transformation matrix, respectively. The active distortion modes are highlighted in orange. Green, blue, and red spheres indicate A/Ln, Cu/Ti, and O atoms, respectively and the archetype phase structure in $Pbnm$ bases is shown with grey octahedra (red sphere as oxygens), and light green spheres indicating A/Ln atoms.

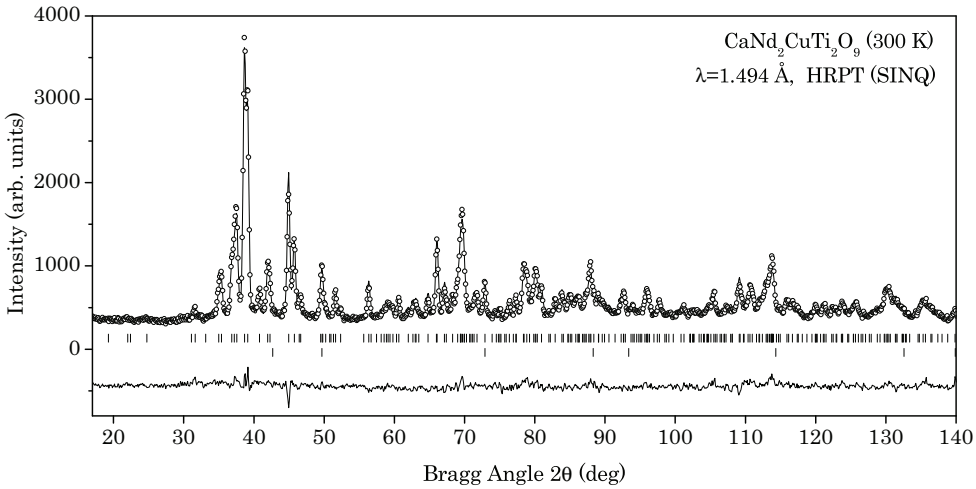

Figure 10.4: Observed (○), calculated (-), and difference of neutron powder diffraction (λ=1.494 Å) Rietveld profiles for $CaNd_2CuTi_2O_9$ at room temperature using structural model with $Pbnm$ space group. In the lower part the Bragg-positions of the phase and steel "impurity" are given.

Table 10.3: Bond lengths (Å), and selected angles (°) for CaLn_2CuTi$_2$O$_9$ (Ln=Pr,Nd,Sm) at room temperature calculated from XRPD pattern with *Pbnm* space group.

	$CaPr_2CuTi_2O_9$	$CaNd_2CuTi_2O_9$	$CaSm_2CuTi_2O_9$
Ca/LnO$_{12}$ polyhedra			
Ca/Ln-O1(×1) (Å)	2.38(2)	2.37(2)	2.31(2)
Ca/Ln-O2(×2) (Å)	2.40(1)	2.38(1)	2.36(1)
Ca/Ln-O1(×1) (Å)	2.48(1)	2.46(2)	2.38(2)
Ca/Ln-O2(×2) (Å)	2.64(1)	2.63(1)	2.61(1)
Ca/Ln-O2(×2) (Å)	2.68(1)	2.67(1)	2.64(1)
Ca/Ln-O1(×1) (Å)	3.15(2)	3.14(2)	3.21(2)
Ca/Ln-O1(×1) (Å)	3.19(1)	3.20(2)	3.35(2)
Ca/Ln-O2(×2) (Å)	3.36(1)	3.37(1)	3.44(1)
<Ca/Ln-O>$_{8\ short}$[a] (Å)	2.54(2)	2.52(2)	2.49(2)
Cu/TiO$_6$ octahedra			
Cu/Ti-O1$_{ax}$(×2) (Å)	1.97(1)	1.97(1)	1.98(1)
Cu/Ti-O2$_{eq}$(×2) (Å)	1.99(1)	1.99(1)	2.01(1)
Cu/Ti-O2'$_{eq}$(×2) (Å)	2.04(1)	2.03(1)	2.03(1)
<Cu/Ti-O> (Å)	2.00(1)	1.99(1)	2.01(1)
∠O1$_{ax}$-Cu/Ti-O2$_{eq}$ (°)	89.4(3)	89.2(3)	90.0(3)
∠O1$_{ax}$-Cu/Ti-O2'$_{eq}$ (°)	89.5(2)	90.4(2)	93.1(2)
∠O2$_{eq}$-Cu/Ti-O2'$_{eq}$ (°)	90.0(2)	90.0(2)	90.4(2)
∠Cu/Ti-O1$_{ax}$-Cu/Ti (°)	154.5(5)	154.1(5)	147.0(5)
∠Cu/Ti-O2$_{eq}$-Cu/Ti (°)	153.3(3)	152.4(3)	150.1(3)

[a] Eight interatomic distances shorter than 3.00 Å.

Bond lengths and selected bond angles for all materials are collected in Table 10.3 and Table 10.4. For comparison, symmetry mode decomposition calculations have been performed and included in Table 10.5 for CaLn_2ZnTi$_2$O$_9$ materials [133]. Cell parameters for CaLn_2BTi$_2$O$_9$ (B=Cu,Zn) and BaLn_2CuTi$_2$O$_9$ are plotted in Figure 10.5; in black, red, and blue color, respectively. Despite the fact that the difference among the transition-metal radius for Cu and Zn is very small, there are significant changes in the structure. Although in both series the relative b cell parameter is the biggest, a and c are exchanged; c is the smallest for Cu series and a for the Zn one. The variation of the b cell parameter along the series compounds is very small compared to that of a and c. $c/2 < a/\sqrt{2} < b/\sqrt{2}$ is characteristic of the so-called O' structure [135], and it is originated by the strong cooperative Jahn-Teller effect, inducing an orbital ordering and distorting of the Cu/TiO$_6$ octahedra. Usually in perovskites, the primary distortion effect is steric and $c/2$ lies between $a/\sqrt{2}$ and $b/\sqrt{2}$, as observed for the Zn compounds [133]. On the one hand, checking the bond lengths for Ca compounds in Table 10.3 there is not a predominant large bond length observed, although Cu/Ti-O2'$_{eq}$ bond length is a little bit larger. The six Cu/Ti-O distances

Table 10.4: Bond lengths (Å), octahedra tilt angles (°), and selected angles (°) for BaLn_2CuTi$_2$O$_9$ (Ln=La,Pr,Nd) at room temperature calculated from XRPD pattern with $I4/mcm$ space group.

	$BaLa_2CuTi_2O_9$	$BaPr_2CuTi_2O_9$	$BaNd_2CuTi_2O_9$
Ba/LnO$_{12}$ polyhedra			
Ba/Ln-O1($\times$4)	2.802(1)	2.792(1)	2.789(1)
Ba/Ln-O1($\times$4)	2.961(7)	3.004(8)	3.024(9)
Ba/Ln-O1($\times$4)	2.649(6)	2.592(7)	2.568(7)
<Ba/Ln-O>	2.804(7)	2.796(8)	2.794(9)
Tilt angle $\psi_{[001]p}$	6.4(2)	8.4(2)	9.3(2)
Cu/TiO$_6$ octahedra			
Cu/Ti-O1$_{ax}$($\times$2)	1.98(1)	1.97(1)	1.97(1)
Cu/Ti-O2$_{eq}$($\times$4)	2.00(1)	2.00(1)	2.00(1)
<Cu/Ti-O>	1.99(1)	1.99(1)	1.99(1)
$\angle$O2$_{eq}$-Cu/Ti-O2'$_{eq}$	90.0(2)	90.0(2)	90.0(2)
$\angle$Cu/Ti-O2$_{eq}$-Cu/Ti	167.2(3)	163.2(3)	161.4(3)

range between 1.95-2.05 Å which are the usually observed distances for Ti-O and Cu-O, respectively. On the other hand, the M_2^+ irrep amplitude, associated to the Jahn-Teller distortion, has small values, probably due to the proportion of the ions occupying the B-site of the perovskite, twice more titanium than copper, the Jahn-Teller effect is not strong enough to be observed as a large distortion in the structure.

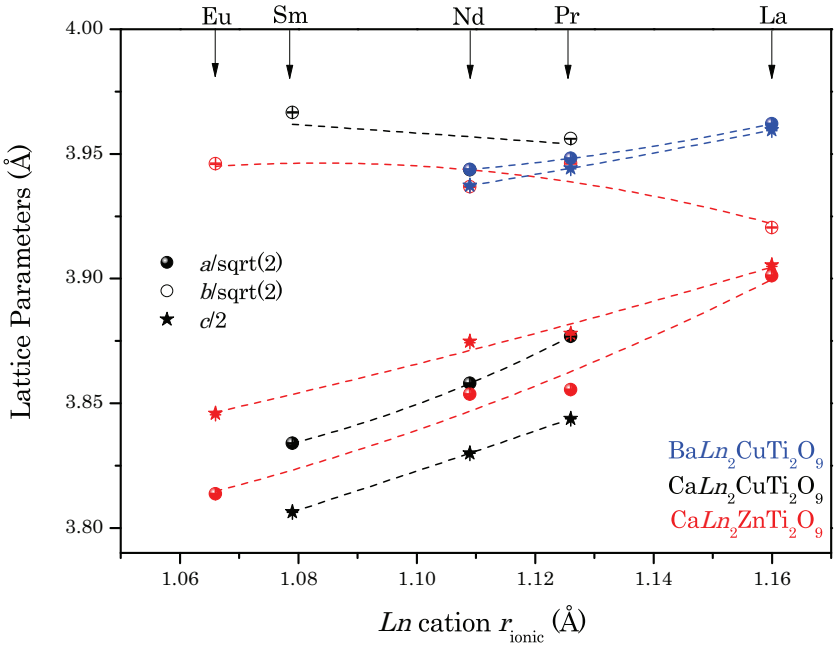

Figure 10.5: Reduced cell parameters as a function of the lanthanide cation ionic radius for $CaLn_2CuTi_2O_9$ (*Ln*=Pr,Nd,Sm) (black), $CaLn_2ZnTi_2O_9$ (*Ln*=La,Pr,Nd,Eu) (red) [133] orthorhombic phases (*Pbnm*), and $BaLn_2CuTi_2O_9$ (*Ln*=La,Pr,Nd) (blue) tetragonal phase (*I*4/*mcm*) at room temperature. The dashed lines are a guide for the eyes.

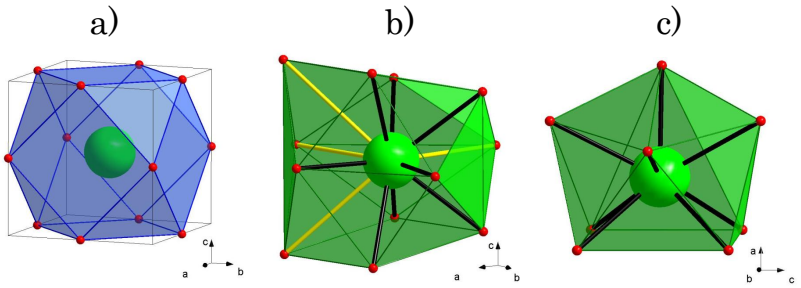

Figure 10.6: The coordination polyhedron for Ca/*Ln* cations occupying the *A*-site of the ABO_3 perovskite; (a) ideal 12-fold coordination (cubo-octahedron), (b) 12-fold coordination of the orthorhombic perovskite (yellow bond larger than the rest), and (c) 8-fold coordination of the orthorhombic perovskite (yellow bonds eliminated to identified the four-fold antiprisma). In (b), black Ca/*Ln*-O bonds indicate the first coordination sphere, whereas the yellow bonds the second. (a) and (b) show the same view, the former in cubic basis and the later in orthorhombic basis. Green, blue and red atoms are representative for Ca/*Ln*, Cu/Ti, and O atoms, respectively.

Table 10.5: Crystal chemistry for CaLn_2CuTi_2O_9 and CaLn_2ZnTi_2O_9 [133] (Ln=La,Pr,Nd,Sm,Eu) perovskites with orthorhombic space group *Pbnm* at room temperature.

	t^a	$t_0{}^b$	$AO_8{}^c$	$< A\text{-O} > (1)^d$	$< A\text{-O} > (2)^e$	$BO_6{}^f$	$< B\text{-O} >^g$	$AO_{12}{}^h$	$\Psi_{[001]}{}^i$	$\Phi_{[110]}{}^j$	R_4^{+k}	M_3^{+l}	X_5^{+m}
Pr	0.877	0.90(2)	26.45(1)	2.54(2)	3.28(2)	10.64(1)	2.00(1)	50.02(1)	9.7(2)	12.8(3)	1.22(3)	0.94(3)	0.53(1)
Nd	0.872	0.90(2)	26.05(1)	2.52(2)	3.27(2)	10.56(1)	1.99(1)	49.46(1)	10.1(2)	12.9(4)	1.25(4)	0.95(4)	0.55(1)
Sm	0.866	0.88(2)	25.33(1)	2.49(2)	3.36(2)	10.74(1)	2.01(1)	49.18(1)	11.5(2)	16.0(1)	1.40(4)	1.09(4)	0.70(2)
Crystal chemistry of CaLn_2ZnTiO_9 [133]													
La	0.883	0.921(1)	26.97(1)	2.60(1)	3.15(1)	10.55(1)	1.99(1)	50.66(1)	8.25(7)	11.203(1)	1.052(7)	0.812(9)	0.298(1)
Pr	0.875	0.885(1)	25.82(1)	2.52(1)	3.33(1)	10.85(1)	2.02(1)	49.79(1)	8.96(8)	18.407(1)	1.518(9)	0.863(9)	0.571(3)
Nd	0.871	0.892(1)	25.92(1)	2.53(1)	3.29(1)	10.70(1)	2.00(1)	49.82(1)	9.72(7)	14.904(1)	1.336(7)	0.949(8)	0.556(3)
Eu	0.861	0.879(1)	25.28(1)	2.49(1)	3.35(1)	10.74(1)	2.00(1)	49.01(1)	10.66(5)	16.053(1)	1.473(5)	1.036(5)	0.669(2)

[a] t Goldschmidt tolerance factor, calculated from tabulated Shannon radii [48].

[b] t_0 observed tolerance factor, calculated from observed interatomic distances.

[c,h] AO_8 and AO_{12} volumes of polyhedra (Å^3) with A-site cation in eight- and twelve-fold coordination.

[d,e] $< A\text{-O} >$(1) and $< A\text{-O} >$(2) mean-bond lengths (Å) for the first and second coordination spheres.

[f] BO_6 volume of octahedra (Å^3) with B-site cation in six-fold coordination.

[g] $< B\text{-O} >$ mean-bond lengths (Å) for BO_6 polyhedra.

[i,j] $\Psi_{[001]}$ and $\Phi_{[110]}$ octahedra tilt angles (°) along [001] and [110] cubic perovskite directions.

[k,l,m] R_4^+, M_3^+ and X_5^+ distortion irrep amplitudes (Å).

$CaLn_2CuTi_2O_9$ structure refinements revealed that the A cation in ABO_3 is surrounded by twelve neighboring O atoms at distances ranging from 2.31(2) to 3.44(1) Å for CaSm and 2.38(2) to 3.36(1) Å for CaPr Table 10.3. Even replacing a larger cation in the A-site of the perovskite comparing to that in $CaTiO_3$, the $CaLn_2CuTi_2O_9$ compounds are characterized by a large distortion. As expected for such distorted structures, the A-site coordination polyhedron is completely distorted, as can be observed in Figure 10.6. Four of the twelve A-O bonds are longer than 2.7 Å Figure 10.6(b)(yellow bonds); in spite of the replacement by a larger cation, those bonds become shorter Figure 10.7(a). The other eight shortest A-O bond lengths conforming the first coordination sphere become longer by the substitution of a larger lanthanide cation Figure 10.7(a). That trend has been reported in other lanthanide containing compounds [45, 46, 125]. It is a common behavior for all of them that the radius of the first coordination sphere (limited by the eighth shortest bonds) increases, whereas the radius of the second coordination sphere (limited by the eighth to the twelfth shortest bonds) decreases with the substitution of a larger lanthanide in A-site. The reason to achieve the coordination polyhedra with lower coordination than $^{xii}Ln^{3+}$ is the tilting of B-cation surrounding octahedra, to compensate for the misfit of the lanthanide cations in the interstitial space amongst the octahedra. Comparing the results for Cu and Zn families, the mean first and second coordination sphere bond lengths are similar for compounds with the same lanthanide cation Figure 10.7(a); the B-site cation chemical pressure is not enough to cause important changes in the distances.

When the minimum A-B distance is shorter than the maximum A-O distance, the B-cation gets inside the second coordination sphere. Marezio *et al.* [44] suggested that this fact promotes the lengthening of the second coordination sphere radius, due to a screening effect. In Figure 10.7(b) it is shown the B-site cation position for each material. It is clearly seen that for all compounds, except for $CaLa_2ZnTi_2O_9$, the B-cation is inside the second coordination sphere: the minimum A-B distance is always shorter than the maximum A-O. It is worth mentioning that as happened with the first and second coordination sphere distances, the largest A-O distance and shortest A-B distance are the same for the compounds with the same lanthanide.

The change in symmetry with alkaline-earth and lanthanide substitution is necessarily related to the relative volume expansions of the lanthanide cation polyhedra. The smaller Ψ and Φ angles of the octahedral linkage when increasing the lanthanide size reduces the deformation of the polyhedra, as the so-called Goldschmidt or tolerance factor (which quantifies the misfit of the size of the three sites ions) increases Figure 10.7(e). Although for Ca or Ba compounds the symmetry is maintained due to small differences among lanthanide cations it is clearly observed the reduction of the distortion: the ampli-

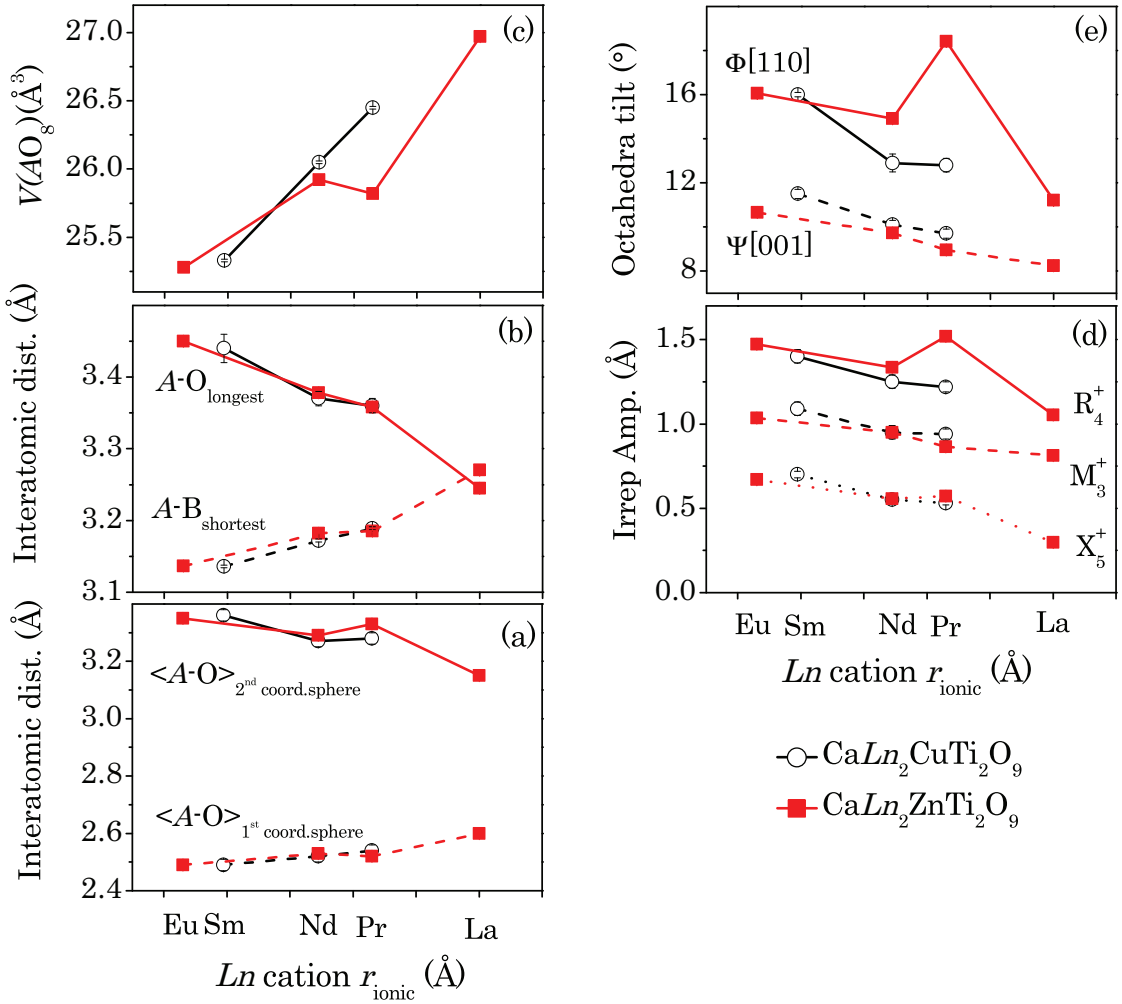

Figure 10.7: Variation of (a) mean A-O bond lengths (Å) for first coordination sphere (<A-O>(1)) and second coordination sphere (<A-O>(2)); (b) A-B interatomic minimum distances and A-O maximum distances (Å); (c) first coordination sphere volume (Å^3) (AO_8); (d) distortion irrep amplitudes for $Pm\bar{3}m \rightarrow Pbnm$ symmetry breaking; and (e) Cu/TiO_6 octahedra $\Phi_{[110]p}$ and $\Psi_{[001]p}$ tilt angles (°), for CaLn_2CuTi_2O_9 (black circle) and CaLn_2ZnTi_2O_9 [133] (red square) compounds at room temperature.

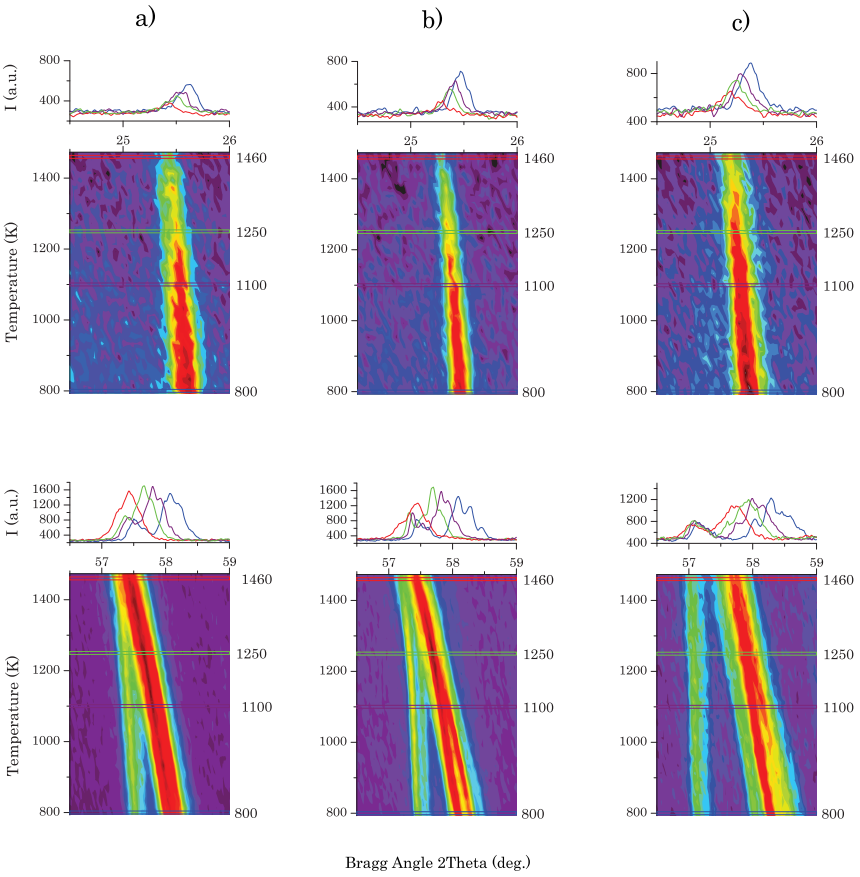

Figure 10.8: Extracts from the laboratory X-ray diffraction ($\lambda_{K\alpha1}$=1.5406 Å and $\lambda_{K\alpha2}$=1.5444 Å) pattern projections for (a) $CaPr_2CuTi_2O_9$, (b) $CaNd_2CuTi_2O_9$ and (c) $CaSm_2CuTi_2O_9$ from 800 to 1460 K, showing the evolution of the (111) primitive reflection and (221) cubic reflection as a function of temperature.

tude of the main distortion modes decrease from 1.40(4) Å for CaSm to 1.22(3) Å for CaPr compound, and from 0.35(9) Å for BaNd to 0.27(6) Å for BaLa.

Even having a relatively large distortion in the Ca containing materials, it might be possible to induce a structural phase transition while heating the sample at high temperatures. With that purpose, to observe experimentally the possible temperature induced phase transitions, high temperature conventional X-ray powder diffraction measurements were performed from 770 to 1670 K, Figure 10.8. It is noted that the peak positions shift to lower 2θ, due to the thermal expansion. In the upper part of Figure 10.8, the 24.5-26° 2θ range is plotted, showing the (111) reflection in the orthorhombic space group *Pbnm* (related to *hkl* reflections with $h+k+l=2n+1$); and in the lower part the cubic (221) reflection, as function of temperature. It is clearly observed that the (111) reflection does not disappear at higher temperatures, indicating, at most, a structural phase transition to another

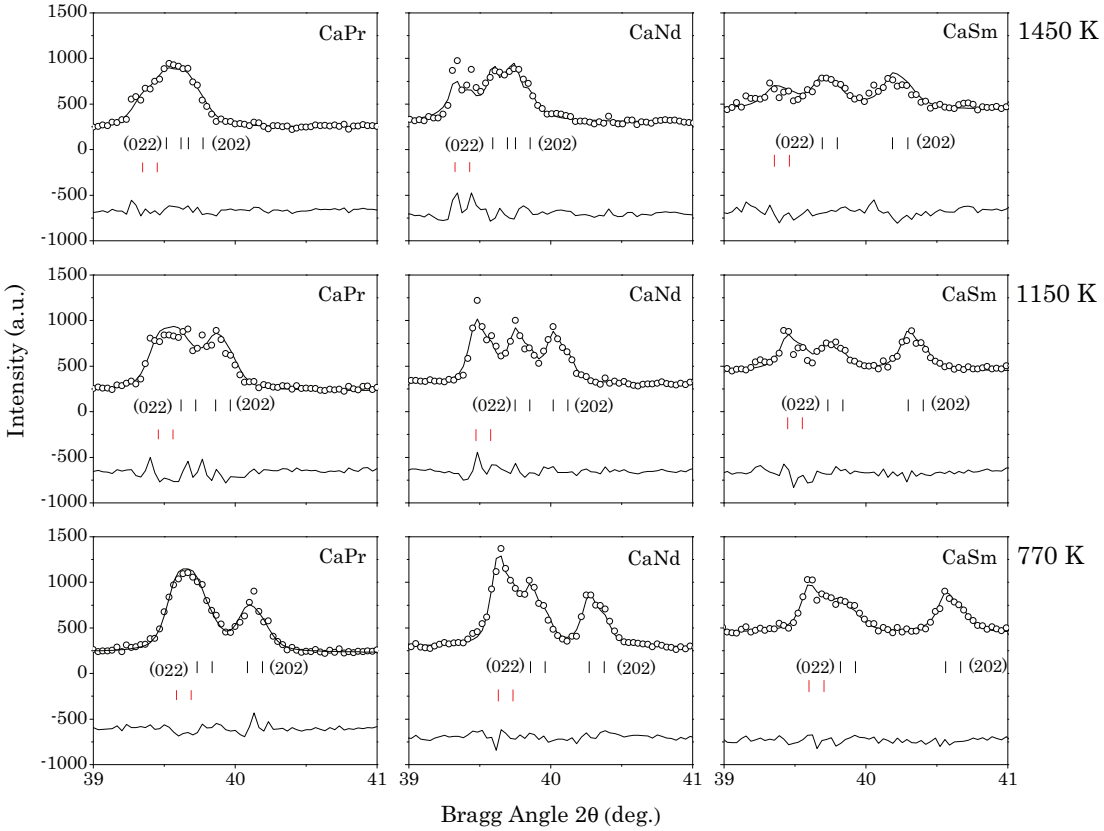

Figure 10.9: Portion of the laboratory X-ray powder diffraction ($\lambda_{K\alpha 1}$=1.5406 Å and $\lambda_{K\alpha 2}$=1.5444 Å) profiles for $CaLn_2CuTi_2O_9$ showing the evolution in temperature of the (002)-(202) reflections in *Pbnm*, at 770 K, 1150 K and 1450 K. The bars in the lower part of the graphics correspond to the Bragg reflections' positions; red (lower) bars indicate impurity phase (diffractometer platinum filament).

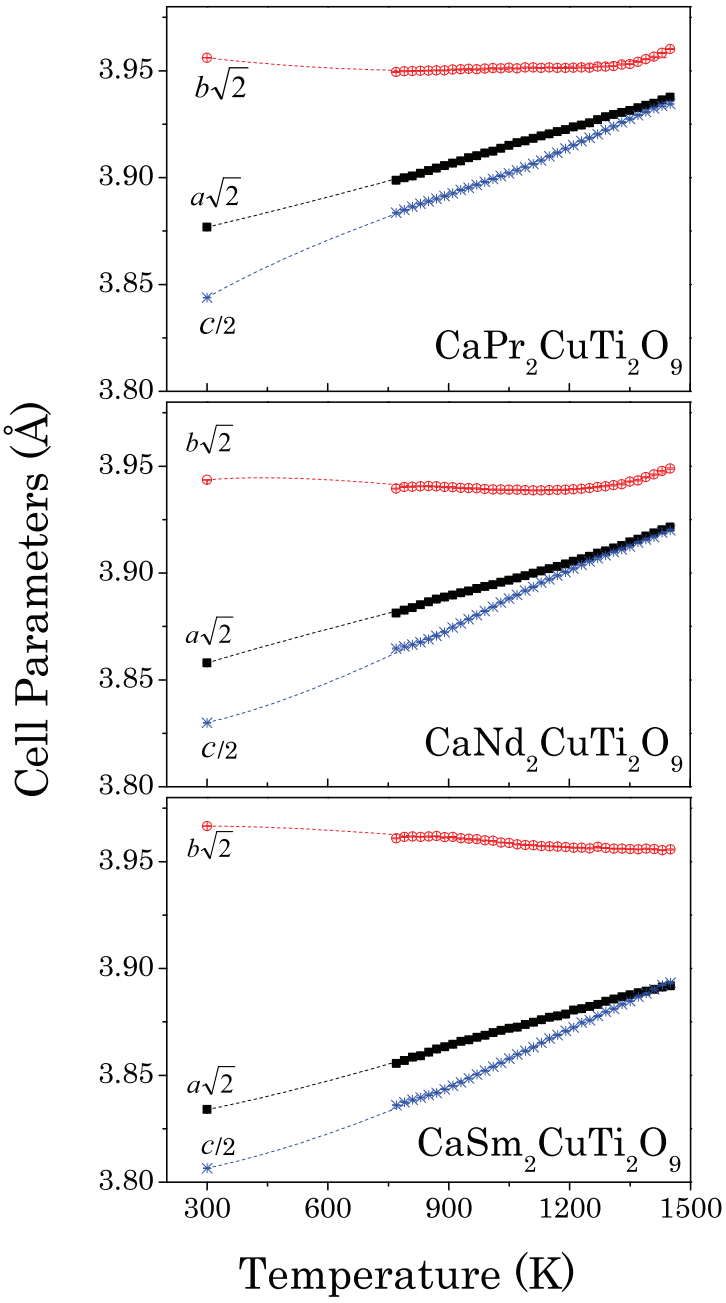

Figure 10.10: Variation of the reduced cell parameters in the orthorhombic phase (space group *Pbnm*) with temperature for $CaLn_2CuTi_2O_9$ (*Ln*=Pr,Nd,Sm) from laboratory X-ray diffraction patterns. Dashed lines between points are guide to the eyes.

primitive space group, or to another space group with $h+k+l=2n+1$ reflection condition, *e.g*. *Cmcm* space group. However, the diffraction pattern analysis does not reveal any hiding of peaks at high temperatures; although CaPr X-ray diffraction data at 1450 K could be refined in *Cmcm* space group. The $K_{\alpha 1}$ and $K_{\alpha 2}$ Cu wavelengths at X-ray high temperature measurements makes difficult to see the splitting of (022,202) type reflections in *Pbnm* Figure 10.9.

In Figure 10.10 thermal evolution of the cell parameters in *Pbnm* symmetry is shown for Ca containing compounds. The trend followed by the three compounds is similar: *b* cell parameter almost remains unchanged along 1200 K, and *a* and *c* cell parameters expand. The cubic (221) reflection shown in the lower part of Figure 10.8 is split into (132)(024)(312)(204) reflections in the orthorhombic *Pbnm* bases. The (024)(312)(204) peaks shift to lower 2θ position with an increase of temperature, while (132) peak position dose not change as much; associated to the almost constant value of *b* lattice. Although peak temperature evolution suggest a getting together of the orthorhombic reflections, and a possible phase transition to *Cmcm* space group could happened, from our data we cannot conclude with certainty if any other phase is observed at high temperatures for $CaPr_2CuTi_2O_9$. Nevertheless, we can conclude that $CaNd_2CuTi_2O_9$ and $CaSm_2CuTi_2O_9$ materials do not suffer any reversible phase transition. Quite the contrary, we observed an irreversible phase-transformation at about 1475 K for all Ca compounds. The irreversibility of the materials is clearly seen in Figure 10.11, since the pattern at RT after annealing at 1500 K shows a completely different diffraction profile.

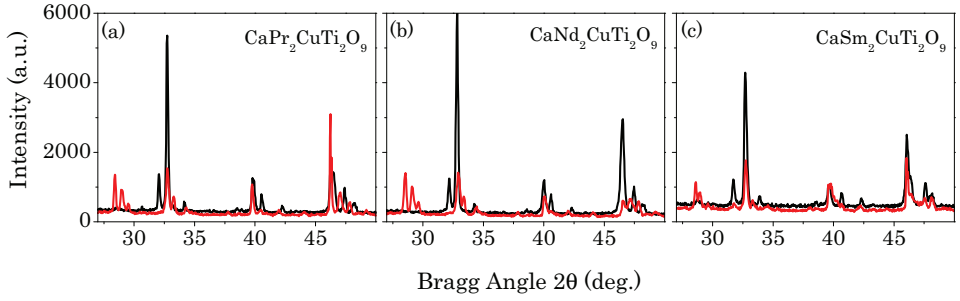

Figure 10.11: X-ray powder diffraction patterns for (a) $CaPr_2CuTi_2O_9$, (b) $CaNd_2CuTi_2O_9$, and (c) $CaSm_2CuTi_2O_9$ at RT, (black) before, and (red) after annealing at 1500 K. The irreversibility of the samples is clearly observed.

10.2 Conclusions

The series $ALn_2CuTi_2O_9$ (A=Ba,Ca; Ln=La,Pr,Nd,Sm) have been synthesized at 1570 K by solid-state synthesis technique. Their structures have been determined by the Rietveld refinement of symmetry adapted modes of powder X-ray diffraction patterns at room and high temperature. Ca compounds adopt the *Pbnm* orthorhombic space group, whereas for the Ba compounds, the crystal system is tetragonal (space group $I4/mcm$).

The effect of the A-site lanthanide size (via the tolerance factor) on the RT structures has been quantified by symmetry mode amplitudes: the larger the homovalent substituted lanthanide cation size ($r_{La}>r_{Pr}>r_{Nd}>r_{Sm}$), the smaller are the mode amplitudes; which means that the structure is more symmetric. An equal observation is done among materials sharing the same type of lanthanide with different alkali earth metals (Ca or Ba). Since the ionic radius of Ba cation is much bigger than Ca cation radius, the former structures have a smaller distortion grade than the laster ones.

Orthorhombic structures contain distorted coordination polyhedra of A-site ions, and it is achieved with lower coordination than $^{xii}Ln^{3+}$, estimated from the A-O distances. Two groups of distances for A-O lengths are clear, belonging to first and to the second coordination spheres. Although A-O bond lengths in the first coordination sphere are larger by substitution of a bigger lanthanide, the second coordination sphere bond lengths show the opposite trend.

The temperature dependence of Ca compound structures have been investigated up to 1670 K. From our experimental data we cannot conclude if the heating of the sample induces a reversible structural phase transition to a more symmetric space group; however around 1475 K an irreversible transition is observed.

Part III

Conclusions and future work

Final Remark and Conclusions

The main conclusions of the work presented in this memory are the following:

1. Lanthanide and ruthenium-containing 13 (10 for the first time) double perovskites have been synthesized at ambient pressure in air by standard Solid State Reaction method:
   - Sr$Nd$$M$$RuO_6$ (M=Zn,Co,Mg,Ni)
   - Sr$Pr$$M$$RuO_6$ (M=Zn,Co,Mg,Ni)
   - Sr$La$$M$$RuO_6$ (M=Zn,Mg)
   - Sr$Ln$$FeRuO_6$ (Ln=La,Pr,Nd)
2. 6 new compounds of $ALn_2CuTi_2O_9$ family have been synthesized by conventional Solid State Reaction method:
   - Ca$Ln_2CuTi_2O_9$ (Ln=La,Nd,Sm)
   - Ba$Ln_2CuTi_2O_9$ (Ln=La,Pr,Nd)
3. All synthesized materials have been structurally characterized at room temperature by conventional X-ray, synchrotron, and/or neutron diffraction techniques:
   - The results obtained by Dr. Milen Gateshki for $SrLaZnRuO_6$, $SrLaMgRuO_6$ and $SrLaFeRuO_6$ compounds by conventional X-ray diffraction techniques agree with the results presented in this work.
   - The rest of the compound structures have been characterized for the first time.
   - Room temperature symmetries for Sr$Ln$$M$$RuO_6$ compounds are:
     - Orthorhombic *Pbnm* for $SrLaFeRuO_6$, $SrPrFeRuO_6$ and $SrNdFeRuO_6$.

  - Monoclinic $P2_1/n$ for SrLaMRuO$_6$ (M=Zn,Mg), SrPrMRuO$_6$ (M=Zn,Co,Mg,Ni) and SrNdMRuO$_6$ (M=Zn,Co,Mg,Ni)
- Room temperature symmetries for ALn_2CuTi$_2$O$_9$ compounds are:
  - Tetragonal $I4/mcm$ for BaLa$_2$CuTi$_2$O$_9$, BaPr$_2$CuTi$_2$O$_9$ and BaNd$_2$CuTi$_2$O$_9$.
  - Orthorhombic $Pbnm$ for CaLa$_2$CuTi$_2$O$_9$, CaNd$_2$CuTi$_2$O$_9$ and CaSm$_2$CuTi$_2$O$_9$.

4. The refinement process of the structures have been done using the *symmetry-adapted modes* as degree of freedom of the structure:
   - Symmetry-mode decomposition of the model structures have been obtained by AMPLIMODES for FullProf; identifying the primary modes in some cases.
   - Active modes of the different symmetry-breaking have been identified by refinement process.
     - $Fm\bar{3}m \rightarrow P2_1/n$: GM_4^+, X_3^+, (X_5^+)
     - $Fm\bar{3}m \rightarrow P4_2/n$: GM_4^+, X_3^+, (X_5^+)
     - $Fm\bar{3}m \rightarrow R\bar{3}$: GM_4^+
     - $Pm\bar{3}m \rightarrow Pbnm$: R_4^+, M_3^+, (X_5^+)
     - $Pm\bar{3}m \rightarrow R\bar{3}c$: R_4^+
     - $Pm\bar{3}m \rightarrow I4/mcm$: R_4^+
   - The room temperature monoclinic SrLnMRuO$_6$, orthorhombic SrLnFeRuO$_6$ and CaLn_2CuTi$_2$O$_9$, or tetragonal BaLn_2CuTi$_2$O$_9$ phases have been classified respect to their observed tolerance factor and active mode amplitudes, showing a general trend: closer the tolerance factor from one, smaller are the distortion mode amplitudes, more symmetric is the structure (Figure 10.12).

5. For SrLaFeRuO$_6$, SrPrFeRuO$_6$ and SrNdFeRuO$_6$ compounds a disordered configuration of B- and B'-site cations have been observed.

6. The rest SrLnMRuO$_6$ compounds show B- and B'-site cation ordering.

7. High temperature structures have been analyzed in 14 of the samples by X-ray and/or neutron studies. Previously, group theory have been used in order to identified the possible phase transitions.
   - $P2_1/n \rightarrow P4_2/n \rightarrow Fm\bar{3}m$ no common phase transition sequence have been observed for SrNdMRuO$_6$ (M=Zn,Co,Mg,Ni) compounds. It is a first-order phase transition.

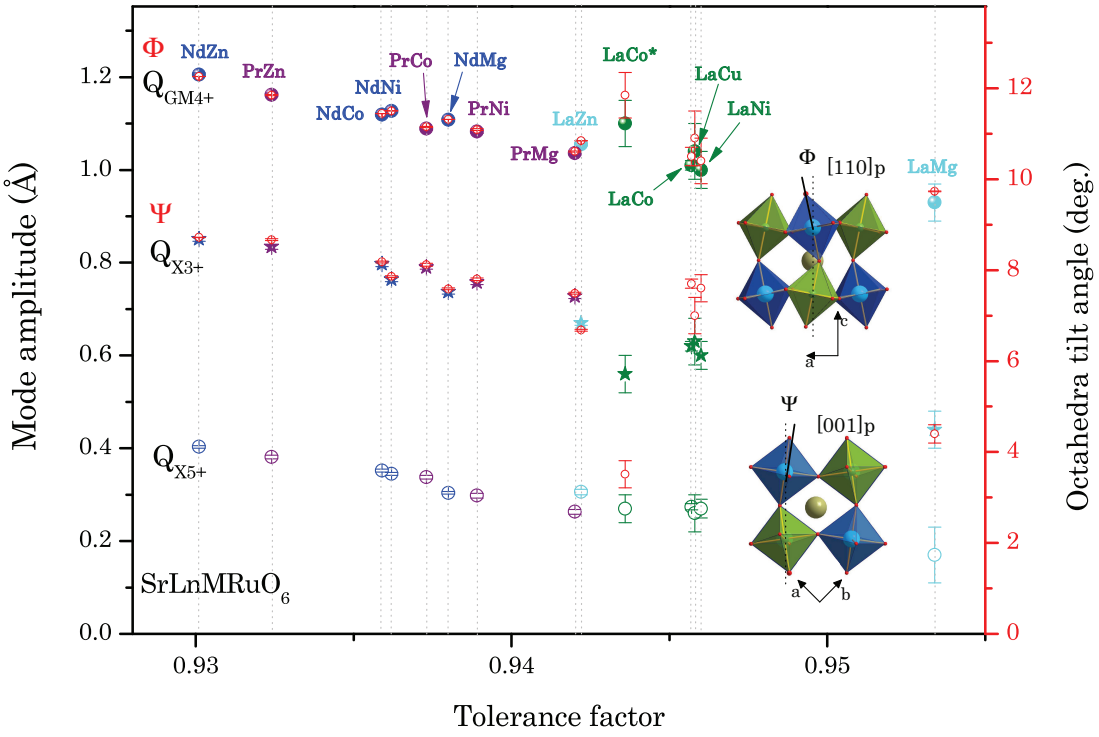

Figure 10.12: Amplitudes of GM_4^+ (fill circles), X_3^+ (stars) and X_5^+ irreps (empty circles) conforming the RT phase of the $SrLaMRuO_6$ (M=Zn^a, Mg^a) (light-blue), $SrLaMRuO_6$ (M=Cu^b [116], Ni^b [116], Co^{*c} [111], Co^a [115]), $SrNdMRuO_6$ (M=Zn^a, Co^a, Mg^a, Ni^a) (dark-blue) and $SrPrMRuO_6$ (M=Zn^a, Co^a, Mg^a, Ni^a) (purple) compounds, and Ψ and Φ tilt angles (red symbols), as obtained from the NPD^a, synchrotron radiation^b or XRPD^c data refinement, in function of calculated tolerance factors. Lines are guide to the eyes.

- $P2_1/n \rightarrow R\bar{3}$ first-order phase transition sequence for $SrPrMgRuO_6$ and $SrPrNiRuO_6$ compounds is observed.
- No phase transition is observed for $SrPrZnRuO_6$ up to 1360 K.
- $SrLaZnRuO_6$ and $SrLaMgRuO_6$ compounds show a first-order $P2_1/n \rightarrow R\bar{3}$ phase transition, with a coexistence range of ∼150 K.
- $Pbnm \rightarrow R\bar{3}c$ first-order phase transition is observed for $SrPrFeRuO_6$ compound.
- No phase transition is observed for $CaPr_2CuTi_2O_9$ and $CaNd_2CuTi_2O_9$ materials up to 1475 K. However, for $CaLa_2CuTi_2O_9$ material $Pbnm \rightarrow Cmcm$ phase transition could happen, although it is not possible to say with certainty if the transition has taken place.

8. A phase-diagram has been tried to construct for SrLnMRuO$_6$ series Figure 10.13. A

general trend is observed for all compounds in the transition temperatures: smaller the distortion mode amplitudes (more symmetric the structure), smaller is the transition temperature.

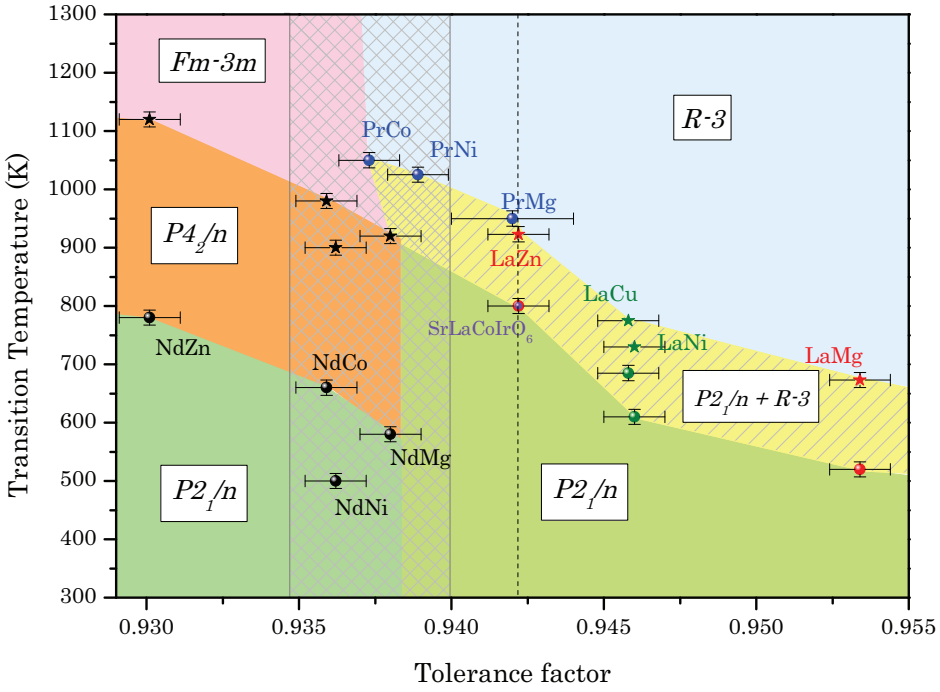

Figure 10.13: Tolerance factor and temperature dependence phase diagram of $SrLaMRuO_6$ (M=Zn(PW),Cu[116],Mg(PW),Ni[116]), $SrNdMRuO_6$ (M=Zn,Co,Mg,Ni) [120] and $SrPrMRuO_6$ (M=Co,Mg,Ni) [125]. PW stands for present work. Two green tonality are used in $P2_1/n$ phase to distinguish the different transition sequences. Two-phase region separating $P2_1/n$ from $R\bar{3}$ is shown in striped-yellow area. Grilled area highlights two phase transition overlapped area. Vertical dotted line is indicative of the same theoretical tolerance factor for $SrLaZnRuO_6$ and $SrLaCoIrO_6$ [127].

9. Magnetic structures have been characterized by NPD technique for $SrLaFeRuO_6$, $SrPrFeRuO_6$ and $SrNdFeRuO_6$ compounds.

   - In disagreement with found in the bibliography [114] $SrLaFeRuO_6$ material shows magnetic ordering at room temperature. The magnetic moment is due to the entity formed by disordered arrangements of Fe and Ru cations in 4*a* Wyckoff site. The model describes a spin canted-AFM structure.
   - Magnetic ordering is also observed for $SrPrFeRuO_6$ and $SrNdFeRuO_6$ compounds at room temperature. $SrNdFeRuO_6$ is ferromagnetic. $SrPrFeRuO_6$ shows a more complex magnetic structure, due to the presence of two magnetic sites generated by Pr and Fe/Ru entity; shows a strictly ferrimagnetic structure.

Future work

The current study has been focused on the research topic of structural characterization and phase transition studies of perovskite-like materials. Previously Dr. M. Gateshki [136] and Dr. A. Faik [137] have worked on it. In this thesis, apart of studying new families of double and triple perovskites (Sr$Ln M$RuO$_6$ and AA'_2CuTi$_2$O$_9$), has gain importance a different approach of analyzing the structures. The symmetry-mode analysis perspective has been used, which was already mentioned at the last part of the thesis of Dr. Faik. In general, the use of symmetry adapted modes in the description of distorted structures, introduces a natural physical hierarchy between the structural parameters. This can be useful not only for investigating the physical mechanisms that stabilize the phase, but also for pure crystallographic purposes, as has been shown along the work presented in this manuscript.

This work opens a new window towards a new perspective in the study of crystalline structures; that still nowadays, is not very popular between the researchers. But has been seen along the manuscript that it is a very powerful analysis method, for example to study isostructural materials.

Further work will focused on a new family of perovskite type materials prone to form *A*-site layered and *B*-site ordered or disordered cation arrangement; using the symmetry-mode analysis instead of refining the atomic coordinates in the Rietveld refinements. For that purpose, since the difference in oxidation state is an important contributing factor, Sr^{2+} will be substituted by Na^{1+} ion in Sr$Ln B$RuO$_6$ formula.

We have recently begun investigating NaLaCrRuO$_6$ and NaNdCrRuO$_6$ materials; trying to crystallize Na and *Ln* cations in a *A*-site layered arrangement, whereas Cr and Ru ions disordered in *B* perovskite site. Several synthesis methods will be used with the

aim of crystallizing two different type of materials, with A-site layered and B-site ordered or disordered arrangement (Figure 10.14).

The analysis of these new materials could help to answer the unexpected tendency for A-site cations to order (into layers), since the A-site cation ordering is much less common than B-site cation ordering.

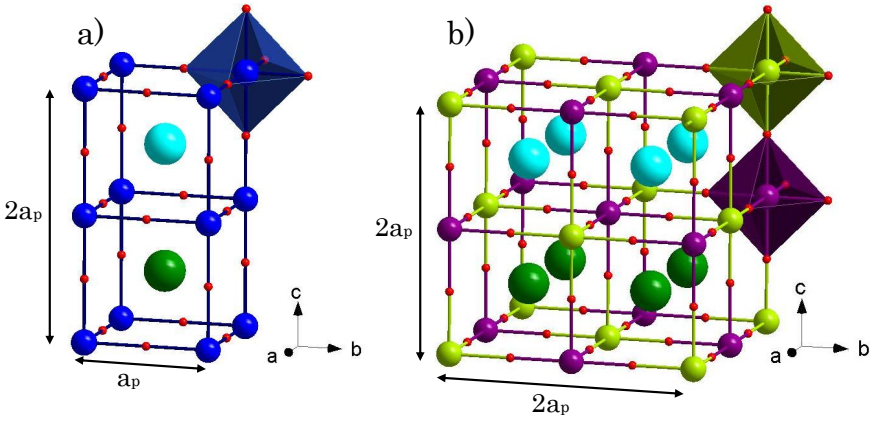

Figure 10.14: Cation ordering schemes for A-site 2D (layered) ordering in $AA'BB'O_6$ perovskites, B and B' completely (a) disordered and (b) ordered arrangement.

Appendices

Appendix A

Symmetry-mode decomposition of the structures

During the thesis multiple phases symmetry mode decompositions have been done, in some cases for comparative purpose and in some others cases for rejecting the models. In order not to lose all the calculations and for a future need, all the information is collected in the following pages.

In the first two tables (Table A.1 and Table A.2) the initial information for Amplimodes and the results of the symmetry-mode decomposition for SrLaMRuO$_6$ materials [111, 115, 124] and for CaLn_2CuTi$_2$O$_9$ [133] are shown. The irrep amplitudes listed in the Table A.1 and Table A.2 have been used for comparative purposes along the manuscript in Chapter 7 and in Chapter 10, respectively.

The rest of the information is divided in two different sections. In the former, the structural information of the SrNdMRuO$_6$, SrPrMRuO$_6$, SrLaMRuO$_6$ and SrLnFeRuO$_6$ phases, and in the laster some other perovskites structural information is written; in both cases in user friendly format for Bilbao Crystallographic Server Programs; giving all the necessary information for Amplimodes calculations.

Table A.1: Input information for AMPLIMODES (1/2a-1/2b,1/2a+1/2b,c;0,0,0 transformation matrix) and symmetry mode decomposition for $SrLaCuRuO_6$ [116], $SrLaNiRuO_6$ [116], $SrLaCoRuO_6$ [115] and $SrLaCoRuO_6{}^*$ [111] monoclinic ordered double perovskites.

225
7.9209 7.9209 7.9209 90.00 90.00 90.00
6

Ru	1	4a	0.00000	0.00000	0.00000
M	1	4b	0.50000	0.50000	0.50000
Sr	1	8c	0.25000	0.25000	0.25000
O	1	24e	0.24714	0.00000	0.00000

$SrLaNiRuO_6$ [116]
14
5.5759(1) 5.5422(1) 7.8490(1) 90.00 90.00(1) 90.00
6

Ru	1	2a	0.50000	0.50000	0.50000
Ni	1	2b	0.50000	0.50000	0.00000
Sr	1	8c	0.0026(4)	0.5206(1)	0.2497(2)
O	1	4e	0.289(2)	0.776(2)	0.037(3)
O	2	4e	0.234(2)	0.277(2)	0.026(3)
O	3	4e	-0.063(2)	0.995(1)	0.255(2)

$SrLaCuRuO_6$ [116]
14
5.6052(1) 5.5724(1) 7.8420(1) 90.00 89.982(1) 90.00
6

Ru	1	2a	0.50000	0.50000	0.50000
Cu	1	2b	0.50000	0.50000	0.00000
Sr	1	8c	0.0029(7)	0.5193(2)	0.2499(8)
O	1	4e	0.287(3)	0.776(4)	0.037(4)
O	2	4e	0.233(4)	0.282(4)	0.025(5)
O	3	4e	-0.069(2)	0.995(2)	0.257(3)

$SrLaCoRuO_6$ [115]
14
5.5903(2) 5.5639(2) 7.8744(2) 90.00 90.03(1) 90.00
6

Ru	1	2a	0.50000	0.50000	0.50000
Co	1	2b	0.50000	0.50000	0.00000
Sr	1	8c	0.0033(6)	0.5218(4)	0.251(1)
O	1	4e	0.2886(8)	0.780(1)	0.0355(6)
O	2	4e	0.2324(9)	0.274(1)	0.0264(7)
O	3	4e	-0.0662(5)	0.0938(6)	0.255(1)

$SrLaCoRuO_6{}^*$ [111]
14
5.5693(3) 5.5679(3) 7.8858(3) 90.00 90.28(1) 90.00
6

Ru	1	2a	0.50000	0.50000	0.50000
Co	1	2b	0.50000	0.50000	0.00000
Sr	1	8c	-0.0026(6)	0.5206(1)	0.2554(3)
O	1	4e	0.268(3)	0.763(3)	0.040(2)
O	2	4e	0.225(4)	0.294(4)	0.029(3)
O	3	4e	-0.070(3)	0.993(1)	0.263(2)

Irrep	Isotropy subgroup	Dim	Amplitude (Å)			
			$SrLaNiRuO_6$	$SrLaCuRiO_6$	$SrLaCoRuO_6$	$SrLaCoRuO_6{}^*$
GM_1^+	$Fm\bar{3}m$	1	0.23(3)	0.26(5)	0.19(1)	0.31(5)
GM_3^+	$I4/mmm$	1	0.01(4)	0.01(5)	0.01(1)	0.09(5)
GM_4^+	$C2/m$	1	1.00(4)	1.04(6)	1.01(1)	1.10(5)
GM_5^+	$C2/m$	4	0.13(3)	0.10(5)	0.16(1)	0.45(2)
X_2^+	$P4_2/mnm$	1	0.01(3)	0.02(5)	0.01(1)	0.08(4)
X_3^+	$P4/mnc$	1	0.60(3)	0.63(5)	0.62(1)	0.56(4)
X_5^+	$Pnnm$	3	0.27(2)	0.26(4)	0.274(7)	0.27(3)
Global distortion (Å)			1.2266	1.2717	1.2440	1.3810

K-vector: GM_1^+ (0,0,0), GM_3^+ (0,0,0), GM_4^+ (0,0,0), GM_5^+ (0,0,0), X_2^+ (0,1,0), X_3^+ (0,1,0), X_5^+ (0,1,0)
Direction: GM_1^+ (a), GM_3^+ (a,0), GM_4^+ (a,a,0), GM_5^+ (-b,a,-a), X_2^+ (0,a,0), X_3^+ (0,a,0), X_5^+ (a,a,0,0,a,-a)

Table A.2: Input information for AMPLIMODES (a+b,a-b,-2c;0.5,0.5,0 transformation matrix) and symmetry mode decomposition for CaLn_2ZnTi_2O_9 (Ln=La,Pr,Nd,Eu) [133] orthorhombic disordered perovskites.

221
3.8438 3.8438 3.8438 90.00 90.00 90.00
3

Ti	1	1a	0.00000	0.00000	0.00000
Ca	1	1b	0.50000	0.50000	0.50000
O	1	3d	0.50000	0.00000	0.00000

$(CaLa_2)(ZnTi_2)O_9$
62
5.5171(2) 5.5444(2) 7.8109(5) 90.00 90.00 90.00
4

Ti	1	4b	0.50000	0.00000	0.00000
Ca	1	4c	0.9963(5)	0.0269(1)	0.25000
O	1	4c	0.0699(5)	0.4947(3)	0.25000
O	2	8d	0.7201(7)	0.2948(5)	0.0335(4)

$(CaPr_2)(ZnTi_2)O_9$
62
5.4524(2) 5.5807(2) 7.7559(5) 90.00 90.00 90.00
4

Ti	1	4b	0.50000	0.00000	0.00000
Ca	1	4c	0.9909(4)	0.0473(2)	0.25000
O	1	4c	0.1160(5)	0.4771(6)	0.25000
O	2	8d	0.7110(7)	0.2904(5)	0.0407(5)

$(CaNd_2)(ZnTi_2)O_9$
62
5.4498(2) 5.5675(2) 7.7496(5) 90.00 90.00 90.00
4

Ti	1	4b	0.50000	0.00000	0.00000
Ca	1	4c	0.9905(3)	0.0467(1)	0.25000
O	1	4c	0.0922(5)	0.4792(6)	0.25000
O	2	8d	0.7101(6)	0.2974(5)	0.0408(4)

$(CaEu_2)(ZnTi_2)O_9$
62
5.3933(2) 5.5806(2) 7.6917(5) 90.00 90.00 90.00
4

Ti	1	4b	0.50000	0.00000	0.00000
Ca	1	4c	0.9869(4)	0.0561(1)	0.25000
O	1	4c	0.0992(5)	0.4747(3)	0.25000
O	2	8d	0.7037(4)	0.2990(3)	0.0462(2)

Irrep	Isotropy subgroup	Dim	Amplitude (Å)			
			$(CaLa_2)(CuTi_2)O_9$	$(CaPr_2)(CuTi_2)O_9$	$(CaNd_2)(CuTi_2)O_9$	$(CaEu_2)(CuTi_2)O_9$
R_4^+	*Imma*	1	1.052(7)	1.518(9)	1.336(7)	1.473(5)
R_5^+	*Imma*	1	0.046(6)	0.284(8)	0.132(5)	0.152(4)
X_5^+	*Cmcm*	1	0.298(1)	0.571(3)	0.556(3)	0.669(2)
M_2^+	*P*4/*mbm*	4	0.162(9)	0.015(9)	0.082(8)	0.029(5)
M_3^+	*P*4/*mbm*	1	0.812(9)	0.863(9)	0.949(8)	1.036(5)
Global distortion (Å)			1.3727	1.8588	1.7375	1.9273

K-vector: R_4^+ (1/2,1/2,1/2), R_5^+ (1/2,1/2,1/2), X_5^+ (0,1/2,0), M_2^+ (1/2,1/2,0), M_3^+ (1/2,1/2,0)
Direction: R_4^+ (0,a,-a), R_5^+ (0,a,a), X_5^+ (0,0,a,0,0,0), M_2^+ (a,0,0), M_3^+ (a,0,0)

A.1 Symmetry-mode decomposition of studied structures

The symmetry-mode decomposition of all the structures studied along this thesis are gathered below.

A.1.1 $Fm\bar{3}m$ (ITA No. 225) $\rightarrow$ $P2_1/n$ (ITA No. 14)

```
High symmetry structure
Setting used: FM-3M

225
7.920942 7.920942 7.920942 90.00 90.00 90.00
4
Ru 1 4a  0.000000 0.000000 0.000000
M  1 4b  0.500000 0.500000 0.500000
Sr 1 8c  0.250000 0.250000 0.250000
O  1 24e 0.247140 0.000000 0.000000

# Transformation matrix (Setting P121/n1)
[   1/2   1/2     0 ] [      0]
[  -1/2   1/2     0 ] [      0]
[     0     0     1 ] [      0]
```

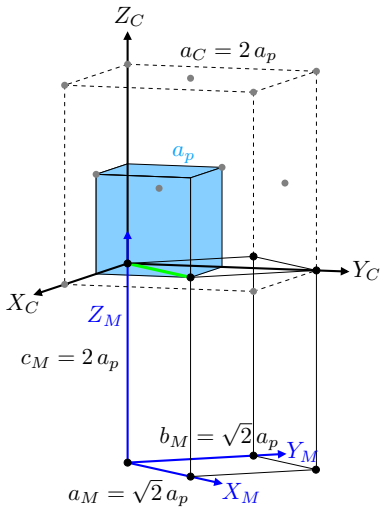

Figure A.1: Relative orientation of the unit cell of the prototype cubic simple perovskite ($Pm\bar{3}m$)(blue), of the prototype cubic double perovskite ($Fm\bar{3}m$) (dashed line), and the distorted monoclinic $P2_1/n$ of the double perovskite (solid line).

```
Low symmetry structure
Setting used: P121/N1

# SrNdZnRuO6
014
5.55697 5.59321 7.86471 90.00 90.013 90.00
6
Zn 1 2b  0.000000 0.000000  0.500000
Ru 1 2a  0.000000 0.000000  0.000000
Sr 1 4e -0.006600 0.464510  0.749900
O  1 4e -0.277100 0.216800 -0.036200
O  2 4e -0.798200 0.294200  0.040000
O  3 4e  0.075300 0.012800  0.758000

# SrNdCoRuO6
014
5.54281 5.55500 7.8333 90.00 90.044 90.00
6
Co 1 2b  0.000000 0.000000  0.500000
Ru 1 2a  0.000000 0.000000  0.000000
Sr 1 4e -0.007300 0.468800  0.751600
O  1 4e -0.286000 0.203100 -0.036900
O  2 4e -0.781200 0.277000  0.033900
O  3 4e  0.070800 0.009100  0.758800

# SrNdMgRuO6
014
5.54335 5.55369 7.8361 90.00 90.052 90.00
6
Mg 1 2b  0.000000 0.000000  0.500000
Ru 1 2a  0.000000 0.000000  0.000000
Sr 1 4e -0.006300 0.472900  0.749400
O  1 4e -0.286500 0.205000 -0.038600
O  2 4e -0.775600 0.274500  0.029300
O  3 4e  0.072100 0.009000  0.754300

# SrNdNiRuO6
014
5.53006 5.53876 7.8166 90.00 90.015 90.00
6
Ni 1 2b  0.000000 0.000000  0.500000
Ru 1 2a  0.000000 0.000000  0.000000
Sr 1 4e -0.005300 0.469800  0.756300
O  1 4e -0.272200 0.223300 -0.028000
O  2 4e -0.790100 0.292000  0.039800
O  3 4e  0.077700 0.008400  0.759400
```

```
Low symmetry structure
Setting used: P121/N1

# SrPrZnRuO6
014
5.56808 5.59283 7.87394 90.00 90.025 90.00
6
Zn 1 2b  0.000000 0.000000  0.500000
Ru 1 2a  0.000000 0.000000  0.000000
Sr 1 4e -0.005300 0.467200  0.753700
O  1 4e -0.278400 0.215000 -0.037700
O  2 4e -0.796300 0.290700  0.037700
O  3 4e  0.070400 0.015000  0.756500

# SrPrCoRuO6
014
5.55504 5.56079 7.84747 90.00 90.051 90.00
6
Co 1 2b  0.000000 0.000000  0.500000
Ru 1 2a  0.000000 0.000000  0.000000
Sr 1 4e -0.006700 0.469300  0.752000
O  1 4e -0.277500 0.214100 -0.029100
O  2 4e -0.790000 0.285300  0.038100
O  3 4e  0.070900 0.010900  0.754900

# SrPrMgRuO6
014
5.55901 5.55587 7.85018 90.00 89.954 90.00
6
Mg 1 2b  0.000000 0.000000  0.500000
Ru 1 2a  0.000000 0.000000  0.000000
Sr 1 4e -0.008300 0.476000  0.748500
O  1 4e -0.272600 0.220400 -0.032600
O  2 4e -0.794200 0.285100  0.032800
O  3 4e  0.064200 0.008300  0.750700

# SrPrNiRuO6
014
5.54586 5.54072 7.82905 90.00 90.0819 90.00
6
Ni 1 2b  0.000000 0.000000  0.500000
Ru 1 2a  0.000000 0.000000  0.000000
Sr 1 4e -0.003200 0.472800  0.753500
O  1 4e -0.285100 0.211600 -0.037400
O  2 4e -0.783900 0.278600  0.033400
O  3 4e  0.064900 0.012500  0.754100
```

```
Low symmetry structure
Setting used: P121/N1

# SrLaZnRuO6
014
5.60355 5.58739 7.9016 90.00000 90.051 90.00000
6
Zn 1 2b  0.000000 0.000000  0.500000
Ru 1 2a  0.000000 0.000000  0.000000
Sr 1 4e -0.003400 0.474600  0.751800
O  1 4e -0.267600 0.220300 -0.029400
O  2 4e -0.792300 0.280100  0.037100
O  3 4e  0.066600 0.006300  0.753100

# SrLaMgRuO6
014
5.5848 5.5584 7.872 90.00000 89.94 90.00000
6
Mg 1 2b  0.000000 0.000000  0.500000
Ru 1 2a  0.000000 0.000000  0.000000
Sr 1 4e  0.000000 0.486000  0.753000
O  1 4e -0.284000 0.216000 -0.028000
O  2 4e -0.759000 0.251000  0.021000
O  3 4e  0.066000 0.003000  0.744000
```

```
Symmetry Modes Summary
Atoms WP Modes
O1  24e GM1+(1) GM3+(1) GM4+(1) GM5+(2) X2+(1) X3+(1) X5+(2)
Sr1 8c  GM5+(2) X5+(1)

Summary of Amplitudes
K-vector Irrep Direction Isotropy Subgroup Dimension
(0,0,0) GM1+ (a)             Fm-3m (225)    1
(0,0,0) GM3+ (a,0)           I4/mmm (139)   1
(0,0,0) GM4+ (a,a,0)         C2/m (12)      1
(0,0,0) GM5+ (-b,a,-a)       C2/m (12)      4
(0,1,0) X2+  (0,a,0)         P4_2/mnm (136) 1
(0,1,0) X3+  (0,a,0)         P4/mnc (128)   1
(0,1,0) X5+  (a,a,0,0,a,-a)  Pnnm (58)      3
```

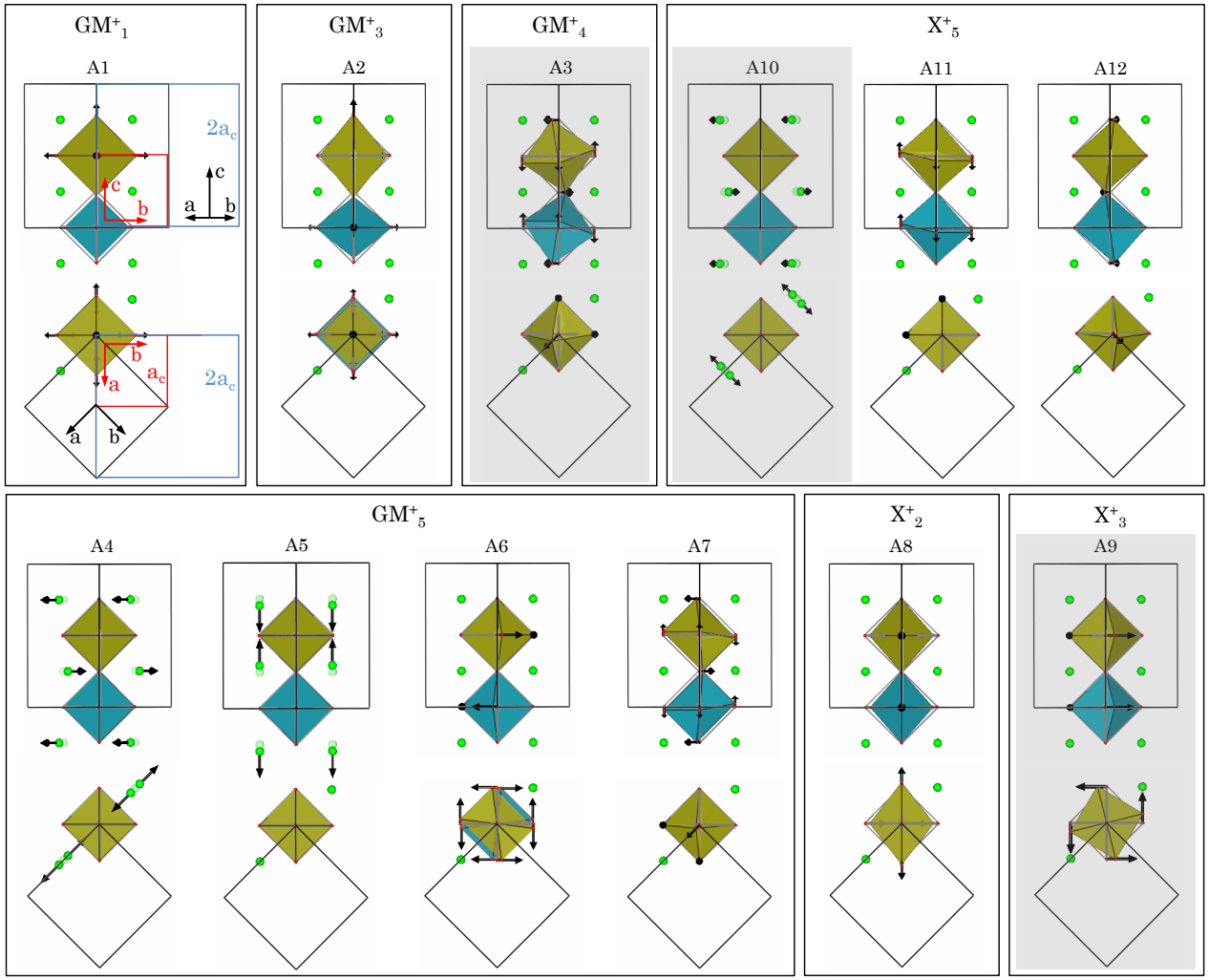

Figure A.2: Geometrical representations of the distortion modes of the symmetry-breaking from the cubic prototype phase into the monoclinic $P2_1/n$ phase: $GM_3^+(1)$, $GM_3^+(1)$, $GM_4^+(1)$, $GM_5^+(4)$, $X_2^+(1)$, $X_3^+(1)$ and $X_5^+(3)$. The numbers in parenthesis indicate the number of modes transforming according to the corresponding irrep. The principal modes are highlighted in grey.

A.1.2 $Fm\bar{3}m$ (ITA No. 225) $\rightarrow$ $P4_2/n$ (ITA No. 86)

```
High symmetry structure
Setting used: FM-3M

225
7.920942 7.920942 7.920942 90.00 90.00 90.00
4
Ru 1 4a  0.000000 0.000000 0.000000
M  1 4b  0.500000 0.500000 0.500000
Sr 1 8c  0.250000 0.250000 0.250000
O  1 24e 0.247140 0.000000 0.000000

# Transformation matrix (Setting P42/n [origin 2])
[     1     0     0 ] [      0]
[     0     1     0 ] [      0]
[     0     0     1 ] [      0]
```

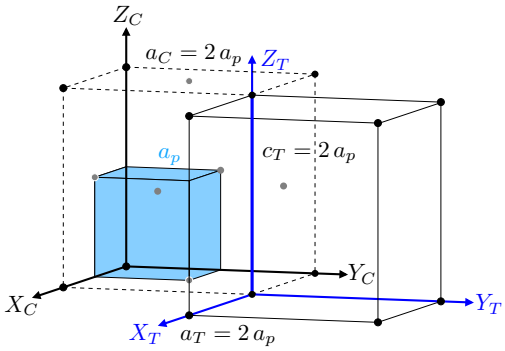

Figure A.3: Relative orientation of the unit cell of the prototype cubic simple perovskite ($Pm\bar{3}m$)(blue), of the prototype cubic double perovskite ($Fm\bar{3}m$) (dashed line), and the distorted tetragonal $P4_2/n$ of the double perovskite (solid line).

```
Low symmetry structure
Setting used: P42/N:2

# SrNdCoRuO6
086
7.9043 7.9043 7.9071 90.00 90.00 90.00
8
Sr 1 2a 0.250000  0.250000  0.250000
Sr 3 2b 0.750000  0.750000  0.250000
Sr 2 4e 0.750000  0.250000  0.760500
Ru 1 4c 0.000000  0.000000  0.000000
Co 1 4d 0.500000  0.500000  0.500000
O  1 8g 0.025500  0.005300  0.237000
O  2 8g 0.253300 -0.044000 -0.019400
O  3 8g 0.037000  0.243800 -0.033000
```

```
Symmetry Modes Summary
Atoms WP Modes
O1  24e GM1+(1) GM3+(1) GM4+(1) X2+(1) X3+(1) X4+(2) X5+(2)
Sr1 8c  X5+(1)

Summary of Amplitudes
K-vector Irrep Direction Isotropy Subgroup Dimension
(0,0,0) GM1+ (a)           Fm-3m (225)      1
(0,0,0) GM3+ (a,0)         I4/mmm (139)     1
(0,0,0) GM4+ (0,0,a)       I4/m (87)        1
(0,1,0) X2+  (0,a,0)       P4_2/mnm (136)   1
(0,1,0) X3+  (-a,0,-a)     P4_2/nnm (134)   1
(0,1,0) X4+  (a,b,a)       P4_2/nnm (134)   2
(0,1,0) X5+  (0,0,0,a,0,0) P4_2/ncm (138)   3
```

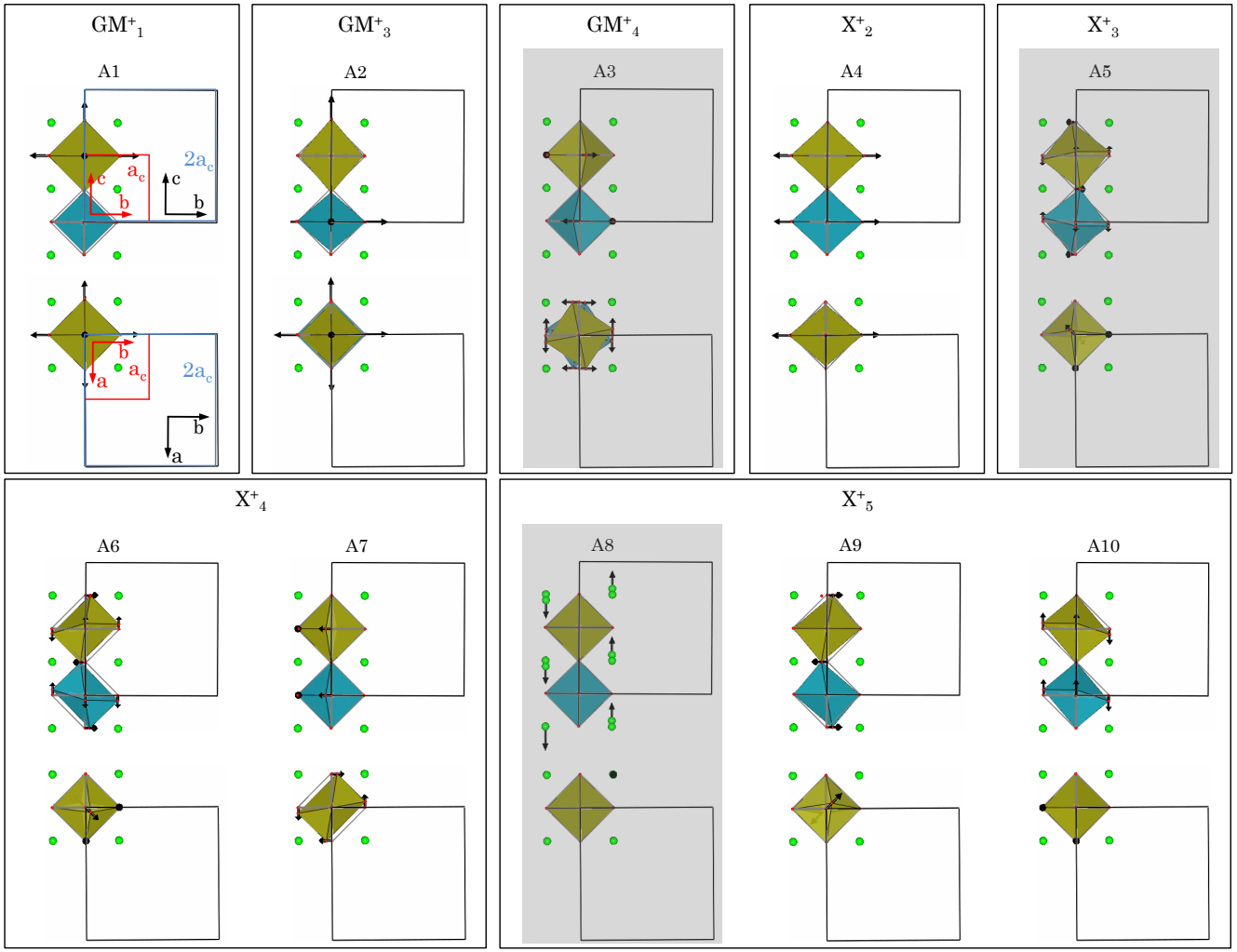

Figure A.4: Geometrical representations of the distortion modes of the symmetry breaking from the cubic prototype phase into the tetragonal $P4_2/n$ phase: $GM_3^+(1)$, $GM_3^+(1)$, $GM_4^+(1)$, $X_2^+(1)$, $X_3^+(1)$, $X_4^+(2)$ and $X_5^+(3)$. The numbers in parenthesis indicate the number of modes transforming according to the corresponding irrep. The principal modes are highlighted in grey.

A.1.3 $Fm\bar{3}m$ (ITA No. 225) $\rightarrow$ $R\bar{3}$ (ITA No. 148)

```
High symmetry structure
Setting used: FM-3M

225
7.920942 7.920942 7.920942 90.00 90.00 90.00
4
Ru 1 4a  0.000000 0.000000 0.000000
M  1 4b  0.500000 0.500000 0.500000
Sr 1 8c  0.250000 0.250000 0.250000
O  1 24e 0.247140 0.000000 0.000000

# Transformation matrix (Setting R-3 hexagonal)
[  -1/2     0     1 ] [      0]
[   1/2  -1/2     1 ] [      0]
[     0   1/2     1 ] [      0]
```

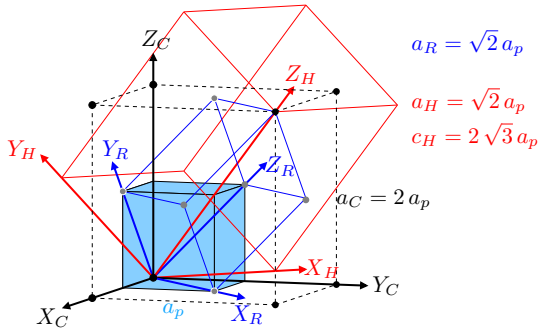

Figure A.5: Relative orientation of the unit cell of the prototype cubic simple perovskite ($Pm\bar{3}m$)(blue), and the distorted rhombohedral $R\bar{3}$ of the double perovskite (solid line).

```
Low symmetry structure
Setting used: R-3:H

# SrPrMgRuO6
148
5.61494 5.61494 13.7096 90.00 90.00 120.00
4
Ru 1 3a  0.000000 0.000000 0.000000
Mg 1 3b  0.000000 0.000000 0.500000
Sr 1 6c  0.000000 0.000000 0.246700
O  1 18f 0.664500 0.873500 0.078100

# SrPrNiRuO6
148
5.59810 5.59810 13.6659 90.00 90.00 120.00
4
Ru 1 3a  0.000000 0.000000 0.000000
Ni 1 3b  0.000000 0.000000 0.500000
Sr 1 6c  0.000000 0.000000 0.256000
O  1 18f 0.672800 0.882200 0.085200
```

```
Low symmetry structure
Setting used: R-3:H

# SrLaZnRuO6
148
5.64184 5.64184 13.7140 90.00 90.00 120.00
4
Ru 1 3a  0.000000 0.000000 0.000000
Zn 1 3b  0.000000 0.000000 0.500000
Sr 1 6c  0.000000 0.000000 0.249800
O  1 18f 0.661700 0.877900 0.079500

# SrLaMgRuO6
148
5.5983 5.5983 13.6449 90.00 90.00 120.00
4
Ru 1 3a  0.000000 0.000000 0.000000
Mg 1 3b  0.000000 0.000000 0.500000
Sr 1 6c  0.000000 0.000000 0.254000
O  1 18f 0.670000 0.881000 0.082100
```

Symmetry Modes Summary

Atoms	WP	Modes
O1	24e	GM1+(1) GM4+(1) GM5+(1)
Sr1	8c	GM5+(1)

Note: The primary mode is written in bold letters

Summary of Amplitudes

K-vector	Irrep	Direction	Isotropy Subgroup	Dimension
(0,0,0)	GM1+	(a)	Fm-3m (225)	1
(0,0,0)	GM4+	(a,a,a)	R-3 (148)	1
(0,0,0)	GM5+	(a,a,a)	R-3m (166)	2

A.1.4 $Pm\bar{3}m$ (ITA No. 221) $\rightarrow$ $Pbnm$ (ITA No. 62)

```
High symmetry structure
Setting used: PM-3M

# SrLnMRuO6 double perovskites
221
3.954497 3.954497 3.954497 90.00 90.00 90.00
3
Fe 1 1a 0.000000 0.000000 0.000000
Sr 1 1b 0.500000 0.500000 0.500000
O  1 3d 0.500000 0.000000 0.000000

# AA'2CuTi2O9 triple perovskites
221
3.8438 3.8438 3.8438 90.00 90.00 90.00
3
Ti 1 1a 0.000000 0.000000 0.000000
Ca 1 1b 0.500000 0.500000 0.500000
O  1 3d 0.500000 0.000000 0.000000

# Transformation matrix (Setting Pbnm)
[     1     1     0 ] [    1/2]
[    -1     1     0 ] [    1/2]
[     0     0     2 ] [      0]
```

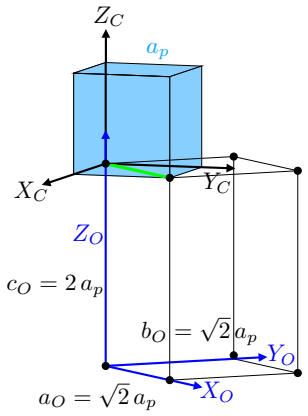

Figure A.6: Relative orientation of the unit cell of the prototype cubic simple perovskite ($Pm\bar{3}m$)(blue), and the distorted orthorhombic $Pbnm$ of the double perovskite (solid line).

```
Low symmetry structure
Setting used: PBNM

# SrLaFeRuO6
062
5.57524 5.5463 7.8557 90.00 90.00 90.00
4
Fe 1 4a  0.000000  0.500000 0.000000
Sr 1 4c  0.000000 -0.016600 0.250000
O  1 4c -0.066100  0.507000 0.250000
O  2 8d  0.727700  0.271900 0.528900

# SrPrFeRuO6
062
5.54772 5.5463 7.8390 90.00 90.00 90.00
4
Fe 1 4a  0.000000  0.500000 0.000000
Sr 1 4c  0.000700 -0.024500 0.250000
O  1 4c -0.079000  0.509600 0.250000
O  2 8d  0.722300  0.278400 0.529100

# SrNdFeRuO6
062
5.53565 5.54323 7.8257 90.00 90.00 90.00
4
Fe 1 4a  0.000000  0.500000 0.000000
Sr 1 4c  0.002300 -0.029400 0.250000
O  1 4c -0.083700  0.508900 0.250000
O  2 8d  0.722900  0.279000 0.529800
```

```
Low symmetry structure
Setting used: PBNM

# CaPr2CuTi2O9
062
5.4821 5.5942 7.6869 90.00 90.00 90.00
4
Ti 1 4a  0.5000   0.0000     0.0000
Ca 1 4c  0.0069   0.0452     0.2500
O  1 4c  0.4230   0.0190     0.7500
O  2 8d  0.0770   0.5190     0.2500

# CaNd2CuTi2O9
062
5.4557 5.5760 7.6594 90.00 90.00 90.00
4
Ti 1 4a  0.5000   0.0000     0.0000
Ca 1 4c -0.0079  -0.0467     0.7500
O  1 4c  0.4230   0.0200     0.7500
O  2 8d  0.2020   0.7900     0.4580

# CaSm2CuTi2O9
062
5.4221 5.6097 7.6129 90.00 90.00 90.00
4
Ti 1 4a  0.5000   0.0000     0.0000
Ca 1 4c -0.0109  -0.0558     0.7500
O  1 4c  0.4060   0.0330     0.7500
O  2 8d  0.1970   0.7970     0.4560
```

Symmetry Modes Summary
Atoms WP Modes
O1 3d R4+(1) R5+(1) X5+(1) M2+(1) M3+(1)
Sr1 1b R5+(1) X5+(1)

Summary of Amplitudes

K-vector	Irrep	Direction	Isotropy Subgroup	Dimension
(1/2,1/2,1/2)	R4+	(0,a,a)	Imma (74)	1
(1/2,1/2,1/2)	R5+	(0,a,-a)	Imma (74)	2
(0,1/2,0)	X5+	(0,0,0,-a,0,0)	Cmcm (63)	2
(1/2,1/2,0)	M2+	(a,0,0)	P4/mbm (127)	1
(1/2,1/2,0)	M3+	(a,0,0)	P4/mbm (127)	1

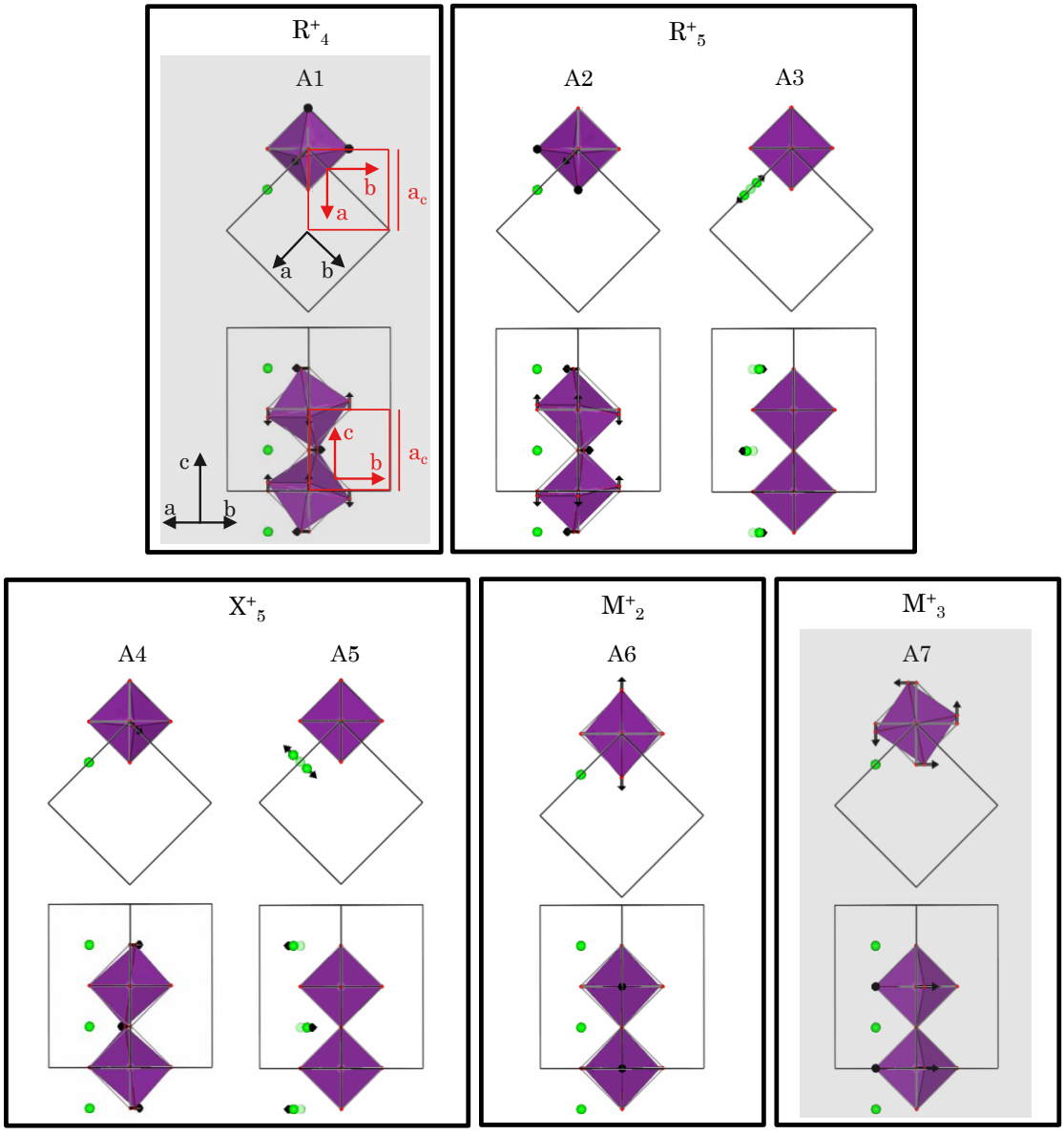

Figure A.7: Geometrical representation of the five irrep distortions allowed in the *Pbnm* configuration, corresponding to M_2^+, M_3^+, R_4^+, R_5^+ and X_5^+.

A.1.5 $Pm\bar{3}m$ (ITA No. 221) $\rightarrow$ $I4/mcm$ (ITA No. 140)

```
High symmetry structure
Setting used: PM-3M

221
3.954497 3.954497 3.954497 90.00 90.00 90.00
3
Ti 1 1a 0.000000 0.000000 0.000000
Ba 1 1b 0.500000 0.500000 0.500000
O  1 3d 0.500000 0.000000 0.000000

# Transformation matrix
[     1     1     0 ] [      0]
[    -1     1     0 ] [      0]
[     0     0     2 ] [      0]
```

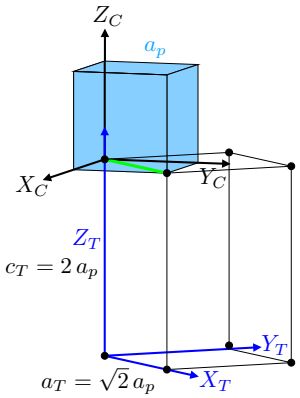

Figure A.8: Relative orientation of the unit cell of the prototype cubic simple perovskite ($Pm\bar{3}m$)(blue), and the distorted tetragonal $I4/mcm$ of the double perovskite (solid line).

```
Low symmetry structure
Setting used: I4/MCM

# BaLa2CuTi2O9
140
5.6032 5.6032 7.9192 90.00 90.00 90.00
4
Ba 1 4b 0.000000 0.500000 0.250000
Ti 1 4c 0.000000 0.000000 0.000000
O  1 4a 0.000000 0.000000 0.250000
O  2 8h 0.268000 0.232000 0.000000

# BaPr2CuTi2O9
140
5.5837 5.5837 7.8882 90.00 90.00 90.00
4
Ba 1 4b 0.000000 0.500000 0.250000
Ti 1 4c 0.000000 0.000000 0.000000
O  1 4a 0.000000 0.000000 0.250000
O  2 8h 0.275000 0.225000 0.000000

# BaNd2CuTi2O9
140
5.5773 5.5773 7.8743 90.00 90.00 90.00
4
Ba 1 4b 0.000000 0.500000 0.250000
Ti 1 4c 0.000000 0.000000 0.000000
O  1 4a 0.000000 0.000000 0.250000
O  2 8h 0.273000 0.227000 0.000000
```

Symmetry Modes Summary
Atoms WP Modes
O1 3d R4+(1)
Note: The primary mode is written in bold letters

Summary of Amplitudes

K-vector	Irrep	Direction	Isotropy Subgroup	Dimension
(1/2,1/2,1/2)	R4+	(a,0,0)	I4/mcm (140)	1

A.1.6 $Pm\bar{3}m$ (ITA No. 221) $\rightarrow$ $R\bar{3}c$ (ITA No. 167)

```
High symmetry structure
Setting used: PM-3M

221
3.954497 3.954497 3.954497 90.00 90.00 90.00
3
Fe 1 1a 0.000000 0.000000 0.000000
Sr 1 1b 0.500000 0.500000 0.500000
O  1 3d 0.500000 0.000000 0.000000

# Transformation matrix (Setting R-3c hexahonal)
[     0     1     2 ] [      0]
[    -1     0     2 ] [      0]
[     1    -1     2 ] [      0]
```

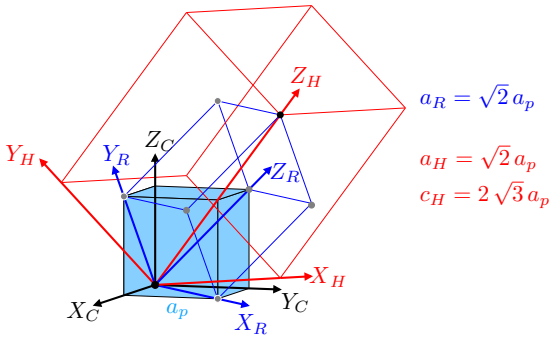

Figure A.9: Relative orientation of the unit cell of the prototype cubic simple perovskite ($Pm\bar{3}m$)(blue), and the distorted rhombohedral $R\bar{3}c$ of the double perovskite (solid line).

```
Low symmetry structure
Setting used: R-3C:H

# SrPrFeRuO6
167
5.59773 5.59773 13.7199 90.00 90.00 120.00
3
Sr 1 6a  0.333330 0.666670 0.916670
Fe 1 6b  0.000000 0.000000 0.000000
O  1 18e 0.875700 0.666670 0.916670

Symmetry Modes Summary
Atoms WP Modes
O1 3d R4+(1)
Note: The primary mode is written in bold letters

Summary of Amplitudes
K-vector     Irrep    Direction Isotropy Subgroup Dimension
(1/2,1/2,1/2) R4+     (a,a,a)    R-3c (167)       1
```

A.2 Symmetry-mode decomposition of other perovskite structures

A.2.1 $Fm\bar{3}m$ (ITA No. 225) $\rightarrow I2/m$ (ITA No. 12)

```
High symmetry structure
Setting used: FM-3M

225
7.920942 7.920942 7.920942 90.00 90.00 90.00
4
C 1 4a  0.000000 0.000000 0.000000
B 1 4b  0.500000 0.500000 0.500000
A 1 8c  0.250000 0.250000 0.250000
O 1 24e 0.247140 0.000000 0.000000

# Transformation matrix (Setting I12/m1)
[   1/2   1/2     0 ] [      0]
[  -1/2   1/2     0 ] [      0]
[     0     0     1 ] [      0]

Low symmetry structure
Setting used: I12/M1

# A. Faik et al./J. Solid State Chemistry 182 (2009) 1717-1725
012
5.5574 5.5782 7.8506 90.00 90.06 90.00
5
C 1 2a  0.000000 0.000000 0.000000
B 1 2d  0.000000 0.000000 0.500000
A 1 4i  0.499900 0.000000 0.250400
O 1 4i -0.039000 0.000000 0.249000
O 2 8j  0.246000 0.249000 0.015000

Symmetry Modes Summary
Atoms WP Modes
O1  24e GM1+(1) GM3+(1) GM4+(1) GM5+(2)
A1 8c  GM5+(2)
Note: The primary mode is written in bold letters

Summary of Amplitudes
K-vector Irrep Direction Isotropy Subgroup Dimension
(0,0,0)  GM1+  (a)        Fm-3m (225)        1
(0,0,0)  GM3+  (a,0)      I4/mmm (139)       1
(0,0,0)  GM4+  (a,a,0)    C2/m (12)          1
(0,0,0)  GM5+  (-b,a,-a)  C2/m (12)          4
```

A.2.2 $Fm\bar{3}m$ (ITA No. 225) $\rightarrow$ $I4/m$ (ITA No. 87)

```
High symmetry structure
Setting used: FM-3M

225
7.920942 7.920942 7.920942 90.00 90.00 90.00
4
C 1 4a  0.000000 0.000000 0.000000
B 1 4b  0.500000 0.500000 0.500000
A 1 8c  0.250000 0.250000 0.250000
O 1 24e 0.247140 0.000000 0.000000

# Transformation matrix
[   1/2   1/2     0 ] [      0]
[  -1/2   1/2     0 ] [      0]
[     0     0     1 ] [      0]

Low symmetry structure
Setting used: I4/M

# A. Faik et al./J. Solid State Chemistry 182 (2009) 1717-1725
087
5.5668 5.5668 7.8899  90.00  90.00  90.00
5
C 1 2a 0.000000 0.000000 0.000000
B 1 2b 0.000000 0.000000 0.500000
A 1 4d 0.000000 0.500000 0.250000
O 1 4e 0.000000 0.000000 0.243100
O 2 8h 0.282500 0.205300 0.000000

Symmetry Modes Summary
Atoms WP Modes
O1 24e GM1+(1) GM3+(1) GM4+(1)
Note: The primary mode is written in bold letters

Summary of Amplitudes
K-vector Irrep Direction Isotropy Subgroup Dimension
(0,0,0)  GM1+  (a)         Fm-3m (225)      1
(0,0,0)  GM3+  (a,0)       I4/mmm (139)     1
(0,0,0)  GM4+  (0,0,a)     I4/m (87)        1
```

A.2.3 $Pm\bar{3}m$ (ITA No. 221) $\rightarrow$ $Bmm2$ (ITA No. 38)

```
High symmetry structure
Setting used: PM-3M

221
3.843816 3.843816 3.843816 90.00 90.00 90
3
B  1 1a 0.000000 0.000000 0.000000
A  1 1b 0.500000 0.500000 0.500000
O  1 3d 0.000000 0.000000 0.500000

# Transformation matrix (Setting Bmm2)
[     1     0    -1 ] [      0]
[    -1     0    -1 ] [      0]
[     0     1     0 ] [      0]

Low symmetry structure
Setting used: BMM2

# N. Ishizawa et al./J. Solid State Chem. 183 (2010) 2731-2738 (ICSD 247571)
038
5.643295   3.943177   5.671877  90.000000  90.000000  90.000000
4
B  1 2a 0.000000 0.000000  0.100000
A  1 2b 0.000000 0.500000  0.480230
O  1 4d 0.220860 0.000000  0.244430
O  2 2b 0.000000 0.500000 -0.013420

Symmetry Modes Summary
Atoms WP Modes
O1  3d GM4-(2) GM5-(1)
A1  1b GM4-(1)
B1  1a GM4-(1)
Note: The primary mode is written in bold letters

Summary of Amplitudes
K-vector Irrep Direction Isotropy Subgroup Dimension
(0,0,0)  GM4-  (a,a,0)    Amm2 (38)        4
(0,0,0)  GM5-  (0,a,-a)   Amm2 (38)        1
```

A.2.4 $Pm\bar{3}m$ (ITA No. 221) $\rightarrow$ $Cmcm$ (ITA No. 63)

```
High symmetry structure
Setting used: PM-3M

221
3.954497 3.954497 3.954497 90.00 90.00 90.00
3
B 1 1a 0.000000 0.000000 0.000000
A 1 1b 0.500000 0.500000 0.500000
O 1 3d 0.500000 0.000000 0.000000

# Transformation matrix (Setting Cmcm)
[     0     0     2 ] [      0]
[     2     0     0 ] [    1/2]
[     0     2     0 ] [    1/2]

Low symmetry structure
Setting used: CMCM

# B.J. Kennedy et al./J. Phys.: Condens. Matter 11 (1999) 1479-1488
063
7.7642 7.7674 7.7667 90.00 90.00 90.00
6
A 1 4c 0.000000 0.000000 0.250000
A 2 4c 0.000000 0.505000 0.250000
B 1 8d 0.250000 0.250000 0.000000
O 1 8e 0.278000 0.000000 0.000000
O 2 8f 0.000000 0.226000 0.032000
O 3 8g 0.280000 0.251000 0.250000

Symmetry Modes Summary
Atoms WP Modes
O1 3d R4+(1) R5+(1) X5+(1) M3+(1) M4+(1)
A1 1b R5+(1) X5+(1)

Summary of Amplitudes
K-vector     Irrep Direction Isotropy Subgroup Dimension
(1/2,1/2,1/2) R4+  (a,0,0)        I4/mcm (140)   1
(1/2,1/2,1/2) R5+  (a,0,0)        I4/mmm (139)   2
(0,1/2,0)     X5+  (0,0,0,0,-a,a) Pmma (51)      2
(1/2,1/2,0)   M3+  (0,a,0)        P4/mbm (127)   1
(1/2,1/2,0)   M4+  (0,a,0)        P4/mmm (123)   1
```

A.2.5 $Pm\bar{3}m$ (ITA No. 221) $\rightarrow$ $Imma$ (ITA No. 74)

```
High symmetry structure
Setting used: PM-3M

221
3.954497 3.954497 3.954497 90.00 90.00 90.00
3
B 1 1a 0.000000 0.000000 0.000000
A 1 1b 0.500000 0.500000 0.500000
O 1 3d 0.500000 0.000000 0.000000

# Transformation matrix (Setting Imma)
[     1     0     1 ] [    1/2]
[     1     0    -1 ] [    1/2]
[     0     2     0 ] [      0]

Low symmetry structure
Setting used: IMMA

# T. Yang et al./J. Mater. Chem. 21 (2011) 199-205 (ICSD 180007)
074
5.729 8.1065 5.730 90.00 90.00 90.00
4
B 1 4b 0.500000 0.000000 0.000000
A 1 4e 0.000000 0.250000 0.000000
O 1 4e 0.000000 0.250000 0.470000
O 2 8g 0.250000 0.986000 0.250000

Symmetry Modes Summary
Atoms WP Modes
O1 3d R4+(1) R5+(1)
A1 1b R5+(1)
Note: The primary mode is written in bold letters

Summary of Amplitudes
K-vector     Irrep Direction Isotropy Subgroup Dimension
(1/2,1/2,1/2) R4+  (0,a,a)   Imma (74)          1
(1/2,1/2,1/2) R5+  (0,a,-a)  Imma (74)          2
```

A.2.6 $Pm\bar{3}m$ (ITA No. 221) $\rightarrow$ $P4mm$ (ITA No. 99)

```
High symmetry structure
Setting used: PM-3M

221
4.0260 4.0260 4.0260 90.00 90.00 90.00
3
B 1 1a 0.000000 0.000000 0.000000
A 1 1b 0.500000 0.500000 0.500000
O 1 3d 0.000000 0.000000 0.500000

# Transformation matrix
[     1     0     0 ] [    1/2]
[     0     1     0 ] [    1/2]
[     0     0     1 ] [      0]

Low symmetry structure
Setting used: P4MM

# Y. Idemoto et al./J. Ceram. Soc. Jpn. 112 (2004) 40-45 (ICSD 55700)
099
4.0260 4.0260 4.1241 90.00 90.00 90.00
4
A 1 1a 0.000000 0.000000 0.000000
B 1 1b 0.500000 0.500000 0.574000
O 1 1b 0.500000 0.500000 0.084000
O 2 2c 0.500000 0.000000 0.605000

Symmetry Modes Summary
Atoms WP Modes
O1 3d GM4-(2)
A1 1b GM4-(1)
B1 1a GM4-(1)
Note: The primary mode is written in bold letters

Summary of Amplitudes
K-vector Irrep Direction Isotropy Subgroup Dimension
(0,0,0)  GM4-   (0,0,a)     P4mm (99)        4
```

A.2.7 $Pm\bar{3}m$ (ITA No. 221) $\rightarrow$ $P4/mbm$ (ITA No. 127)

```
High symmetry structure
Setting used: PM-3M

221
3.954497 3.954497 3.954497 90.00 90.00 90.00
3
B 1 1a 0.000000 0.000000 0.000000
A 1 1b 0.500000 0.500000 0.500000
O 1 3d 0.500000 0.000000 0.000000

# Transformation matrix
[     1     1     0 ] [      0]
[    -1     1     0 ] [      0]
[     0     0     1 ] [      0]

Low symmetry structure
Setting used: P4/MBM

# R.B. Macquart et al./ J. Solid State Chemistry 183 (2010) 2400-2405 (ICSD 247537)
127
5.69526 5.69526 4.03082 90.000000 90.000000 90.000000
4
B 1 2a 0.000000 0.000000 0.000000
O 1 2b 0.000000 0.000000 0.500000
A 1 2c 0.000000 0.500000 0.500000
O 2 4g 0.256600 0.756600 0.000000

Symmetry Modes Summary
Atoms WP Modes
O1 3d M3+(1)
Note: The primary mode is written in bold letters

Summary of Amplitudes
K-vector    Irrep Direction Isotropy Subgroup Dimension
(1/2,1/2,0) M3+   (a,0,0)     P4/mbm (127)     1
```

Appendix B

Instrumentation

Synthesis furnaces

The manufacture of the different materials presented in this memory was done using several tubular furnaces with horizontal temperature gradient (the majority of them Carbolite furnaces) as shown in Figure B.1 and Figure B.3. Depending on the calefactory resistance the furnaces can overcome 1700 K; and in most of them exists the possibility to work with controlled atmosphere. This is possible due to a gas circulation system (Ar, O_2, N_2), entering and leaving through the covers that seal both ends of the tube. The characteristic of manipulated furnaces are shown in Table B.1.

Table B.1: Horizontal tube furnaces characteristic table.

Type	Location	T_{max} (°C)	Heating elements	Heating (°C/min)	T constant (h)	Cooling
Tander S.L.	[1]UPV/EHU	900	1 zone	5	24	Controlled
Carbolite CTF 12/65/550	[1]UPV/EHU	1200	1 zone	5	17	Controlled
Carbolite STF 15/75/450	[1]UPV/EHU	1500	1 zone	5	17	Controlled
AGNI Ceram-Aix RHT 175-50-300-1H	[2]UPV/EHU	1750	1 zone		160	Controlled
Carbolite CTF 12/65	ILL	1000	1 zone	5	17	Free fall
Carbolite TZF 12/65/550	ILL	1200	3 zone	5	17	Controlled
Carbolite STF 16/–/450	ILL	1600	1 zone	5	17	Controlled

[1]UPV/EHU: Inorganic Chemistry depart.
[2]UPV/EHU: Applied Physics II depart.

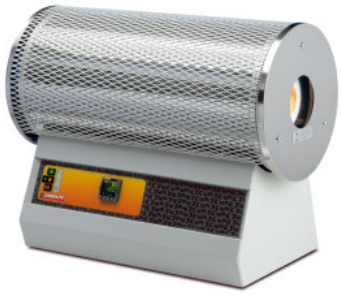

Figure B.1: Carbolite CTF 12/65/550 furnace.

Figure B.2: Tander S.L. furnace.

Figure B.3: AGNI Ceram-Aix RHT 175-50-300-1H furnace.

X-ray powder diffractometers

Stoe STADI-P		
Place	Applied Physics II and Condensed Matter Physics dept.	Leioa (Spain)
Radiation type	Laboratory X-rays	Cu tube
Monochromator	Ge(111)	$\lambda_{K\alpha 1} = 1.5406$ Å
Detector	PSD	2θ=-70−135°
Sample environment	Heater	
Characteristics	Bragg-Brentano geomety	

Figure B.4: Stoe STADI-P laboratory X-ray powder diffractometer.

Philips X'Pert MPD

Place	UPV/EHU general services (SGIker)	Leioa (Spain)
Radiation type	Laboratory X-rays	Cu tube
Monochromator	Graphite secundary	$\lambda_{K\alpha 1} = 1.5406$ Å
Detector	PW3011/10 proportional detector	2θ=5−130°
Sample environment	Anton Paar HTK16	RT−1273 K (vacuum)
Characteristics	Focalized Bragg-Brentano geometry	
	Sample changer	15 positions

Figure B.5: Philips X'Pert MPD laboratory X-ray powder diffractometer.

Bruker Advance D8 Vário		
Place	UPV/EHU general services (SGIker)	Leioa (Spain)
Radiation type	Laboratory X-rays	Cu tube
Monochromator	Primary Vário	$\lambda_{K\alpha 1} = 1.5406$ Å
Detector	Sol-X energy dispersive	2θ=0.5−140°
Sample environment		RT
Characteristics	Bragg-Brentano geometry	
	Window to avoid fluorescence	
	Sample changer	Plain samples
		Transmission configuration
		Capillary

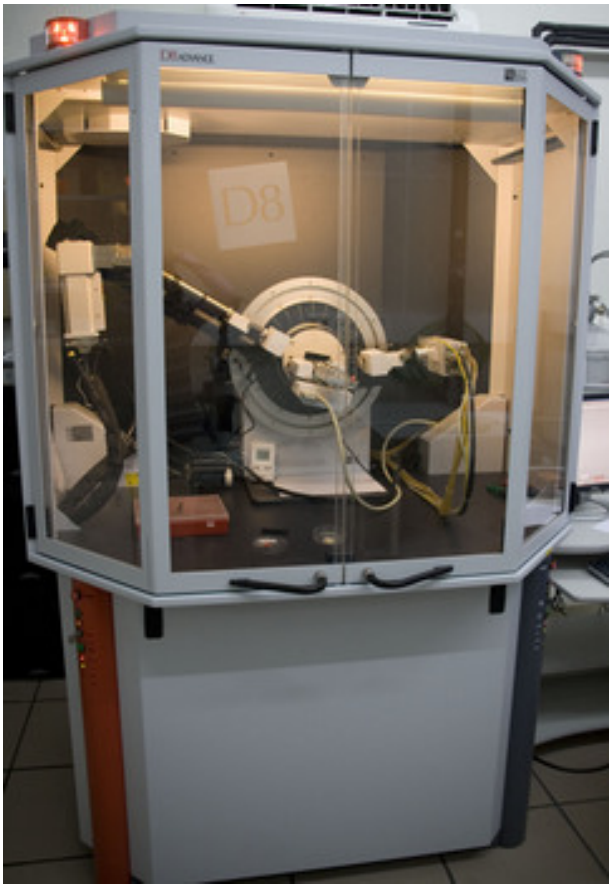

Figure B.6: Bruker Advance D8 Vário laboratory X-ray powder diffractometer.

Bruker Advance D8 Vantec

Place	UPV/EHU general services (SGIker)	Leioa (Spain)
Radiation type	Laboratory X-rays	Cu tube
Monochromator	—	$\lambda_{K\alpha 1}$ and $\lambda_{K\alpha 2}$
Detector	One dimension Våntec detector	2θ=15−120°
Sample environment	Anton Paar HTK2000	RT−1873 K (vacuum)
	MRI-TC wide	170−300 K
Characteristics	Bragg-Brentano geometry	
	High temperature configuration	Platinum sample-holder
	Low temperature configuration	Steel sample-holder

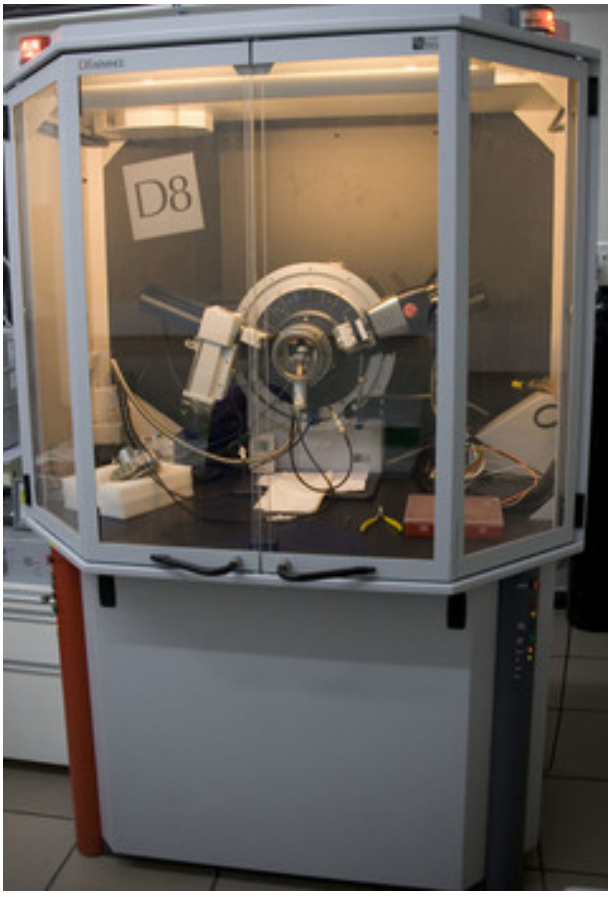

Figure B.7: Bruker Advance D8 Vantec laboratory X-ray powder diffractometer.

Synchrotron radiation powder diffractometers

11-BM-B [138]

Place	Argonne National Laboratory	Argonne (USA)
Radiation type	Synchrotron radiation	Bending magnet
Monochromator	Si(111)	0.318−2.256 Å
Detector	Scintillator	
Sample environment	Cryostream	80−500 K
Characteristics	Fast measurements	<=1 h
	High resolution	$<2\times10^{-4}\ \Delta Q/Q$
	Robot for unattended operation	

Figure B.8: Powder diffractometer from 11-BM-B line in Argonne National Laboratory Synchrotron.

BM-25-Brach A [139]

Place	Spline, ESRF	Grenoble (France)
Radiation type	Synchrotron radiation	Bending magnet
Monochromator	Pseudo channel-cut type Si(111) or Si(311)	0.28−2.48 Å
Detector	Si(Li)	13 elements
Sample environment	Low temperature	80 K
	High temperature	1000 K
Characteristics	Capillary	
	Flat samples	
	Angular resolution	0.0001°

Figure B.9: Powder diffractometer from BM25-Branch A line in ESRF.

Neutron powder diffractometers

HRPT [140]

Place	SINQ-PSI	Villigen (Swiss)
Radiation type	Neutrons	Thermal
Monochromator	Take-off angle	120°
	Ge(311)	2.4097 Å
	Ge(511)	1.5384 Å
	Take-off angle	90°
	Ge(511)	1.886 Å
	Ge(533)	1.494 Å
	Ge(822)	1.154 Å
Detector	^{3}He, 1600 wires	2θ=0−160°
Sample environment	Closed cycle refrigerator	4−325 K
	Helium cryostat	1.5 K<
	Dilution cryostat	50 mK<
	Small furnace	350−700 K
	Tantalum furnace	375−1400 K
	ILL-type furnace	500−1800 K
	Magnet	<4 T
	Supraconducting magnet	<15 T
	Pressure device	<14, <100 kbar
Characteristics	Oscillating radial collimator	Removes sample environment contamination
	Sample changer	Room temperature, 8 sample 1.5−315 K, 4 sample

Figure B.10: HRPT neutron powder diffractometer.

SPODI [141][142]

Place	FRM II	Garching (Germany)
Radiation type		Thermal neutrons
Monochromator	Take-off angle	155°
	Ge(331)	$\lambda = 2.537$ Å
	Ge(551)	$\lambda = 1.549$ Å
	Ge(771)	$\lambda = 1.111$ Å
	Take-off angle	135°
	Ge(331)	$\lambda = 2.396$ Å
	Ge(551)	$\lambda = 1.463$ Å
	Ge(771)	$\lambda = 1.050$ Å
Detector	He^3 80 tubes	2θ=0−160°
Sample environment	Closed-cycle cryostat	3−550 K; (with ^{3}He insert: T_{min}=0.5 K)
	High temperature furnace	RT−2100 K (vacuum)
	Mirror furnace (in air)	RT−1500 K
	Cryomagnet	B_{max}=5 T, T_{min}=4 K
	Paris-Edinburgh cell	P_{max}=10 GPa
	Rotatable tensile rig	F_{max}=50 kN (uniaxial tension and pressure)
		M_{max}=50 Nm (torsion)
	Device for electric fields	V_{max}=35 kV ($\approx$ 7 kV/mm)
	Potentiostat for electrochemical treatment of materials	VMP3
Characteristics	Soller collimators	Removes sample environment contamination

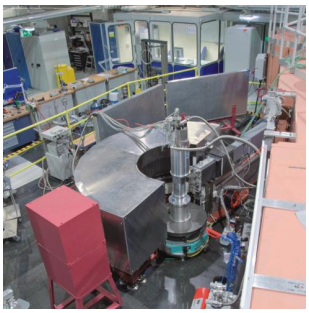

Figure B.11: SPODI neutron powder diffractometer.

D2B

Place	ILL	Grenoble (France)
Radiation type	Neutrons	Thermal
Monochromator	Take-off angle	135°
	Ge(557)	$\lambda = 1.051$ Å
	Ge(337)	$\lambda = 1.28$ Å
	Ge(551)	$\lambda = 1.464$ Å
	Ge(335)	$\lambda = 1.594$ Å (optimum)
	Flux at sample	10^6 n cm^{-2}s^{-1} (HR [1])
		10^7 n cm^{-2}s^{-1} (HI [2])
	Ge(331)	$\lambda = 2.398$ Å
	Ge(113)	$\lambda = 3.152$ Å
Detector	^{3}He, 128 tubes	2θ=5−165°
Sample environment	Cryostat	1.5−300 K
	Cryocooler	3.5−700 K
	Dilution cryostat	50−4000 mK
	Cryofurnace	1.5−525 K
	Furnace	200−1000 K
	Pressure device	2 GPa (4−300 K)
	Cryomagnet	
Characteristics	Environment changer	6 positions (ex.: furnace, displex, 4 room temperature positions)

[1]High resolution; [2]High intensity

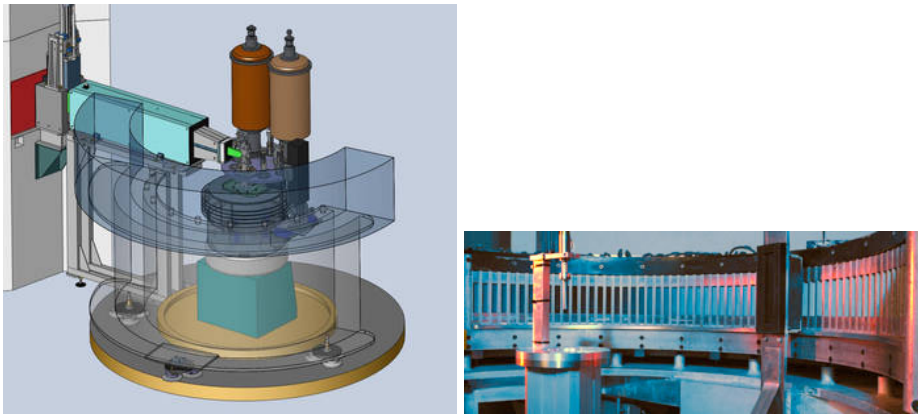

Figure B.12: D2B neutron powder diffractometer.

D1B

Place	ILL	Grenoble (France)
Radiation type	Neutrons	Thermal
Monochromator	Take-off angle	44,22°
	Pyrolytic graphite (002)	$\lambda = 2.52$ Å
	Flux at sample	6.5×10^6 n cm^{-2}s^{-1}
	Ge(331)	$\lambda = 1.28$ Å
	Flux at sample	0.4×10^6 n cm^{-2}s^{-1}
Detector	^{3}He, 1280 cells	2θ=0−128°
Sample environment	Cryostat	1.7−300 K
	Furnace	<800 °C
		<2500 °C
	Electromagnet	1 T (vertical or horizontal gap)
	Eulerian cradle	Texture analysis
Characteristics	Radial oscillating collimator	Removes sample environment contamination

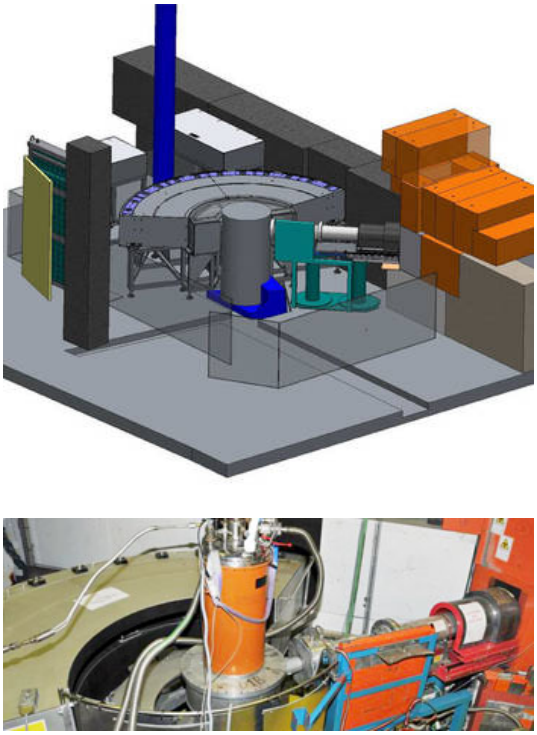

Figure B.13: D1B neutron powder diffractometer.

Table B.2: List of samples studied during the thesis and the instruments in which the measurements have been done. ✓stands for measured at such instrument/condition.

	XRPD					SXRPD		NPD											
	Stoe	Philips	Bruker Vario	Bruker Vantec		BM-11-B	BM-25-A	SPODI			HRPT			D2B			D1B	
	RT	RT	RT	LT	HT	RT	RT	LT	RT	HT	LT	RT	HT	LT	RT	HT	LT	HT
$SrNdZnRuO_6$	✓		✓	✓	✓	✓			✓									
$SrNdCoRuO_6$	✓		✓	✓	✓	✓		✓	✓	✓							✓	
$SrNdMgRuO_6$	✓		✓	✓	✓	✓			✓									
$SrNdNiRuO_6$	✓		✓	✓	✓	✓		✓	✓								✓	
$SrNdFeRuO_6$	✓		✓	✓	✓			✓	✓								✓	✓
$SrPrZnRuO_6$	✓		✓	✓	✓		✓					✓	✓					
$SrPrCoRuO_6$	✓		✓	✓	✓		✓								✓		✓	
$SrPrMgRuO_6$	✓		✓	✓	✓		✓								✓	✓		
$SrPrNiRuO_6$	✓		✓	✓	✓		✓						✓		✓		✓	
$SrPrFeRuO_6$	✓		✓	✓	✓		✓						✓		✓		✓	✓
$SrLaZnRuO_6$	✓	✓					✓								✓	✓		
$SrLaCoRuO_6$	✓	✓					✓										✓	
$SrLaMgRuO_6$	✓	✓					✓								✓	✓		
$SrLaNiRuO_6$	✓	✓					✓										✓	
$SrLaFeRuO_6$	✓	✓					✓								✓		✓	✓
$CaPr_2CuTi_2O_9$	✓		✓		✓						✓	✓						
$CaNd_2CuTi_2O_9$	✓		✓		✓							✓	✓					
$CaSm_2CuTi_2O_9$	✓		✓		✓													
$BaLa_2CuTi_2O_9$	✓		✓		✓													
$BaPr_2CuTi_2O_9$	✓		✓		✓							✓						
$BaNd_2CuTi_2O_9$	✓		✓		✓							✓	✓					

LT: low temperature; RT: room temperature; HT: high temperature

Appendix C

Synthesis of bismuth-containing perovskites

Bismuth-containing perovskites have been extensively studied, since multiferroicity may be observed as a consequence of the presence of Bi^{3+} $6s^2$ lone pair electrons combining with the magnetism from transition metal cations. The presence of off-centered Bi^{3+} cation displacement often drives to polar superstructures with considerable ferroelectricity. Moreover, from the coupling of the transition metal cations spins, ferromagnetic or antiferromagnetic ordering is expected.

Although ferroelectricity and ferromagnetism can be found in diverse systems, the multiferroic materials, which show simultaneously electric and magnetic ordering in a single phase, are relatively rare. Despite the fact that the existence of two or more independent ferroic order parameters in one material provide mesmerizing physical properties, the coupling between electric and magnetic properties gives rise to additional phenomena; *e.g*. magnetoelectric effects. It is noteworthy the large application potential that have these kind of materials for new devices. Nevertheless, the driving forces for ferroelectricity and ferromagnetism are generally incompatible: ferroelectricity requires structural distortion to allow electric polarization, whereas magnetic ions tend to be stabilized in centrosymmetric structures; hence it is difficult to have multiferroic materials.

Bismuth containing perovskites have attracted much interest due to their potential multiferroism and lead-free ferroelectric materials. BiMO$_3$ simple perovskites have been investigated where M is a 3d transition metal, Sc, Cr, Mn, Fe, Co, or Ni. Among them, $BiFeO_3$ is ferroelectric with high Curie temperature T_C $\sim$1123 K, and antiferromagnetic

with the high Néel temperature T_N ∼642 K [143]. However, multiferroic properties have been enhanced doping $BiFeO_3$ with lanthanides, such as La^{3+} or Er^{3+} [144]. $BiMnO_3$ is a unique compound among BiMO$_3$ (M=Cr [145],Fe [143],Co [75],Ni [146]), because $BiMnO_3$ is the only material that shows true ferrimagnetic ordering at T_C=99-105 K [147][148]; the rest have antiferromagnetic ordering. Nevertheless, there are several discrepancies among different works on space group assignment and ferroelectric transition temperature. Although $C2$ (ITA No.5) is the most probable space group [147], some other authors propose $C2/m$ (ITA No.12) [149]. It is not easy to show ferroelectricity lack of single crystals and low resistance on film; the ferroelectric transition temperature is discussed to be, 450 K (orbital ordering) [149] or 750-770 K (centrosymmetric-noncentrosymmetric space group transition) [147, 150]. What is clear is that the material has multiferroic properties below 105 K. Is is noteworthy that, even having studied BiMO$_3$ materials for several years there are disparities in space group assignation, and in some cases centrosymmetric space groups have been ascribed to multiferroic phases.

High-pressure techniques have been used to design bismuth-containing double perovskite Bi_2NiMnO_6 [151]. The structure is highly distorted with a monoclinic $C2$ space group, in which the Ni^{2+} and Mn^{4+} cations are ordered in a rock-salt configuration. Although two ferroic orderings (ferroelectric, T_{C-FE}=485 K; and ferromagnetic, T_{C-FM}=140 K) occur independently, both ordering coexist below 140 K, showing multiferroic properties. Other $Bi_2BB'O_6$ double perovskites have been theoretically explored and predicted to have multiferroic properties such as, Bi_2FeCrO_6 [2]. Nevertheless, such a predicted double perovskite compound with long range B-site cation ordering is not likely to form since Fe^{3+} (r=0.645 Å) and Cr^{3+} (r=0.615 Å) have the same charge and very similar ionic radii. Hence, metastable Bi$(Fe_{0.5}Cr_{0.5})O_3$ disordered simple perovskite structure with random occupancy of Fe^{3+} and Cr^{3+} is expected to adopt [152, 153]. Nechache *et al*. [154] have grown Bi_2CrFeO_6 ordered thin films and nanostructures with exceptional multiferroic properties at room temperature.

With the goal of searching new multiferroic materials, between 2008 October and 2009 December together with Irene Urcelay, we performed several synthesis attempts (Solid State reaction, co-precipitation, single crystal, Bridgman vertical furnace); although non of them gave the expected results. In the equations C.1 to C.17 are listed the tried chemical reactions, and in Table C.1 synthesis procedures.

- $BiNaCoWO_6$ synthesis

$$Bi_2O_3 + 2C_2H_3O_2Na + 2CoO + 2WO_3 \tag{C.1}$$

$$Bi(NO_3)_3 \cdot 5H_2O + C_2H_3O_2Na + CoCl_2 \cdot 6H_2O + \frac{1}{12}(NH_4)_6H_2W_{12}O_{40} \cdot xH_2O \quad (C.2)$$

$$Bi_2O_3 + Na_2WO_4 \cdot 2H_2O + 2CoO + WO_3 \quad (C.3)$$

$$Bi_2O_3 + Na_2CO_3 + 2CoO + 2WO_3 \quad (C.4)$$

$$Bi_2O_3 + Na_2O + 2CoO + 2WO_3 \quad (C.5)$$

- $BiNaNiWO_6$ synthesis

$$Bi_2O_3 + 2C_2H_3O_2Na + 2NiO + 2WO_3 \quad (C.6)$$

$$Bi(NO_3)_3 \cdot 5H_2O + C_2H_3O_2Na + Ni(NO_3)_2 \cdot 6H_2O + \frac{1}{12}(NH_4)_6H_2W_{12}O_{40} \cdot xH_2O \quad (C.7)$$

$$Bi_2O_3 + Na_2CO_3 + 2NiO + 2WO_3 \quad (C.8)$$

- $BiNaCoSbO_6$ synthesis

$$Bi_2O_3 + 2C_2H_3O_2Na + 2CoO + Sb_2O_5 \quad (C.9)$$

$$Bi_2O_3 + Na_2CO_3 + 2CoO + Sb_2O_5 \quad (C.10)$$

- $BiNaNiSbO_6$ synthesis

$$Bi_2O_3 + 2C_2H_3O_2Na + 2NiO + Sb_2O_5 \quad (C.11)$$

$$Bi_2O_3 + Na_2CO_3 + 2NiO + Sb_2O_5 \quad (C.12)$$

- Bi_2CoFeO_6 synthesis

$$Bi_2O_3 + CoO + \frac{1}{2}Fe_2O_3 \quad (C.13)$$

- Bi_2CrFeO_6 synthesis

$$Bi_2O_3 + \frac{1}{2}Cr_2O_3 + \frac{1}{2}Fe_2O_3 \quad (C.14)$$

$$2Bi(NO_3)_3 \cdot 5H_2O + Cr(NO_3)_3 \cdot 9H_2O + Fe(NO_3)_3 \cdot 9H_2O + 50KOH \quad (C.15)$$

- Bi_2CrCoO_6 synthesis

$$Bi_2O_3 + \frac{1}{2}Cr_2O_3 + CoO \quad (C.16)$$

- Bi_2CrMnO_6 synthesis

$$Bi_2O_3 + \frac{1}{2}Cr_2O_3 + \frac{1}{2}Mn_2O_3 \quad (C.17)$$

$$2Bi(NO_3)_3 \cdot 5H_2O + Cr(NO_3)_3 \cdot 9H_2O + Mn(NO_3)_2 \cdot 4H_2O + 50KOH \quad (C.18)$$

- Bi_2MnFeO_6 synthesis

$$2Bi(NO_3)_3 \cdot 5H_2O + Mn(NO_3)_2 \cdot 4H_2O + Fe(NO_3)_3 \cdot 9H_2O + 50KOH \quad (C.19)$$

- $BiLaMnCrO_6$ synthesis

$$Bi(NO_3)_3 \cdot 5H_2O + \frac{1}{2}La_2O_3 + Mn(NO_3)_2 \cdot 4H_2O + Cr(NO_3)_3 \cdot 9H_2O + 50KOH \quad \text{(C.20)}$$

- $BiLaMnFeO_6$ synthesis

$$Bi(NO_3)_3 \cdot 5H_2O + \frac{1}{2}La_2O_3 + Mn(NO_3)_2 \cdot 4H_2O + Fe(NO_3)_3 \cdot 9H_2O + 50KOH \quad \text{(C.21)}$$

Table C.1: Synthesis reaction, method, treatment atmosphere, last treatment temperature (K) and duration (h) for double perovskite materials synthesis.

Reaction	Synthesis Method	Atmosphere	Synthesis T (K)	Duration (h)
(C.1)	Ceramic	Air	1120	10h
(C.2)	Ceramic	Air	1070	10h
(C.3)	Ceramic	Air	1170	10h
(C.4)	Ceramic	Air	1120	10h
(C.5)	Ceramic	Air	1120	10h
	Gold tube	Air	1180	3 days
	Bridgman	Air		
(C.6)	Ceramic	Air	1120	10h
	Bridgman	Air		
(C.7)	Co-precipitation	Air	1070	10h
(C.8)	Co-precipitation	Air	1070	10h
(C.9)	Ceramic	Air	1670	10h
	Ceramic	N_2	1170	10h
(C.10)	Ceramic	Air	1670	10h
(C.11)	Ceramic	Air	1670	10h
(C.12)	Ceramic	Air	1670	10h
(C.13)	Ceramic	Air	1070	10h
	Co-precipitation	Air	1020	10h
(C.14)	Ceramic	Air	1270	10h
(C.15)	Hydrothermal	Air	445	3.5 days
(C.16)	Ceramic	Air	1670	10h
(C.17)	Ceramic	Air	1170	10h
	Co-precipitation	Air	1070	10h
(C.18)	Hydrothermal	Air	445	3.5 days
(C.19)	Hydrothermal	Air	445	3.5 days
(C.20)	Hydrothermal	Air	445	3.5 days
(C.21)	Hydrothermal	Air	445	3.5 days
(C.22)	Hydrothermal	Air	445	3.5 days

Ceramic (Solid State reaction method): heating of mixture of solid starting materials at different temperature and duration.
Gold: single crystal attempt in a sealed golden tube from a mixture of solid starting materials.
Bridgman (Bridgman vertical furnace): resistibly heated vertical furnace, with axial temperature distribution in 3 zones (high-, gradient, and low temperature). The melt is homogenized in H_T zone, while the grown crystal can be annealed in the L_T zone.
Co-precipitation: mixture of solid starting materials (salts, nitrates, organic agents) in water, mixing magnetically, evaporating the water, and heating at different temperature and duration.
Hydrothermal: crystallization of substances from high temperature aqueous solutions at high-vapor pressure.

- $BiLaCrFeO_6$ synthesis

$$Bi(NO_3)_3 \cdot 5H_2O + \frac{1}{2}La_2O_3 + Cr(NO_3)_9 \cdot 9H_2O + Fe(NO_3)_3 \cdot 9H_2O + 50KOH \tag{C.22}$$

Although in most of the cases it was observed by simple eye that the reactions were not successful: many phases (Figure C.1), melted samples, diffusion of the agents in the crucible (Figure C.2 and Figure C.3)... electron microscopy experiments were performed in order to investigate the formed phases. An example of the observed phases is shown in Figure C.4.

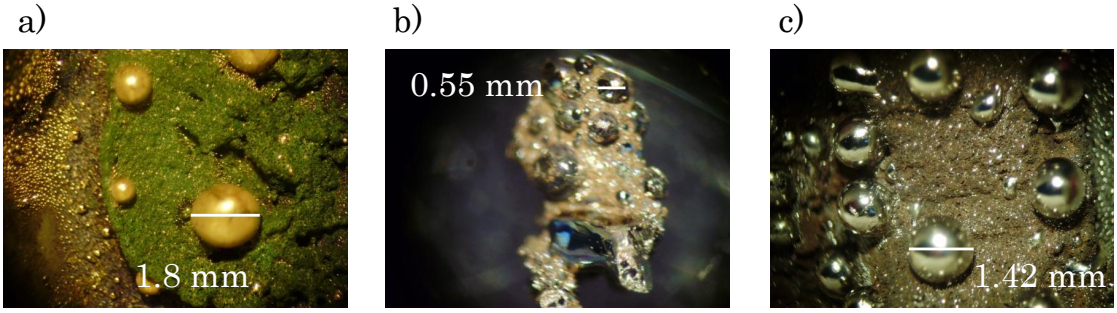

Figure C.1: Examples of synthesis results for (a) Bi_2CrCoO_6 ceramic essay eq.C.16, (b) Bi_2CrMnO_6 ceramic essay eq.C.17, and (c) Bi_2CrMnO_6 co-precipitation essay eq.C.17. Spherical shape bismuth oxide phases were formed in (b) and (c); and in (a) some other phase was formed as can be observed in the color. Apart from bismuth oxide phase, some other phases were formed, as the blue crystal in (b)).

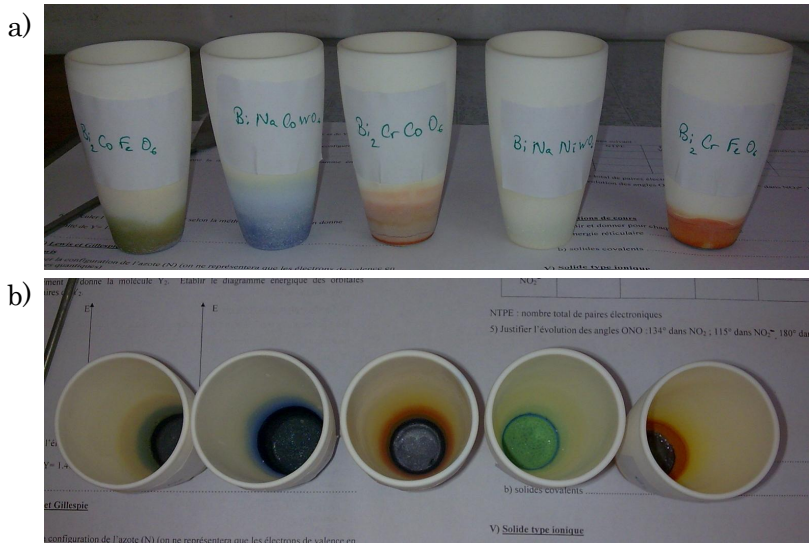

Figure C.2: Photograph of the crucibles used in the Bridgman Vertical Furnace method with eq.C.13, eq.C.4, eq.C.16, eq.C.8, and eq.C.14 agents; the diffusion of the agents is clearly observed.

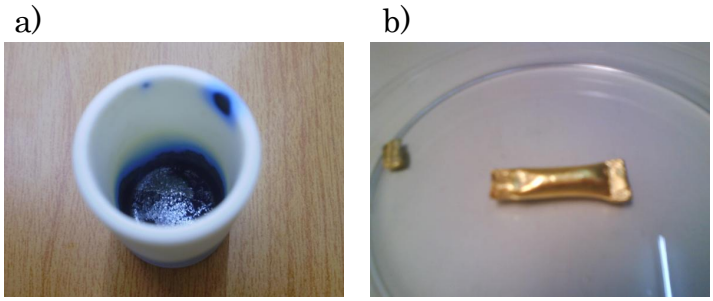

Figure C.3: Final result of the single crystal attempt with eq.C.5 agents, performed using a sealed gold tube.

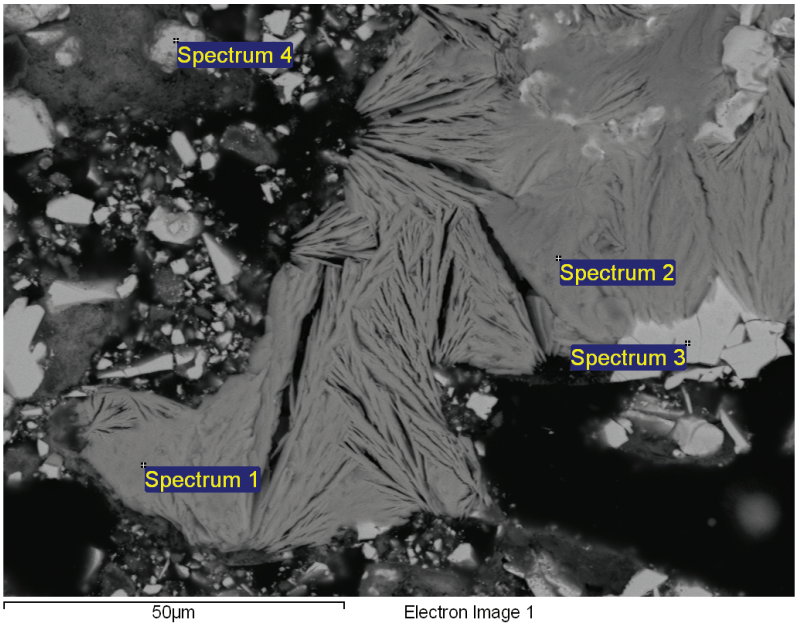

Figure C.4: Electron microscopy image for $BiNaCoWO_6$ (eq.C.3) sample at 1070 K. *Spectrum 1*: 59.86% O, 16.46% Na, 1.28% Co, 22.40% W, 0.00% Bi; *spectrum 2*: 65.65% O, 14.49% Na, 0.38% Co, 19.48% W, 0.00% Bi; *spectrum 3*: 60.34% O, 0.17% Na, 0.71% Co, 12.70% W, 26.08% Bi; *spectrum 4*: 59.48% O, 0.47% Na, 1.28% Co, 12.30% W, 26.47% Bi. Atomic % normalized according to a fixed list of elements.

Bibliography

[1] W. Brixel, J.P. Rivera, A. Steiner and H. Schmidt (1988) *Ferroelectrics* **79** 201-204
http://dx.doi.org/10.1080/00150198808229431.

[2] P. Baettig and N. A. Spaldin (2005) *Appl. Phys. Lett.* **86** 012505-3
http://dx.doi.org/10.1063/1.1843290.

[3] W.E. Pickett, R. Weht and A.B. Shick (1999) *Phys. Rev. Lett.* **83** 3713-3716
http://dx.doi.org/10.1103/PhysRevLett.83.3713.

[4] J. M. Longo, P. M. Raccah and J. B. Goodenough (1968) *J. Appl. Phys.* **39** 1327-1328
http://dx.doi.org/10.1063/1.1656282.

[5] P. D. Battle, T. C. Gibb, C. W. Jones and F. Studer (1989) *J. Solid State Chem.* **78** 281-293
http://www.sciencedirect.com/science/article/pii/0022459689901096.

[6] P. Khalifah, K.D. Nelson, R. Jin, Z.Q. Mao, Y. Liu, Q. Huang, X.P.A. Gao, A.P. Ramirez and R.J. Cava (2001) *Nature* **411** 669-671
http://dx.doi.org/10.1038/35079534.

[7] G. Rose (1839) scripsit. Ann. Phys., Berlin Bd48.S.558
De novis quibusdam fossilibus, quae in montibus uraliis inveniuntur.

[8] V. M. Goldschmidt (1926) *Naturwissenschaften* **14** 477-485
http://dx.doi.org/10.1007/BF01507527.

[9] W. Hönle, G. Miller and A. Simon (1988) *J. Solid State Chem.* **75** 147-155
http://www.sciencedirect.com/science/article/pii/002245968890312X.

[10] V. Luaña, A. Costales and A. M. Pendás (1997) *Phys. Rev. B* **55** 4285-4297
http://dx.doi.org/10.1103/PhysRevB.55.4285.

[11] A. Clearfield (1963) *Acta Cryst.* **16** 135-142
http://dx.doi.org/10.1107/S0365110X6300030X.

[12] F. Gingl, T. Vogt, E. Akiba and K. Yvon (1999) *J. Alloys and Comp.* **282** 125-129 http://www.sciencedirect.com/science/article/pii/S0925838898008342.

[13] H. Sreemoolanadhan, R. Ratheesh, M. T. Sebastian and P. Mohanan (1997) *Mat. Lett.* **33** 161-165 http://www.sciencedirect.com/science/article/pii/S0167577X97001006.

[14] R. J. Cava, B. Batlogg, R. B. Dovervan, D. W. Murphy, S. Sunshine, T. Siegrist, J. P. Remeika, E. A. Rietman, S. Zahurak and G. P. Espinosa (1987) *Phys. Rev. Lett.* **58** 1676-1679 http://dx.doi.org/10.1103/PhysRevLett.58.1676.

[15] S. M. Rao, K. J. Wang, N. Y. Yen, Y. Y. Chen, C. B. Tsai, S. Neeleshwar, M. K. Wu, J. K. Srivastava, M. C. Ling, H. L. Liu and D. C. Ling (2006) *Appl. Phys. Lett.* **89** 232509-3 http://dx.doi.org/10.1063/1.2402902.

[16] B. B. Karki, L. Stixrude, S. J. Clark, M. C. Warren, G. J. Ackland and J. Crain (1997) *American Mineralogist* **82** 635-638.

[17] C. Michel, L. Er-Rakho and B. Raveau (1985) *Mat. Res. Bull.* **20** 667-671 http://www.sciencedirect.com/science/article/pii/0025540885901448.

[18] D. E. Cox, B. Noheda, G. Shiranen, Y. Uesu, K. Fujishiro and Y. Yamada (2001) *Appl. Phys. Lett.* **79** 400-402 http://dx.doi.org/10.1063/1.1384475.

[19] K-I. Kobayashi, T. Kimura, H. Sawada, K. Terakura and Y. Tokura (1998) *Nature* **395** 677-680 http://dx.doi.org/10.1038/27167.

[20] Y. N. Lee, R. M. Lago, J.-L. G. Fierro and J. González (2001) *Applied Catalysis, A: General* **215** 245-256 http://www.sciencedirect.com/science/article/pii/S0926860X01005361.

[21] C. H. Kim, G. Qi, K. Dahlberg and W. Li (2010) *Science* **327** 1624-1627 http://dx.doi.org/10.1126/science.1184087.

[22] K. Ueda, H. Tabata and T. Kawai (1998) *Science* **280** 1064-1066 http://dx.doi.org/10.1126/science.280.5366.1064.

[23] K. Leinenweber and J. Parise (1995) *J. Solid State Chem.* **114** 277-281 http://dx.doi.org/10.1006/jssc.1995.1040.

[24] P. M. Woodward, D. E. Cox, T. Vogt, C. N. R. Rao and A. K. Cheetham (1999) *Chem. Mater.* **11** 3528-3538 http://dx.doi.org/10.1021/cm990281d.

[25] T. Sekiya, T. Yamamoto and Y. Torii (1984) *Bull. Chem. Soc. Japan.* **57** 1859-1862 http://dx.doi.org/10.1246/bcsj.57.1859.

[26] K. R. Poeppelmeier, J. P. Thiel, J. T. Vaughey, M. T. Anderson, D. A. Groenke, C. L. Stern, B. Dabrowski, D. G. Hinks and A. W. Mitchell (1991) *Physica C* **185-189** 525-526 http://www.sciencedirect.com/science/article/pii/092145349192065J.

[27] M. C. Knapp and P. M. Woodward (2006) *J. Solid State Chem.* **179** 1076-1085 http://dx.doi.org/10.1016/j.jssc.2006.01.005.

[28] A. Faik, M. Gateshki, J. M. Igartua, J. L. Pizarro, M. Insausti, R. Kaindl and A. Grzechnik (2008) *J. Solid State Chem.* **181** 1759-1766 http://dx.doi.org/10.1016/j.jssc.2008.03.029.

[29] J. B. Goodenough and R. I. Dass (2000) *Int. J. Inorg. Mater.* **2** 3-9 http://www.sciencedirect.com/science/article/pii/S1466604999000690.

[30] J. Lindén, M. Karppinen, T. Shimada, Y. Yasukawa and H. Yamauchi (2003) *Phys. Rev. B* **68** 174415-5 http://dx.doi.org/10.1103/PhysRevB.68.174415.

[31] M. T. Anderson, K. B. Greenwood, G. A. Taylor and K. R. Poeppelmeier (1993) *Prog. Sol. State Chem.* **22** 197-233 http://www.sciencedirect.com/science/article/pii/007967869390004B.

[32] A. K. Azad, S. G. Eriksson, A. Mellergård, S. A. Ivanov, J. Eriksen and H. Rundlöf (2002) *Mater. Res. Bull.* **37** 1797-1813 http://www.sciencedirect.com/science/article/pii/S0025540802008723.

[33] E. J. Cussen, J. F. Vente, P. D. Battle and T. C. Gibbb (1997) *J. Mater. Chem* **7** 459-463 http://dx.doi.org/10.1039/a607083c.

[34] A. Faik, J. M. Igartua, E. Iturbe-Zabalo and G. J. Cuello (2010) *J. Mol. Struc.* **963** 145-152 http://dx.doi.org/10.1016/j.molstruc.2009.10.027.

[35] P. W. Barnes, M. W. Lufaso and P. Woodward (2006) *Acta Cryst. B* **62** 384-396 http://dx.doi.org/10.1107/S0108768106002448.

[36] A. Faik, D. Orobengoa, E. Iturbe-Zabalo and J. M. Igartua (2012) *J. Solid State Chem.* **192** 273-283 http://dx.doi.org/10.1016/j.jssc.2012.04.019.

[37] M. W. Lufaso, P. M. Woodward and J. Goldberger (2004) *J. Solid State Chem.* **177** 1615-1659 http://dx.doi.org/10.1016/j.jssc.2003.12.020.

[38] P. M. Woodward (1996) PhD thesis, Oregon State University *Structural distortion, phase transitions, and cation ordering in the perovskite and tungsten trioxide structures*.

[39] P. Woodward, R. D. Hoffmann and A. W. Sleight (1994) *J. Mater. Res.* **9** 2118-2127 http://dx.doi.org/10.1557/JMR.1994.2118.

[40] T. K. Mandal, V. V. Poltavets, M. Croft and M. Greenblatt (2008) *J. Solid State Chem.* **181** 2325-2331
http://dx.doi.org/10.1016/j.jssc.2008.04.038.

[41] A. M. Glazer (1972) *Acta Cryst. B* **28** 3384-3392
http://dx.doi.org/10.1107/S0567740872007976.

[42] A. M. Glazer (1975) *Acta Cryst. A* **31** 756-762
http://dx.doi.org/10.1107/S0567739475001635.

[43] H. D. Megaw (1973) W.B. Saunders, Philadelphia
Crystal Structures - A working Approach.

[44] M. Marezio, J. P. Remeika and P. D. Dernier (1970) *Acta Cryst. B* **26** 2008-2022
http://dx.doi.org/10.1107/S0567740870005319.

[45] R. P. Liferovich and R. H. Mitchell (2004) *J. Solid State Chem.* **177** 2188-2197
http://dx.doi.org/10.1016/j.jssc.2004.02.025.

[46] R. H. Mitchell and R. P. Liferovich (2005) *J. Solid State Chem.* **178** 2586-2593
http://dx.doi.org/10.1016/j.jssc.2005.05.016.

[47] R. H. Mitchell and R. P. Liferovich (2004) *J. Solid State Chem.* **177** 4420-4427
http://dx.doi.org/10.1016/j.jssc.2004.09.031.

[48] R. D. Shannon (1976) *Acta Cryst. A* **32** 751-767
http://dx.doi.org/10.1107/S0567739476001551.

[49] J. B. Philipp, P. Majewski, L. Alff, A. Erb, R. Gross, T. Graf, M. S. Brandt, J. Simon, T. Walther, W. Mader, D. Topwal and D. D. Sarma (2003) *Phys. Rev. B* **68** 144431-13
http://dx.doi.org/10.1103/PhysRevB.68.144431.

[50] K. S. Aleksandrov (1976) *Kristallografiya* **21** 249-255.

[51] P. M. Woodward (1997) *Acta Cryst. B* **53** 32-43
http://dx.doi.org/10.1107/S0108768196010713.

[52] C. J. Howard and H. T. Stokes (1998) *Acta Cryst. B* **54** 782-789
http://dx.doi.org/10.1107/S0108768198004200.

[53] E. P. Wigner (1938) *Trans. Faraday Soc.* **34** 678-685
http://dx.doi.org/10.1039/TF9383400678.

[54] E. J. W. Verwey (1939) *Nature* **144** 327-328
http://dx.doi.org/10.1038/144327b0.

[55] E. J. W. Verwey and P. W. Haayman (1941) *Physica* **8** 979-987
http://www.sciencedirect.com/science/article/pii/S0031891441800056.

[56] C. Zener (1951) *Phys. Rev.* **82** 403-405
http://dx.doi.org/10.1103/PhysRev.82.403.

[57] M. Uehara, S. Mori, C. H. Chen and S. W. Cheong (1999) *Nature* **399** 560-563
http://dx.doi.org/10.1038/21142.

[58] J. B. Goodenough (1955) *Phys. Rev* **100** 564-573
http://dx.doi.org/10.1103/PhysRev.100.564.

[59] P. G. Radaelli, D. E. Cox, M. Marezio and S. W. Cheong (1997) *Phys. Rev. B* **55** 3015-3023
http://dx.doi.org/10.1103/PhysRevB.55.3015.

[60] S. Mori, C. H. Chen and S. W. Cheong (1998) *Nature* **392** 473-476
http://dx.doi.org/10.1038/33105.

[61] D. E. Cox and A. W. Sleight (1976) *Solid State Comm.* **19** 969-973
http://www.sciencedirect.com/science/article/pii/0038109876906323.

[62] D. E. Cox and A. W. Sleight (1979) *Acta. Cryst. B* **35** 1-10
http://dx.doi.org/10.1107/S0567740879002417.

[63] Q. Zhou and B. J. Kennedy (2004) *Solid State Comm.* **132** 389-392
http://dx.doi.org/10.1016/j.ssc.2004.08.002.

[64] P. M. Woodward, D. E. Cox, E. Moshopoulou, A. W. Sleight and S. Morimoto (2000) *Phys. Rev. B* **62** 844-855
http://dx.doi.org/10.1103/PhysRevB.62.844.

[65] J. B. Torrance, P. Lacorre, A. I. Nazzal, E. J. Ansaldo and C. Niedermayer (1992) *Phys. Rev. B* **45** 8209-8212
http://dx.doi.org/10.1103/PhysRevB.45.8209.

[66] J. A. Alonso, J. L. García-Muñoz, M. T. Fernández-Díaz, M. A. G. Aranda, M. J. Martínez-Lope and M. T. Casais (1999) *Phys. Rev. Lett.* **82** 3871-3874
http://dx.doi.org/10.1103/PhysRevLett.82.3871.

[67] J. A. Alonso, M. J. Martínez-Lope, M. T. Casais, J. L. García-Muñoz and M. T. Fernández-Díaz (2000) *Phys. Rev. B* **61** 1756-1763
http://dx.doi.org/10.1103/PhysRevB.61.1756.

[68] T. Saito, M. Azuma, E. Nishibori, M. Takata, M. Sakata, N. Nakayama, T. Arima, T. Kimura, C. Urano and M. Takano (2003) *Physica B* **329-333** 866-867
http://www.sciencedirect.com/science/article/pii/S092145260202584X.

[69] H. A. Jahn and E. Teller (1937) *Proc. R. Soc. London A* **161** 220-235
http://dx.doi.org/10.1098/rspa.1937.0142.

[70] J. P. Attfield (2006) *Solid State Sci.* **8** 861-867
http://dx.doi.org/10.1016/j.solidstatesciences.2005.02.011.

[71] J. B. Goodenough (1963) John Wiley & Sons, New York-London
Magnetism and the Chemical Bond.

[72] K. H. J. Buschow and F. R. Boerde (2003) Kluwer Academic/Plenum Publisher, New York
Physics of Magnetism and Magnetic Materials p.8.

[73] P. M. Woodward, J. Goldberger, M. W. Stoltzfus, H. W. Eng, R. A. Ricciardo, P. N. Santhosh, P. Karen and A. R. Moodenbaugh (2008) *J. Am. Ceram. Soc.* **91** 1796-1806
http://dx.doi.org/10.1111/j.1551-2916.2008.02412.x.

[74] E. O. Wollan and W. C. Koehler (1955) *Phys. Rev.* **100** 545-563
http://dx.doi.org/10.1103/PhysRev.100.545.

[75] A. A. Belik, S. Iikubo, K. Kodama, N. Igawa, S.-I. Shamoto, S. Niitaka, M. Azuma, Y. Shimakawa, M. Takano, F. Izumi and E. Takayama-Muromachi (2006) *Chem. Mater.* **18** 798-803
http://dx.doi.org/10.1021/cm052334z.

[76] W. C. Koehler, E. O. Wollan and M. K. Wilkinson (1960) *Phys. Rev.* **118** 58-70
http://dx.doi.org/10.1103/PhysRev.118.58.

[77] M. A. Gilleo (1957) *Acta Cryst.* **10** 161-166
http://dx.doi.org/10.1107/S0365110X57000535.

[78] A. J. Williams, A. Gillies, J. P. Attfield, G. Heymann, H. Huppertz, M. J. Martínez-Lope and J. A. Alonso (2006) *Phys. Rev. B* **73** 104409-7
http://dx.doi.org/10.1103/PhysRevB.73.104409.

[79] S. Picozzi, K. Yamauchi, G. Bihlmayer and S. Blügel (2006) *Phys. Rev. B* **74** 094402-5
http://dx.doi.org/10.1103/PhysRevB.74.094402.

[80] A. Arulraj, K. Ramesha, J. Gopalakrishnan and C. N. R. Rao (2000) *J. Solid State Chem.* **155** 233-237
http://dx.doi.org/10.1006/jssc.2000.8939.

[81] Y. Krockenberger, M. Reehuis, M. Tovarc, K. Mogareb, M. Jansenb and L. Alff (2007) *J. Magn. Magn. Mat.* **310** 1854-1856
http://dx.doi.org/10.1016/j.jmmm.2006.10.648.

[82] Y. Su, J. Zhang, Z. Feng, L. Li, B. Li, Y. Zhou, Z. Chen and S. Cao (2010) *J. Appl. Phys* **108** 013905-6
http://dx.doi.org/10.1063/1.3457905.

[83] X. L. Wang, M. James, J. Horvat and S. X. Dou (2002) *Supercond. Sci. Technol.* **15** 427-430
http://dx.doi.org/10.1088/0953-2048/15/3/328.

[84] H. M. Rietveld (1969) *J. Appl. Cryst.* **2** 65-71
http://dx.doi.org/10.1107/S0021889869006558.

[85] J. Rodríguez-Carvajal (1993) *Physica B* **192** 55-69
http://www.sciencedirect.com/science/article/pii/092145269390108I.

[86] I. D. Brown and D. Altermatt (1985) *Acta Cryst. B* **41** 244-247
http://dx.doi.org/10.1107/S0108768185002063.

[87] H. T. Stokes, D. M. Hatch and J. D. Wells (1991) *Phys. Rev. B* **43** 11010-11018
http://dx.doi.org/10.1103/PhysRevB.43.11010.

[88] M. I. Aroyo and J. M. Perez-Mato (1997) *Phase Trans.* **63** 235-255
http://dx.doi.org/10.1080/01411599708228797.

[89] M. I. Aroyo and J. M. Perez-Mato (1998) *Acta Cryst. A* **54** 19-30
http://dx.doi.org/10.1107/S0108767397010106.

[90] C. J. Howard, B. J. Kennedy and P. M. Woodward (2003) *Acta Cryst. B* **59** 463-471
http://dx.doi.org/10.1107/S0108768103010073.

[91] C. J. Howard and H. T. Stokes (2004) *Acta Cryst. B* **60** 674-684
http://dx.doi.org/10.1107/S0108768104019901.

[92] C. J. Howard and H. T. Stokes (2005) *Acta Cryst. A* **61** 93-111
http://dx.doi.org/10.1107/S0108767304024493.

[93] D. Orobengoa, C. Capillas, M. I. Aroyo and J. M. Perez-Mato (2009) *J. Appl. Cryst.* **42** 820-833
http://dx.doi.org/10.1107/S0021889809028064.

[94] D. Orobengoa (2010) PhD thesis, Universidad del País Vasco/Euskal Herriko Unibertsitatea
Desarrollo de bases de datos cristalográficos on-line y de herramientas para el estudio grupo-teórico de materiales ferróicos y multiferróicos.

[95] B. J. Campbell, H. T. Stokes, D. E. Tanner and D. M. Hatch (2006) *J. Appl. Cryst.* **39** 607-614
http://dx.doi.org/10.1107/S0021889806014075.

[96] M. I. Aroyo, J. M. Perez-Mato, C. Capillas, E. Kroumova, S. Ivantchev, G. Madariaga, A. Kirov and H. Wondratsechek (2006) *Z. Kristallogr.* **221** 15-27
http://dx.doi.org/10.1524/zkri.2006.221.1.15.

[97] M. I. Aroyo, A. Kirov, C. Capillas, J. M. Perez-Mato and H. Wondratsechek (2006) *Acta Cryst. A* **62** 115-128
http://dx.doi.org/10.1107/S0108767305040286.

[98] C. Capillas, E. S. Tasci, G. Florde la, D. Orobengoa, J. M. Perez-Mato and M. I. Aroyo (2011) *Z. Kristallogr.* **226(2)** 186-196
http://dx.doi.org/10.1524/zkri.2011.1321.

[99] H. T. Stokes, D. M. Hatch and B. J. Campbell (2007) ISOTROPY http://stokes.byu.edu/isotropy.html.

[100] B. J. Kennedy and B. A. Hunter (1998) *Phys. Rev. B* **58** 653-658 http://dx.doi.org/10.1103/PhysRevB.58.653.

[101] C.-Q. Jin, J.-S. Zhou, J. B. Goodenough, Q. Q. Liu, J. G. Zhao, L. X. Yang, Y. Yu, R. C. Yu, T. Katsura, A. Shatskiy and E. Ito (2008) *Proc. Nat. Acad. Sci.* **20** 7115-7119 http://dx.doi.org/10.1073/pnas.0710928105.

[102] L. Klein, L. Antognazza, T. H. Geballe, M. R. Beasley and A. Kapitulnik (1999) *Phys. Rev. B* **60** 1448-1451 http://dx.doi.org/10.1103/PhysRevB.60.1448.

[103] S. A. J. Kimber, J. A. Rodgers, H. Wu, C. A. Murray, D. N. Argyriou, A. N. Fitch, D. I. Khomskii and J. P. Attfield (2009) *Phys. Rev. Lett.* **102** 046409-4 http://dx.doi.org/10.1103/PhysRevLett.102.046409.

[104] I. I. Mazin and D. J. Singh (1997) *Phys. Rev. Lett.* **79** 733-736 http://dx.doi.org/10.1103/PhysRevLett.79.733.

[105] K. Ishida, H. Mukuda, Y. Kitaoka, K. Asayama, Z. Q. Mao, Y. Mori and Y. Maeno (1998) *Nature* **396** 658-660 http://dx.doi.org/10.1038/25315.

[106] M. Ito, Y. Yasui, M. Kanada, H. Harashina, S. Yoshii, K. Murata, M. Sato, H. Okumura and K. Kakurai (2001) *J. Phys. Chem. Solids* **62** 337-341 http://www.sciencedirect.com/science/article/pii/S0022369700001591.

[107] M. K. Wu, D. Y. Chen, F. Z. Chien, S. R. Sheen, D. C. Ling, C. Y. Tai, G. Y. Tseng, D. H. Chen and F. C. Zhang (1997) *Z. Phys. B* **102** 37-41 http://dx.doi.org/10.1007/s002570050262.

[108] I. Fernandez, R. Greatrex and N. N. Greenwood (1980) *J. Solid State Chem.* **32** 97-104 http://www.sciencedirect.com/science/article/pii/0022459680902728.

[109] K.-P. Hong, Y.-H. Choi, Y.-U. Kwon, D.-Y. Jung, J.-S. Lee, H.-S. Shim and C.-H. Lee (2000) *J. Solid State Chem.* **150** 383-390 http://dx.doi.org/10.1006/jssc.1999.8611.

[110] P. Rozier, K. Jansson and M. Nygren (2000) *Mater. Res. Bull.* **35** 1391-1400 http://www.sciencedirect.com/science/article/pii/S0025540800003536.

[111] S. Kim and P. D. Battle (1995) *J. Solid State Chem.* **114** 174-183 http://dx.doi.org/10.1006/jssc.1995.1025.

[112] T. Horikubi, T. Mori, H. Nonobe and N. Kamegashira (1999) *J. Alloys and Comp.* **289** 42-47 http://www.sciencedirect.com/science/article/pii/S0925838899001450.

[113] A. Sasaki, Y. Doi and Y. Hinatsu (2009) *J. Alloys and Comp.* **477** 900-904
http://dx.doi.org/10.1016/j.jallcom.2008.11.041.

[114] R. Shaheen, J. Bashir, M. Nasir Khan, R. Rauf and M. Siddique (2008) *Solid State Sci.* **10** 1408-1411
http://dx.doi.org/10.1016/j.solidstatesciences.2008.01.034.

[115] J. W. G. Bos and J. P. Attfield (2004) *Chem. Mater.* **16** 1822-1827
http://dx.doi.org/10.1021/cm0497733.

[116] M. Gateshki and J. M. Igartua (2003) *Mater. Res. Bull.* **38** 1893-1900
http://dx.doi.org/10.1016/j.materresbull.2003.09.001.

[117] A. Faik, J. M. Igartua, M. Gateshki and G. J. Cuello (2009) *J. Solid State Chem.* **182** 1717-1725
http://dx.doi.org/10.1016/j.jssc.2009.04.014.

[118] W. T. Fu and D. J. W. IJdo (2006) *J. Solid State Chem.* **179** 1022-1028
http://dx.doi.org/10.1016/j.jssc.2005.12.031.

[119] L. Ortega-San Martín, J. P. Chapman, G. Cuello, J. González-Calbet, M. I. Arriortua and T. Rojo (2005) *Z. Anorg. Allg. Chem.* **631** 2127-2130
http://dx.doi.org/10.1002/zaac.200570028.

[120] E. Iturbe-Zabalo, J. M. Igartua, A. Faik, A. Larrañaga, M. Hoelzel and G. J. Cuello (2013) *J. Solid State Chem.* **198** 24-38
http://dx.doi.org/10.1016/j.jssc.2012.09.007.

[121] M. Retuerto, M. J. Martínez-Lope, M. García-Hernández, M. T. Fernández-Díaz and J. A. Alonso (2008) *Eur. J. Inorg. Chem.* **4** 588-595
http://dx.doi.org/10.1002/ejic.200700753.

[122] A. Faik, E. Iturbe-Zabalo, I. Urcelay and J. M. Igartua (2009) *J. Solid State Chem.* **182** 2656-2663
http://dx.doi.org/10.1016/j.jssc.2009.07.021.

[123] L. Ortega-San Martín, J. P. Chapman, M. Insausti E. Hernández-Bocanegra, M. I. Arriortua and T. Rojo (2004) *J. Phys.: Condens. Matter.* **16** 3879-3888
http://dx.doi.org/10.1088/0953-8984/16/23/008.

[124] M. Gateshki, J. M. Igartua and A. Faik (2007) *J. Solid State Chem.* **180** 2248-2255
http://dx.doi.org/10.1016/j.jssc.2007.05.022.

[125] E. Iturbe-Zabalo, J. M. Igartua, A. Larrañaga, V. Pomjakushin, G. Castro and G. J. Cuello (2012) *Solid State Ionics* Submitted.

[126] M. A. Carpenter (2000) Reviews in Mineralogy Geochemistry, Mineralogical Society of America
Transformation Processes in Minerals vol.39, p.35-64.

[127] N. Narayanan, D. Mikhailova, A. Senyshyn, D. M. Trots, R. Laskowski, P. Blaha, K. Schwarz, H. Fuess and H. Ehrenberg (2010) *Phys. Rev. B* **82** 024403-12 http://dx.doi.org/10.1103/PhysRevB.82.024403.

[128] F. N. Sayed, S. N. Achary, O. D. Jayakumar, S. K. Deshpande, P. S. R. Krishna, S. Chatterjee, P. Ayyub and A. K. Tyagi (2010) *AIP Conf. Proc.* **26** 567-577 http://dx.doi.org/10.1063/1.3530457.

[129] Bertaut E. F. (1963) G. T. Rado and H. Suhl (Eds.), Academic Press, New York. and London *Magnetism* p. 149.

[130] A. S. Wills (2000) *Physica B* **276** 680-681 http://www.sciencedirect.com/science/article/pii/S0921452699017226.

[131] J. M. Perez-Mato, D. Orobengoa and M. I. Aroyo (2010) *Acta Cryst. A* **66** 558-590 http://dx.doi.org/10.1107/S0108767310016247.

[132] R. B. Macquart, B. J. Kennedy and M. Avdeev (2010) *J. Solid State Chem.* **183** 2400-2405 http://dx.doi.org/10.1016/j.jssc.2010.08.001.

[133] A. Aatiq and A. Boukhari (2004) *Mat. Lett.* **58** 2406-2411 http://dx.doi.org/10.1016/j.matlet.2004.02.023.

[134] B. J. Kennedy, Q. Zhou and M. Avdeev (2011) *J. Solid State Chem.* **184** 2987-2993 http://dx.doi.org/10.1016/j.jssc.2011.08.028.

[135] A. Moure, T. Hungría, A. Castro, J. Galy, O. Peña, J. Tartaj and C. Moure (2010) *Chem. Mater.* **22** 2908-2915 http://dx.doi.org/10.1021/cm100236q.

[136] M. Gateshki (2003) PhD thesis, Universidad del País Vasco/Euskal Herriko Unibertsitatea *Estudio, mediante métodos de difracción, de la estructura y las transiciones de fase en las perovskitas dobles* Sr_2MWO_6 *(M=Mn,Cu,Ni,Co,Fe,Zn,Mg) Y* La_2NiRuO_6.

[137] A. Faik (2009) PhD thesis, Universidad del País Vasco/Euskal Herriko Unibertsitatea *Estudio de las estructuras y de las transiciones de fase en nuevos materiales de wolframio (*$Sr_2M^{2+}W^{6+}O_6$*) y de antimonio (*$A_2M^{3+}Sb^{5+}O_6$*) con estructuras de perovskita doble*.

[138] J. Wang, B. H. Toby, P. L. Lee, L. Ribaud, S. M. Antao, C. Kurtz, M. Ramanathan, R. B. V. Dreele and M. A. Beno (2008) *Rev. Sci. Instrum.* **79** 085105-7 http://dx.doi.org/10.1063/1.2969260.

[139] G. R. Castro (1998) *J. Synchrotron Rad.* **5** 657-660 http://dx.doi.org/10.1107/S0909049597019079.

[140] P. Fischer, G. Frey, M. Koch, M. Könnecke, V. Pomjakushin, J. Schefer, R. Thut, N. Schlumpf, R. Bürge, U. Greuter, S. Bondt and E. Berruyer (2000) *Physica B* **276-278** 146-147 http://www.sciencedirect.com/science/article/pii/S092145269901399X.

[141] R. Gilles, G. Artus, J. Saroun, H. Boysen and H. Fuess (2000) *Physica B* **276-278** 87-88
http://www.sciencedirect.com/science/article/pii/S092145269901371X.

[142] M. Hoelzel, A. Senyshyn, N. Juenke, H. Boysen, W. Schmahl and H. Fuess (2012) *Nucl. Instrum. Meth. A* **667** 32-37
http://dx.doi.org/10.1016/j.nima.2011.11.070.

[143] G. Catalan and J. F. Scott (2009) *Adv. Mater.* **21** 2463-2485
http://dx.doi.org/10.1002/adma.200802849.

[144] R. Rai, S. K. Mishra, N. K. Singh, S. Sharma and A. L. Kholkin (2011) *Current Appl. Phys.* **11** 508-512
http://dx.doi.org/10.1016/j.cap.2010.09.003.

[145] S. Niitaka, M. Azuma, M. Takan, E. Nishibori, M. Takata and M. Sakata (2004) *Solid State Ionics* **172** 557-559
http://dx.doi.org/10.1016/j.ssi.2004.01.060.

[146] S. Ishiwata, M. Azuma, M. Takano, M. Takata E. Nishibori, M. Sakatac and K. Katod (2002) *J. Mater. Chem.* **12** 3733-3737
http://dx.doi.org/10.1039/b206022a.

[147] Z. H. Chi, H. Yang, S. M. Feng, F. Y. Li, R. C. Yu and C. Q. Jin (2007) *J. Mag. Mag. Mat* **310** e358-e360
http://dx.doi.org/10.1016/j.jmmm.2006.10.335.

[148] T. Atou, H. Chiba, K. Ohoyama, Y. Yamaguchi and Y. Syono (1999) *J. Solid State Chem.* **145** 639-642
http://dx.doi.org/10.1006/jssc.1999.8267.

[149] A. A. Belik, S. Iikubo, T. Yokosawa, K. Kodama, N. Igawa, S. Shamoto, M. Azuma, M. Takano, K. Kimoto, Y. Matsui and E. Takayama-Muromachi (2007) *J. Am. Chem. Soc.* **129** 971-977
http://dx.doi.org/10.1021/ja0664032.

[150] C.-H. Yang, T. Y. Koo and Y. H. Jeong (2007) *J. Mag. Mag. Mat.* **310** 1168-1170
http://dx.doi.org/10.1016/j.jmmm.2006.10.278.

[151] Y. Shimakawa, M. Azuma and N. Ichikawa (2011) *Materials* **4** 153-168
http://dx.doi.org/10.3390/ma4010153.

[152] M. R. Suchomel, C. I. Thomas, M. Allix, M. J. Rosseinsky, A. M. Fogg and M. F. Thomas (2007) *Appl. Phys. Lett.* **90** 112909-3
http://dx.doi.org/10.1063/1.2713757.

[153] D. H. Kim, H. N. Lee, M. D. Biegalski and H. M. Christen (2007) *Appl. Phys. Lett.* **91** 042906-3
http://dx.doi.org/10.1063/1.2763964.

[154] R. Nechache and F. Rosei (2012) *J. Solid State Chem.* **189** 13-20
http://dx.doi.org/10.1016/j.jssc.2012.01.022.

Scientific contributions

Publications

Scientific contributions directly related to the work summarized in this report

1. **E. Iturbe-Zabalo**, J.M. Igartua, A. Aatiq, V. Pomjakushin. *"A structural study of the $CaLn_2CuTi_2O_9$ (Ln=Pr,Nd,Sm) and $BaLn_2CuTi_2O_9$ (Ln=La,Pr,Nd) triple perovskite series"* (2013) *J. Mol. Struc.* **1034** 134-143
http://dx.doi.org/10.1016/j.molstruc.2012.08.049.

2. **E. Iturbe-Zabalo**, J.M. Igartua, A. Faik, A. Larrañaga, M. Hoelzel, G.J. Cuello. *"Crystal structures and high-temperature phase-transitions in $SrNdMRuO_6$ (M=Zn,Co,Mg,Ni) double perovskites studied by symmetry-mode analysis"* (2013) *J. Solid State Chem.* **198** 24-38
http://dx.doi.org/10.1016/j.jssc.2012.09.007.

3. **E. Iturbe-Zabalo**, O. Fabelo, M. Gateshki, J.M. Igartua. *"Mode-crystallography analysis and magnetic structures of $SrLnFeRuO_6$ (Ln=La,Pr,Nd) disordered perovskites"* (2012) *Acta Cryst. B*, accepted for publication.

4. **E. Iturbe-Zabalo**, J.M. Igartua, M. Gateshki, G.J. Cuello. *"Room- and high-temperature structural characterization of $SrLaZnRuO_6$ and $SrLaMgRuO_6$ ordered double perovskites"* (2012) *J. Appl. Cryst.*, under revision.

5. **E. Iturbe-Zabalo**, J.M. Igartua, A. Faik, A. Larrañaga, V. Pomjakushin, G.J. Cuello. *"Structural study of $SrPrZnRuO_6$, $SrPrCoRuO_6$, $SrPrMgRuO_6$ and $SrPrNiRuO_6$ double perovskite oxides by symmetry-adapted mode analysis"* (2012) *J. Phys. Condens. Matter*, submitted.

Other scientific contributions

6. A. Faik, **E. Iturbe-Zabalo**, I. Urcelay, J.M. Igartua. *"Crystal Structures and High-Temperature Phase Transitions of Sr_2MSbO_6 (M= La, Sm) novel double perovskite oxides"* (2009) *J. Solid State Chem.* **182** 2656-2663
http://dx.doi.org/10.1016/j.jssc.2009.07.021.

7. A. Faik, I. Urcelay, **E. Iturbe-Zabalo**, J.M. Igartua. *"Cationic ordering and role of the A-site cation on the structure of the new double perovskites $Ca_{2-x}Sr_xRSbO_6$ R=La,Sm and (x = 0; 0,5; 1)"* (2010) *J. Mol. Struc.* **963** 145-152
http://dx.doi.org/10.1016/j.molstruc.2010.05.024.

8. A. Faik, J.M. Igartua, **E. Iturbe-Zabalo**, G.J. Cuello. *"A study of the crystal structures and the phase transitions of Sr_2FeSbO_6, $SrCaFeSbO_6$ and Ca_2FeSbO_6 double perovskite oxides"* (2010) *J. Mol. Struc.* **977** 137-144
http://dx.doi.org/10.1016/j.molstruc.2009.10.027.

9. T.I Milenov, P.M. Rafailov, V. Tomov, R.P. Nikolova, V. Skumryev, J.M. Igartua, G. Madariaga, G.A. López, **E.Iturbe-Zabalo**, M.M. Gospodinov. *"Growth and characterization of $Pb_3Ni_{1.5}Mn_{5.5}O_{15}$ single crystal"* (2011) *J. Phys. Condens. Matter* **23** 156001-156005
http://dx.doi.org/10.1088/0953-8984/23/15/156001.

10. A. Faik, D. Orobengoa, **E. Iturbe-Zabalo**, J.M. Igartua.*"A study of the crystal structures and the phase-transitions of the ordered double perovskites Sr_2ScSbO_6 and Ca_2ScSbO_6"* (2012) *J. Solid State Chem.* **192** 273-283
http://dx.doi.org/10.1016/j.jssc.2012.04.019.

Contribution in conferences

Contribution in conferences directly related to the work summarized in this report

1. **Title:** Crystallographic studies on SrLnFeRuO$_6$ (Ln=La,Pr,Nd) disordered perovskites
   Authors: E. Iturbe-Zabalo, O. Fabelo, M. Gateshki, J.M. Igartua
   Type of participation: Poster
   Conference: : 13th European Powder Diffraction Conference (EPDIC)
   Place and year: Grenoble, France; 2012

2. **Title:** Structural relationship and phase diagram for SrLnMRuO$_6$ perovskites
   Authors: E. Iturbe-Zabalo, J.M. Igartua
   Type of participation: Oral
   Conference: VI Reunión de la Sociedad Española de Técnicas Neutrónicas (SETN)
   Place and year: Segovia, Spain; 2012

3. **Title:** Structures and temperature induced phase-transition studies of perovskite type materials. Symmetry-mode analysis
   Authors: E. Iturbe-Zabalo, J.M. Igartua
   Type of participation: Oral
   Conference: III Reunión de Jóvenes Cristal
   Place and year: La Laguna, Spain; 2011

4. **Title:** Structural study of SrPrMRuO$_6$ double perovskites by symmetry-mode analysis
   Authors: E. Iturbe-Zabalo, G. Cuello, J.M. Igartua
   Type of participation: Poster
   Conference: : XXII Congress and General Assembly of the International Union of Crystallography (IUCr)
   Place and year: Madrid, Spain; 2011

5. **Title:** Crystal structure and structural phase-transitions of double perovskite ruthenates by symmetry mode analysis
   Authors: E. Iturbe-Zabalo, J.M. Igartua, A. Faik, G.J. Cuello, M. Hoelzel
   Type of participation: Poster
   Conference: : 5$^{\text{th}}$ European Conference on Neutron Scattering (ECNS)
   Place and year: Prague, Check Republic; 2011

6. **Title:** Thermal Study of the Structures and Phase Transitions of New Possibly Functional Materials: $A'A''_2CuTi_2O_9$ (A'=Ca,Ba) and (A''=Pr,Nd) Triple Perovskites
   Authors: E. Iturbe-Zabalo, J.M. Igartua, G.J. Cuello, A. Aatiq
   Type of participation: Poster
   Conference: : 9th Conference on Solid State Chemistry
   Place and year: Prague, Check Republic; 2010

7. **Title:** Synthesis, structure and thermal evolution of new $SrNdMRuO_6$ (M=Ni,Co,Fe,Mg,Zn) double perovskites
   Authors: E. Iturbe-Zabalo, J.M. Igartua, G.J. Cuello
   Type of participation: Poster
   Conference: 9th Summer School on Condensed Matter Research, Magnetic Phenomena
   Place and year: Zuoz, Switzerland; 2010

8. **Title:** Synthesis, structure and thermal evolution of new $A'A''_2CuTi_2O_9$ (A'=Ca,Ba) and (A''=Pr,Nd) Triple Perovskites
   Authors: E. Iturbe-Zabalo, J.M. Igartua, G.J. Cuello, A. Aatiq
   Type of participation: Poster
   Conference: V Reunión de la Sociedad Española de Técnicas Neutrónicas (SETN)
   Place and year: Gijón, Spain; 2010

9. **Title:** Structures and phase transitions at low- and high- temperature of new possibly functional materials: $SrNdMRuO_6$ (M=Ni,Co,Fe,Mg,Zn) double perovskites
   Authors: E. Iturbe-Zabalo, J.M. Igartua, G.J. Cuello
   Type of participation: Poster
   Conference: XX Symposium - 20th anniversary Hercules
   Place and year: Grenoble, France; 2010

Other contribution in conferences

10. **Title:** Crystal structures and phases transitions of a new double perovskites oxides $Sr_{2-x}Ca_xLnSbO_6$ (Ln=La, Sm and 0<x<1)
    Authors: A. Faik, E. Iturbe-Zabalo, I. Urcelay, J.M. Igartua
    Type of participation: Poster
    Conference: 11th European Powder Diffraction Conference (EPDIC)
    Place and year: Warsaw, Poland; 2008

11. **Title:** Crystal structures and phase transitions of antimony double perovskites
    Authors: A. Faik, E. Iturbe-Zabalo, I. Urcelay, J.M. Igartua
    Type of participation: Poster
    Conference: IV Reunión de la Sociedad Española de Técnicas Neutrónicas (SETN)
    Place and year: San Feliu de Guixols, Spain; 2008

12. **Title:** Structures and high-temperature phase transitions of Sr_2MSbO_6 (M=Sc,Cr,Fe) double perovskite oxides
    Authors: A. Faik, I. Urcelay, E. Iturbe-Zabalo, J.M. Igartua
    Type of participation: Poster
    Conference: : XXI Congress and General Assembly of the International Union of Crystallography (IUCr)
    Place and year: Osaka, Japan; 2008

Experiments in international research facilities

In the following lines are listed the experiments that have been performed in international research facilities to achieve the culmination of this thesis:

1. **Title:** Structures and phase transitions at low- and high-temperature of new possibly functional materials: $A'A''_2CuTi_2O_9$ (A'=Ca,Ba) and (A''=Pr,Nd) triple perovskites
   Instrument: HRPT (SINQ)
   Experimental n°: 20091256
   Date: 8-12 June 2010

2. **Title:** Structures and phase transitions at low- and high-temperature of new possibly functional materials: $SrNdMRuO_6$ (M=Ni,Co,Fe,Mg,Zn)
   Instrument: SPODI (FRMII)
   Experimental n°: 4456
   Date: 8-12 July 2010

3. **Title:** Thermal evolution of $SrLaCoRuO_6$: magnetic and nuclear structures
   Instrument: D1B (ILL)
   Experimental n°: INTER-196
   Date: 25-29 July 2010

4. **Title:** Test experiment on OrientExpress: $Pb_3Ni_{1.5}Mn_{5.5}O_{15}$
   Instrument: ORIENT EXPRESS (ILL)
   Experimental n°: INTER-1899
   Date: 30 November - 1 December 2010

5. **Title:** Structural and Magnetic characterization of the new possibly multiferroic: $Pb_3Ni_{1.5}Mn_{5.5}O_{15}$
   Instrument: D15 and D2B (ILL)
   Experimental n°: 5-41-585
   Date: 3-6 and 15-16 December 2010

6. **Title:** Structures and phase transitions at low- and high-temperature of new double perovskites: $SrNdMRuO_6$ (M=Ni,Co,Fe,Mg,Zn)
   Instrument: D2B (ILL)
   Experimental n°: 5-23-609
   Date: 10-13 December 2010

7. **Title:** Determination of the symmetry of the ferroelectric phase in multiferroic $BiFeO_3$: a neutron diffraction study aided by group-theoretical computer tools
   Instrument: D2B (ILL)
   Experimental n°: 5-24-426
   Date: 13-15 December 2010

8. **Title:** Characterization of the new possibly multiferroic: $Pb_3Ni_{1.5}Mn_{5.5}O_{15}$
   Instrument: BM25-A (SpLine, ESRF)
   Experimental n°: 25-01-796
   Date: 7-12 April 2011

9. **Title:** Structural and magnetic characterization at low- and high-temperature of $SrPrMRuO_6$ (M=Mg,Co,Ni,Zn,Fe) Double Perovskite
   Instrument: HRPT (SINQ)
   Experimental n°: 20101302
   Date: 8-11 August 2011

10. **Title:** Structural and magnetic characterization at low- and high-temperature of SrPrMRuO$_6$ (M=Mg,Co,Ni,Zn) double perovskite
    Instrument: D1B and D2B (ILL)
    Experimental n°: 5-24-459
    Date: 28-29 July and 9-12 September 2011

11. **Title:** SrNdCoRuO$_6$, SrNdNiRuO$_6$, SrLaCoRuO$_6$
    Instrument: D1B (ILL)
    Experimental n°: INTER-224
    Date: 15 October 2011

12. **Title:** Rear-earth cation influence in the crystal and magnetic structure of SrLnFeRuO$_6$ (Ln=La,Nd,Pr) double perovskite
    Instrument: D1B (ILL)
    Experimental n°: 5-24-458
    Date: 16-18 November 2011

Table C.2: List of publications and the performed experiments in each case.

Publication 1	Exp1
Publication 2	Exp2/Exp11
Publication 3	Exp2/Exp6/Exp8/Exp9/Exp10/Exp12
Publication 4	Exp8/Exp9
Publication 5	Exp6/Exp8/Exp10

Resumen

En las últimas décadas el estudio de materiales tipo perovskita ha tenido una transcendencia fundamental en la investigación científica y en las aplicaciones tecnológicas debido, sobre todo, a sus propiedades eléctricas y magnéticas, en la mayoría de los casos fuertemente ligadas con los cambios estructurales inducidos por la temperatura y/o la presión. La introducción de más de un catión en las posiciones de la perovskita simple (ABO_3) ha generado un amplio abanico de estructuras de tipo perovskita, como las perovskitas dobles $(AA')(BB')O_6$, las perovskitas triples $(AA'_2)(BB'_2)O_9$... La perovskita ideal forma un empaquetamiento cúbico, pero habitualmente se descubren estructuras distorsionadas con menor simetría que la cúbica. Las distorsiones en las perovskitas normalmente son causadas por desplazamientos de los cationes B desde los centros de los octaedros BO_6, por factores electrónicos (e.g. iones con efecto Jahn-Teller) y, en la mayoría de los casos, por rotaciones e inclinaciones de los octaedros. Debido a estas distorsiones disminuye la simetría de la estructura.

Uno de los factores que más influyen en las rotaciones de los octaedros es la naturaleza de los cationes colocados en los sitios cubo-octaédricos (cationes A). Por ejemplo, las perovskitas con cationes de Ba^{2+} en la posición A, típicamente cristalizan con simetría cúbica; sin embargo, si es el Ca^{2+}, por ejemplo, el que ocupa esa misma posición, la estructura tiende a tener una simetría ortorrómbica o monoclínica. Por otro lado, la simetría de una perovskita con Sr^{2+}, que tiene un tamaño intermedio entre el de Ba^{2+} y el del Ca^{2+}, dependerá mucho del resto de los cationes que formen la estructura y, muchas veces, no es tarea fácil la asignación correcta del grupo espacial.

Los cambios en la simetría de las estructuras, es decir las rotaciones e inclinaciones de los octaedros, se pueden observar mediante la difracción de polvo de rayos-X y de neutrones. Estos últimos nos darán una información más detallada sobre las posiciones de

los oxígenos, ya que los rayos-X interaccionan con los electrones y siendo estos átomos los más ligeros en los materiales que se han estudiado, su contribución puede ser apantallada por la respuesta de átomos mas pesados.

En este trabajo se han estudiado dos familias de perovskitas: trece perovskitas dobles (SrLaMRuO$_6$, M=Zn,Mg,Fe; SrPrMRuO$_6$, M=Zn,Co,Mg,Ni,Fe; SrNdMRuO$_6$, M=Zn,Co, Mg,Ni,Fe), diez de ellas sintetizadas por primera vez y seis nuevas perovskitas triples (CaLn_2CuTi$_2$O$_9$, Ln=Pr,Nd,Sm; BaLn_2CuTi$_2$O$_9$, Ln=La,Pr,Nd). El estudio se ha centrado en la síntesis y caracterización estructural de dichos compuestos, determinando las estructuras cristalinas a temperatura ambiente, así como las posibles transiciones de fase estructurales que puedan ser inducidas por la temperatura (alta y baja temperatura). En algunos de los materiales, se han estudiado las estructuras magnéticas. Los compuestos se han analizado mediante difracción de rayos-X, de radiación sincrotrón y de neutrones y los datos se han analizado utilizando el método de Rietveld.

El procedimiento utilizado en el refinamiento por el método de Rietveld no a sido el más habitual; en este caso, se han sustituido las coordenadas atómicas individuales por coordenadas colectivas: las amplitudes de los modos que describen la distorsión de una fase prototipo. Este método de describir la distorsión de las estructuras, basado en la teoría de grupos, va ganando adeptos en los últimos años y puede llegar a ser una herramienta muy útil para el análisis de las perovskitas en general, puesto que éstas sufren una gran cantidad de transiciones de fase estructurales.

Los materiales de la familia del rutenio estudiados en este trabajo presentan dos tipos de ordenamiento entre los cationes M y Ru en los sitios B y B' de la perovskita doble ($AA'BB'$O$_6$). Los materiales con Zn, Co, Mg y Ni presentan un ordenamiento total en su red cristalina, con los cationes M en el estado de oxidación 2+ y el rutenio en el estado de oxidación 5+. Sin embargo, en los materiales de Fe, Fe^{3+} y Ru^{4+} forman una red cristalina totalmente desordenada. Todos los materiales a temperatura ambiente, excepto los materiales con Fe, cristalizan en la simetría monoclínica $P2_1/n$ y los materiales con Fe en la simetría ortorrómbica $Pbnm$.

La descomposición de la distorsión de las fases a temperatura ambiente se ha realizado utilizando una fase prototipo virtual, con simetría cúbica en ambos casos, pero con grupos espaciales diferentes $Fm\bar{3}m$ y $Pm\bar{3}m$ (totalmente ordenados y completamente desordenados, respectivamente). La descomposición de los modos adaptados a la simetría se ha realizado utilizando el programa AMPLIMODES y el posterior refinamiento de los modos colectivos mediante el paquete de programas FullProf Suit.

Mediante la teoría de grupos, uno puede saber si existe una única irrep activa que provoque una ruptura de simetría total desde la fase prototipo hasta la fase de baja simetría. Si ocurriese así, el resto de los modos que apareciesen en la ruptura de simetría serían modos secundarios, que son aquellos que aparecen solamente como un efecto inducido. Sin embargo, existen algunas rupturas de simetría que no cumplen el tener una única irrep activa. Esto quiere decir que la ruptura de simetría total no puede ser explicada por una única irrep, ya que la simetría de la fase distorsionada no es un subgrupo isótropo de la pase prototipo. Esta situación es muy común en las perovskitas distorsionadas. En estos casos, generalmente, no hay una única combinación de irreps que dé lugar a la estructura final observada y aunque mediante la teoría de grupos se pueden excluir algunas combinaciones, normalmente, son necesarios otro tipo de métodos (e.g. método de Rietveld).

El refinamiento de los datos de difracción de neutrones de los materiales SrLnMRuO$_6$ mediante el método de Rietveld a dispuesto una jerarquía de los modos, expresada en un orden descendiente de las amplitudes de los mismos. La fase distorsionada monoclínica $P2_1/n$ se puede describir con la ayuda de las irreps GM_4^+ y X_3^+; y la fase ortorrómbica *Pbnm* por medio de R_4^+ y M_3^+. Aún sabiendo qué irreps son necesarias para romper la simetría, se deben respetar los datos experimentales y la información estructural se ha dado, en todos los casos, teniendo en cuenta las amplitudes de todos los modos.

Las amplitudes de los modos que se transforman de acuerdo a las irreps observadas en todos los compuestos en función del factor de tolerancia (t), muestran una tendencia general de disminución según t se aproxima a 1. Esto quiere decir que los materiales con los mayores lantánidos ($r_{La} > r_{Pr} > r_{Nd}$) en la posición A' de la perovskita doble, serán más simétricos. Sin embargo, esta tendencia se observa a la inversa cuando nos referimos a los cationes en la posición B de la perovskita doble. En este caso, cuanto mayor sea el radio iónico del catión, mayor es la distorsión que sufre la estructura y mayores, por tanto, las amplitudes de los modos que se obtienen en los refinamientos.

Mediante diferentes cálculos de Rietveld de los datos de neutrones a temperatura ambiente hemos observado que las amplitudes de los modos para distintas estructuras no varían cuando los factores de desplazamiento atómicos de los oxígenos se refinan cada uno por separado o ligados. Cuando el refinamiento se realiza con ligaduras (cuando todos tengan el mismo valor) por ejemplo, se obtiene un valor que es el valor medio de los valores que se obtendrían si se liberasen cada uno por separado. Esto mismo se ha podido observar a altas temperaturas. Esta observación se a utilizado para aligerar los cálculos, ligando los oxígenos.

En los materiales SrLnMRuO$_6$ (M=Zn,Co,Mg,Ni) se han estudiado los estados de

coordinación de los cationes en las posiciones A y A' de la perovskita doble. Es sabido que los estados de coordinación de los lantánidos en la posición A de la perovskita, cuando estas están distorsionadas, se ve reducido. Esto es debido a las inclinaciones y/o rotaciones de los octaedros, que inducen alargamientos y acortamientos de las distancias interatómicas; manteniendo ocho distancias cortas y cuatro largas para el caso de estos materiales. Los dos grupos de distancias forman lo que es conocido como la primera y segunda esfera de coordinación para los cationes en la posición A. Todos los materiales se comportan de la misma manera: el volumen de la primera esfera de coordinación aumenta de tamaño con la sustitución de un lantánido mayor (efecto estérico). Sin embargo, entre los materiales de la serie con el mismo lantánido, el volumen no varía. La tendencia de la segunda esfera de coordinación es la expansión del volumen con la disminución del radio iónico del lantánido. Entre todos los compuesto los que poseen Mg en su red cristalina no siguen esta tendencia, probablemente debido a su naturaleza: no es metal de transición.

Entre los trece materiales Sr$Ln$$MRuO_6$ se han observado tres secuencias de transiciones de fase estructurales, dos de ellas en los materiales totalmente ordenados y una tercera en los desordenados.

Los materiales SrNdMRuO_6 (M=Zn,Co,Mg,Ni) transforman a altas temperaturas siguiendo la siguiente secuencia de transiciones de fase:

$$P2_1/n \rightarrow P4_2/n \rightarrow Fm\bar{3}m$$

mientras que los materiales SrLaMRuO_6 (M=Zn,Mg) y SrPrMRuO_6 (M=Mg,Ni) transforman a altas temperaturas según ésta otra:

$$P2_1/n \rightarrow R\bar{3} \rightarrow (Fm\bar{3}m)$$

Las temperaturas de las transiciones de fase estructurales observadas en estos compuestos en función del factor de tolerancia (t), muestran una tendencia general de disminución según t se va acercando a 1. En Sr$Ln$$MRuO_6$ (Ln=La,Pr; M=Zn,Mg,Ni), se observa también, que existe un rango de temperatura en la que coexisten la fase monoclínica y la trigonal.

SrPrFeRuO_6, con desorden completo entre los cationes Fe y Ru, transforma a altas temperaturas siguiendo esta otra secuencia de transiciones de fase:

$$Pbnm \rightarrow R\bar{3}c \rightarrow (Fm\bar{3}m)$$

En todos ellos se a seguido la evolución de las amplitudes de los modos con la temperatura, observando la disminución de las amplitudes según crece la temperatura; indicando una progresión hacia una estructura más simétrica. Todas las transiciones de fase estructurales estudiadas son de primer orden.

Las estructuras magnéticas de los materiales Sr$Ln M$RuO_6 (Ln=La,Pr,Nd; M=Co,Ni,Fe) se han estudiado mediante difracción de neutrones. Los materiales con Co y Ni sufren una transición magnética alrededor de 80 K, mientras que los compuestos de Fe se transforman entorno a 450 K. Los vectores de propagación que describen la estructura magnética son (1/2,0,1/2) y (0,0,0) para los materiales con SrLnCoRuO_6 y SrLnNiRuO_6, y SrLnFeRuO_6, respectivamente. El análisis de las estructuras magnéticas se ha llevado a cabo utilizando el análisis de representaciones descrita por Bertaut. Los modelos magnéticos que más se ajustan a los datos indican que SrLaFeRuO_6 y SrNdFeRuO_6 tienen un orden antiferromagnético con los spines canteados a lo largo de a y c, respectivamente. Sin embargo, SrPrFeRuO_6 muestra una estructura más compleja, debido a los dos sitios magnéticos generados por el cation de Pr y Fe/Ru. En este caso, el momento magnético total es puramente ferrimagnético. Por otro lado, no se a podido discernir entre los posibles diferentes modelos para los materiales SrLnCoRuO_6 y SrLnNiRuO_6, debido a la baja intensidad de la señal magnética.

La serie (CaLn_2CuTi_2O_9, Ln=Pr,Nd,Sm; BaLn_2CuTi_2O_9, Ln=La,Pr,Nd) de las perovskitas triples se ha estudiado a temperatura ambiente y a altas temperaturas. Aunque en este tipo de compuestos con proporciones 1:2 pudiese existir un ordenamiento entre los cationes Cu y Ti, que tendría una fase prototipo diferente ($P\bar{3}m1$) a los que se han estudiado hasta ahora, el análisis de los datos de difracción no han dejado lugar a duda: Cu y Ti están totalmente desordenados en la posición B de la perovskita simple. Los materiales CaLn_2CuTi_2O_9 cristalizan a temperatura ambiente en la simetría ortorrómbica $Pbnm$, mientras que BaLn_2CuTi_2O_9 cristalizan en la tetragonal $I4/mcm$. Mediante la teoría de grupos se ha sabido que la ruptura de simetría total a la fase tetragonal es posible mediante un único modo activo, R_4^+.

Los materiales con Ca se han estudiado a altas temperaturas, con la intención de observar alguna transición de fase estructural. Sin embargo, no se a podido observar ninguna.